

# Georgeite: A rare gem for catalysis

Paul John Smith

*February 2015*

Thesis submitted in accordance with the requirement of Cardiff  
University for the degree of Doctor of Philosophy



Johnson Matthey



Cardiff Catalysis Institute  
Sefydliad Catalyddu Caerdydd

*“All things excellent are as difficult as they are rare”*

**Baruch Spinoza**

## DECLARATION

This work has not been submitted in substance for any other degree or award at this or any other university or place of learning, nor is being submitted concurrently in candidature for any degree or other award.

Signed.....(candidate)      Date.....

## STATEMENT 1

This thesis is being submitted in partial fulfilment of the requirements for the degree of doctor of philosophy (PhD).

Signed.....(candidate)      Date.....

## STATEMENT 2

This thesis is the result of my own independent work/investigation, except where otherwise stated. Other sources are acknowledged by explicit references. The views expressed are my own.

Signed.....(candidate)      Date.....

## STATEMENT 3

I hereby give consent for my thesis, if accepted, to be available online in the University's Open Access repository and for inter-library loan, and for the title and summary to be made available to outside organisations.

Signed.....(candidate)      Date.....

## STATEMENT 4: PREVIOUSLY APPROVED BAR ON ACCESS

I hereby give consent for my thesis, if accepted, to be available online in the University's Open Access repository and for inter-library loans **after expiry of a bar on access previously approved by the Academic Standards and Quality Committee.**

Signed.....(candidate)      Date.....

## Summary

The amorphous hydroxycarbonate termed georgeite has been investigated as a catalyst precursor for the preparation of Cu/ZnO/Al<sub>2</sub>O<sub>3</sub> industrial catalysts. A co-precipitation route is currently used to prepare crystalline hydroxycarbonate precursors, but georgeite is difficult to prepare in this methodology due to its low stability.

However, georgeite is shown to be readily prepared by supercritical anti-solvent precipitation using CO<sub>2</sub> and by modifying the co-precipitation route. Using georgeite precursors provides access to a new class of Cu/ZnO/Al<sub>2</sub>O<sub>3</sub> catalysts. Such catalysts illustrate superior activity and stability in comparison to the industrial catalyst for the low temperature shift (LTS) reaction. This is achieved without alumina, suggesting this component could be made redundant in future catalyst design. For methanol synthesis, georgeite derived catalysts also display superior activity to comparison to the industrial standard for the initial 10 hours. However, the severe deactivation rate is a fundamental problem which hinders their performance. Alumina is seen as an essential component in this reaction.

Extensive characterisation of georgeite was carried out to rationalise the catalyst performances. Malachite is widely cited as the optimum hydroxycarbonate precursor so this phase was also investigated for direct comparison. Georgeite is a distinct phase and not a nano-scale form of malachite. The structures are different down to the shortest level of ordering possible. The calcination step was optimised for both precursors, which results in the formation of highly strained CuO crystallites, < 5 nm in diameter, which are stabilised by residual carbonate. Georgeite retains distinct carbonate species forming a modified carbonate metal oxide. The high thermal stability of this carbonate enables smaller crystallites to be maintained through the whole catalyst preparation. The retention of the highly porous meso-structure of the precursor is also essential for optimum catalyst performance. Moreover for the LTS reaction, construction of optimum catalysts is correlated to negligible sodium loadings.

## Abstract

The industrial Cu/ZnO/Al<sub>2</sub>O<sub>3</sub> heterogeneous catalyst has been in commercialisation for more than 50 years, whilst ambiguity still remains regarding its synthesis procedure. This involves a multi-step process, whereby each of these steps contributes to the resulting microstructural features of the final state catalyst. The initial step involves preparation of a crystalline hydroxycarbonate by aqueous co-precipitation using metal nitrates and sodium carbonate. This is a highly sensitive technique, whereby the retention of residual nitrates and alkali metals is highly influential on the resulting catalyst activity. These impurities are poisons and inhibit the full potential of such catalysts from being exploited. Furthermore, the manufacture of these catalyst materials requires renewed research and investment in order to be more compliant with green chemistry. The widespread utilisation of nitrate salts is primarily attributed to their low cost and significant solubility in aqueous media. However, production of nitrate waste streams places a pronounced burden and strain on our environment and has resulted in government legislation. In many studies, the mineral malachite has been identified as the optimum hydroxycarbonate phase for the role of catalyst precursor. However, whilst fine-tuning of the precipitation route has taken place over the years regarding its optimization, it has in essence remained largely unchanged during this timeframe.

Consequently, the work presented in this thesis focuses on identifying, understanding and improving sustainable synthesis routes for the preparation of Cu/ZnO/Al<sub>2</sub>O<sub>3</sub> catalysts that are devoid of nitrate and alkali-metal reagents. Two preparation routes using precipitation techniques for the production of hydroxycarbonates is reported which fulfil these requirements. This involves using supercritical CO<sub>2</sub> as an anti-solvent precipitant, as well as utilising a modified co-precipitation methodology based on the current industrial procedure. Moreover, efforts have specifically focused on the preparation of the amorphous hydroxycarbonate termed georgeite. Thus the work neglects the large volume of literature reporting malachite as the optimum catalyst precursor. The ability to readily manufacture what was previously known to be a rare mineralogical phase could potentially open up additional applications.

A series of Cu, Zn and Al containing georgeite precursor materials were produced from metal acetate salts using the semi-continuous supercritical CO<sub>2</sub> anti-solvent (SAS) process. The addition of water to the system was found to result in a phase transformation of the resulting precipitate from a disordered mixed metal acetate to the georgeite phase. The physicochemical properties of the precipitant are also highly sensitive to the content of water used, whereby a compromise must be struck between enhancing the content of georgeite produced in the resulting precipitate and maintaining an optimum homogeneous system to operate in. Despite georgeite being a meta-stable

phase, it is shown to be readily made. It is capable of incorporating both zinc and aluminium into its phase, which enhances the thermal stability of the material. This can be achieved without the production of additional by-phases, which currently implies no limit to the degree of zinc and aluminium incorporation. The choice of aluminium reagent has been investigated, whereby the aluminium acetylacetonate salt and an aluminium boehmite sol have been identified as suitable reagents. Alternatively, georgeite precursors can be readily prepared by co-precipitation using ammonium carbonate reagents. Whilst the simultaneous formation of a copper-ammine complex hinders the precipitation process, these materials can still compete against conventional malachite precursors. This is attributed to the exclusion of sodium carbonate in the preparation which renders the avoidance of catalytic poisons. However, precursors prepared by co-precipitation are still illustrated to be inferior to those prepared using supercritical technology.

Georgeite derived catalysts prepared by both SAS and co-precipitation techniques are shown to be capable of competing against established industrial catalysts derived from crystalline precursors. For methanol synthesis, the georgeite catalysts have superior activity for the initial 10 hours but a severe deactivation phenomenon appears to hinder their performance and is a fundamental problem in this chemical process. It is plausible that this deactivation is correlated to the density of intermediate chemical species on the catalyst surface, which facilitates Cu sintering. However in direct contrast, these catalysts display exceptionally superior performance in comparison to the industrial standard for the LTS reaction, both in terms of catalyst activity and stability. This can be achieved without the alumina component which could eventually make it redundant in the construction of these catalysts. It is emphasised that these significant findings will permanently alter the way georgeite is perceived in the field of Cu/ZnO/Al<sub>2</sub>O<sub>3</sub> catalysts regarding how these distinct catalysts operate under testing conditions.

Evidently, the 'structure-activity' relationship was examined in more detail using state of the art techniques to rationalise these catalyst behaviours. This involved examination of both georgeite and malachite precursors, and their subsequent evolution into final state catalysts. This enabled a direct comparison to be made which could shed new light on their unique properties. It was determined that both precursors have a porous meso-structure, which is found to be a key attribute of an optimum catalyst. However, the formation of intimately mixed, poorly structured phases derived from high temperature carbonate species with negligible sodium loadings are also expressed as essential components of an optimum catalyst, and this is readily achieved from georgeite precursors.

## Acknowledgements

First and foremost, I would like to acknowledge and express my sincere gratitude to my supervisor Professor Graham Hutchings for the immeasurable amount of support, guidance and constructive criticism provided throughout this study. I am forever grateful for being given the opportunity to work within the Cardiff Catalysis Institute at Cardiff University, as well as being awarded a challenging yet interesting PhD which has enabled me to obtain a diverse range of skills across both the scientific and academic spectrum.

I am also conscious of a very considerable debt I owe to various other pioneers of the subject, who together have also provided invaluable guidance and motivation, enabling me to exploit my full potential, whilst simultaneously making these times an enjoyable and fruitful experience. In particular I would like to outline my deepest gratitude to Dr Simon Kondrat. There is no doubt that the work presented herein would be of such a high standard without his intervention. The advice, guidance, tuition and motivation provided was truly remarkable and will never be forgotten. In particular, I often found the informal discussions most useful which will always make me smile and it is without doubt that I wish Simon all the very best in his future career. Special thanks must also be given to the rest of the academic team in Cardiff which continuously supported me. In no particular order I would like to thank Professor Stuart Taylor, Professor Michael Spencer, Dr Tom Davies and Dr Jon Bartley. Together we were the 'supercrit team' and I would like to think we shared many great laughs whilst developing some very high profile science which I hope one day will be published.

This study was joint funded and sponsored by the Engineering and Physical Sciences Research Council (EPSRC) and Johnson Matthey. I would therefore like to thank both establishments for making this work possible. This involved a collaboration between Cardiff University, Johnson Matthey and the UK catalysis hub. Special thanks must therefore also be given to a series of individuals who are experts in their own fields. At Johnson Matthey I would like to thank my industrial supervisors Gordon Kelly and Colin Park. The formal meetings provided a fresh perspective and were extremely insightful, especially in identifying areas requiring additional investigation. I also appreciate allowing me to spend time at Johnson Matthey and to yield some valuable industrial experience. I also have to thank Dr Leon van der Water, Helen Stanness and Colin Ranson for technical help regarding the catalyst preparation, testing and analysis. At the UK catalysis hub I would like to thank Dr Peter Wells and Dr Phil Carter for their assistance regarding the implementation and analysis of state of the art EXAFS and PDF data, which would not have been possible from the author alone. Additional thanks must also go to Dr Catherine Brooks for kindly

carrying out valuable EGA analysis at Harwell. Together this collection of individuals enabled essential findings to be obtained, which provides the core principles and foundation of this work.

At Cardiff University there are still many individuals that warrant my sincerest gratitude. Without the ‘workshop boys’, who are Steven Morris, Alun Davies and John Cavanagh this work would again not have been possible. Despite your busy workloads I appreciate the considerable time and effort spent assisting me regarding the maintenance of instrumentation, especially during my early years where ‘cross-threading’ was the norm. I would also like to thank Chris Morgan in maintaining the high quality of the labs, as well as Georgi Lalev for assistance with TEM and STEM imaging.

However, my time in the Cardiff Catalysis Institute would not have been complete without the countless banter, laughs and socially stimulating times I endured amongst my peers. After all a certain Professor would always say to us “Work hard, play hard”. It would be difficult to mention everyone without making an extensive list but you all know who you are. However, a small number of people deserve additional thanks, not just for providing me with special memories but for the additional support and help when required. In no particular order, I would like to thank the soon-to-be doctors Benjamin Yeo, Samuel Pattison, Gavin King, David Watson and John Mark Douthwaite. Thank you for making this such an enjoyable experience and I hope we remain friends for many, many years.

Finally, I have to of course thank my family for their continuous support and inspiration, not just for these last few years but throughout my entire life. Thank you so much Mum and Dad as well as my brothers Andrew and Steven. You always were very supportive with the decisions I made and words simply cannot express how much you have always helped me.

Cardiff University, February 2015

Paul John Smith

## List of abbreviations

acac	Acetylacetonate
ADF	Annular Dark Field
at	Atomic
BET	Brunauer Emmett Teller
CHN	Carbon, Hydrogen and Nitrogen
CP	Co-precipitation
DFT	Density Functional Theory
DRIFTS	Diffuse Reflectance Infrared Fourier Transform Spectroscopy
DRUVS	Diffuse Reflectance Ultra Violet-Visible Spectroscopy
DTA	Differential Thermal Analysis
EDX	Energy Dispersive X-Ray analysis
EGA	Evolved Gas Analysis
EXAFS	Extended X-Ray Absorption Fine Structure
FT-IR	Fourier Transform Infrared Spectroscopy
GAS	Gas Anti-Solvent
HT-CO <sub>3</sub>	High temperature carbonate
HTS	High Temperature Shift
ICP-MS	Inductively Coupled Plasma Mass Spectrometry
JM	Johnson Matthey
LTS	Low Temperature Shift
M	Molar (or mol dm <sup>-3</sup> )

MCP	Mixture Critical Point
MP-AES	Microwave Plasma Atomic Emission Spectroscopy
PDF	Pair Distribution Function
ppm	Parts per million
RESS	Rapid Expansion of Saturated Solutions
SA	Surface Area
SAS	Supercritical Anti-Solvent
sc-CO <sub>2</sub>	Supercritical CO <sub>2</sub>
SCF	Supercritical Fluid
SEM	Scanning Electron Microscopy
STEM	Scanning Transmission Electron Microscopy
TCD	Thermal Conductivity Detector
TEM	Transmission Electron Microscopy
TGA	Thermogravimetric Analysis
TPD	Temperature Programmed Desorption
TPR	Temperature Programmed Reduction
vol	Volume
WGS	Water Gas Shift
wt	Weight
XAS	X-Ray Absorption Spectroscopy
XPS	X-Ray Photoelectron Spectroscopy
XANES	X-Ray Absorption Near Edge Structure
XRD	X-Ray Diffraction

## Contents

Declaration/statements.....	ii
Summary.....	iii
Abstract.....	iv
Acknowledgements.....	vi
List of abbreviations.....	viii
<b>1.0. Introduction.....</b>	<b>1</b>
1.1. Introduction.....	1
1.2. Basic principles of catalysis.....	1
1.2.1. Definition of catalysis.....	1
1.2.2. Essential functions of catalyst systems.....	4
1.2.3. Classification of catalyst systems.....	5
1.2.4. Green chemistry and its relation to catalysis.....	5
1.3. Literature review of Cu/ZnO/Al <sub>2</sub> O <sub>3</sub> heterogeneous catalyst systems: Synthesis of highly dispersed solids and their activity.....	6
1.3.1. Preparation of Cu/ZnO/Al <sub>2</sub> O <sub>3</sub> catalysts and their 'structure-activity' relationship .....	6
1.3.2. Methanol synthesis.....	16
1.3.3. The low temperature shift (LTS) reaction.....	23
1.3.4. Conclusions.....	28
1.4. Outline of thesis.....	28
1.5. Catalyst preparation using supercritical fluid precipitation.....	31
1.5.1. Introduction to supercritical fluids: definition, properties and applications.....	31
1.5.2. Preparation of catalysts using supercritical fluids.....	34
1.5.3. Catalysts prepared by scCO <sub>2</sub> anti-solvent precipitation.....	39
1.6. References.....	41

<b>2.0. Experimental</b> .....	51
2.1. Introduction.....	51
2.2. Materials.....	51
2.3. Catalyst preparation.....	51
2.3.1. Supercritical anti-solvent precipitation.....	52
2.3.1.1. SAS apparatus.....	52
2.3.1.2. Catalyst preparation.....	54
2.3.2. Co-precipitation.....	55
2.4. Characterisation.....	57
2.4.1. X-Ray diffraction (XRD).....	57
2.4.2. Extended X-ray absorption fine structure (EXAFS).....	59
2.4.3. Pair distribution function (PDF).....	61
2.4.4. Thermogravimetric analysis (TGA), differential thermal analysis (DTA) and evolved analysis (EGA).....	62
2.4.5. Temperature programmed reduction (TPR) and temperature programmed desorption (TPD).....	63
2.4.6. Infrared spectroscopy.....	64
2.4.7. Raman spectroscopy.....	65
2.4.8. Diffuse reflectance ultra violet-visible spectroscopy (DRUVS).....	67
2.4.9. Brunauer Emmet Teller (BET) and density functional theory (DFT) Monte Carlo analysis.....	67
2.4.10. Copper surface area analysis.....	69
2.4.11. Helium pycnometry.....	71
2.4.12. Scanning electron microscopy (SEM), transmission electron microscopy (TEM) and scanning transmission electron microscopy (STEM).....	71
2.4.13. Microwave plasma atomic emission spectroscopy (MP-AES).....	72
2.4.14. Inductively coupled plasma mass spectrometry (ICP-MS).....	74
2.5. Catalyst testing.....	74
2.5.1. Methanol synthesis.....	75
2.5.2. Low temperature water gas shift (LTS) reaction.....	75
2.6. References.....	77

<b>3.0. Optimization of precipitation synthesis routes to georgeite hydroxycarbonate catalyst precursors.....</b>	<b>79</b>
3.1. Introduction.....	79
3.2. Optimization of the content of water used as a co-solvent in binary copper-zinc SAS systems.....	79
3.2.1. Results and discussion.....	80
3.2.2. Conclusions from water content optimization.....	91
3.3. Optimization of the binary Cu/Zn molar ratio of SAS prepared zincian georgeite.....	93
3.3.1. Results and discussion.....	93
3.3.2. Conclusions from optimization of the Cu/Zn molar ratio.....	101
3.4. Incorporation of aluminium into SAS prepared zincian georgeite.....	102
3.4.1. Results and discussion.....	103
3.4.2. Conclusions from aluminium incorporation into SAS prepared zincian georgeite.....	115
3.5. Synthesis of zincian georgeite by co-precipitation.....	116
3.5.1. Results and discussion.....	117
3.5.2. Conclusions from co-precipitation studies on zincian georgeite.....	130
3.6. Catalyst testing of georgeite materials.....	131
3.6.1. Results and discussion.....	131
3.6.2. Conclusions from catalyst testing.....	141
3.7. References.....	142
<b>4.0. Deciphering key structural differences between georgeite and malachite hydroxycarbonates</b>	<b>146</b>
.....	146
4.1. Introduction.....	146
4.2. Determining physicochemical properties of copper and copper-zinc hydroxycarbonate phases.....	147
4.2.1. Results and discussion.....	148
4.2.2. Conclusions from studies on the physicochemical properties of copper and copper-zinc hydroxycarbonate phases.....	155
4.3. Investigating the thermal decomposition behaviour of copper and copper-zinc hydroxycarbonate phases.....	157

4.3.1. Results and discussion.....	157
4.3.2. Conclusions from thermal decomposition studies on copper and copper-zinc hydroxycarbonate phases.....	182
4.4. Examining final state catalyst derived from zincian georgeite and zincian malachite from <i>in-situ</i> reduction studies.....	183
4.4.1. Results and discussion.....	183
4.4.2. Conclusions from <i>in-situ</i> reduction studies on final state catalysts derived from zincian georgeite and zincian malachite.....	188
4.5. References.....	189
<b>5.0. Conclusions and future work.....</b>	<b>193</b>
5.1. Conclusions.....	193
5.2. Future work.....	204
5.3. References.....	207
<b>6.0. Supplementary.....</b>	<b>209</b>

## 1.0. Introduction

### 1.1. Introduction

The wide spread utilisation of catalysts in the chemical and pharmaceutical industries has shaped the world in which we live. Essential resources such as fertilisers, medicine, energy carriers and plastics are just some examples from an extensive list which are fundamental in order to maintain our quality of life. The availability of such materials at a reasonable price is a result of industry and commercialisation whereby catalysis lies at the heart of these principles. Even if products can be manufactured alternatively without catalysis it often comes at a heavy price. Catalysts provide access to alternative synthesis routes of reduced energy consumption which subsequently facilitates a reduction of polluting gas emissions in our atmosphere. Thus catalysis also lies at the heart of green chemistry which uses the concept 'sustainability' to distinguish methods and processes that ensure the long term productivity of our environment. Consequently, the demand for improved catalyst systems from a commercial, environmental and academic perspective is the continuous driving force for the globalised interest in catalysis research which is implemented in numerous developed countries today.

### 1.2. Basic principles of catalysis

#### 1.2.1. Definition of catalysis

A catalyst is a small amount of a substance present in a reaction system that accelerates the desired chemical reaction(s), but little changes during the reaction<sup>(1,2)</sup>. Similarly, it is described as a substance that increases the rate at which a chemical system approaches equilibrium, without being consumed in the process. Catalysis is the phenomenon of a catalyst in action. The origin of these terms was first introduced in 1836 by J. J. Berzelius in order to rationalise strange findings observed from the noble metals platinum and palladium. The word catalysis actually comes from two Greek words, the prefix *cata-* meaning down, and the verb *lysein* meaning to split or break.

For a given chemical process the fundamental principle of catalysis is associated with the lowering of the activation energy. This is the minimum quantity of energy reacting species must possess in order to undergo a specified reaction. However, to truly understand catalysis it is first important to define and distinguish thermodynamic and kinetic concepts. Chemical thermodynamics defines whether or

not a chemical reaction will proceed and if so how far as defined by the equilibrium position. This arises because there can only be one value for the standard Gibbs free energy change in any given reaction (**Equations 1.1** and **1.2.**).

**Equation 1.1.**             $\Delta G = \Delta H - T \Delta S$

**Equation 1.2.**             $\Delta G = - R T \ln(K)$

Whereby  $\Delta G$  = the Gibbs free energy,  $\Delta H$  = enthalpy,  $T$  = temperature,  $\Delta S$  = entropy,  $R$  = the Gas constant =  $8.314 \text{ (J K}^{-1} \text{ mol}^{-1}\text{)}$  and  $K$  = the equilibrium constant. This implies that a forward chemical process with negative Gibbs free energy will be spontaneous, with larger negative values resulting in larger equilibrium constants and hence yield. However, it is important to appreciate that thermodynamics cannot tell us how fast such processes will proceed. How fast the equilibrium is attained is defined by chemical kinetics. Clearly, in the design of chemical processes both concepts matter. If the kinetics is favourable a viable reaction could still be ruled out by the thermodynamics. In other words if the rate is fast a chemical process will still not be deemed plausible if the yield is low and the equilibrium constant is small. Likewise, there is no applicability in having a system which can potentially attain a high yield of product if the equilibrium cannot be reached within a suitable timescale.

The Gibbs free energy, enthalpy and entropy are state functions. This means they depend only on the initial and final states of the system and not the path taken to move from one to the other. However this is not apparent regarding reaction kinetics and it is this key principle which enables the function of a catalyst to be truly understood. A catalyst can increase the rate only of a reaction that is already thermodynamically feasible. It cannot initiate one that is thermodynamically impossible whereby catalysed reactions are as much subject to the laws of thermodynamics as un-catalysed ones. Instead a catalyst modifies the reaction kinetics and allows the equilibrium to be reached at a faster rate simply by providing an alternative chemical pathway of lower activation energy to proceed through. These various different pathways are governed by different reaction mechanisms and chemical processes will always proceed *via* the route of lowest activation energy. A suitable example involves the oxidation of carbon monoxide by palladium (**Equation 1.3.** and **Figure 1.1.**).



The energy difference between the reactants (initial) and product (final) states is governed by the thermodynamic parameters of the system and in this process it is exothermic (2. blue) with a  $\Delta H$  value of  $-284 \text{ kJ mol}^{-1}$ , regardless of the presence of the palladium catalyst. However, without the use of the catalyst a considerably large energy input is required in order to overcome the activation

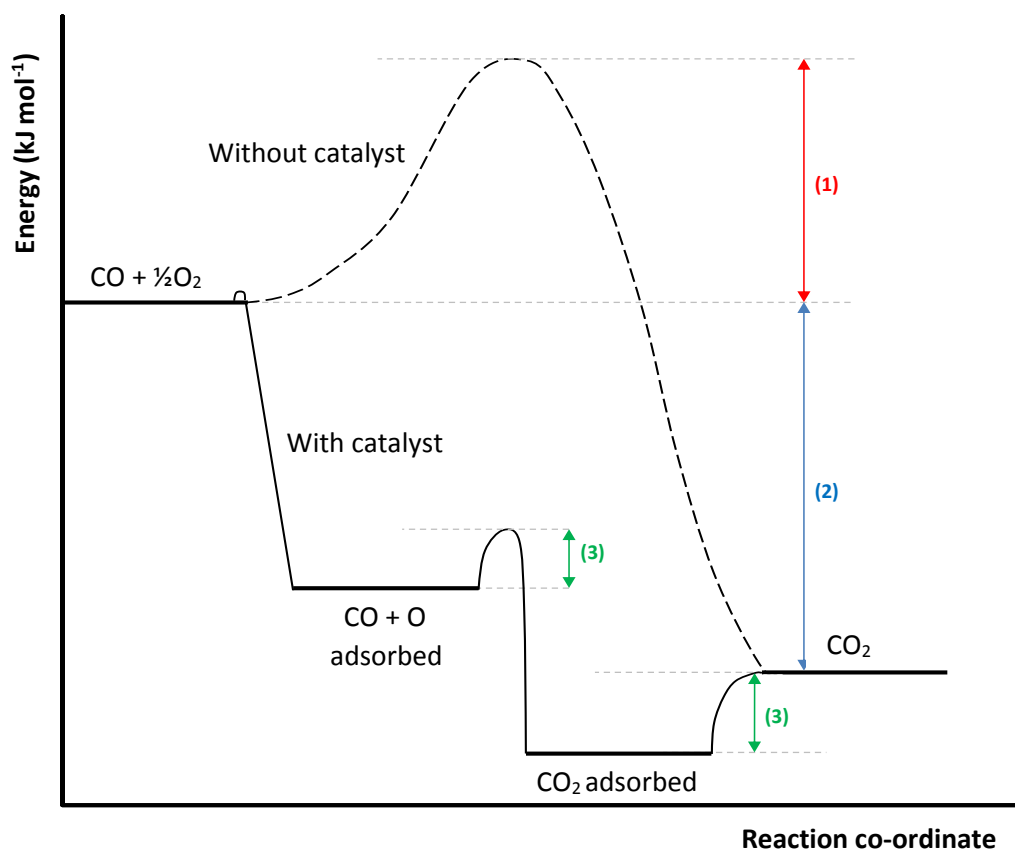


**Figure 1.1.** Energy diagram of  $\text{CO} + \frac{1}{2}\text{O}_2 \rightarrow \text{CO}_2$  catalysed by palladium. The initial and final states do not change by the presence of the catalyst<sup>(2)</sup>.

energy associated with this reaction pathway (1. red). Since  $\Delta G$  is also negative this energy barrier also helps to explain why the forward reaction does not spontaneously occur. When the catalyst is present the reaction pathway, and hence mechanism, changes whereby three essential points should be noted. Firstly, after each catalytic cycle one molecule of  $\text{CO}_2$  is produced and the catalyst returns to its initial state. Secondly, regarding the catalytic process, an oxygen molecule in which two oxygen atoms are strongly bonded dissociates into two oxygen atoms on the surface of palladium with a very low energy barrier. Thirdly and most importantly, these resulting oxygen atoms are highly reactive and this is the basic principle of a good catalyst. If these atoms are too stable the subsequent step becomes highly endothermic with a large secondary activation energy barrier and the reaction might not take place. If the first step is too exothermic it might occur very easily but again the subsequent step would become very endothermic and the overall reaction may not proceed. Alternatively if the first step was highly endothermic, as seen for the un-catalysed reaction, it may not take place. Therefore, it is clear that a good catalyst is defined as having moderate affinity to the key intermediate which itself has moderate thermodynamic stability. It is also apparent that the total activation energy required for the catalysed pathway (3. green) is lower than the un-catalysed pathway (red) which fully illustrates the practicality of catalysis.

### 1.2.2. Essential functions of catalyst systems

The activity, selectivity, durability and cost of preparation are the criteria used to assess a catalyst regarding its applicability for commercialisation.

*Activity* refers to the rate that the chemical equilibrium is reached. A catalyst with negligible activity may proceed at a similar rate to the un-catalysed procedure. Alternatively, a reaction which does not occur in the absence of a catalyst may proceed in its presence. Catalysts of higher activity could result in smaller reactors or less catalyst material being utilised which will have cost implications.

*Selectivity* is a parameter which rises in importance as the complexity of the reaction increases from the subsequent number of observed products. As seen in the case of CO oxidation ([Equation 1.3.](#)) there is only one product to consider and therefore selectivity is not of any importance in this application. However this is not true for the majority of chemical reactions investigated. Considering the homogeneous oxidation of propene as an example, if the reaction was allowed to proceed through to completion from leaving the reaction mixture in contact with the catalyst indefinitely, the final products would be CO<sub>2</sub> and water. However, it is possible to isolate a large number of intermediate or metastable oxidation products in good yield such as acrolein, acetic acid and acrylic acid. This further illustrates the benefits of catalysis since as there is no fundamental reason why a catalysed reaction should give the same initial products as an un-catalysed reaction despite the final products always being identical.

*Durability* or catalyst lifetime is important in the context of commercialised catalysts. Whilst catalysts are defined as 'substances that are not consumed within chemical processes' in reality this is not the case as they gradually deteriorate with time. A broad range of factors can induce deactivation. Examples include implementing routine thermal cycling events which results in sintering of active components, the gradual build-up of by-products on the catalyst surface which block active sites and the long term exposure to poison impurities that originate from reactant gas feeds. It is important to appreciate that catalysts which are expensive to prepare could still be commercialised if the durability can compensate for it.

*Cost of preparation* includes the materials used to prepare catalysts as well as the expense and complexity associated with the preparation itself. Catalysts which can be prepared using cheap abundant materials from energy sustainable synthetic routes are clearly more likely to be utilised but a decision must be made which also takes the catalyst performance into consideration.

### 1.2.3. Classification of catalyst systems

Catalysts can be divided and classified into three types; homogeneous, heterogeneous and enzymes. When the catalyst is of the same phase as the reactants and no phase boundary exists we speak of homogeneous catalysis. Examples include nitrous oxide catalysing the oxidation of sulphur dioxide in the gas phase or when acids or bases catalyse the mutarotation of glucose in the liquid phase.

However, when a phase boundary separates the catalyst from the reactants we speak of heterogeneous catalysis. An example includes the synthesis of ammonia catalysed by iron whereby in this case the reactants are gaseous and the catalyst is a solid. Another example is the hydrogenation of nitrobenzene to aniline catalysed by palladium. In this case, the catalyst is still a solid but nitrobenzene is of the liquid phase. This is particularly important to emphasise as the work presented herein is of heterogeneous catalysis.

In nature enzymatic catalysts are predominant for most metabolic reactions. Enzymes are large, complex organic molecules, usually in the form of proteins that form a lyophilic colloid. They are considered quite different to the other two forms of catalysis.

### 1.2.4. Green chemistry and its relation to catalysis

The principle of green chemistry is the design and manufacture of desired products while aiming to eliminate the production of compounds hazardous to the environment and human health<sup>(3)</sup>. As reported by Horvath and Anastas, catalysis remains one of the most important fields of green chemistry by providing atom-economical, selective, and energy efficient solutions to many industrially important problems<sup>(4)</sup>. It is a necessity to use catalytic reagents, which are as optimised as possible, at the expense of atom inefficient and environmentally harmful stoichiometric reagents for these reasons.

However, correlating catalysis to the principles of green chemistry is often counter intuitive. Whilst there is no doubt that the performances of catalysts assist in fulfilling the requirements of green chemistry this is not often the case regarding their preparation. In other words, in order for catalysis to truly be considered as a key component of green chemistry the synthesis routes used to manufacture these materials must also be rendered green and obey the same principles. The literature reports a vast array of synthetic procedures used in the production of specific catalyst systems but in particular nitrate salt reagents are frequently used. The low cost and high solubility of various nitrate salts is most likely attributed to their widespread use. However, high concentrations of nitrate in aqueous waste effluents is environmentally harmful and requires extensive waste water

treatment<sup>(5,6)</sup>. The principles of green chemistry state that this should be avoided for chemical synthesis processes. This is now a major problem as the UK government has recently introduced a nitrate initiative as well as severely limiting the amount of nitrate effluent that can be disposed to watercourses. More importantly, nitrate effluent production has been banned in specific months of the year. It can be seen that whilst utilising salts of high solubility is often desirable from a research or academic perspective this in turn is highly undesirable from an environmental perspective. The negative charge of the nitrate anion prevents it from being effectively bound to soil and consequently leaches. Nitrates can rapidly concentrate in lakes, rivers as well as our groundwater supply resulting in eutrophication and blue baby syndrome.

### 1.3. Literature review of Cu/ZnO/Al<sub>2</sub>O<sub>3</sub> heterogeneous catalysts: Synthesis of highly dispersed solids and their activity

This thesis specifically focuses on the Cu/ZnO/Al<sub>2</sub>O<sub>3</sub> catalyst which is a highly established, multi-component system utilised in industry. However, before the objectives of this thesis are outlined it is first essential to present the vast array of literature already reported on this catalyst system. This will put everything into context and allow for a better understanding of this field of research as well as the subsequent objectives outlined for this project. The first section of this review focuses predominantly on catalyst preparation with optimisation of the various synthetic parameters in conjunction to the 'structure-activity' relationship. The two subsequent sections predominantly focus on the performance of these catalysts for methanol synthesis and the low temperature shift reaction (LTS) respectively.

#### 1.3.1. Preparation of Cu/ZnO/Al<sub>2</sub>O<sub>3</sub> catalysts and the 'structure-activity' relationship

The industrial preparation of Cu/ZnO/Al<sub>2</sub>O<sub>3</sub> catalysts is extensive and consists of a multi-step procedure (**Figure 1.2.**). Each step subsequently contributes to the structural characteristics of the catalyst finally derived making it a highly sensitive process. Consequently, optimization of each step is essential to yield a catalyst of commercial value. Many authors correlate the performance of the final state catalyst to each of these individual procedures, in other words to the 'memory' of the catalyst of its origin<sup>(7-12)</sup>.

The first step of the multi-step procedure regards preparation of the catalyst precursor. This is achieved by aqueous co-precipitation simply by mixing together solutions of sodium carbonate and metal nitrates (Cu, Zn and Al). The resulting precipitate yields the catalyst precursor which is a metal

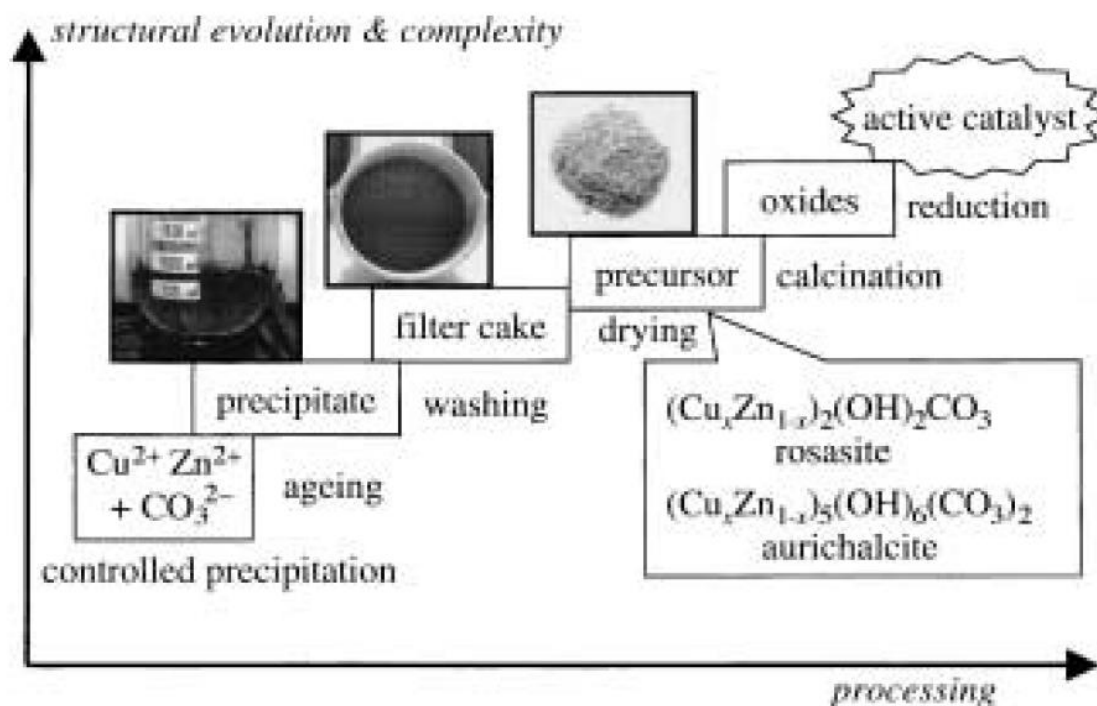


**Figure 1.2.** Scheme of the preparation procedure for Cu/ZnO catalysts *via* hydroxycarbonate precursors<sup>(7)</sup>.

hydroxycarbonate. However the procedure is complex and highly sensitive with a significant range of synthesis parameters to consider such as: pH (constant or uncontrolled), temperature, reagent type ( $\text{Na}_2\text{CO}_3$ ,  $\text{K}_2\text{CO}_3$  or  $(\text{NH}_4)_2\text{CO}_3$ ), the metal molar ratio, concentration of starting solutions, stirring rate as well as the subsequent ageing conditions (time, temperature and pH control). These conditions determine the type of hydroxycarbonate which is produced. Typical crystalline phases obtained going from Cu-rich to Zn-rich compositions in binary preparations are malachite  $\text{Cu}_2(\text{OH})_2\text{CO}_3$ , zincian malachite  $(\text{Cu}_x\text{Zn}_y)_2(\text{OH})_2\text{CO}_3$ , aurichalcite  $(\text{Cu}_x\text{Zn}_y)_5(\text{OH})_6(\text{CO}_3)_2$  and hydrozincite  $\text{Zn}_5(\text{OH})_6(\text{CO}_3)_2$ <sup>(11)</sup>. Precipitates can consist of just a single phase (monophasic) or be a mixture of several of these phases (polyphasic). As a result of the complexity of the procedure, many studies only focus on the binary system, whereby Al nitrate is excluded, to use as a model in order to derive a better understanding of the preparation. In the ternary system, when Al is also considered, hydrotalcite-like compounds have also been reported with composition  $(\text{Cu}_x\text{Zn}_y)_{n-1}\text{Al}_n(\text{OH})_2(\text{CO}_3)_{x/2} \cdot m\text{H}_2\text{O}$ <sup>(13-14)</sup>. However, it is important to appreciate that the precipitation conditions do not just influence the nature of the phase(s) produced. Such conditions also influence the chemical composition and microstructure of the resulting precursor. This in turn influences the performance of the resulting catalyst, which is frequently referred to as the 'structure-activity' relationship. After the hydroxycarbonate precursor has been filtered and retained it is washed several times in hot water to remove by-product impurities before drying overnight. The resulting calcination step results in the thermal decomposition of specific ligands (nitrate, carbonate and hydroxyl) to produce an intimately

mixed metal oxide material with general formula  $(\text{CuO})_x/(\text{ZnO})_y/(\text{Al}_2\text{O}_3)_z$ . The final step is often termed the 'catalyst activation' step. An *in-situ* reduction is required in order to reduce the CuO component into the active Cu species. As a result of the highly exothermic nature of this process, extremely mild conditions must be utilised, including the use of highly dilute reduction feeds (2%  $\text{H}_2/\text{N}_2$ ) and low ramp rates (0.5-1 °C/min)<sup>(15-16)</sup>. Trace amounts of oxygen will result in the metallic Cu component being re-oxidised, and therefore, this step takes place once the reactor has been charged with the oxide material.

The majority of literature in this field of research has focused on the synthesis of the catalyst precursor using the industrial co-precipitation route. The importance of this step is reflected in the fact that the meso-structure and degree of metal dispersion (Cu, Zn and Al) in the final state catalyst can be traced back to the original catalyst precursor. Whilst optimisation of the resulting thermal treatment steps is of high importance this simply regards identifying the most mild conditions, in order to retain the highest degree of metal dispersion possible in the final state catalyst. The level of metal dispersion cannot be improved after the co-precipitation process, and so must be considered the most important in the multi-step procedure.

Under typical conditions utilised by industry the initial precipitate that forms in the co-precipitation process has been identified as georgeite<sup>(17,18)</sup>. Georgeite is a sky-blue, amorphous, Cu-based hydroxycarbonate mineral, although it has been illustrated that  $\text{Zn}^{2+}$  ions can also be incorporated into the phase<sup>(17)</sup>. The literature to date which has specifically studied georgeite is significantly limited. It is considered highly rare in mineralogical form which can be attributed to its low stability. It was first reported in 1979 by Bridge and co-workers in the Carr Boyd nickel deposit in Western Australia<sup>(19)</sup>. An ideal molecular formula for the phase was derived as  $\text{Cu}_5(\text{CO}_3)_3(\text{OH})_4 \cdot 6\text{H}_2\text{O}$ . Interestingly a universal feature reported for amorphous minerals is occluded water trapped within the structure<sup>(20)</sup>. The Britannia mine in North Wales is the only other known location georgeite has been discovered in mineralogical form. In terms of its synthetic preparation, georgeite formation has recently been reported to be favourable despite its apparent low stability<sup>(21)</sup>. Whilst many studies now acknowledge the initial formation of georgeite, it is often neglected at the expense of crystalline hydroxycarbonates for the role of catalyst precursor. Such studies have also reported that georgeite is an amorphous form of malachite with the exact same molecular formula<sup>(17,21-22)</sup>, in contrast to the original formula derived by Bridge and co-workers. This illustrates how the mineral is still not well understood and heavily overlooked.

The initial georgeite precipitate is not stable in the resulting mother liquor solution and lowers its free energy by 'ageing' into crystalline hydroxycarbonates. The solution is left to age under heat with

continuous stirring. This phenomenon is reported to occur by a solution and re-crystallisation process rather than a solid state transformation<sup>(17,23)</sup>. Since only crystalline hydroxycarbonates have been intensely investigated as catalyst precursors many research groups have outlined the importance of the ageing step and studies have focused on its optimisation<sup>(5,8,11-12,17,22-33)</sup>. These findings frequently report apparent observations that occur during the phenomenon including a temporary sharp drop in pH during crystallisation, a subsequent increase in the turbidity (or decrease in the viscosity) of the mother liquor solution as well as an apparent colour change from blue (georgeite) to green (malachite/aurichalcite) (**Figure 1.3.**). Spencer also reports the evolution of CO<sub>2</sub> during the transformation, including the initial formation of zincian malachite and aurichalcite which ages further into a single monophasic malachite precursor of higher Zn content<sup>(28)</sup>. Ageing is seen to be essential for redistributing the metal phases (Cu, Zn and Al) in order to achieve highly dispersed metal crystallites in the resulting catalyst. Consequently, this can also be correlated to a higher surface area and a higher concentration of contact points between the Cu-ZnO-Al<sub>2</sub>O<sub>3</sub> boundaries.

There is still some disagreement in the literature regarding determination of the optimum hydroxycarbonate phase. Several research groups have outlined aurichalcite as the optimum catalyst precursor<sup>(29,34-37)</sup>. However, considerable work has been carried out in this field by Behrens and co-workers who have illustrated to a high level of certainty that malachite is the optimum phase as a result of both meso- and nano-structuring effects (**Figure 1.4.**)<sup>(5,11,22,33,38)</sup>. This arises simply from the

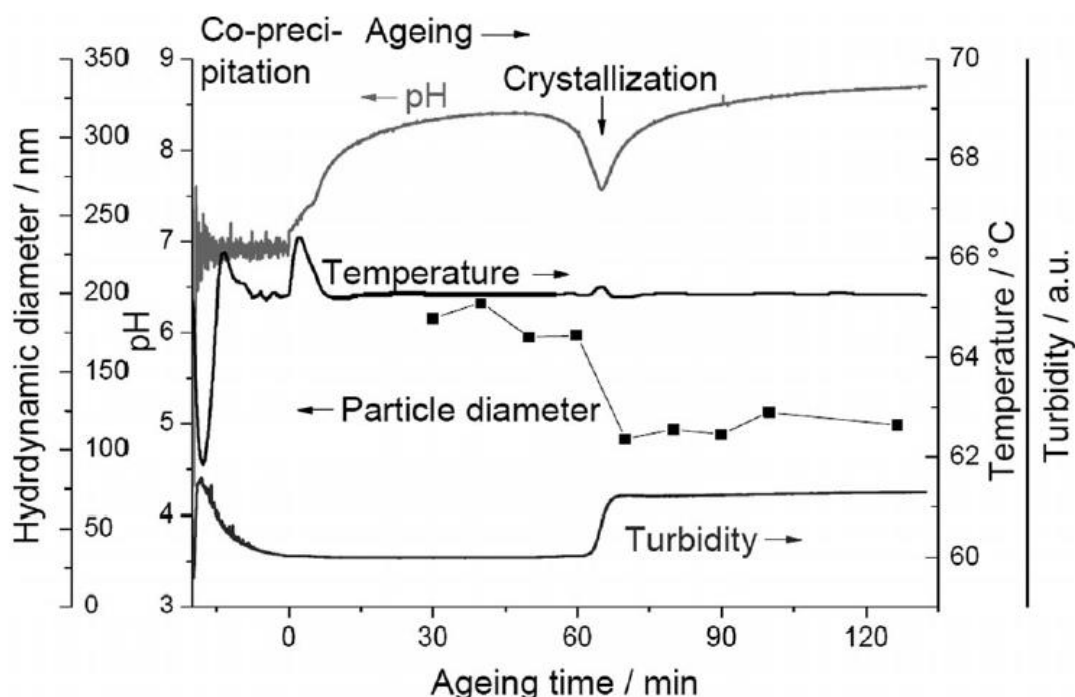


**Figure 1.3.** Evolution of pH, reactor temperature, and turbidity during co-precipitation as a function of ageing time (with constant pH = 7 and temperature = 65 °C)<sup>(11)</sup>.

unique, highly porous structure this phase crystallises into that derives from thin, interwoven nano-scale needles. As illustrated in the preparation scheme, the initial georgeite precipitate is shown to have no porosity and thus inferior physicochemical properties in comparison to malachite. During the subsequent calcination step the individual needles decompose into CuO and ZnO whilst pseudo-morphs of the precursor needles can still be observed from using optimum conditions. This step is associated with nano-structuring. Clearly, in the case of the binary precursor the effectiveness of nano-structuring depends critically on the Zn content. The closer a hypothetical Cu/Zn molar ratio of 1/1 is achieved, the higher the degree of mixing and dilution of the Cu component. Consequently, after calcination this will yield smaller oxide crystallites with higher surface area. With careful control of the final ‘activation’ step optimum catalysts can be derived with retention of the optimum porous meso-structure. Interestingly, aurichalcite and hydrotalcite hydroxycarbonates are capable of incorporating higher contents of Zn into their lattice and can achieve the desired Cu/Zn molar ratio of 1/1. Unfortunately, these phases crystallise have considerably more bulky and platelet-like morphology<sup>(14,33)</sup>. Therefore, whilst the resulting Cu crystallites are smaller they will be embedded in bulky aggregates due to the unfavourable meso-structure derived from these phases. This highlights the importance of constructing porous networks in order to render the optimised active sites accessible.

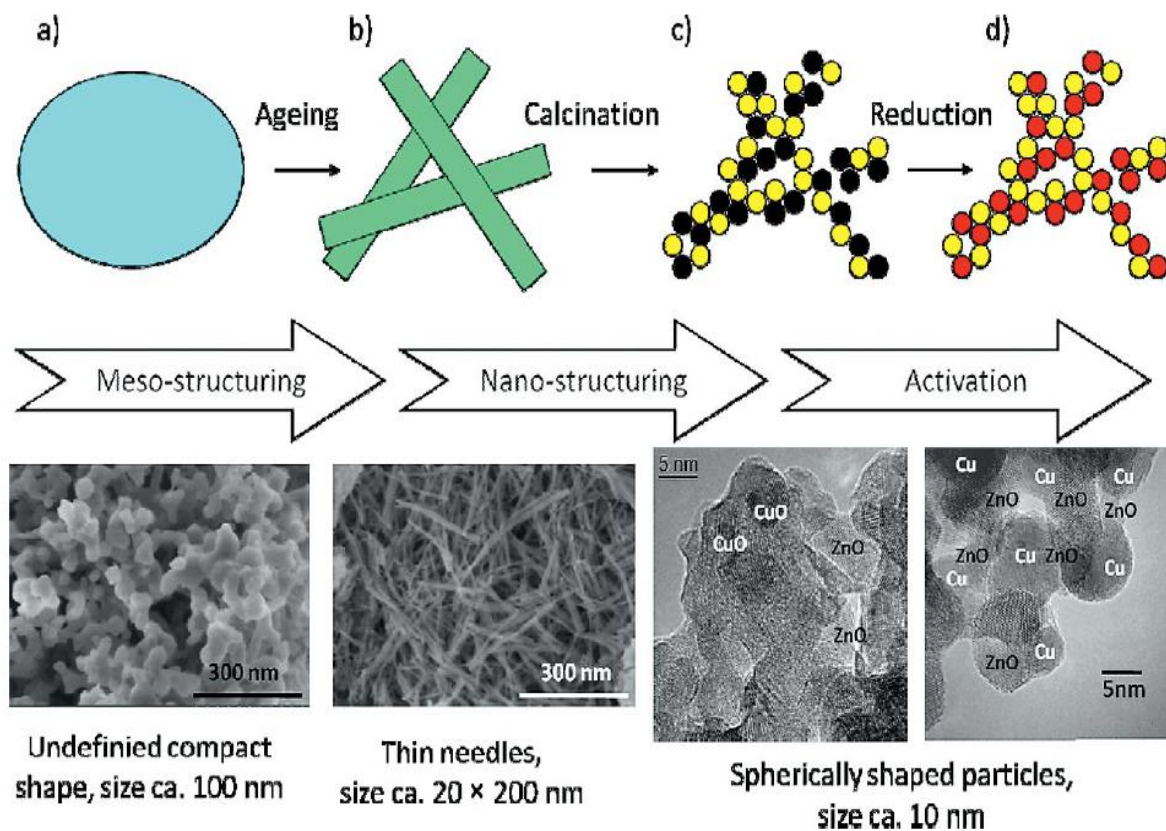


**Figure 1.4.** A simplified preparation scheme of a Cu/ZnO catalyst with electron microscopy images included. Phases in steps are as follows: (a) georgeite, (b) malachite, (c) CuO and ZnO and (d) Cu and ZnO<sup>(11)</sup>.

The optimum Cu/Zn or Cu/Zn/Al molar ratio therefore correlates to the maximum incorporation of Zn and Al into the malachite lattice to achieve optimum dilution and dispersion of the metallic components. The maximum amount of Zn that can be incorporated into the malachite lattice has been reported to be 27 at.%(38). Therefore the optimum Cu/Zn molar ratio is close to 2/1 which is frequently used in research studies. It should be noted however that there is some confusion in the literature as zincian malachite is often misidentified as rosasite(7,38). Both minerals have general chemical composition  $(\text{Cu}_x\text{Zn}_y)_2(\text{OH})_2\text{CO}_3$  but the latter is capable of incorporating larger quantities of zinc into its lattice with  $0.3 < x < 0.5$ . For these structurally related phases it has also been determined that the metal centres are surrounded by six oxygen ligands with octahedral coordination geometry. In certain instances this gives rise to the Jahn-Teller effect. This phenomenon distorts ideal  $\text{MO}_6$  octahedra units into geometries which are energetically more favourable. Interestingly, the severity is dependent upon the electron configuration of the metal whereby for  $\text{Cu}^{2+}$  ( $d^9$ ) this is highly pronounced whilst for  $\text{Zn}^{2+}$  ( $d^{10}$ ) centres it does not apply. In relation to this, one striking difference between these phases is the orientation of the Jahn-Teller elongated axis of the  $\text{CuO}_6$  octahedra in the unit cell. Unfortunately, it is not possible to prepare rosasite by the co-precipitation route as it is not energetically favourable. Behrens and Girgsdies proposed that this is probably a result of the increasing concentration of regular  $\text{MO}_6$  octahedra, which destabilises the aligned arrangement of the Jahn-Teller distortions present in malachite. Instead when Zn contents > 27% are utilised, aurichalcite formation is apparent which evidently results in a polyphasic precursor.

The findings reported on malachite and rosasite were predominantly determined from XRD which is one of the most powerful analytical tools in the evaluation of crystalline materials. It should also be highlighted that the Jahn-Teller effect in conjunction to XRD analysis is responsible for determining the maximum incorporation of Zn possible into the malachite lattice. The Jahn-Teller effect facilitates the elongation of the two axial Cu-O bond lengths in relation to the 4 equatorial bonds. Therefore, as more non Jahn-Teller  $\text{Zn}^{2+}$  replaces  $\text{Cu}^{2+}$  inside the crystal structure the d-spacing of the lattice planes perpendicular to the axial metal-oxygen bonds decreases. These lattice planes have been identified as the (20-1) and (21-1) reflections in the XRD pattern, which shift to higher  $2\theta$  values with increasing Zn content (Figure 1.5.)(5,33,38-39). Therefore, from simply measuring the d-spacing of these reflections an accurate indication of the binary atomic ratio can be derived for monophasic malachite precursors. Similar methodology was used to identify the optimum Al content which was reported to be 3.3 at.%(14).

Many research groups also have focused on optimising several other synthesis parameters of the co-precipitation route, with pH and temperature outlined in particular as important variables. Li and

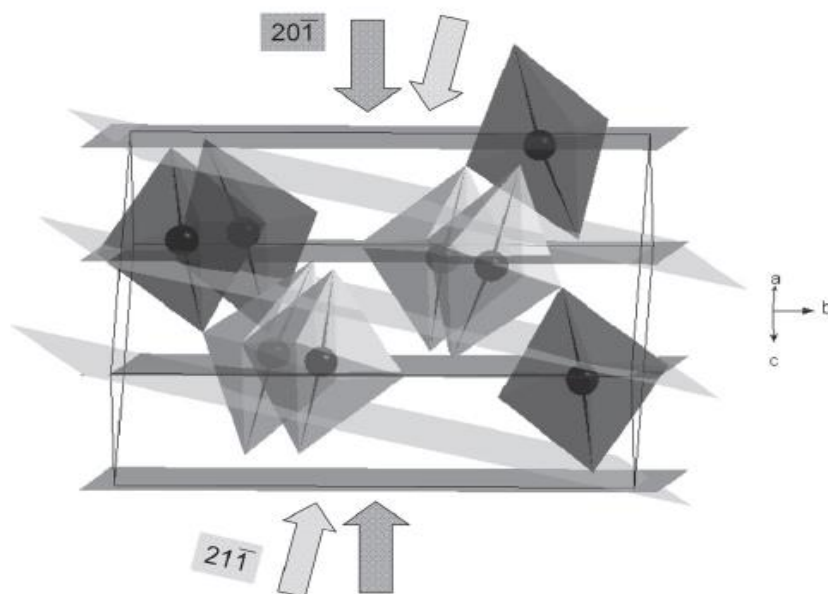


**Figure 1.5.** Unit cell of malachite illustrating CuO<sub>6</sub> units with Jahn Teller elongated bonds. Strongest unit cell contraction with Cu/Zn substitution is indicated with arrows. Carbonate groups omitted for clarity<sup>(38)</sup>.

co-workers investigated pH and temperature and determined that pH exerts its effect through altering the phase composition since the malachite phase was obtained using a constant pH of 7 whereby hydroxynitrates were produced with  $\text{pH} \leq 6$ <sup>(40)</sup>. Moreover, from correlating the conditions to the resulting activity for methanol synthesis temperature was identified to function through altering the precipitation kinetics. The findings concluded that pH 7 and 70 °C produced the most active catalyst. From titration experiments, Behrens and co-workers fully outlined the importance of maintaining a constant pH around 7 whereby it was concluded that Cu<sup>2+</sup> does not precipitate at  $\text{pH} < 3$ , whilst Zn<sup>2+</sup> and Al<sup>3+</sup> do not precipitate at  $\text{pH} < 5$ <sup>(11,41)</sup>. With pH values  $\geq 9$ , CuO formation was apparent from oxolation. The work highlight the importance of achieving simultaneous precipitation of all three metal species around controlled neutral pH values. Interestingly, temperature was found to influence the minimum pH required for precipitation of each metal with decreasing temperature requiring more basic conditions for total metal precipitation. In contrast, Kienar and co-workers investigated a range of pH values between 6.3-9.2 and concluded that the performance of the resulting catalyst increased for methanol synthesis with pH<sup>(42)</sup>. Interestingly, at pH 9 they determined that the resulting precursor was largely amorphous and contained malachite, aurichalcite and Zn<sub>4</sub>CO<sub>3</sub>(OH)<sub>6</sub>·H<sub>2</sub>O phases. In similar studies by Jung and co-workers, a range of pH values between 4-11 were investigated whereby it was determined that the catalyst with highest activity for methanol synthesis was also obtained using a pH of 9<sup>(26)</sup>. Farahani and co-workers investigated a range of synthetic parameters including temperature and ageing time whereby it was reported that the optimum ageing time is dictated by temperature<sup>(25)</sup>. At 40 °C the performance of the catalyst was shown to increase with ageing time whilst at 80 °C the ageing process became unfavourable if

extended for long durations. It is therefore clear that certain studies have illustrated how certain parameters can directly influence others, making the co-precipitation procedure more complex than originally anticipated. This is illustrated by several authors who reported aurichalcite as the optimum precursor for methanol synthesis<sup>(35,43)</sup>. In these studies a solution of nitrates was added to a solution of sodium bicarbonate and therefore the constant pH methodology was not utilised. Behrens and co-workers have also investigated pH and temperature in relation to the ageing procedure from decoupling the phenomenon from the initial precipitation process using *in-situ* EDXRD analysis<sup>(22)</sup>. Interestingly, pH was shown to control the mechanism of Zn incorporation into the malachite lattice. At pH 7, direct co-condensation of  $\text{Cu}^{2+}$  and  $\text{Zn}^{2+}$  into the malachite lattice occurs whilst between 5-6.5 a Cu rich malachite and Zn storage phase first form. The latter mechanism was shown to lead to a higher Zn incorporation into the phase. This clearly illustrates the importance of controlling the acidity of the mother solution even after the initial precipitation. In related studies, Baltes and co-workers investigated the effect of pH control during the ageing step<sup>(8)</sup>. It was determined that the activity of the catalyst activity was 40% lower when the pH was not controlled during ageing. Finally, in terms of optimisation of the co-precipitation route, several research groups have investigated the role of counter ions ( $\text{Na}^+$ ,  $\text{K}^+$ ,  $\text{NH}_4^+$ ) not directly required for the formation of hydroxycarbonates but still present within the mother liquor solution during their formation<sup>(9,44-45)</sup>. The retention of alkali metals from carbonate reagents is detrimental to the resulting catalyst activity, and therefore, washing is considered essential after ageing in order to minimise the content retained. Residual sodium accelerates crystallisation after calcination, reduces the resulting Cu surface area, hinders the reduction of CuO and binds  $\text{CO}_2$  more strongly to the catalyst surface. Jun and co-workers attributed this to the retained  $\text{NaNO}_3$  inhibiting the interaction of the CuO phase with the ZnO matrix<sup>(45)</sup>. However, whilst alkali metals can be avoided from using  $(\text{NH}_4)_2\text{CO}_3$ , Simson and co-workers have reported that these resulting precursors are slightly Cu deficient as ammonia inhibits its complete precipitation by forming a copper-ammine complex<sup>(9)</sup>. However, it was still concluded that this precipitation reagent has the potential to replace the conventionally used  $\text{Na}_2\text{CO}_3$  reagent. Whilst less attention has been paid to the subsequent thermal treatment steps, several authors have reported some significant findings. Clearly, even if the initial co-precipitation step is fully optimised an inferior catalyst can still be derived if these steps are not optimised themselves. As previously mentioned, the ligands associated with the hydroxycarbonate decompose to yield a mixed metal oxide during the calcination procedure (**Figure 1.4.**). However this scheme is too simplistic. Many research groups have identified and outlined the importance of retained carbonate species, also termed high temperature carbonate (HT- $\text{CO}_3$ ), after calcination<sup>(8,10,13,23,34,37,39,46-49)</sup>. It is apparent that under optimum calcination temperatures total decomposition to the mixed metal oxide does not

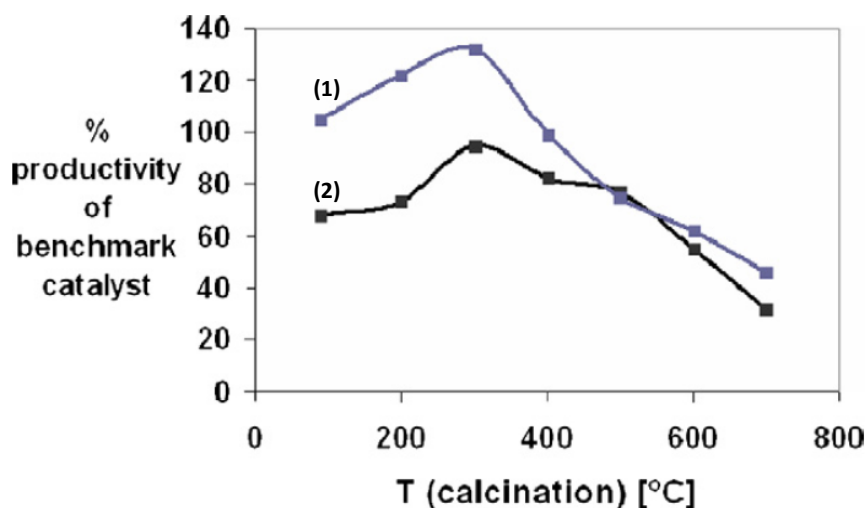


**Figure 1.6.** Influence of calcination temperature on methanol productivity. The catalyst precursors used were prepared by co-precipitation at 70 °C with a constant pH of (1) 7 and (2) 9<sup>(8)</sup>.

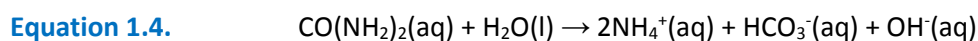
occur. The resulting material itself is often termed a carbonate-modified metal oxide. Interestingly aurichalcite has been reported to have a higher concentration of retained HT-CO<sub>3</sub> than malachite phases<sup>(7,39,47)</sup>. Consequently, Millar and co-workers concluded that aurichalcite was the optimum precursor and reported that strongly bound carbonate anions in this phase may stabilise the formation of intimately mixed, small Cu and ZnO species<sup>(37)</sup>. Furthermore, several of these studies have reported that HT-CO<sub>3</sub> acts as a growth inhibitor to sintering of the metallic components during both thermal treatment steps whilst assisting in dispersing and stabilising these optimum crystallites. Bems and co-workers in particular have illustrated the benefit of retained HT-CO<sub>3</sub> activity for methanol synthesis, highlighting it as an essential component of an optimum catalyst. It was determined that a catalyst prepared with no HT-CO<sub>3</sub> had a lower Cu surface area, a reduced activity for methanol synthesis as well as a reduced intrinsic catalyst activity (activity normalised to Cu surface area)<sup>(10)</sup>. Baltes and co-workers studied a range of calcination temperatures, between 100-700 °C, in order to optimise this parameter and concluded that the optimum temperature was in the range 250-300 °C (Figure 1.6.)<sup>(8)</sup>. Interestingly, XRD analysis of these materials indicated that the optimum materials displayed the lowest degree of crystallinity. It was also deduced that HT-CO<sub>3</sub> could assist during the reduction treatment by facilitating the formation of smaller crystallites from lowering the reduction potential of the dilute hydrogen feed. Interestingly, several authors have also investigated the effect of water on the calcination step. Behrens and Fujita research groups concluded that the presence of water during heat treatment results in loss of HT-CO<sub>3</sub> with enhanced crystallisation and growth of CuO crystallites<sup>(46-47)</sup>. Consequently, higher ramp rates are unfavourable as they increase the partial pressure of water vapour during decomposition of the hydroxycarbonate phases. Interestingly, Fujita also investigated the reduction step and concluded that the choice of reductant was critical. The exothermicity of the reduction of CuO to Cu metal, combined with the

relatively high copper loadings, results in the local temperature of CuO crystallites rising during the process which can be prevented by using MeOH as an alternative reductant.

From the extensive work implemented regarding optimisation of the industrial co-precipitation route it can be concluded in large agreement that the desired synthesis procedure is as follows: A constant pH methodology must be utilised during both precipitation and ageing. A pH between 6-7 can be regarded as optimal within a certain temperature window of 65-75 °C. Consequently, such high temperatures should not utilise long, extended ageing times. The optimum precursor is malachite, whereby the optimum metal molar ratio is set to maximise the amount of Zn and Al incorporated into the lattice without simultaneous formation of aurichalcite or hydrotalcite phases (72 at.% Cu and 28 at.% Zn for the binary precursor and 68.7 at.% Cu, 28.0 at.% Zn and 3.3 at.% Al for the ternary precursor). Washing is then essential to remove residual poisons especially when using alkali metal reagents. Calcination and reduction must be performed under mild conditions (low ramp rates and temperature) whereby retention of residual carbonate after calcination leads to optimum catalysts.

At this point it is important to briefly review several groups who have attempted to manufacture Cu/ZnO/Al<sub>2</sub>O<sub>3</sub> catalysts using alternative preparation routes to the industrial procedure. Kurts and co-workers reported that the deposition-precipitation of Cu onto high specific surface area ZnO particles and the chemical vapour deposition (CVD) of diethyl Zn were effective techniques from enlarging the Cu-ZnO interface<sup>(50)</sup>. Tanaka and co-workers investigated catalysts prepared by impregnation for the LTS reaction whereby the optimum loading was determined to be 5 wt.% Cu/ 5 wt.% ZnO/Al<sub>2</sub>O<sub>3</sub>. Unfortunately, such catalysts were not able to compete against co-precipitated catalysts at 200 °C as a result of deactivation<sup>(51)</sup>. The co-precipitation procedure has been modified into 2-steps by Chu and co-workers using tetraethylammonium hydroxide (TEAH) and polyethylene glycol (PEG) surfactants to prepare catalysts for MeOH synthesis<sup>(52)</sup>. They concluded that addition of 2% TEAH in the course of co-precipitation exhibited superior catalyst performance due to formation of smaller Cu crystallites. The MeOH space time yield was 1.26 times greater than the same catalyst prepared without surfactant. In related studies, Budiman and co-workers have also modified the co-precipitation route and in particular, from replacing the water solvent with ethylene glycol for preparation of the metal nitrate solution they report a Cu surface area of 45.5 ±1.7 m<sup>2</sup> g<sup>-1</sup>. This apparently is the largest Cu surface area ever reported in the literature<sup>(34)</sup>. Agrell and co-workers have compared hydroxycarbonates prepared by standard co-precipitation to oxalate precursors formed by water-in-oil microemulsion<sup>(53)</sup>. The hydroxycarbonate precursors exhibited a significantly higher Cu dispersion (10.3%) compared to the oxalate precursors (3.4-5.7%), although the particle

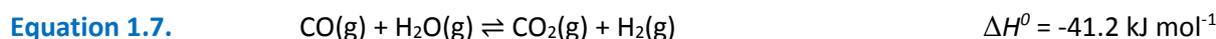
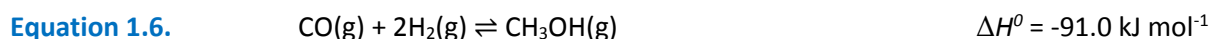
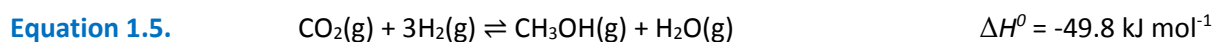
size distribution was narrower for the latter. Bao and co-workers prepared a Cu/ZnO catalyst with mesoporosity using the sol-gel method<sup>(54)</sup>. The resulting Cu/ZnO material had a large surface area, homogeneous element distribution and various mesopore sizes in the range 2-10 nm. However, high activity and selectivity for methanol synthesis was coupled to using an alcohol promoter and were not directly compared against commercial catalysts. Karelavic and co-workers have prepared catalysts by a citrate method and in this case they did compare these catalysts to reference catalysts prepared by co-precipitation, whereby it was concluded they were much more active<sup>(55)</sup>. This was attributed to the good contact between Cu<sup>0</sup> and ZnO phases. Finally, some groups have investigated preparation of binary and ternary catalysts by homogeneous precipitation from urea hydrolysis<sup>(56-57)</sup>. This technique is relatively similar to the current industrial method. Urea is mixed into the metal nitrate solution at room temperature before heating to 90 °C. This induces hydrolysis of urea to generate *in-situ* precipitants. (Equation 1.4.).



This has the advantage of avoiding a concentration gradient within the solution and furthermore provides an alternative route to producing hydroxycarbonate phases. Interestingly, these catalysts were reported to have higher activity for the LTS reaction to the conventional catalysts. However, despite all these efforts the conventional co-precipitation route remains the commercial methodology for constructing Cu/ZnO/Al<sub>2</sub>O<sub>3</sub> catalysts. This has clearly been determined from evaluating a specific range of criteria (Section 1.2.2.).

### 1.3.2. Methanol synthesis

MeOH is a primary liquid petrochemical which is of considerable importance in the chemical and energy industries. In 2009 the worldwide production of MeOH was around 40 million metric tons<sup>(11)</sup>. Whilst it can be used as an energy carrier for hydrogen storage and transportation it is also primarily used as a chemical feedstock or intermediate. With just one carbon unit per molecule it can be considered a clean liquid fuel and can provide convenient storage of energy for fuel cell applications, particularly in transportation and mobile devices. Furthermore, MeOH has been used as a common chemical feedstock for several important chemicals such as acetic acid, formaldehyde, chloromethane and methyl *tert*-butyl ether (MTBE) for over 30 years<sup>(58)</sup>. It is also used to make numerous materials including plastics, paints, pigments, dyes and refrigerants. The catalysed synthesis of MeOH over Cu/ZnO/Al<sub>2</sub>O<sub>3</sub> catalysts in industry corresponds to the conversion of synthesis gas (or syn-gas), a mixture of CO, CO<sub>2</sub> and H<sub>2</sub>, according to the following three reactions (Equations 1.5.-1.7.).



Since its inception, this process has been optimised to yield MeOH with > 99% selectivity and 75% energy efficiency, and has thus become the exclusive means of MeOH production<sup>(11,59)</sup>. The catalysts are kinetically selective as formation of hydrocarbons is thermodynamically favoured. The typical composition of a commercial Cu/ZnO/Al<sub>2</sub>O<sub>3</sub> catalyst is 60% CuO, 30% ZnO and 10% Al<sub>2</sub>O<sub>3</sub>. In addition, typical reactions conditions operated in industry are around 240-260 °C and 50-100 bar.

Despite the extensive work implemented in this field there is still debate concerning the mechanism, active site(s), rate determining step, chemical intermediates, role of ZnO and even the source of carbon responsible for producing MeOH. Studies carried out by Chinchin and co-workers in the 1980's determined the following: from testing a range of Cu/ZnO catalysts with various supports the activity for MeOH synthesis was found to correlate linearly with the Cu<sup>0</sup> surface area (**Figure 1.7.**). Under industrial conditions the Cu surface area is partially oxidised to an extent which depends on the composition of the synthesis gas. From isotopic labelling using <sup>14</sup>CO and <sup>14</sup>CO<sub>2</sub> tracers it was determined that CO<sub>2</sub> is the major reactant under industrial conditions. Furthermore, there is no carbon containing surface intermediate common to both MeOH synthesis and the LTS reaction<sup>(60-61)</sup>.

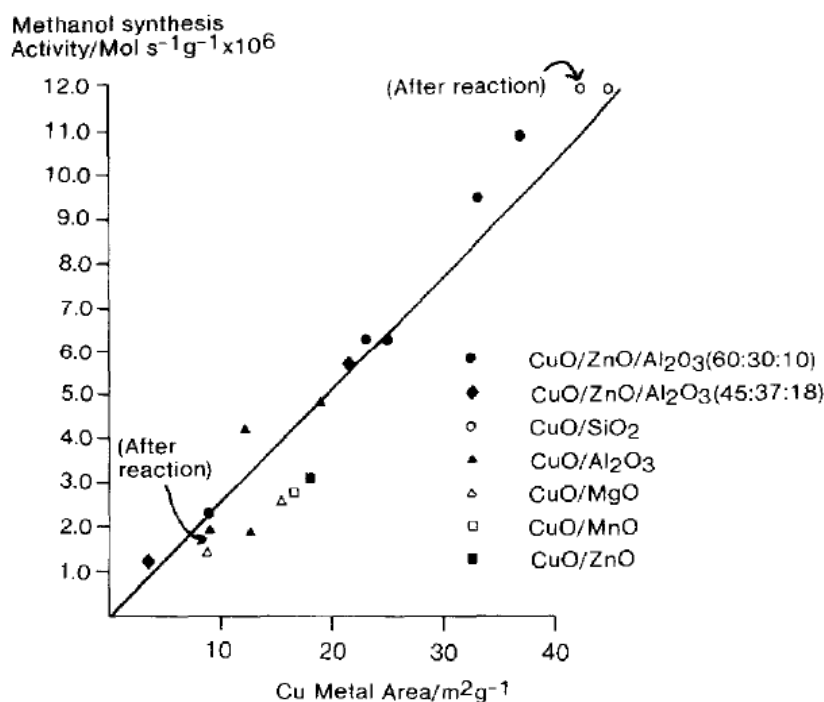
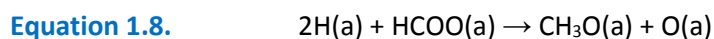


**Figure 1.7.** MeOH synthesis activity as a function of copper metal area<sup>(60)</sup>.

In later work, Spencer verified these findings and also reported that CO<sub>2</sub> was converted to MeOH *via* a formate intermediate<sup>(59,62,-64)</sup>. Furthermore, of particular importance it was noted that the nature of the mechanism and rate determining step strongly depends on the reaction conditions utilised. Under typical industrial conditions there is no synergy between Cu and ZnO, hydrogenolysis of the formate intermediate is the rate determining step (**Equation 1.8.**) and the activity is directly proportional to Cu<sup>0</sup> surface area.



However, many academic researchers use much milder reaction conditions and consequently support effects become significant, the rate determining step switches to hydrogen chemisorption and ZnO assists by acting as a hydrogen sink that supplies the Cu active sites from a spillover mechanism. Moreover, after illustrating the formation of carbonate species from reaction of CO<sub>2</sub> with Cu metal surfaces Spencer also proposed that during reduction, migration of Zn from ZnO crystallites to Cu crystallites gives rise to extensive brass formation<sup>(59,65)</sup>. Consequently when switching to MeOH synthesis conditions, which is strongly oxidising by comparison, surface oxidation gives rise to Cu<sup>+</sup>-O-Zn sites. This was concluded to be responsible for strongly binding specific oxygen species. The hypothesis of brass formation was supported by Jung and co-workers who reported that ZnO only reduced in the vicinity of Cu with MeOH and CO<sup>(66)</sup>.

A broad range of other research groups have also correlated MeOH synthesis activity to the Cu surface area and confirmed the linear relationship with Cu<sup>0</sup> as the active site<sup>(22,52,55,67-68)</sup>. However, not all the literature is in agreement. Studies by Nakamura and co-workers derived a volcano-shaped relation between oxygen coverage on the Cu surface and the specific activity for MeOH formation and attributed it to a surface Cu<sup>+</sup>/Cu ratio controlling the activity<sup>(69)</sup>. Using physical mixtures of Cu/SiO<sub>2</sub> and Zn/SiO<sub>2</sub> they reported that ZnO<sub>x</sub> species migrated from ZnO particles onto the Cu surface resulting in Cu<sup>+</sup> formation. The findings were concluded by assigning Cu<sup>+</sup> as the active site for MeOH synthesis since activity decreased with Cu<sup>0</sup> surface area. Interestingly, other research groups have reported that activity is not simply correlated to Cu<sup>0</sup> alone and that lattice strain and surface defects also contribute<sup>(7,12,31,70-71)</sup>. Whilst not explicitly used for MeOH synthesis, Muhammad and co-workers prepared hydroxycarbonates with ageing (2 hours) and without and concluded that the activity did not correlate linearly to the Cu surface area, but instead coincided with an increase in Cu microstrain<sup>(31)</sup>. These findings for MeOH steam reforming activity were verified by Kniep and co-workers<sup>(12)</sup>. However, several groups have indeed correlated microstrain to MeOH synthesis. Gunter and co-workers investigated a range of catalysts with varying Cu/Zn molar ratios (90/10 through to 10/90) and correlated the findings to a detailed analysis of the microstructure; consisting of Cu

surface area, crystallite size and strain<sup>(70)</sup>. They concluded a positive correlation of turn over frequency for MeOH production with the observed microstrain of Cu crystallites and furthermore, proposed that highly strained Cu particles are stabilised by unstrained ZnO microcrystallites. These findings were also later verified by Kasatkin and co-workers<sup>(71)</sup>.

These conclusions drawn from various groups such as ZnO reduction and migration onto Cu sites and MeOH production being dependant on microstructural features such as Cu surface area and strain was recently combined together by Behrens and co-workers in order to determine the active site for MeOH synthesis. It was reported from a combination of experimental evidence including bulk, surface sensitive and imaging methods and density functional theory (DFT) calculations that the active site consists of Cu steps decorated with Zn atoms<sup>(72)</sup>. Surface defects (steps and kinks) appear as a mechanism for strain relation and therefore are coupled together. Neutron diffraction experiments were used to deduce the stacking fault concentration of particular planes and was shown to have a linear relationship with the intrinsic MeOH activity (**Figure 1.8.**). This bulk defect structure explains the increase in activity from a stronger binding of intermediate species on surface sites. However, the role of ZnO must also be considered. The dynamics of the ZnO component were illustrated in *in-situ* XPS analysis whereby the surface was shown to become Zn enriched during reduction. Furthermore, this process was highlighted to be fully reversible upon re-calcination of the catalyst to confirm a dynamic strong metal support interaction (SMSI) effect<sup>(73-74)</sup>. Close proximity of Cu steps and ZnO<sub>x</sub> therefore results in substitution of Zn into Cu steps, whereby Zn serves as an adsorption site for oxygen-bound intermediates due to its higher oxophilicity.

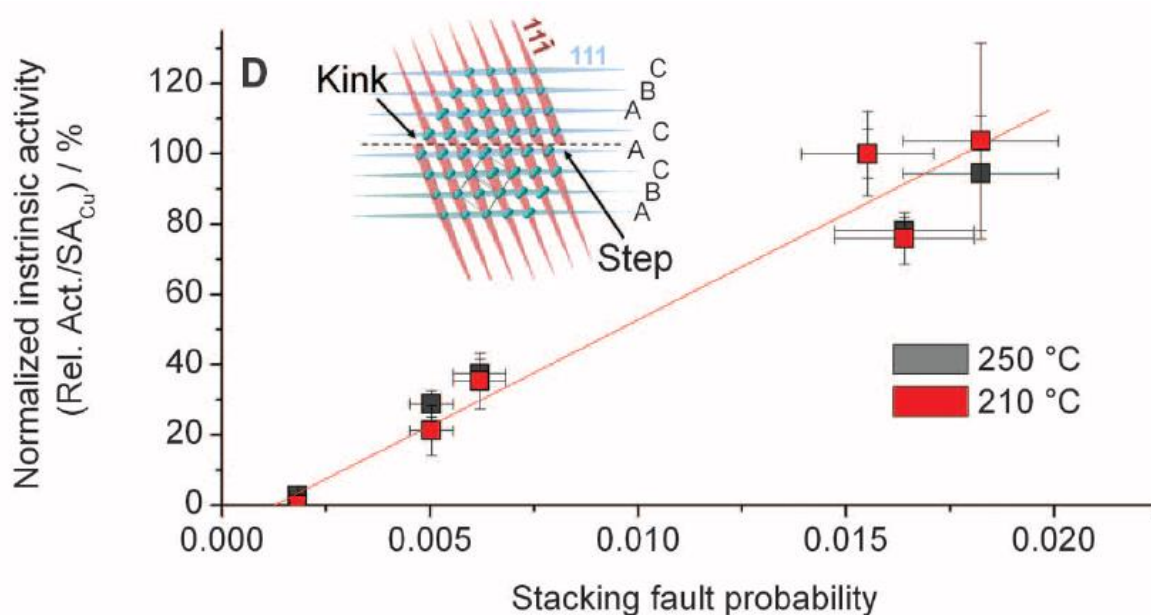


**Figure 1.8.** Relation of the intrinsic activity of Cu to the concentration of stacking faults<sup>(72)</sup>.

The findings drawn indicate that the synthesised state of the catalyst might substantially differ from the working state whereby it self-assembles its active sites under reduction conditions. However, the detailed role of the  $\text{Al}_2\text{O}_3$  refractory oxide component was not explained in these studies. Many papers report enhanced performance either in terms of activity or stability from incorporating the  $\text{Al}_2\text{O}_3$  component into the catalyst<sup>(8,67-68,75-76)</sup>. However, these studies have also not explicitly gone into detail regarding the role of  $\text{Al}_2\text{O}_3$ . As already mentioned, Al is seen as a structural promoter by further assisting in the dilution of the Cu component within the malachite precursor (**Section 1.3.1.**). However Behrens and co-workers also report an additional electronic promotional effect<sup>(14)</sup>. Earlier studies by Miao and co-workers investigated a series of  $\text{ZnO}/\text{Al}_2\text{O}_3$  mixed oxide samples prepared by co-precipitation whereby from the identification of the  $\text{ZnAl}_2\text{O}_4$  spinel phase concluded that Al was being substituted for Zn ions<sup>(77)</sup>. Furthermore, a decrease in crystallinity and unit cell volume of the ZnO phase from substitution was confirmed. The exact same spinel phase was also determined by Porta and co-workers for the preparation of ternary hydroxycarbonates, also by standard co-precipitation<sup>(78)</sup>. They reported that a divalent : trivalent (Zn : Al) metal molar ratio of 0.5 is required for the spinel to form after calcination to at least 350 °C. Behrens investigated this further and concluded that Al incorporation into ZnO increased the defect chemistry of the material, although it was determined to be unstable under reducing conditions, whereby surface migration of Al occurred<sup>(79)</sup>. Overall this observation of a Zn/Al substitution effect was directly correlated to the SMSI effect proposed by Behrens.  $\text{Al}^{3+}$  was reported to improve the n-type semiconductivity of ZnO and modify its reducibility behaviour in relation to this phenomenon<sup>(14)</sup>. A later study also verified that ternary catalysts were richer in defects than binary ones<sup>(80)</sup>.

Despite this significant work carried out by Behrens and co-workers it is also fruitful to review the work carried out by other researchers which can also be used for direct comparison. The proposal of dynamic changes occurring to the catalyst structure during reduction and testing is in agreement with several other groups. A range of transient and kinetic experiments were carried out by Wilmer and Hinrichsen, whereby it was reported that reversible structural alterations depend strongly on reaction conditions and pretreatment<sup>(81)</sup>. The pretreatment was found to induce changes in the morphology of the Cu particles with surface alloying occurring under more severe conditions. These conclusions are also in agreement with Vesborg and co-workers. They identified that MeOH productivity always peaks after pretreatment and used Environmental Transmission Electron Microscopy (ETEM) to observe the changes induced to the catalyst structure during this time<sup>(82)</sup>. The ETEM images determined a gas dependant morphology of the Cu nanoparticles with a marked flattening for a  $\text{H}_2$  : CO gas mixture of 1/1 which was attributed to the initial change in activity. However, not all studies are in agreement with the hypothesis of morphology changes being induced

to the metal crystallites. Choi and co-workers reported that the role of ZnO was not to change the morphology of Cu but to create Cu-Zn sites only<sup>(83)</sup>. From investigating physical mixtures of binary catalysts they identified migration of Zn onto Cu sites. By correlating these observations with the catalyst performances they concluded that this could not be explained by a morphology change. Kleymentov and co-workers have carried out *in-situ* XAS and EXAFS studies and similarly concluded that the structure of the catalyst does not change with pressure, temperature and time on line, even though MeOH synthesis strongly increased during these observations<sup>(84)</sup>. In other studies, Topsoe and Topsoe have used infrared spectroscopy of CO adsorption to elucidate the surface structure of Cu/ZnO catalysts during MeOH synthesis<sup>(85)</sup>. They detected changes in frequency shifts during reduction treatment and since this was not detected for other supported catalysts concluded that this could not be solely interpreted from changes in morphology. The hypothesis of surface alloy formation was proposed which furthermore was reported to be a reversible phenomenon in agreement with Behrens work. Studies by Saito and co-workers have specifically investigated the role of ZnO from examining the effects of ZnO addition to Cu/Al<sub>2</sub>O<sub>3</sub>, Cu/ZrO<sub>2</sub> and Cu/SiO<sub>2</sub> binary catalysts<sup>(86)</sup>. The catalysts were tested for MeOH synthesis and the LTS reaction whereby it was determined that the latter was not effected by ZnO addition whilst for the former it was essential, in combination with high Cu surface area, for high activity. Moreover, in relation to the role of ZnO significant findings have recently been determined by Santiago and co-workers. They examined binary and ternary catalysts for methanol synthesis using CO + H<sub>2</sub> and CO + CO<sub>2</sub> + H<sub>2</sub> reactant gas feeds<sup>(87)</sup>. From examining the effect of co-feeding dimethyl ether and methyl formate into the streams it was discovered that only methyl formate participates in the process. Interestingly, a Cu-free ZnO/Al<sub>2</sub>O<sub>3</sub> catalyst illustrated significant activity when this by-product was simultaneously co-fed and the role of ZnO was assigned as *catalytic partner*.

There is also still a large debate within the literature regarding the source of carbon used for MeOH synthesis. Several groups are in agreement with Chinchin and Spencer and report that MeOH formation only occurs through CO<sub>2</sub> hydrogenation<sup>(88-90)</sup>. Production of MeOH using just CO<sub>2</sub> and H<sub>2</sub> would be highly desirable. From an environmental perspective, the consumption of a greenhouse gas in a chemical process would substantially assist in suppressing global warming whilst simultaneously providing access to an energy source without the consumption of non-renewable energy fuels. However, whilst this can be achieved the presence of CO is essential for increasing the yield of MeOH and decreasing the apparent activation energy of the reaction<sup>(59)</sup>. This of course can have significant implications on reactivity data as many research groups use different syn-gas compositions. As already mentioned, Spencer has illustrated differences in catalyst behaviour from utilising different reaction conditions<sup>(59)</sup> which could explain the large differences in the following

reports. Jadhov and co-workers reported that CO<sub>2</sub> is directly converted to MeOH and not reduced to CO. They propose that CO converts to CO<sub>2</sub> *via* the LTS reaction, which itself can then be converted to MeOH (Equations 1.7. and 1.5. respectively)<sup>(88)</sup>. However, Rozovskii and co-workers report that MeOH synthesis is de-coupled from the LTS reaction but are in agreement regarding CO not being directly hydrogenated to MeOH<sup>(89)</sup>. Excess oxygen atoms were proposed to migrate between CO<sub>2</sub> and H<sub>2</sub>O. Several groups in direct contrast to these large volume of publications report that MeOH synthesis does occur through CO hydrogenation<sup>(91-93)</sup>. The Choi and Nakamura research groups have reported that the active site for CO and CO<sub>2</sub> hydrogenation is different<sup>(92-93)</sup>. In both studies a Cu-O-Zn site was attributed to the active site for CO hydrogenation. ZnO was identified as a promoter from alloying and producing Cu<sup>+</sup> active species. For CO<sub>2</sub> hydrogenation Cu<sup>0</sup> was attributed as the active site which resides at Cu-Zn boundaries. More recently, DFT studies have been carried out by Zuo and co-workers and similarly concluded that both CO and CO<sub>2</sub> have different active sites for hydrogenation. Cu<sup>0</sup> was identified as the active site for CO<sub>2</sub> hydrogenation whilst a partially oxidised Cu<sup>(δ+1)</sup> species were responsible for CO hydrogenation. For low Cu coverage, the charge of Cu was reported to be transferred locally to ZnO indicating that the support was synergistically enhancing the reaction<sup>(91)</sup>.

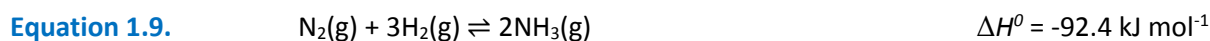
This section on MeOH synthesis is rounded off by briefly mentioning studies on catalyst deactivation. Kurtz and co-workers have reported that CO rich syn-gas feeds accelerate the rate of catalyst deactivation as a result of over-reduction and thermal sintering<sup>(68)</sup>. These findings were concluded after retesting catalysts and correlating the findings to the Cu surface areas. Very recently, DFT calculations have been carried out in other work by Rasmussen and co-workers. Whilst they repeat the hypothesis that CO-rich gas feeds accelerate deactivation, they do not specifically examine the effect of syn-gas composition. Using typical industrial conditions they conclude that the formation of specific mobile, intermediate Cu-X species (in particular CuCO and CH<sub>2</sub>HCOO) on the catalyst surface are predominant for transport of Cu and contribute to sintering<sup>(94)</sup>. Several other groups, however, have reported that deactivation is actually facilitated by the presence of H<sub>2</sub>O. In direct contrast, Wu and co-workers report that CO<sub>2</sub> rich gas feeds and not CO accelerate deactivation<sup>(95)</sup>. This is from the simultaneous formation of H<sub>2</sub>O as by-product from CO<sub>2</sub> conversion, which accelerates Cu<sup>0</sup> crystallisation. This concept of H<sub>2</sub>O facilitating Cu<sup>0</sup> or CuO crystallisation has been previously illustrated elsewhere<sup>(46-47)</sup>. In related work, Martin and Perez-Ramirez concluded that H<sub>2</sub>O plays an ambivalent role<sup>(67)</sup>. Small concentrations promote MeOH synthesis by linking the hydrogenation paths of CO and CO<sub>2</sub> *via* the LTS reaction. However, in large concentrations it was reported that surface hydroxyls inhibit MeOH production. Several groups have examined the effect of various promoters or supports on catalyst performance such as Ga<sup>(96)</sup>, SiO<sub>2</sub><sup>(90,95)</sup> and ZrO<sub>2</sub><sup>(90)</sup>. In particular,

doping catalysts with 0.6 wt.% SiO<sub>2</sub> was found to produce a remarkable increase in stability for multi-component catalysts containing Al<sub>2</sub>O<sub>3</sub>, ZrO<sub>2</sub> and Ga<sub>2</sub>O<sub>3</sub> refractory metal oxides.

### 1.3.3. The low temperature shift (LTS) reaction

Cu/ZnO based catalysts are also applied in a promoted form for the LTS reaction (**Equation 1.7.**), which is used in industry to reduce the CO content in syngas feeds. The LTS reaction actually consists of one half of the water gas shift (WGS) process. The high temperature shift (HTS) reaction functions 100-200 °C above the low temperature system and is catalysed by an iron oxide/ chromium oxide catalyst<sup>(15-16)</sup>. The HTS catalyst is less active but more stable, and therefore higher temperatures are utilised to exploit the reaction kinetics. Exiting CO levels are typically around 3%. The WGS reaction is exothermic and therefore CO conversion increases with decreasing temperature. Consequently, the LTS reaction exploits the thermodynamics of the reaction by operating at lower temperature using the more active Cu/ZnO/Al<sub>2</sub>O<sub>3</sub> catalyst. This overall configuration achieves exit CO levels around 0.1%. From the high partial pressure of steam required for industrial operating conditions the incorporation of Al<sub>2</sub>O<sub>3</sub> into the catalyst is essential to promote stability and hence enhance catalyst performance<sup>(15-16,97-98)</sup>. The typical composition of a commercial Cu/ZnO/Al<sub>2</sub>O<sub>3</sub> catalyst is approximately 33% CuO, 34% ZnO and 33% Al<sub>2</sub>O<sub>3</sub>. In addition, typical reaction conditions operated in industry are around 210-240 °C and 20 bar. It is important to note that the equilibrium constant, and hence thermodynamics, is independent of pressure. Furthermore, these catalysts generally operate in a pore-diffusion limited regime.

The production of hydrogen *via* the WGS reaction is important for future energy technologies such as fuel cells. Polymer electrolyte fuel cells (PEFC) have been extensively studied due to their attractive properties, such as high power density and low emission of NO<sub>x</sub>. However, the largest applications of hydrogen are hydrocracking and the production of ammonia *via* the Haber process (**Equation 1.9.**).



Synthesis of ammonia is essential for the mass production of fertiliser that is responsible for sustaining approximately one third of the world's population. In industry the two stage WGS reaction is operated in ammonia synthesis plants. The WGS reaction provides the only economic means of producing hydrogen in the quantity required for the Haber process. However, the main drawback of this procedure regards the presence of unreacted CO in the product stream. CO is a poison in the Haber process as well in Pt fuel cells and therefore significant efforts have to be made to remove the remaining trace levels of CO. Whilst this can be achieved by methanation, this

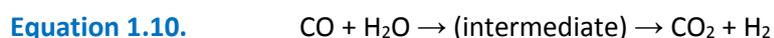
consumes three molecules of hydrogen for every molecule of CO, and therefore is detrimental to the yield of hydrogen produced.

The number of papers on the LTS reaction using Cu/ZnO based catalysts is significantly lower compared to MeOH synthesis. This could imply that it is a less well understood chemical process, whilst controversy still exists in the literature regarding various components of the reaction, including the mechanism and active site. It was previously highlighted that these harsh reaction conditions require higher contents of ZnO and Al<sub>2</sub>O<sub>3</sub> phases (~ 33% each). Therefore, hydroxycarbonate phases which are regularly reported as optimum catalyst precursors in this field include aurichalcite<sup>(34,97)</sup> and hydrotalcite<sup>(99)</sup>. Interestingly, some preparations carried out using the industrial co-precipitation process use a constant pH of 9<sup>(97,100-101)</sup>. It can be expected that more strongly alkaline conditions are chosen to specifically favour formation of these phases.

Many research groups have reported that the catalyst activity is correlated to the Cu surface area<sup>(23,34,56,97,99,102)</sup>, whilst several groups have indicated that there is no correlation<sup>(59,98)</sup>. Studies by Shishido and co-workers prepared binary and ternary catalysts by homogeneous precipitation whereby the activity was illustrated to be dependant on the surface area of Cu metal<sup>(56)</sup>. However, more precise evaluation of the activity in terms of TOF strongly suggested formation of Cu<sup>+</sup> species as the active sites between Cu and ZnO particles. Atake and co-workers also prepared a range of ternary catalysts by homogeneous precipitation and concluded similar findings<sup>(97)</sup>. Whilst activity was found to be dependent on the Cu surface area the TOF calculated (based on Cu surface area) significantly varied depending on the Al content. Furthermore, Saito and co-workers investigated the effect of pretreatment on Cu/ZnO based catalysts and concluded that catalysts were less effected by calcination temperatures ranging between 400-700 °C and by H<sub>2</sub> treatment between 300-500 °C<sup>(102)</sup>. The resulting catalyst activities were also dependant on the Cu surface area. In direct contrast to all of these findings, Kam and co-workers investigated lanthanum doping on the performance of a series of binary and ternary catalysts<sup>(98)</sup>. When doped with the optimum loading of La (2.3 wt.%), the catalyst active sites were shown to be stabilised over extended operating periods, with a decreased rate of deactivation. However, it was illustrated that there was also a simultaneous decrease in specific and Cu<sup>0</sup> surface area, and therefore was concluded that Cu<sup>0</sup> sites were not responsible for the LTS activity. Similarly, Spencer concluded that the LTS activity does not correlate directly with Cu surface area<sup>(59)</sup>. In relation to all these findings Hadden and co-workers stated that there is no single function which can describe the relationship between the Cu metal area and LTS activity of every catalyst<sup>(104)</sup>. However, discrete Cu area-activity relationships are evident within groups of catalysts whose precursor species were formed under identical preparation conditions. From varying

Cu/Zn/Al ratios within certain ‘families’ of specific co-precipitation conditions (including ageing time, pH and temperature), relationships appeared linear between Cu surface area and activity (**Figure 1.9**).

Perhaps the most controversial aspect in this field of work regards the mechanism of the LTS reaction. Two contrasting mechanistic pathways have been proposed based on either: (a) an associative mechanism or (b) a regenerative (redox) mechanism<sup>(15)</sup>. The proposed associative mechanism involves adsorption of both CO and H<sub>2</sub>O onto the catalyst surface to form an intermediate of unspecified structure that subsequently decomposes into reaction products (**Equation 1.10**).



The regenerative mechanism involves the lysis of H<sub>2</sub>O on the catalyst to produce H<sub>2</sub>, with subsequent oxidation of the catalyst surface. The catalyst surface is then reduced by CO to produce CO<sub>2</sub> with the catalyst returning to its original state (**Equations 1.11-1.12**).



Whilst many groups appear to be in agreement that H<sub>2</sub>O dissociation is the rate limiting step<sup>(59,105-108)</sup> several studies indicate either the associative<sup>(98,106)</sup> or regenerative<sup>(97,108-109)</sup> mechanism is occurring

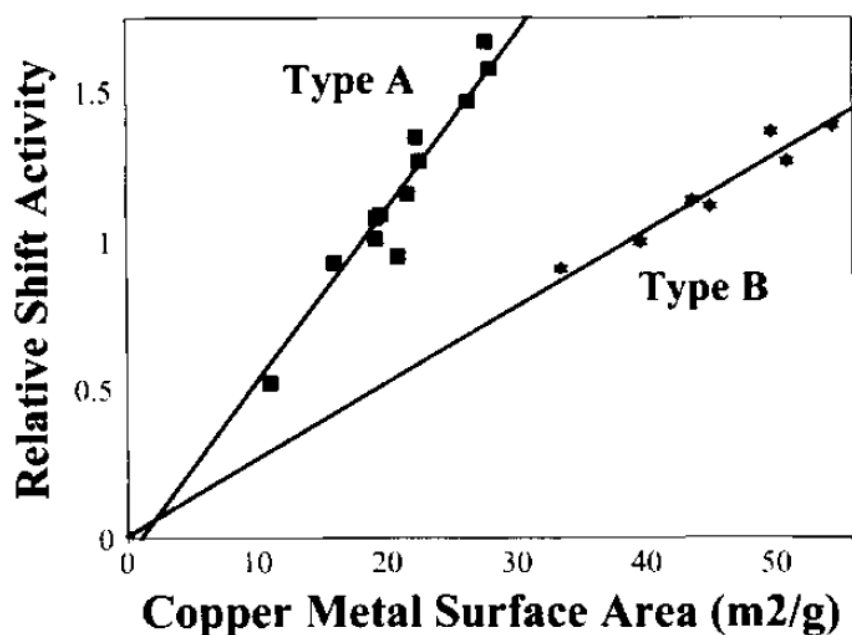


**Figure 1.9.** Relationship between Cu surface area and LTS activity for two discrete groups of Cu/ZnO/Al<sub>2</sub>O<sub>3</sub> catalysts<sup>(104)</sup>.

or even both<sup>(110)</sup>. Referring back to studies by Kam and co-workers, it was concluded that the mechanism proceeds *via* an associative route in the La-doped Cu/ZnO catalytic system<sup>(98)</sup>. From H<sub>2</sub>O and CO TPD studies, they determined that ZnO is primarily responsible for adsorbing H<sub>2</sub>O molecules and that Cu, but not in the form of Cu<sup>0</sup>, was responsible for CO adsorption. In other words, they ruled in favour of bi-functionality whereby CO and H<sub>2</sub>O both adsorb to form carbonaceous intermediates that decompose to the desired products. Very recently, Behrens and co-workers carried out DFT calculations in order to derive energy profile diagrams for the LTS reaction using two active site motifs; a Cu (211) step and a Zn decorated Cu step<sup>(106)</sup>. It was concluded that the Cu-Zn step sites most likely exhibit superior activity and from comparison of the findings obtained for both mechanisms determined that the carboxyl (associative) mechanism is favoured as it provides a pathway of lower energy (**Figure 1.10**). Interestingly, it is seen that the bottleneck of these pathways is significantly lowered from assistance of surface OH\* species (depicted in red). Studies which concluded that the redox mechanism is proceeding in contrast include work carried out by Shishido and co-workers<sup>(56)</sup>. Analysis of binary and ternary catalysts using auger electron spectroscopy indicated the presence of both Cu<sup>0</sup> and Cu<sup>+</sup> after reduction. The Cu<sup>+</sup>/Cu<sup>0</sup> ratio was found to correlate with catalyst activity, and so was concluded that a reduction-oxidation mechanism is likely between Cu<sup>0</sup> ↔ Cu<sup>+</sup>, whereby Cu<sup>+</sup> sites chemisorb and oxidise CO to form CO<sub>2</sub> and Cu<sup>0</sup> whilst this Cu<sup>0</sup> is re-oxidised by H<sub>2</sub>O to form H<sub>2</sub>. Moreover, studies by Nishida and co-workers investigated MgO doping on the activity and sustainability of ternary catalyst for the LTS reaction<sup>(109)</sup>. It was illustrated that trace amounts of MgO enhanced catalyst performance which was attributed to its role as electron donor for Cu<sup>0</sup> active species, resulting in the enhanced stability against oxidative sintering to CuO. It was also attributed to enhancing oxidation-reduction cycles between Cu<sup>0</sup> and

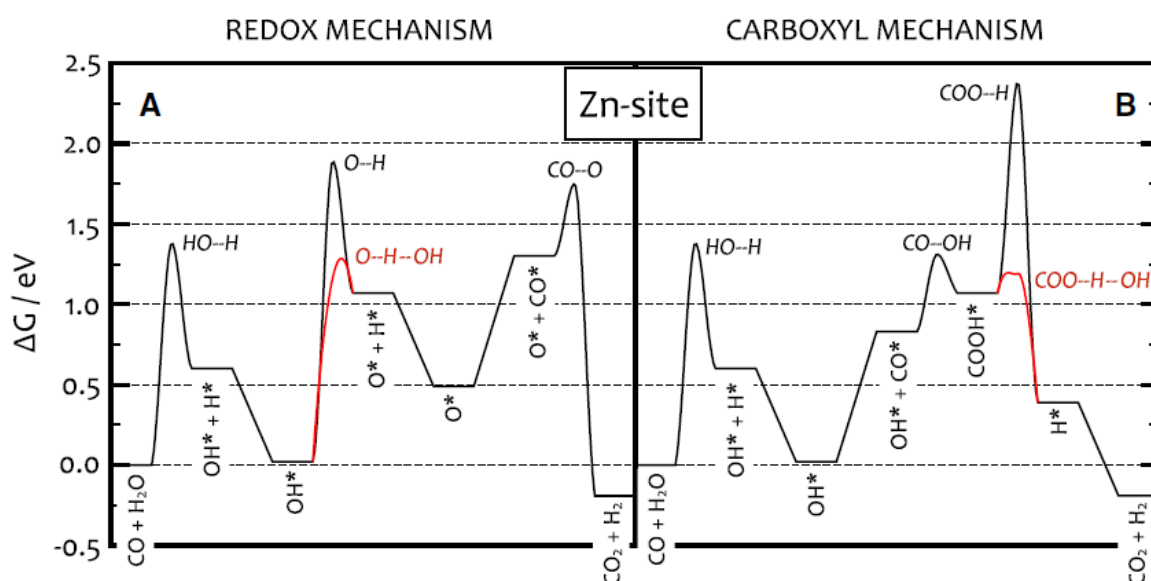


**Figure 1.10.** Gibbs free energy diagrams for: (A) redox and (B) carboxyl mechanisms on a Zn decorated Cu step. Reactions including hydrogen abstraction *via* adsorbed OH\* are depicted in red<sup>(106)</sup>.

Cu<sup>+</sup>. Nakamura and co-workers have also investigated the structure sensitivity of the LTS reaction over metallic Cu(110) and Cu(111) surfaces using UHV surface analysis and performing kinetic measurements<sup>(108)</sup>. Interestingly, it was deduced that the rate is nearly first order in H<sub>2</sub>O pressure and zero order in CO. Furthermore, depending on temperature the Cu(110) surface is four to ten-fold more active than the more densely packed Cu(111) surface due to a reduction in energy of H<sub>2</sub>O dissociation. Strong evidence for a redox mechanism was obtained by comparing the known kinetics of reverse WGS with the rate of dissociative CO<sub>2</sub> adsorption on Cu(110). Finally, a very recent study by Yang and co-workers have also used DFT calculations to examine the WGS reaction over Cu/ZnO<sup>(110)</sup>. They obtained the energetics of the relevant atomic processes and suggested the competition between the carboxyl and redox mechanisms implies both contribute significantly to the WGS activity. Moreover, it was determined that the production rates were strongly dependant on the size and structure of the Cu nanoparticles. However, it should be noted that this work was only based on a simple model consisting of single layer Cu nano-islands supported on a ZnO surface.

It is also worth noting that several groups have reported the presence of residual carbonate, or HT-CO<sub>3</sub> species, during the preparation of catalysts after calcination for LTS testing<sup>(23,34,99-100)</sup>.

Interestingly, aurichalcite-hydroxycarbonates commonly used as catalyst precursors for this reaction have higher contents of HT-CO<sub>3</sub> than the malachite phase as previously mentioned<sup>(13,37,39,47)</sup>. Gines and co-workers determined that a drastic drop in catalyst activity was observed after removal of strong bonded carbonate ions that decomposed between 550-600 °C<sup>(99)</sup>.

In Pt doping studies by Nishida and co-workers, they determined that after calcination of hydroxycarbonate containing precursors to 400 °C interlayer CO<sub>3</sub><sup>2-</sup> anions were still present after incomplete decomposition<sup>(100)</sup>. They concluded that remaining carbonate anions possibly assist in the reconstitution of the original hydroxycarbonate precursor during the Pt doping step, which subsequently improved the activity and sustainability of the catalyst. Very recently, Kowalik and co-workers have investigated the effect of ageing time on LTS activity<sup>(23)</sup>. Interestingly, they reported that the catalyst activity decreased with ageing time although the activity concerned with turn over frequency (TOF) is constant and independent of ageing time. They also determined that the HT-CO<sub>3</sub> content decreased as a function of ageing. Finally, Budiman and co-workers used a modified co-precipitation route to produce aurichalcite-based precursors and from investigating their decomposition concluded that the final decomposition step was associated with ZnCO<sub>3</sub> decomposing to ZnO<sup>(34)</sup>. It was concluded that the presence of carbonate seemed to help produce highly dispersed Cu nanoparticles because it could stabilise the formation of small mixed Cu-Zn mixed oxides.

The review of literature regarding Cu/ZnO based catalysts for the LTS reaction is concluded by briefly mentioning several other areas of work in this field. Several groups have attempted to expand the use of Cu/ZnO/Al<sub>2</sub>O<sub>3</sub> catalysts for mobile and fuel cell applications regarding the removal of CO impurities<sup>(103,111-112)</sup>. Consequently, catalysts have been examined regarding their stability in shut-down/start up procedures. This area is still a work in progress but it has been reported that deactivation is attributed to the blocking or deterioration of active sites due to the formation of Zn<sub>6</sub>Al<sub>2</sub>(OH)<sub>16</sub>CO<sub>3</sub>·4H<sub>2</sub>O species<sup>(103,111)</sup>. Finally, many authors have focused on optimising Cu/ZnO catalysts further for the LTS reaction using various dopants including MgO<sup>(109)</sup>, Cs<sup>(108,113)</sup>, La<sup>(98)</sup>, noble metals<sup>(100)</sup> and alkali metals<sup>(114)</sup>. Whilst doping in many of these studies has been illustrated to result in further optimisation, the presence of certain alkali metals, in particular sodium, has been shown to produce inferior catalysts.

#### 1.3.4. Conclusions

The Cu/ZnO/Al<sub>2</sub>O<sub>3</sub> catalyst has been in commercialisation for over 50 years to manufacture highly valuable chemical intermediates *via* syn-gas transformations. The current global demand for MeOH and H<sub>2</sub> is staggering and will continue to grow as the need for clean, alternative energy sources intensifies. In particular, the demand for MeOH is expected to sharply increase within the next ten years. Consequently, much interest has been paid to the industrial catalyst itself with the majority of studies investigating the 'structure-activity' relationship in conjunction to the preparation conditions of the industrial route. This is an attempt to derive the unrivalled recipe for constructing optimum catalysts. Whilst this is now a saturated field of research with countless volume of papers published annually on Cu/Zn catalysts it is interesting to note that the main focus has been to fine tune or even 'tweak' the current procedure. It has not been radically changed during this timeframe.

Furthermore, significant attention has focused on how such catalysts operate and behave under these chemical processes with much controversy still remaining regarding the mechanism, active site and role of ZnO in particular. It is therefore anticipated that Cu/Zn catalysis will remain a hot topic for many years to come.

#### 1.4. Outline of thesis

This project is a joint collaboration between the Cardiff Catalysis Institute (Cardiff University), Johnson Matthey and the UK Catalysis Hub. After reviewing the extensive volume of literature on Cu/ZnO based catalysts it is clear that it is a saturated field of work with much effort simply been focused on optimising co-precipitation routes for the production of crystalline hydroxycarbonates.

For this field to truly expand it is essential to move away from these principles. It is important to identify concepts within this area which have been largely neglected to ensure a high degree of novelty in future research which simultaneously offers a reasonable degree of potential. Furthermore, it is essential to identify the disadvantages of the current co-precipitation set-up in order to ensure validity and worthwhile significance in such work.

It was mentioned that the amorphous hydroxycarbonate termed georgeite has been highly overlooked in this field of work, especially considering the high level of interest it has attracted. It is well accepted that ageing is an essential step in the production of optimum catalysts and this has largely hindered interest. However, it is also important to appreciate the high level of difficulty in preparing georgeite. It is a metastable phase that is kinetically trapped from transforming into crystalline phases which are thermodynamically favoured. Under the optimum conditions summarised for the co-precipitation set-up georgeite is not stable and the phase simply cannot be isolated and retained. In fact it is not known if a completely pure form of the phase has ever existed. Fortunately, the incorporation of Zn into the phase enhances its stability<sup>(17)</sup> and therefore this does not apply to zincian georgeite. Zn plays a key role in the resulting catalyst system and so this phase still yields significant potential as an alternative catalyst precursor. In fact very recently Kondrat has illustrated that georgeite phases can be readily prepared in large abundance and retained in a stabilised form from using the supercritical CO<sub>2</sub> anti-solvent (SAS) precipitation process<sup>(3)</sup>. These initial studies have demonstrated that catalysts derived from georgeite precursors can compete against established industrial standards tailor made for methanol synthesis and the LTS reaction. As a result of providing access to a new class of Cu/ZnO based catalysts it is clear that further work is essential in order to optimise this synthetic procedure, and derive a greater understanding of the so-called 'structure-activity' relationship, in conjunction to malachite and aurichalcite derived catalysts. This would assist in the rational design of future catalyst systems and facilitate significant advances towards their optimisation.

In addition, whilst highly established and largely optimised the current co-precipitation set-up still displays several drawbacks. The methodology is highly sensitive and therefore issues must be raised regarding the degree of reproducibility in processing materials. The large number of synthesis parameters to consider does not help the cause. Perhaps the main disadvantage regards the starting reagents frequently used: sodium carbonate and metal nitrate salts. Sodium has been illustrated to be a poison to Cu/ZnO based catalysts<sup>(9,44-45,114)</sup>. This highlights the importance of the washing step directly after ageing in order to reduce the loading retained. Clearly, this hinders the full potential of the catalyst system from being exploited as significant sodium levels will always remain. A highly

preferred alternative would be to simply avoid alkali metal based reagents altogether. It should also be noted that residual nitrates have also been reported to be catalyst poisons<sup>(7)</sup>. Moreover, the utilisation of nitrate salts does not abide by the principles of green chemistry (**Section 1.2.4.**) and thus great efforts must be made to avoid their use where possible. Whilst this requirement makes catalyst innovation, design and synthesis much more challenging it should be a fundamental aim and principle for all catalysis researchers.

From these issues identified in the field of Cu/ZnO based catalysts the following objectives have been outlined:

- Optimisation of the supercritical anti-solvent (SAS) precipitation route for georgeite preparation. This includes examination of the following parameters:
  - Optimisation of the water content (vol.%) of the prepared metal acetate solution.
  - Optimisation of the Cu/Zn molar ratio and identifying additional phases simultaneously formed. Determining the maximum incorporation of Zn into the georgeite phase.
  - Incorporation of Al into the georgeite phase. Optimisation of the procedure and identifying additional phases simultaneously formed. Determining the maximum incorporation of Al into the georgeite phase.
- Identifying and optimising additional synthesis routes leading to georgeite formation. Such routes require the following criteria to be satisfied in order comply with the principles of green chemistry and be applicable for commercialisation:
  - Avoidance of nitrate and alkali metal based reagents.
  - Avoidance of high energy consumption processes, including high pressure and temperature.
- Testing and evaluating the performances of resulting georgeite derived catalysts against established industrial catalysts for the following chemical processes:
  - Methanol synthesis.
  - The LTS reaction.
- Extensive characterisation of the amorphous georgeite phase, including a detailed analysis of its evolution into the final state catalyst. Deriving a greater understanding of the 'structure-activity' relationship, with parallel examination of the malachite phase for direct comparison. Great emphasis must be placed on examining the following in particular:
  - The role of HT-CO<sub>3</sub> species.
  - The role of residual sodium regarding the mechanism of deactivation.

The final section of this chapter provides an introduction to supercritical fluids, with a brief literature review on studies which have exploited their properties for the application of catalyst preparation. In **Chapter Two**, details of the experimental procedures carried out in order to achieve the project objectives is presented. **Chapter Three** and **Four** present and discuss the findings which were subsequently obtained. In particular, **Chapter Three** predominantly focuses on optimisation of determined synthesis routes leading to georgeite formation and their subsequent testing carried out at Johnson Matthey. **Chapter Four** follows on from **Chapter Three** and attempts to rationalise the catalyst performances of the georgeite derived catalysts in relation to the industrial catalysts. **Chapter Five** summarises and reflects on all of the findings whilst outlining future work required in this field. Finally, a **Supplementary** is provided that contains additional findings in relation to the main work. All figures and tables in this section are labelled with a prefix **S** (e.g. **Figure S2.**).

## 1.5. Catalyst preparation using supercritical fluid precipitation

### 1.5.1. Introduction to supercritical fluids: definition, properties and applications

A supercritical fluid (SCF) is defined as any substance, the temperature and pressure of which are higher than their critical values, and which has a density close to or higher than its critical density (**Table 1.1.**)<sup>(115)</sup>.

**Table 1.1.** Critical data for selected substances<sup>(115)</sup>.

substance	$T_c$ , K	$P_c$ , atm	$\rho_c$ , g/mL
Ar	150.8	48.0	0.53
CH <sub>4</sub>	190.6	45.8	0.16
Kr	209.4	54.3	0.92
C <sub>2</sub> H <sub>4</sub>	283.1	50.5	0.22
Xe	289.8	58.0	1.15
C <sub>2</sub> F <sub>6</sub>	293.0	30.2	0.62
CHF <sub>3</sub>	299.3	47.9	0.62
CClF <sub>3</sub>	302.0	38.1	0.58
CO <sub>2</sub>	304.2	72.9	0.47
C <sub>2</sub> H <sub>6</sub>	305.5	48.2	0.20
N <sub>2</sub> O <sup>a</sup>	309.7	71.7	0.45
SF <sub>6</sub>	318.7	36.7	0.73
propane	370.3	41.9	0.22
H <sub>2</sub> S <sup>b</sup>	373.5	88.9	0.35
NH <sub>3</sub>	405.6	112.5	0.24
pentane	470.2	33.3	0.23
<sup>1</sup> PrOH	508.5	47.0	0.27
MeOH	513.7	78.9	0.27
EtOH	516.6	63.0	0.28
<sup>1</sup> BuOH	548.2	42.4	0.27
benzene	562.1	48.3	0.30
C <sub>2</sub> H <sub>4</sub> (NH <sub>2</sub> ) <sub>2</sub> (en)	593.0	61.9	0.29
pyridine	620.2	55.6	0.31
H <sub>2</sub> O	647.3	218.3	0.32

It is often most useful to define SCFs in relation to pressure-temperature (P-T) phase diagrams. A P-T phase diagram of a single substance shows areas in pressure-temperature space where, at equilibrium, the substance exists as a solid, liquid or gas (Figure 1.11.)<sup>(116)</sup>. The curves on the diagram represent phase boundaries. It is clear that the phase boundary between the liquid and gas phases does not continue indefinitely and the terminus of the line is denoted at the critical point. This critical point intercepts pressure-temperature space, where the critical pressure and temperature values,  $P_c$  and  $T_c$  are defined. When the pressure of a substance exceeds these critical values the liquid and gas phases converge to form the supercritical phase. It is also worth noting that this phase diagram (Figure 1.11.), which uses H<sub>2</sub>O as an example, describes a single component system only. However, most chemical systems involve at least a binary system with the parameters required to construct a homogeneous supercritical phase now dependant on the concentrations of all these components present. Altering compositions and introducing additional phases to the system to form multi-component systems changes the liquid-vapour equilibrium, and subsequently the mixtures critical point (MCP)<sup>(117-118)</sup>. This is an important concept to consider when utilising supercritical fluids in various applications. Throughout this thesis the prefix 'sc' is used to signify substances of the supercritical state (e.g. scCO<sub>2</sub>).

The properties of SCFs with respect to pressure and temperature has been extensively outlined by Kondrat, Taylor, Wandeler and Baiker<sup>(3,116,119)</sup>. It is clear from the definition of SCFs from the use of

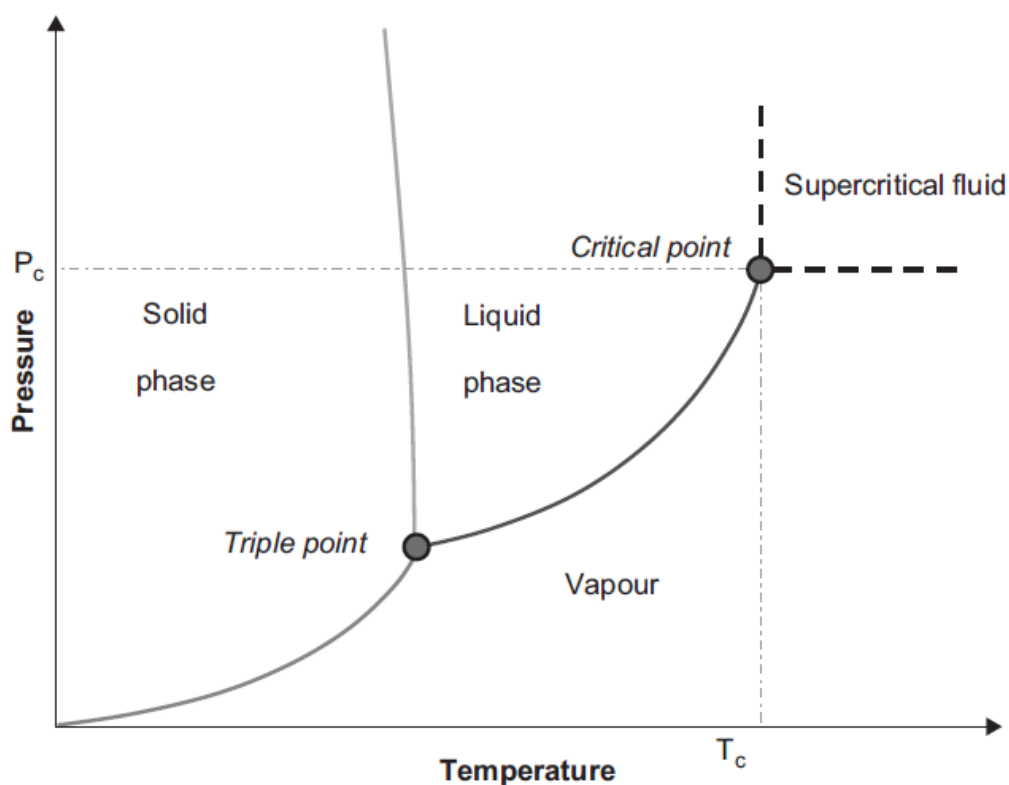


Figure 1.11. P-T phase diagram of H<sub>2</sub>O showing phase regions, phase boundaries and critical points<sup>(116)</sup>.

P-T phase diagrams that their properties lie between those of a liquid and a gas. It is also important to appreciate that some properties are more liquid-like, whereas others are more gas-like. Such properties can significantly change upon slight alterations to both temperature and pressure which renders supercritical fluids highly tuneable. These properties are most sensitive around the critical point in pressure-temperature space with respect to P-T phase diagrams.

It would be expected that at the critical point the density would lie between values typical for the liquid and gaseous state. However, when considering the order of magnitude involved the density of a SCF actually lies closer to the liquid state. The density is seen to increase with increasing pressure and decrease with increasing temperature, whilst becoming less sensitive with increasing distance from the critical point. The dissolving power also depends on density; a liquid displays great dissolving power whilst a gas is a poor solvent. Generally, the solubility of a given solute increases with increasing density and hence pressure. However solubility also increases with increasing vapour pressure of the solute and therefore with respect to temperature could increase, decrease or remain constant, depending on the predominant factor. Whilst the solubility of SCFs are inferior to liquids it is the unique combination with additional gas-phase features which renders them as super-solvents.

In terms of the gas-like properties of SCFs we speak of hydrodynamic properties including viscosity, diffusivity and surface tension. The dynamic viscosity and diffusivity of a SCF are also dependant on pressure and temperature, as is the case for density. As pressure increases and the SCF forms properties which are more liquid-like, the viscosity increases and the diffusivity decreases. This would be expected for a substance which undergoes a phase transformation from the gaseous to the liquid state. Furthermore, an increase in temperature leads to a decrease in viscosity whilst simultaneously resulting in an increase in diffusivity. Below the  $P_c$  and  $T_c$ , surface tension also decreases with respect to both pressure and temperature and becomes zero on reaching the critical point.

The ability to fine tune the dual liquid and gaseous properties of SCFs so that they are tailor made for specific applications is just one of several advantages of utilising such substances. The low viscosities and high diffusion rates subsequently lead to high molecular and macro-scale mass transfer coefficients. Thus, when SCFs are used to induce precipitation for the preparation of materials, the level of super-saturation achieved is at a magnitude considerably larger than that derived from the conventional co-precipitation route. This results in higher nucleation to growth ratios, which provides access to novel materials that cannot be obtained from any alternative methodology. Such materials regularly consist of nanoparticles ( $\leq 50$  nm), with large BET surface

areas ( $\geq 100 \text{ m}^2 \text{ g}^{-1}$ ) and intimately mixed components. In **Section 1.5.3.** specific examples reported from the literature are provided.

Whilst many substances are capable of being used as SCF's (**Table 1.1.**), the majority of studies involving SCFs have focused on using  $\text{CO}_2$ ,  $\text{H}_2\text{O}$ , ethene and ethane<sup>(119)</sup>. However, carbon dioxide ( $T_c = 31.0 \text{ }^\circ\text{C}$ ,  $P_c = 73.8 \text{ bar}$ ) is by far the most widely used SCF in chemistry and extraction processes. This can be attributed to the fact that  $\text{scCO}_2$  is non-flammable, non-toxic, environmentally benign and is available in a high state of purity at a comparably low cost. When used as a solvent, it also has the advantage that it is not very reactive. However, this can be disadvantageous when used as a reactant. It has also been reported to be a particularly poor solvent<sup>(115)</sup>. A useful rule of thumb is that  $\text{scCO}_2$  has solvent properties similar to *n*-hexane. The most numerous exceptions to this rule are fluorinated compounds which show a solubility in  $\text{scCO}_2$  much higher than that in alkanes. They have been coined  $\text{CO}_2$ -phillic. Various alternative SCFs do not provide all of the positive attributes of  $\text{scCO}_2$  by comparison. Both  $\text{sc}$ -ethane and  $\text{sc}$ -ethene are flammable, and the latter can also polymerise. Moreover, whilst water is also cheap, non-toxic, non-flammable and ecologically benign it does require the use of remarkably high pressure and temperature ( $T_c = 374.0 \text{ }^\circ\text{C}$ ,  $P_c = 220.6 \text{ bar}$ ). Furthermore,  $\text{sc-H}_2\text{O}$  is highly corrosive and demands special alloys for their contacting parts.

Kondrat and Taylor have already emphasised how SCFs have found wide applications in several fields as a result of their unique properties<sup>(3,116)</sup>. This includes extraction, a medium for homogeneous<sup>(120)</sup> and heterogeneous<sup>(119)</sup> catalytic reactions and for material synthesis and production. SCFs can also be utilised in chromatography<sup>(121)</sup> and large scale industrial extractions. The high diffusion coefficients and tuneable solvating power make SCFs ideal in well-established separation technologies. In the context of preparation materials, SCFs can be utilised in several ways; as a reactant, a solvent or alternatively as an anti-solvent. A vast array of materials for various applications have been prepared using the properties of SCFs. Reverchon and co-workers have illustrated the production of micrometric particles of paint pigments<sup>(122)</sup>. Several groups have focused on the use of SCFs for the preparation of polymers<sup>(123-124)</sup>. Studies by Sun and co-workers have produced nanoparticles of semi-conductor materials from the rapid expansion of supercritical solutions<sup>(125)</sup>. Finally, studies have also illustrated the use of SCFs for pharmaceutical processing<sup>(126)</sup>.

### 1.5.2. Preparation of catalysts using supercritical fluids

The work reported herein focuses on the utilisation of  $\text{scCO}_2$  using the supercritical anti-solvent (SAS) precipitation methodology for the construction of georgeite precursors. This is a requirement

to fulfil specific objectives of the project (**Section 1.4.**). This technique can be broadly classified as one of three precipitation techniques for the preparation of materials using SCFs:

1. Rapid expansion of supercritical solutions (RESS)
2. Gas anti-solvent (GAS) precipitation
3. Supercritical anti-solvent (SAS) precipitation

Since RESS and GAS are not used in this work they are only briefly discussed here. RESS involves dissolving a solid in a supercritical solvent followed by the rapid depressurisation of the resulting solution, often through a nozzle. As the pressure drops the solvating power of the SCF diminishes rapidly resulting in super-saturation, nucleation and particle formation. Studies have reported that flow rate and nozzle design can dictate particle sizes and morphologies<sup>(115)</sup>. It is important to appreciate that in this procedure the SCF is acting as a solvent. Therefore, it has a clear limitation in that it is only applicable to solid substrates which are soluble in the SCF of choice.

For the latter two techniques the role of the SCF is to act as an anti-solvent. Therefore, in these systems a minimum of three components is present: solvent, solute and anti-solvent. Clearly, this relies on the following three requirements:

1. The solute is soluble in the solvent of choice
2. The solvent and anti-solvent are fully miscible
3. The solute and resulting solvent/anti-solvent mixture are not miscible

As mentioned previously,  $\text{scCO}_2$  is a poor solvent with properties similar to *n*-hexane (**Section 1.5.1.**). Consequently, polar solvents such as water are a poor candidate for this application as it does not fulfil **requirement 2**. With increasing non-polarity of the solvent, the more miscible it is with the  $\text{scCO}_2$  anti-solvent. Solvents which have been used in this methodology include methanol, ethanol, THF, toluene, NMP, DCM and DMSO<sup>(117)</sup>. Unfortunately, the solubility of the solute (salt) within the solvent diminishes rapidly as it increases in non-polarity and this can inhibit fulfilment of **requirement 1**. All of these requirements dictate the choice of starting materials. It should also be noted that whilst it is clearly essential to satisfy **requirement 1** it is undesirable for the solute to be exceptionally soluble in the solvent of choice. The SCF is acting as an anti-solvent and so the stronger the affinity between the solute and solvent the more difficult it becomes to induce precipitation. Failure to fulfil **requirement 3** can also result in reduced yields and nominal compositions not being obtained when more than one solute is utilised.

The GAS methodology is both a dynamic and batch process. It involves injecting  $\text{scCO}_2$  into a prepared solution (i.e. solvent and solute) inside a sealed vessel. As the system is pressurised with

the anti-solvent it will eventually become supercritical. As its properties become more resembling of a SCF, the degree of miscibility between the solvent and anti-solvent increases. Consequently, the prepared solution expands from the new combined solvent/anti-solvent solvent phase, resulting in super-saturation, nucleation and growth of the solute particulates. The overall process alters the phase system from a single, homogeneous phase into a two-phase system. The system then requires washing with the dense gas to remove any remaining solvent that could cause re-dissolution. Clearly, many variables effect the morphology, size and structure as the resulting precipitate including the rate of pressurisation and the maximum level of super-saturation attained. Furthermore, since the density of the SCF is dependent on both pressure and temperature these are also important variables to consider. The level of super-saturation obtained is dictated by the solute concentration in the starting solution and the mol-fraction of anti-solvent in the expanded phase<sup>(3,115)</sup>.

The supercritical anti-solvent (SAS) process is also known as solution enhanced dispersion by SCFs (SEDS) or aerosol solvent extraction system (ASES)<sup>(115)</sup>. These techniques only differ in terms of the detailed design of the nozzles and precipitation chambers rather than the overall principles. The process involves co-injecting the organic solution and scCO<sub>2</sub> into a common vessel (**Figure 1.12.**). Similar to the GAS process, contact between the solution and scCO<sub>2</sub> produces rapid expansion as the resulting solvent/anti-solvent phase to facilitate super-saturation of the solution and precipitation of the desired product. Further down the line the solvent/anti-solvent phase is depressurised, and thus, the solvent can be recollected and theoretically recycled. This occurs because scCO<sub>2</sub> loses its SCF properties upon being depressurized back to the gaseous state. SAS differs from GAS because in

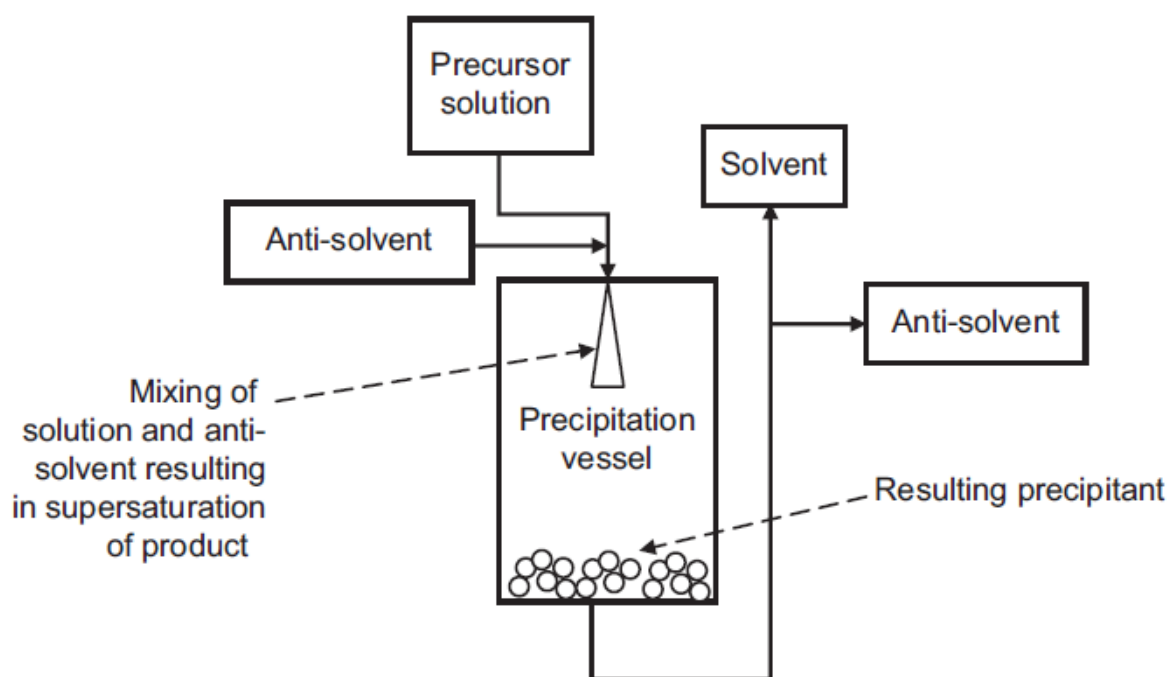


**Figure 1.12.** Schematic of the supercritical anti-solvent (SAS) precipitation process<sup>(3,116)</sup>.

contrast it is both a steady state and semi-continuous process. The prepared solution immediately comes into contact with scCO<sub>2</sub> having specific properties dictated by variables such as pressure and temperature. By comparison, in the GAS process set-up the solution is in direct contact with CO<sub>2</sub> whilst it is being pressurised into a SCF and therefore super-saturation, nucleation and growth processes can consequently begin under sub-critical conditions. The higher super-saturation levels achieved in the SAS process facilitate higher nucleation to growth ratios, resulting in smaller particulates. This frequently results in the formation of amorphous materials.

Clearly, one of the principles that will affect the physicochemical properties of the resulting materials in the SAS set-up is the hydrodynamics of the solution upon contact with the anti-solvent. This includes the nozzle design and the flow rates of the solution and scCO<sub>2</sub> phases. These two independent flow rates define the ratio (either as molar, mass or volumetric) between the solution and scCO<sub>2</sub>. Consideration of the nozzle design is also highly important as it determines the degree of mixing and dispersion between the solution and anti-solvent. In this work, the co-axial nozzle design was used and this will be discussed in more detail in the subsequent chapter. Studies by Czerwonatis and Eggers have examined the atomisation of liquids, and reported that from a derived dimensionless number ( $Z^{**}$ ) and the Reynolds number (the ratio of inertial and viscous forces), it was possible to determine boundaries that describe the disintegration of liquid jets in pressurised systems<sup>(127)</sup>. It was concluded that fine sprays are required to get large surfaces for heat- and mass-transfer applications. Leeke and co-workers have also investigated various SAS parameters including the solution flow rate and nozzle diameter from using TiO(acac)<sub>2</sub> solutions<sup>(6)</sup>. It was concluded that a decrease in the velocity of the solution flow rate resulted in an increased particle size, whilst the mean particle diameter increased with the capillary diameter. Reduction of the solvent/anti-solvent ratio also favours the construction of smaller particulates.

The thermodynamics of the SAS system also governs the physicochemical properties of the resulting precipitate. Significant work has been carried out in this field by Reverchon and co-workers. As previously mentioned, the mixture critical point (MCP) is dependent on the number of components present in the system and their compositions (**Section 1.5.1.**)<sup>(117,118)</sup>. For nanoparticle formation to occur, there must be complete miscibility between the solvent and anti-solvent. In other words, the construction of a homogenous phase system is essential. This is only obtained by operating at pressures higher than the MCP. Operating below the MCP at sub-critical conditions results in the formation of microparticles. However, it is important to note that introduction of a solute (Z) can modify the vapour-liquid equilibria (VLE) which consequently shifts the MCP of the resulting ternary system towards higher pressure in relation to the binary system (**Figure 1.13.**). The MCP will also

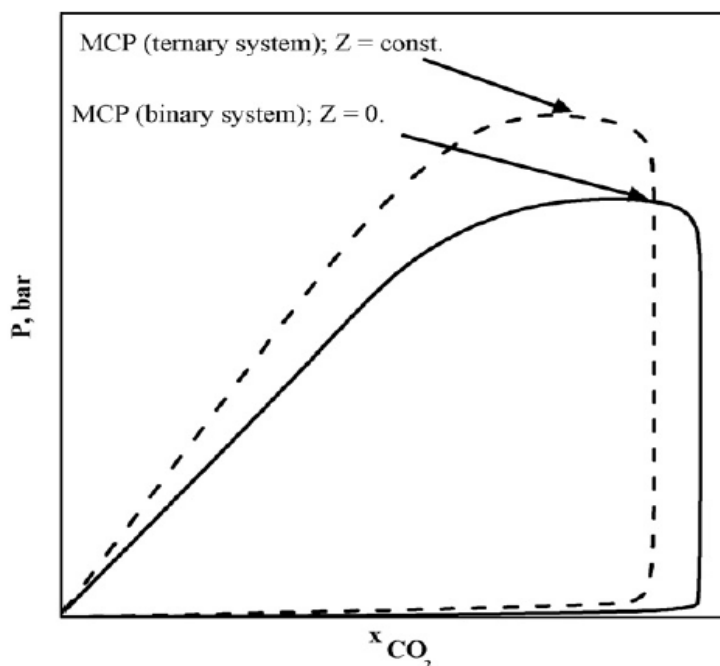


**Figure 1.13.** A possible qualitative modification of the VLE's binary (solid line) system when a third component (Z) is added at a given concentration (hashed line)<sup>(117)</sup>.

shift to higher pressure if the concentration of the solute is increased, and therefore, it is not plausible to consider the MCP of a ternary system coincident to that of the binary system. This implies that for the preparation of nanoparticles using the SAS procedure, it is empirical to operate at pressures significantly higher than the critical pressure of scCO<sub>2</sub> ( $P_c = 73.8$  bar). Subsequent work in this group also identified a linear relationship between the mean particle diameter of the resulting precipitate and the reduced concentration of the prepared starting solution (i.e. the ratio between the concentration used and the saturation concentration). This is extremely useful for the design and construction of prepared materials with defined pore size distributions.

In this context, it is also important to consider the mechanism of precipitation in the SAS procedure. It is clearly correlated to the system pressure in relation to its MCP (**Figure 1.13.**). Reverchon postulates three mechanisms in order to rationalise the dependence of nanoparticle or microparticle formation on pressure. When operating under non-ideal conditions, whereby the applied pressure is below the MCP and a single phase system is not present, the one-drop mechanism applies. The atomisation of the liquid solution through the injector results in the formation of droplets. The fast solubilisation of the SCF into the droplet produces a solid particle in the shape of the droplet. The second mechanism is a derivative of this droplet theory, but in this case the rapid mass transfer of the SCF results in high super-saturation and the formation of several nuclei within the same droplet. Evidently, when we operate at pressures above the MCP nanoparticle formation is apparent and the third mechanism applies. The surface tension between the liquid and anti-solvent phases disappears at a time scale smaller than jet break-up of the solution. No droplets are formed and so nucleation

and growth of nanoparticles result from gas like mixing i.e. gas-to-particle precipitation. It is therefore apparent that the surface tension between the anti-solvent and solution governs the precipitation mechanism, which itself is dictated by the pressure of the system in relation to its MCP. Consequently, near the MCP small changes in the process conditions can produce large changes in the equilibrium surface tension.

### 1.5.3. Catalysts prepared by scCO<sub>2</sub> anti-solvent precipitation

In this final section literature studies which have utilised scCO<sub>2</sub> in the SAS precipitation process for the construction of catalyst materials is briefly reviewed. This can be broadly classified into several categories. The first is the use of this process to produce metal oxides, which are then used as catalyst supports after deposition of active metals. Noble metals such as Au, Pt and Pd are the most frequent active metals used, and in this case are deposited onto the support using non-supercritical methods. Secondly, the technique is used to prepare mixed metal oxide catalysts, which also relates to the work carried out in this thesis. Finally, and most recently the technique has been used to impregnate a non-supercritically prepared support with active metals in a process to make supported metal catalysts. As the latter technique is very recent we will focus specifically on the first two categories.

Research which has been carried out on supported precious metal catalysts for selective red-ox reactions is extensive and is a separate entity outside the scope of this project. However, several studies by Hutchings and co-workers have reported the SAS preparation of metal oxide supports for the synthesis of such catalysts. In particular, using the impregnation methodology Au and Pd nanoparticles were deposited onto CeO<sub>2</sub> supports and tested for CO oxidation and the selective oxidation of a variety of alcohol substrates<sup>(128-129)</sup>. In these studies, precious metals were deposited onto conventional and supercritically prepared CeO<sub>2</sub> supports. This has a significant impact on the size and morphology of the resulting metal nanoparticles. From using the scCeO<sub>2</sub> support, it was reported to enhance the dispersion of the metal nanoparticles, which were < 1 nm in diameter. These catalysts illustrated superior catalyst activity to those prepared using the conventional support for these reactions. Interestingly, for benzyl alcohol oxidation the catalyst activity increased with re-use up until the third use. Since loss of metal was identified during these runs it was concluded that the fresh catalyst had Au and Pd in inactive forms. Similar studies were also carried out using TiO<sub>2</sub> as a support for Au catalysts which were tested for CO oxidation<sup>(130)</sup>. It was determined that Au catalysts supported on the scTiO<sub>2</sub> support were stable and exhibited 100% CO conversion after 6 hours testing. In comparison, using the untreated TiO<sub>2</sub> support such catalysts only displayed a CO conversion of 10% over the same duration (**Figure 1.14.**).

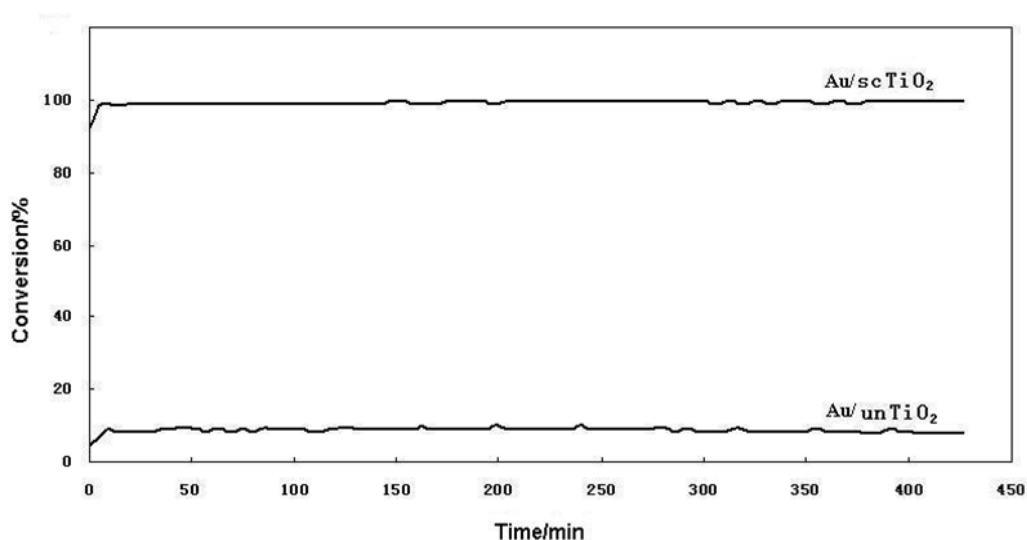


**Figure 1.14.** Catalyst performance of Au/scTiO<sub>2</sub> and Au/unTiO<sub>2</sub> for CO oxidation at 25 °C<sup>(130)</sup>.

Considerable work has evidently focused on the preparation of mixed metal oxide catalyst materials using the SAS methodology. Vanadium phosphate catalysts have been prepared using different techniques by Hutchings and co-workers and evaluated for the oxidation of *n*-butane to maleic anhydride<sup>(129,131)</sup>. Interestingly, activity was found to correlate with surface area whilst the specific activity appeared insensitive to the preparation methodology. However, when using the SAS technique the resulting sc-VPO material clearly exhibited the highest activity out of all catalysts investigated, and was also found to be totally amorphous before and after use as a catalyst. Subsequent studies determined that cobalt appears to act as a catalyst poison despite this metal being well known as promoter for crystalline vanadium phosphate catalysts. It was concluded that it effected the morphology of the material and the oxidation state of vanadium. Studies by Marin and co-workers have prepared novel cobalt zinc oxide catalyst by SAS precipitation for the Fischer-Tropsch reaction<sup>(133)</sup>. They examined the addition of water to the SAS procedure and determined it had a significant impact on the physicochemical properties of the resulting precipitate and subsequent catalyst activity. Without using water, the resulting precursor was a highly mixed metal acetate which decomposed upon calcination to give wurtzite type Zn<sub>1-x</sub>Co<sub>x</sub>O and spinel type Zn<sub>x</sub>Co<sub>3-x</sub>O<sub>4</sub> phases. Interestingly, the addition of water instead resulted in the production of a carbonates with enhanced phase separation. However, this provided a more active Co surface area which was found to be more favourable for the formation of C<sub>5+</sub> products. In similar work, a series of metal oxide catalysts (Fe<sub>3</sub>O<sub>4</sub>, NiO, CuO and Co<sub>3</sub>O<sub>4</sub>) were prepared by SAS and evaluated for the total oxidation of propane<sup>(134)</sup>. It was also concluded that water addition resulted in carbonate species. The Co<sub>3</sub>O<sub>4</sub> material achieved BET surface areas > 100 m<sup>2</sup> g<sup>-1</sup> when prepared using water and was found to be the most active catalyst, achieving 50% propane conversion at 175 °C. Interestingly, Reverchon and co-workers reported trace amounts of carbonate present in the preparation of ZnO

using DMSO and NMP solvents<sup>(135)</sup>. This illustrates that even with trace amounts of water present in the system, which is difficult to avoid, carbonate formation is evident. Studies have also been carried out by Hutchings and co-workers for the preparation of solid homogeneous mixtures of  $\text{Cu}^{2+}$  and  $\text{Mn}^{3+}$ <sup>(136)</sup>. After calcination, the resulting  $\text{CuMn}_2\text{O}_4$  phase had a branch chainlike structure with a length between 160-200 nm. This morphology cannot be obtained by the conventional co-precipitation method and was also more than twice as active per unit surface area for CO oxidation. Later studies also investigated the addition of water to the system and determined that small quantities resulted in mixed acetate precursors, with BET surface areas  $> 200 \text{ m}^2 \text{ g}^{-1}$ <sup>(137)</sup>. This further enhanced the resulting catalyst activity for CO oxidation. Kondrat and co-workers have also investigated the preparation of mixed Cu-Mn oxides using SAS preparation and reported that the phase and subsequent catalyst activity for CO oxidation could be tailor made from the calcination treatment<sup>(138)</sup>. The SAS procedure enabled the preparation of well mixed Cu-Mn precursors, whereby Cu supported  $\text{MnO}_x$  or  $\text{CuMnO}_x$  spinel phases could be produced after heat treatment depending on the oxygen content. From using static air in the thermal treatment the content of the spinel phase increased, which was correlated to an increase in catalytic activity. Several groups have also prepared hollow and solid  $\text{MnO}_x\text{-CeO}_2$  nanospheres by SAS precipitation for the selective reduction of NO with  $\text{NH}_3$ <sup>(139-141)</sup>. Solid solutions and oxygen vacancies were identified in these samples, whilst it was determined that the hollow spheres exhibited a higher NO conversion. This was attributed to higher surface area, better oxygen mobility and a richer surface active oxygen surface. From the addition of surfactants such as PVP, the interconnectivity and agglomeration of the nanoparticles was inhibited, which also lead to higher surface area and an increase in NO conversion by 10%. Finally, several papers have reported the preparation of mixed  $\text{CeO}_2\text{-ZrO}_2$  catalysts with addition of  $\text{Al}_2\text{O}_3$ <sup>(142)</sup> and Cu<sup>(143)</sup>. It was determined that  $\text{Al}^{3+}$ ,  $\text{Zr}^{4+}$  and  $\text{Cu}^{2+}$  ions were all incorporated into the  $\text{CeO}_2$  lattice to form solid solutions and oxygen vacancies. For the Cu-Ce-Zr-O composite oxide, it was determined that doping  $\text{Cu}^{2+}$  using the SAS process in comparison to the impregnation method resulted in superior activity for CO oxidation. This was attributed to a higher concentration of oxygen vacancies, increased lattice distortion and better dispersion of  $\text{Cu}^{2+}$  in the resulting catalyst system.

## 1.6. References

1 G. C. Bond, Heterogeneous Catalysis: Principles and Applications, Second Edition, Oxford Science Publications, 1987.

- 2 M. Misono, *Heterogeneous Catalysis of Mixed Oxides, Perovskite and Heteropoly Catalysts*, Elsevier, 2013.
- 3 S. A. Kondrat, PhD Thesis, Cardiff University, 2011.
- 4 I. T. Horvath and P. T. Anastas, *Chemical Reviews*, 2007, **107**, 2167-2168.
- 5 M. Behrens, S. Kibner, F. Girgsdies, I. Kasatkin, F. Hermerschmidt, K. Mette, H. Ruland, M. Muhler and R. Schlögl, *Chem. Commun.*, 2011, **47**, 1701-1703.
- 6 T. Lu, S. Blackburn, C. Dickinson, M. J. Rosseinsky, G. Hutchings, S. Axon and G. A. Leeke, *Powder Technology*, 2009, **188**, 264-271.
- 7 B. Bems, M. Schur, A. Dassenoy, H. Junkes, D. Herein and R. Schlögl, *Chem. Eur. J.*, 2003, **9**, 2039-2052.
- 8 C. Baltes, S. Vukojevic and F. Schuth, *Journal of Catalysis*, 2008, **258**, 334-344.
- 9 G. Simson, E. Prasetyo, S. Reiner and O. Hinrichsen, *Applied Catalysis A: General*, 2013, **450**, 1-12.
- 10 M. Schur, B. Bems, A. Dassenoy, I. Kassatkine, J. Urban, H. Wilmes, O. Hinrichsen, M. Muhler and R. Schlögl, *Angew. Chem. Int. Ed.*, 2003, **42**, 3815-3817.
- 11 M. Behrens and R. Schlögl, *Z. Anorg. Allg. Chem.*, 2013, **639**, 2683-2695.
- 12 B. L. Kniep, T. Ressler, A. Rabis, F. Girgsdies, M. Baenitz, F. Steglich and R. Schlögl, *Angew. Chem. Int. Ed.*, 2004, **43**, 112-115.
- 13 M. Behrens, I. Kasatkin, S. Kuhl and G. Weinberg, *Chem. Mater.*, 2010, **22**, 386-397.
- 14 M. Behrens, S. Zander, P. Kurr, N. Jacobsen, J. Senker, G. Koch, T. Ressler, R. W. Fischer and R. Schlögl, *Journal of the American Chemical Society*, 2013, **135**, 6061-6068.
- 15 C. Rhodes, G. J. Hutchings and A. M. Ward, *Catalysis Today*, 1995, **23**, 43-58.
- 16 M. V. Twigg, *Catalyst Handbook*, Second Edition, Manson Publishing, 1989.
- 17 A. M. Pollard, M. S. Spencer, R. G. Thomas, P. A. Williams, J. Holt and J. R. Jennings, *Applied Catalysis A: General*, 1992, **85**, 1-11.
- 18 A. M. Pollard, R. G. Thomas and P. A. Williams, *Mineralogical Magazine*, 1991, **55**, 163-166.
- 19 P. J. Bridge, J. Just and M. H. Hey, *Mineralogical Magazine*, 1979, **43**, 97-98.

- 20 A. F. Rogers, *The Journal of Geology*, 1917, **25**, 515-541.
- 21 M. A. J. Hartig, N. Jacobsen and W. Peukert, *Chemical Engineering Science*, 2014, **109**, 158-170.
- 22 S. Zander, B. Seidlhofer and M. Behrens, *Dalton Trans.*, 2012, **41**, 13413-13422.
- 23 P. Kowalik, M. Konkol, K. Antoniak, W. Prochniak and P. Wiercioch, *Journal of Molecular Catalysis A: Chemical*, 2014, **392**, 127-133.
- 24 W. Danjun, T. Furong, Z. Huahua, S. Huanling and C. Lingjun, *Chinese Journal of Catalysis*, 2011, **32**, 1452-1456.
- 25 B. V. Farahani, F. H. Rajabi, M. Bahmani, M. Ghelichkhani and S. Sahebdehfar, *Applied Catalysis A: General*, 2014, **482**, 237-244.
- 26 H. Jeong, C. H. Cho and T. H. Kim, *Reac. Kinet. Mech. Cat.*, 2012, **106**, 435-443.
- 27 D. Waller, D. Stirling, F. S. Stone and M. S. Spencer, *Faraday Discuss. Chem. Soc.*, 1989, **87**, 107-120.
- 28 M. S. Spencer, *Catalysis Letters*, 2000, **66**, 255-257.
- 29 S. Fujita, A. M. Satriyo, G. C. Shen and N. Takezawa, *Catalysis Letters*, 1995, **34**, 85-92.
- 30 A. A. Mirzaei, H. R. Shaterian, S. H. Taylor and G. J. Hutchings, *Catalysis Letters*, 2003, **87**, 103-108.
- 31 E. N. Muhamad, R. Irmawati, Y. H. Taufiq-Yap, A. H. Abdullah, B. L. Kniep, F. Girgsdies and T. Ressler, *Catalysis Today*, 2008, **131**, 118-124.
- 32 D. M. Whittle, A. A. Mirzaei, J. S. J. Hargreaves, R. W. Joyner, C. J. Kiely, S. H. Taylor and G. J. Hutchings, *Phys. Chem. Chem. Phys.*, 2002, **4**, 5915-5920.
- 33 M. Behrens, *Journal of Catalysis*, 2009, **267**, 24-29.
- 34 A. Budiman, M. Ridwan, S. M. Kim, J. Choi, C. W. Yoon, J. Ha, D. J. Suh and Y. Suh, *Applied Catalysis A: General*, 2013, **462-463**, 220-226.
- 35 S. Fujita, Y. Kanamori, A. M. Satriyo and N. Takezawa, *Catalysis Today*, 1998, **45**, 241-244.
- 36 Y. Kawamura, K. Yamamoto, N. Ogura, T. Katsumata and A. Igarashi, *Journal of Power Sources*, 2005, **150**, 20-26.

- 37 G. J. Millar, I. H. Holm, P. J. R. Uwins and J. Drennan, *J. Chem. Soc., Faraday Trans.*, 1998, **94**, 593-600.
- 38 M. Behrens and F. Girgsdies, *Z. Anorg. Allg. Chem.*, 2010, **636**, 919-927.
- 39 M. Behrens, F. Girgsdies, A. Trunschke and R. Schlögl, *Eur. J. Inorg. Chem.*, 2009, 1347-1357.
- 40 J.-L. Li and T. Inui, *Applied Catalysis A: General*, 1996, **137**, 105-117.
- 41 M. Behrens, D. Brennecke, F. Girgsdies, S. Kibner, A. Trunschke, N. Nasrudin, S. Zakaria, N. F. Idris, S. B. A. Hamid, B. Kniep, R. Fischer, W. Busser, M. Muhler and R. Schlögl, *Applied Catalysis A: General*, 2011, **392**, 93-102.
- 42 C. Kiener, M. Kurtz, H. Wilmer, C. Hoffmann, H.-W. Schmidt, J.-D. Grunwaldt, M. Muhler and F. Schuth, *Journal of Catalysis*, 2003, **216**, 110-119.
- 43 G. Shen, S. Fujita, S. Matsumoto and N. Takezawa, *Journal of Molecular Catalysis A: Chemical*, 1997, **124**, 123-136.
- 44 J. Wu, S. Luo, J. Toyir, M. Saito, M. Takeuchi and T. Watanabe, *Catalysis Today*, 1998, **45**, 215-220.
- 45 K. Jun, W. Shen, K. S. Rama Rao and K. Li, *Applied Catalysis A: General*, 1998, **174**, 231-238.
- 46 S. Fujita, S. Moribe, Y. Kanamori, M. Kakudate and N. Takezawa, *Applied Catalysis A: General*, 2001, **207**, 121-128.
- 47 A. Tarasov, J. Schumann, F. Girgsdies, N. Thomas and M. Behrens, *Thermochimica Acta*, 2014, **591**, 1-9.
- 48 S. Kaluza, M. Behrens, N. Schiefenhovel, B. Kniep, R. Fischer, R. Schlögl and M. Muhler, *ChemCatChem*, 2011, **3**, 189-199.
- 49 M. H. Stacey and M. Shannon in: B. Baeret and L. C. Dufour, *Reactivity of Solids*, Elsevier, 1985.
- 50 M. Kurtz, N. Bauer, C. Buscher, H. Wilmer, O. Hinrichsen, R. Becker, S. Rabe, K. Merz, M. Driess, R. A. Fischer and M. Muhler, *Catalysis Letters*, 2004, **92**, 49-52.
- 51 Y. Tanaka, T. Utaka, R. Kikuchi, K. Sasaki and K. Eguchi, *Applied Catalysis A: General*, 2003, **238**, 11-18.
- 52 Z. Chu, H. Chen, Y. Yu, Q. Wang and D. Fang, *Journal of Molecular Catalysis A: Chemical*, 2013, **366**, 48-53.

- 53 J. Agrell, M. Boutonnet, I. Melian-Cabrera and J. L. G. Fierro, *Applied Catalysis A: General*, 2003, **253**, 201-211.
- 54 J. Bao, Z. Liu, Y. Zhang and N. Tsubaki, *Catalysis Communications*, 2008, **9**, 913-918.
- 55 A. Karelavic, A. Bargibant, C. Fernandez and P. Ruiz, *Catalysis Today*, 2012, **197**, 109-118.
- 56 T. Shishido, M. Yamamoto, D. Li, Y. Tian, H. Morioka, M. Honda, T. Sano and K. Takehira, *Applied Catalysis A: General*, 2006, **303**, 62-71.
- 57 G. J. A. A. Soler-Illia, R. J. Candal, A. E. Regazzoni and M. A. Blesa, *Chem. Mater.*, 1997, **9**, 184-191.
- 58 X. Liu, G. Q. Lu, Z. Yan and J. Beltramini, *Ind. Eng. Chem. Res.*, 2003, **42**, 6518-6530.
- 59 M. S. Spencer, *Topics in Catalysis*, 1999, **8**, 259-266.
- 60 G. C. Chinchen, K. C. Waugh and D. A. Whan, *Applied Catalysis*, 1986, **25**, 101-107.
- 61 G. C. Chinchen, P. J. Denny, D. G. Parker, M. S. Spencer and D. A. Whan, *Applied Catalysis*, 1987, **30**, 333-338.
- 62 M. S. Spencer, R. Burch and S. E. Golunski, *J. Chem. Soc. Faraday Trans.*, 1990, **86**, 3151-3152.
- 63 M. S. Spencer, *Catalysis Letters*, 1999, **60**, 45-49.
- 64 M. S. Spencer, *Catalysis Letters*, 1998, **50**, 37-40.
- 65 M. S. Spencer, *Surface Science*, 1995, **339**, L897-L901.
- 66 K. Jung, O. Joo and S. Han, *Catalysis Letters*, 2000, **68**, 49-54.
- 67 O. Martin and J. Perez-Ramirez, *Catal. Sci. Technol.*, 2013, **3**, 3343-3352.
- 68 M. Kurtz, H. Wilmer, T. Genger, O. Hinrichsen and M. Muhler, *Catalysis Letters*, 2003, **86**, 77-80.
- 69 J. Nakamura, T. Uchijima, Y. Kanai and T. Fujitani, *Catalysis Today*, 1996, **28**, 223-230.
- 70 M. M. Gunter, T. Ressler, B. Bems, C. Buscher, T. Genger, O. Hinrichsen, M. Muhler and R. Schlögl, *Catalysis Letters*, 2001, **71**, 37-44.
- 71 I. Kasatkin, P. Kurr, B. Kniep, A. Trunschke and R. Schlögl, *Angew. Chem. Int. Ed.*, 2007, **46**, 7324-7327.

- 72 M. Behrens, F. Studt, I. Kasatkin, S. Kuhl, M. Havecker, F. Abild-Pedersen, S. Zander, F. Girgsdies, P. Kurr, B. Kniep, M. Tovar, R. W. Fischer, J. K. Norskov and R. Schlögl, *Science*, 2012, **336**, 893-897.
- 73 T. Kandemir, F. Girgsdies, T. C. Hansen, K. Liss, I. Kasatkin, E. L. Kunkes, G. Wowsnick, N. Jacobsen, R. Schlögl and M. Behrens, *Angew. Chem. Int. Ed.*, 2013, **52**, 5166-5170.
- 74 M. Behrens, *Angew. Chem. Int. Ed.*, 2014, **53**, 12022-12024.
- 75 F. Arena, G. Mezzatesta, G. Zafarana, G. Trunfio, F. Frusteri and L. Spadaro, *Journal of Catalysis*, 2013, **300**, 141-151.
- 76 M. V. Twigg and M. S. Spencer, *Topics in Catalysis*, 2003, **22**, 191-203.
- 77 S. Miao, R. Naumann d'Alnoncourt, T. Reinecke, I. Kasatkin, M. Behrens, R. Schlögl and Martin Muhler, *Eur. J. Inorg. Chem.*, 2009, 910-921.
- 78 P. Porta, M. C. Campa, G. Fierro, M. L. Jacono, G. Minelli, G. Moretti and L. Stoppa, *J. Mater. Chem.*, 1993, **3**, 505-511.
- 79 M. Behrens, G. Lolli, N. Muratova, I. Kasatkin, M. Havecker, R. Naumann d'Alnoncourt, O. Storcheva, K. Kohler, M. Muhler and R. Schlögl, *Phys. Chem. Chem. Phys.*, 2013, **15**, 1374-1381.
- 80 T. Kandemir, I. Kasatkin, F. Girgsdies, S. Zander, S. Kuhl, M. Tovar, R. Schlögl and M. Behrens, *Top Catal.*, 2014, **57**, 188-206.
- 81 H. Wilmer and O. Hinrichsen, *Catalysis Letters*, 2002, **82**, 117-122.
- 82 P. C. K. Vesborg, I. Chorkendorff, I. Knudsen, O. Balmes, J. Nerlov, A. M. Molenbroek, B. S. Clausen and S. Helvig, *Journal of Catalysis*, 2009, **262**, 65-72.
- 83 Y. Choi, K. Futagami, T. Fujitani and J. Nakamura, *Applied Catalysis A: General*, 2001, **208**, 163-167.
- 84 E. Kleymentov, J. Sa, J. Abu-Dahrieh, D. Rooney, J. A. van Bokhoven, E. Troussard, J. Szlachetko, O. V. Safonova and M. Nachttegaal, *Catal. Sci. Technol.*, 2012, **2**, 373-378.
- 85 N. Topsoe and H. Topsoe, *Topics in Catalysis*, 1999, **8**, 267-270.
- 86 M. Saito, J. Wu, K. Tomoda, I. Takahara and K. Murata, *Catalysis Letters*, 2002, **83**, 1-4.
- 87 M. Santiago, K. Barbera, C. Ferreira, D. Curulla-Ferre, P. Kolb and J. Perez-Ramirez, *Catalysis Communications*, 2012, **21**, 63-67.

## Chapter One

- 88 S. G. Jadhav, P. D. Vaidya, B. M. Bhanage and J. B. Joshi, *Chemical Engineering Research and Design*, 2014, **92**, 2557-2567.
- 89 A. Y. Rozovskii and G. I. Lin, *Topics in Catalysis*, 2003, **22**, 137-150.
- 90 M. Saito and K. Murata, *Catalysis Surveys from Asia*, 2004, **8**, 285-294.
- 91 Z. Zuo, P. Han, Z. Li, J. Hu and W. Huang, *Applied Surface Science*, 2012, **261**, 640-646.
- 92 Y. Choi, K. Futagami, T. Fujitani and J. Nakamura, *Catalysis Letters*, 2001, **73**, 27-31.
- 93 J. Nakamura, Y. Choi and T. Fujitani, *Topics in Catalysis*, 2003, **22**, 277-285.
- 94 D. B. Rasmussen, T. V. W. Janssens, B. Temel, T. Bligaard, B. Hinnemann, S. Helveg and J. Sehested, *Journal of Catalysis*, 2012, **293**, 205-214.
- 95 J. Wu, M. Saito, M. Takeuchi and T. Watanabe, *Applied Catalysis A: General*, 2001, **218**, 235-240.
- 96 S. Kang, J. W. Bae, P. S. Sai Prasad, J. Oh, K. Jun, S. Song and K. Min, *Journal of Industrial and Engineering Chemistry*, 2009, **15**, 665-669.
- 97 I. Atake, K. Nishida, D. Li, T. Shishido, Y. Oumi, T. Sano and K. Takehira, *Journal of Molecular Catalysis A: Chemical*, 2007, **275**, 130-138.
- 98 R. Kam, C. Selomulya, R. Amal and J. Scott, *Journal of Catalysis*, 2010, **273**, 73-81.
- 99 M. J. L. Gines, N. Amadeo, M. Laborde and C. R. Apesteguia, *Applied Catalysis A: General*, 1995, **131**, 283-296.
- 100 K. Nishida, I. Atake, D. Li, T. Shishido, Y. Oumi, T. Sano, K. Takehira, *Applied Catalysis A: General*, 2008, **337**, 48-57.
- 101 W. Fu, Z. Bao, W. Ding, K. Chou and Q. Li, *Catalysis Communications*, 2011, **12**, 505-509.
- 102 M. Saito, K. Tomoda, I. Takahara, K. Murata and M. Inaba, *Catalysis Letters*, 2003, **89**, 11-13.
- 103 P. Guo, L. Chen, Q. Yang, M. Qiao, H. Li, H. Li, H. Xu and K. Fan, *International Journal of Hydrogen Energy*, 2009, **34**, 2361-2368.
- 104 R. A. Hadden, P. J. Lambert and C. Ranson, *Applied Catalysis A: General*, 1995, **122**, L1-L4.
- 105 K. Yao, S. Wang, X. Gu, H. Su and W. Li, *Chinese Journal of Catalysis*, 2013, **34**, 1705-1711.
- 106 F. Studt, M. Behrens and F. Abild-Pedersen, *Catal. Lett.*, 2014, **144**, 1973-1977.

- 107 R. J. Madon, D. Braden, S. Kandoi, P. Nagel, M. Mavrikakis and J. A. Dumesic, *Journal of Catalysis*, 2011, **281**, 1-11.
- 108 J. Nakamura, J. M. Campbell and C. T. Campbell, *J. Chem. Soc. Faraday Trans.*, 1990, **86**, 2725-2734.
- 109 K. Nishida, D. Li, Y. Zhan, T. Shishido, Y. Oumi, T. Sano and K. Takehira, *Applied Clay Science*, 2009, **44**, 211-217.
- 110 L. Yang, A. Karim and J. T. Muckerman, *J. Phys. Chem. C*, 2013, **117**, 3414-3425.
- 111 P. Guo, L. Chen, G. Yu, Y. Zhu, M. Qiao, H. Xu and K. Fan, *Catalysis Communications*, 2009, **10**, 1252-1256.
- 112 X. Liu, P. Guo, S. Xie, Y. Pei, M. Qiao and K. Fan, *International Journal of Hydrogen Energy*, 2012, **37**, 6381-6388.
- 113 P. Kowalik, W. Prochniak, M. Konkol and T. Borowiecki, *Applied Catalysis A: General*, 2012, **423-424**, 15-20.
- 114 P. Kowalik, W. Prochniak and T. Borowiecki, *Catalysis Today*, 2011, **176**, 144-148.
- 115 J. A. Darr and M. Poliakoff, *Chem. Rev.*, 1999, **99**, 495-541.
- 116 S. A. Kondrat and S. H. Taylor in: J. Spivey, Y. Han and K. Dooley, *Catalysis: Volume 26*, Royal Society of Chemistry, 2014.
- 117 E. Reverchon, I. D. Marco and E. Torino, *J. of Supercritical Fluids*, 2007, **43**, 126-138.
- 118 E. Reverchon, G. Caputo and I. D. Marco, *Ind. Eng. Chem. Res.*, 2003, **42**, 6406-6414.
- 119 R. Wandeler and A. Baiker, *Cattech*, 2000, **4**, 128-143.
- 120 P. G. Jessop, T. Ikariya and R. Noyori, *Chem. Rev.*, 1999, **99**, 475-493.
- 121 T. Greibrokk, *Journal of Chromatography A*, 1995, **703**, 523-536.
- 122 E. Reverchon, R. Adami, I. D. Marco, C. G. Laudani and A. Spada, *J. of Supercritical Fluids.*, 2005, **35**, 76-82.
- 123 S. Yeo and E. Kiran, *J. of Supercritical Fluids*, 2005, **34**, 287-308.
- 124 M. Sarkari, I. Darrat and B. L. Knutson, *AIChE Journal*, 2000, **46**, 1850-1859.

- 125 Y. Sun and H. W. Rollins, *Chemical Physics Letters*, 1998, **288**, 585-588.
- 126 S. Bristow, T. Shekunov, B. Y. Shekunov and P. York, *J. of Supercritical Fluids*, 2001, **21**, 257-271.
- 127 N. Czerwonatis and R. Eggers, *Chem. Eng. Technol.*, 2001, **24**, 619-624.
- 128 P. J. Miedziak, Z. Tang, T. E. Davies, D. I. Enache, J. K. Bartley, A. F. Carley, A. A. Herzing, C. J. Kiely, S. H. Taylor and G. J. Hutchings, *J. Mater. Chem.*, 2009, **19**, 8619-8627.
- 129 G. J. Hutchings, *Top Catal*, 2009, **52**, 982-987.
- 130 Z. Tang, J. K. Bartley, S. H. Taylor and G. J. Hutchings, Preparation of TiO<sub>2</sub> Using Supercritical CO<sub>2</sub> Antisolvent Precipitation (SAS): A Support for High Activity Gold Catalysts, Elsevier Science BV, 2005, **162**, 219-226.
- 131 G. J. Hutchings, J. A. Lopez-Sanchez, J. K. Bartley, J. M. Webster, A. Burrows, C. J. Kiely, A. F. Carley, C. Rhodes, M. Havecker, A. Knop-Gericke, R. W. Mayer, R. Schlögl, J. C. Volta and M. Poliakoff, *Journal of Catalysis*, 2002, **208**, 197-210.
- 132 J. A. Lopez-Sanchez, J. K. Bartley, A. Burrows, C. J. Kiely, M. Havecker, R. Schlögl, J. C. Volta, M. Poliakoff and G. J. Hutchings, *New J. Chem.*, 2002, **26**, 1811-1816.
- 133 R. P. Marin, S. A. Kondrat, T. E. Davies, D. J. Morgan, D. I. Enache, G. B. Combes, S. H. Taylor, J. K. Bartley and G. J. Hutchings, *Catal. Sci. Technol.*, 2014, **4**, 1970-1978.
- 134 R. P. Marin, S. A. Kondrat, R. K. Pinnell, T. E. Davies, S. Golunski, J. K. Bartley, G. J. Hutchings and S. H. Taylor, *Applied Catalysis B: Environmental*, 2013, **140-141**, 671-679.
- 135 E. Reverchon, G. Della Porta, D. Sannino and P. Ciambelli, *Powder Technology*, 1999, **102**, 127-134.
- 136 Z. Tang, C. D. Jones, J. K. W. Aldridge, T. E. Davies, J. K. Bartley, A. F. Carley, S. H. Taylor, M. Allix, C. Dickinson, M. J. Rosseinsky, J. B. Claridge, Z. Xu, M. J. Crudace and G. J. Hutchings, *ChemCatChem*, 2009, **1**, 247-251.
- 137 Z. R. Tang, S. A. Kondrat, C. Dickinson, J. K. Bartley, A. F. Carley, S. H. Taylor, T. E. Davies, M. Allix, M. J. Rosseinsky, J. B. Claridge, Z. Xu, S. Romani, M. J. Crudace and G. J. Hutchings, *Catal. Sci. Technol.*, 2011, **1**, 740-746.
- 138 S. A. Kondrat, T. E. Davies, Z. Zu, P. Boldrin, J. K. Bartley, A. F. Carley, S. H. Taylor, M. J. Rosseinsky and G. J. Hutchings, *Journal of Catalysis*, 2011, **281**, 279-289.

- 139 D. Jiang, M. Zhang and H. Jiang, *Materials Letters*, 2011, **65**, 1222-1225.
- 140 D. Jiang, M. Zhang, G. Li and H. Jiang, *Catalysis Communications*, 2012, **17**, 59-63.
- 141 H. Wang, H. Jiang, L. Kuang and M. Zhang, *J. of Supercritical Fluids*, 2014, **92**, 84-92.
- 142 H. Pan, J. Haoxi and Z. Minhua, *Journal Of Rare Earths*, 2012, **30**, 524-528.
- 143 K. Li, H. Pan, S. Huanhua, J. Haoxi and Z. Minhua, *Journal Of Rare Earths*, 2013, **31**, 137-144.

## 2.0. Experimental

### 2.1. Introduction

A range of copper, zinc and aluminium containing materials were prepared and characterised using a variety of techniques, with selected catalysts tested for methanol synthesis and the LTS reaction at Johnson Matthey. This chapter reports the details of catalyst preparation, including the materials used and the instrumentation set-ups, techniques and conditions used for characterisation of materials. Furthermore, the reaction conditions used for catalyst testing, including a brief overview of reactor designs, is provided.

### 2.2. Materials

All materials, solvents and gases used in this work for the preparation of catalyst materials is presented (**Table 2.1.**). Deionised water was provided in-house (sodium level determined < 1 ppm).

**Section 2.3.** provides details on materials, solvents and gases used for characterisation.

**Table 2.1.** List of materials, solvents and gases used for preparation of catalyst materials.

Material	Supplier	Purity grade
Copper (II) acetate monohydrate	Sigma Aldrich	puriss. p. a., ≥ 99.0%
Zinc (II) acetate dihydrate	Sigma Aldrich	puriss. p. a., ≥ 99.0%
Aluminium (III) acetylacetonate	Sigma Aldrich	99%
Aluminium (III) L-lactate	Sigma Aldrich	95%
Nitric acid	Sigma Aldrich	ACS Grade, 70%
Aluminium (III) pseudo-boehmite	Johnson Matthey	-
Ethanol	Fischer Scientific	Absolute 99.8%, Certified AR
Carbon dioxide (CO <sub>2</sub> )	BOC	CP Grade
Sodium carbonate	Acros Organics	99+%
Ammonium carbonate	Acros Organics	ACS and Extra Pure Grades
Ammonium bicarbonate	Acros Organics	99%

### 2.3. Catalyst preparation

In **Chapter One** the focus and aims of the work were outlined. This involves the preparation of georgeite hydroxycarbonates using precipitation routes devoid of nitrate and alkali-metal reagents.

In this section the details and strategies of synthesis routes which fulfil these requirements is presented.

### 2.3.1. Supercritical anti-solvent (SAS) precipitation

#### 2.3.1.1. SAS apparatus

The production of catalyst materials using scCO<sub>2</sub> was performed using tailor made apparatus manufactured by Separex (**Figure 2.1(A)**). This instrumentation has the potential to operate in both batch (GAS) and semi-continuous (SAS) set-ups, although only the latter was considered for the purposes of this work.

Opening the liquid CO<sub>2</sub> cylinder results in a phase transformation to the gaseous CO<sub>2</sub> state in the line from de-pressurisation. In order to maintain a liquid CO<sub>2</sub> phase which is required for pumping, the CO<sub>2</sub> was chilled with a demineralised water/ glycol mixture (20% glycol) cooled to -4 °C using a Hitema chiller (**C1**). A dual piston pump was used to pump and thus control the CO<sub>2</sub> flow rate, and had the capability to achieve flow rates up to 18 kg/h ( $\pm 1$  kg/h). The purpose of pumping was also to achieve CO<sub>2</sub> pressures in the system greater than the cylinder pressure (~55 bar), in order to operate at pressures required to form scCO<sub>2</sub> and an optimum homogeneous system ( $\geq 110$  bar). Before being introduced to prepared solutions, the scCO<sub>2</sub> passed through a separate heater (**H1**). The line passing through this heater was coiled, in order to extend the exposure time of the scCO<sub>2</sub> to the set temperature. This allowed the thermal equilibrium to be reached prior to coming in contact with prepared solutions. These prepared solutions were simultaneously pumped into the system using a calibrated HPLC pump. Flow rates up to 10 ml/min ( $\pm 0.1$  ml/min) could be obtained. The pressure was first worked up above the system operating pressure in order to introduce the solution into the set-up without backflow. A filter was also included on the HPLC tubing to prevent any residual solids remaining in prepared metal solutions from being consumed into the system.

The scCO<sub>2</sub> and prepared solutions were co-fed into the precipitation vessel using a co-axial nozzle set-up (**Figure 2.1(B-C)**). This arrangement consists of an inner and outer tube. The prepared solutions were pumped through the inner tube (inner diameter = 1 mm, wall thickness = 0.294 mm therefore total diameter = 1.588 mm) whilst sc-CO<sub>2</sub> was pumped through the outer tube (inner diameter = 4.95 mm, wall thickness = 0.7 mm therefore total diameter = 6.35 mm). The inner tube was 1.5 mm longer than the outer tube and therefore extended further into the precipitation vessel.

The precipitation vessel was a 1 L stainless steel extraction unit, equipped with a lip seal and filter disk (pore size 0.5 micron). During operation this vessel was fixed into a stainless steel basket with

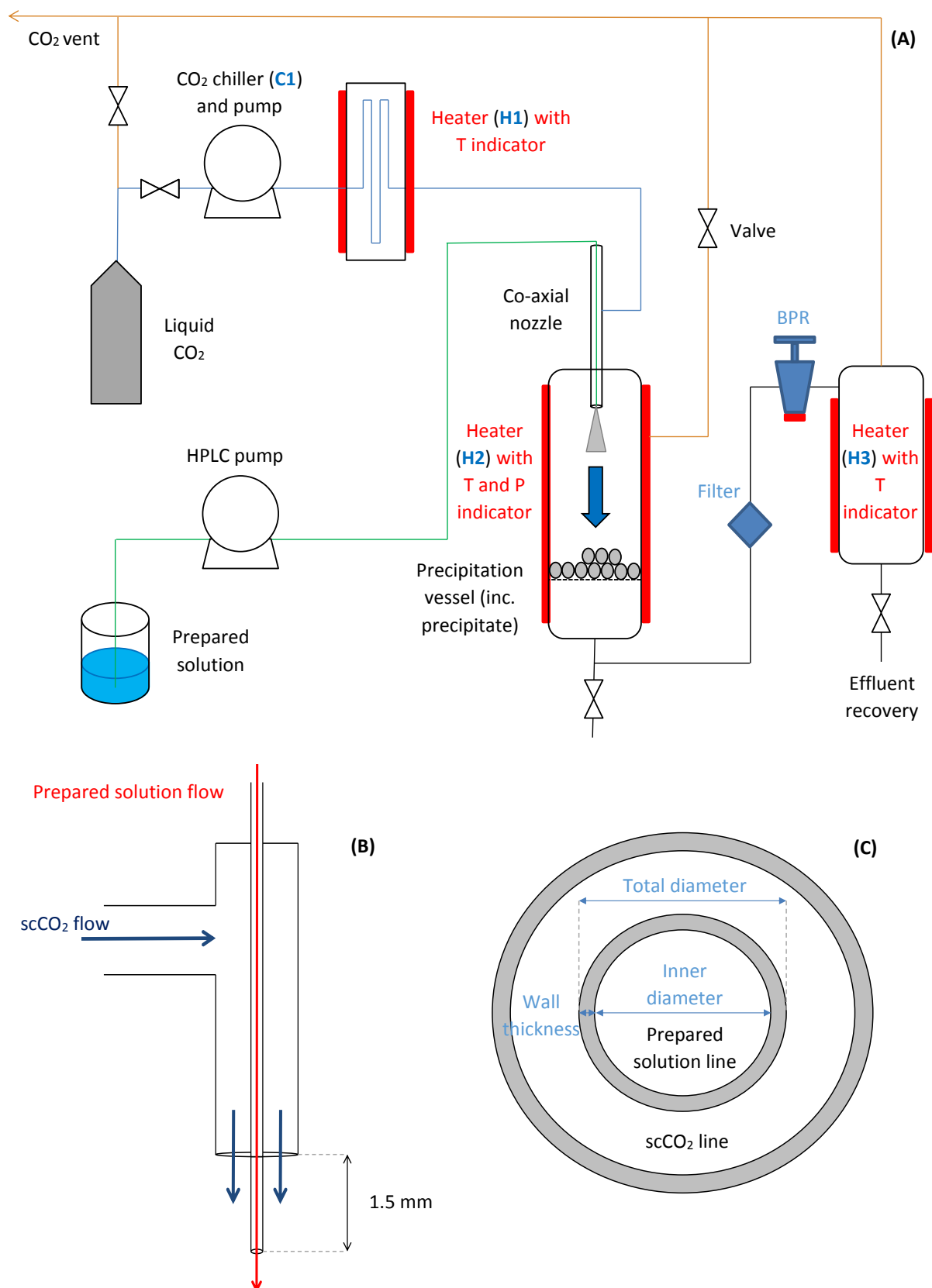


**Figure 2.1.** (A) Schematic of Separex apparatus in SAS mode including lines for scCO<sub>2</sub> (blue), prepared solution (green), resulting effluent (black) and ventilation (yellow). The co-axial nozzle design is also provided in more detail including both (B) side and (C) end views. An indication of the measurements taken of the inner nozzle is provided for clarity. See main text for actual measurements.

heating potential (H2). The basket was equipped with a temperature probe and pressure transducer and had the capacity to operate up to 400 bar and 150 °C. The resulting precipitate collected on the filter disk, whilst the scCO<sub>2</sub> and any miscible phases passed straight through. A filter was placed further down line in order to collect any solid material which by-passed the precipitation vessel. This was to prevent any disruptions to the back pressure regulator (BPR), which was used to control the pressure of the entire system. The BPR essentially consists of a needle present in the line which can be wound further in or out in order to dictate the amount of CO<sub>2</sub> exiting the system at a given time. After passing through the BPR, the pressure reduces back down to atmospheric and therefore the CO<sub>2</sub> undergoes a highly endothermic phase transformation from supercritical to gaseous. Consequently, the properties associated with the supercritical phase are lost resulting in any miscible organic solvents precipitating out. A third heater (H3) set to 100 °C was used to combat the resulting cooling with the organic solvents collected as the gaseous CO<sub>2</sub> went to vent. Overall this instrumentation is a powerful tool for producing reasonable yields in suitable timeframes, with the capability of operating under a broad range of synthesis conditions. The main drawback relates to the lack of a window on the precipitation vessel, which prevented observation of phase systems during the production of materials.

#### 2.3.1.2. Catalyst preparation

The Separex apparatus described above was used to prepare a range of copper, zinc and aluminium containing phases for the purposes of this work. An example of a typical preparation is provided here. Specific details for each experiment which deviate from this will be given in subsequent chapters: A mixed solution of Cu(OAc)<sub>2</sub>.H<sub>2</sub>O (4 mg/ml) and Zn(OAc)<sub>2</sub>.2H<sub>2</sub>O (2.13 mg/ml) was prepared in a 10 vol.% H<sub>2</sub>O/ethanol mixture (500 ml) to give a nominal Cu/Zn molar ratio of 2/1. Unfortunately the preparation is restricted by the low solubility of the Cu(OAc)<sub>2</sub>.H<sub>2</sub>O salt in ethanol, whereby concentrations much greater than 4 mg/ml cannot be obtained. The liquefied CO<sub>2</sub> was pumped to give a flow rate of 6.5 kg/h and the whole system was pressurised up to 110 bar and held at 40 °C. Initially pure solvent (10 vol.% H<sub>2</sub>O/ethanol) was pumped through the fine capillary into the precipitation vessel, with a flow rate of 6.5 ml/min for 15 minutes, in co-current mode with scCO<sub>2</sub> in order to obtain steady state conditions inside the vessel. After this initial period the flow of liquid solvent was stopped and the mixed acetate solution was delivered at a flow rate of 6.5 ml/min. This gave a scCO<sub>2</sub>/metal solution molar ratio of 22/1. The system pressure and temperature were maintained and the preparation conditions were carefully controlled. Leak checks were also periodically carried out throughout the procedure using snoop solution. As the solution exited the capillary the droplet and scCO<sub>2</sub> rapidly diffused into each other, causing expansion and reducing

solvent power. The solute precipitated rapidly and when all the solution had been processed a drying step was carried out. Pure ethanol was pumped at 6.5 ml/min co-currently with scCO<sub>2</sub> for 30 minutes, before leaving with just scCO<sub>2</sub> to pump for a further hour. This was to wash the vessel in case residual solvent condensed during depressurisation and partly solubilised the precipitated powder, modifying its morphology. Furthermore, it was essential to completely dry georgeite phases to prevent subsequent ageing into malachite. When the drying step was completed the scCO<sub>2</sub> flow rate was stopped, the vessel was depressurised to atmospheric pressure and the precipitate was collected. Experiments were conducted for approximately 3.5 hours which resulted in the synthesis of approximately 1.5 g of solid.

### 2.3.2. Co-precipitation

Aqueous co-precipitation is an established catalyst preparation technique and is widely used in both academia and industry. As mentioned in **Chapter One**, it is the commercial route used for the production of copper based hydroxycarbonate catalyst precursors. The ability to form well mixed, nanoscale materials from cheap starting reagents using energy sustainable preparation conditions is largely attributed to its success. Moreover, the metal nitrate salts frequently used are significantly soluble in aqueous media (copper nitrate > 137.8 g/100 ml and zinc nitrate > 43 g/100 ml) and therefore this methodology has the capacity to scale up the production of catalyst material. The process simply relies on an *in-situ* chemical reaction, whereby highly soluble reactant chemicals convert into less soluble or even in-soluble products. This induces a super-saturation of the product material, resulting in homogeneous nucleation and growth from a thermodynamically controlled approach<sup>(1)</sup>. Consequently, assuming the reaction goes to completion yields of 100% are readily obtained. Cu/ZnO/Al<sub>2</sub>O<sub>3</sub> catalysts with copper crystallite sizes in the range 5-15 nm have been reported from using this approach<sup>(2)</sup>. However, it should be noted that there are several drawbacks associated with this technique. It has previously been mentioned that the alkali metal and nitrate reagents frequently used are detrimental from a commercial and environmental perspective. The mass production of aqueous nitrate waste in particular is highly problematic. Whilst this by-product has the potential to be used in alternative applications, the energy required to concentrate it down into a useable form exceeds the benefits of utilising it for commercialisation. Moreover, whilst extensive research has been carried out in order to fully optimise the process it is still not fully understood. Co-precipitation is a highly sensitive technique with a significantly large number of synthesis parameters to consider, and each of these variables can drastically alter the physiochemical properties of the resulting precipitate.

The aqueous co-precipitation route used in industry for the production of Cu/ZnO/Al<sub>2</sub>O<sub>3</sub> catalysts was modified for the purposes of this work regarding the preparation of georgeite precursors. Specific details of experiments will be given in subsequent chapters. However, a typical preparation is provided here: A mixed solution of Cu(OAc)<sub>2</sub>·H<sub>2</sub>O (0.35 M) and Zn(OAc)<sub>2</sub>·2H<sub>2</sub>O (0.175 M) was prepared in deionised H<sub>2</sub>O (100 ml) to give a nominal Cu/Zn molar ratio of 2/1. An aqueous solution of (NH<sub>4</sub>)<sub>2</sub>CO<sub>3</sub> as precipitant was also prepared (0.525 M, 250 ml). Both solutions were stirred in round bottom flasks and heated to 40 °C before being simultaneously pumped drop-wise into a stirred and heated glass jacket reactor with a starting volume of 30 ml deionised water (**Figure 2.2.**). During the precipitation process pH, temperature and ageing time were controlled. While the metal acetate solution was being pumped continuously the (NH<sub>4</sub>)<sub>2</sub>CO<sub>3</sub> solution was added to maintain a constant pH (6.5-7) using a Hanna pH probe and meter. The co-precipitation was stopped when all of the metal acetate solution had been added. The precipitate was then allowed to age for 15 minutes, with the mother liquor solution left stirring at constant temperature (40 °C). These mild ageing conditions were specifically chosen to prevent ageing of the georgeite precipitate into the malachite phase. The pH was not controlled during this time, which has also been referred to as ‘free ageing’<sup>(3)</sup>. After ageing the precipitates were filtered and in some cases a washing step was then applied using deionised water at ambient temperature (1 L).

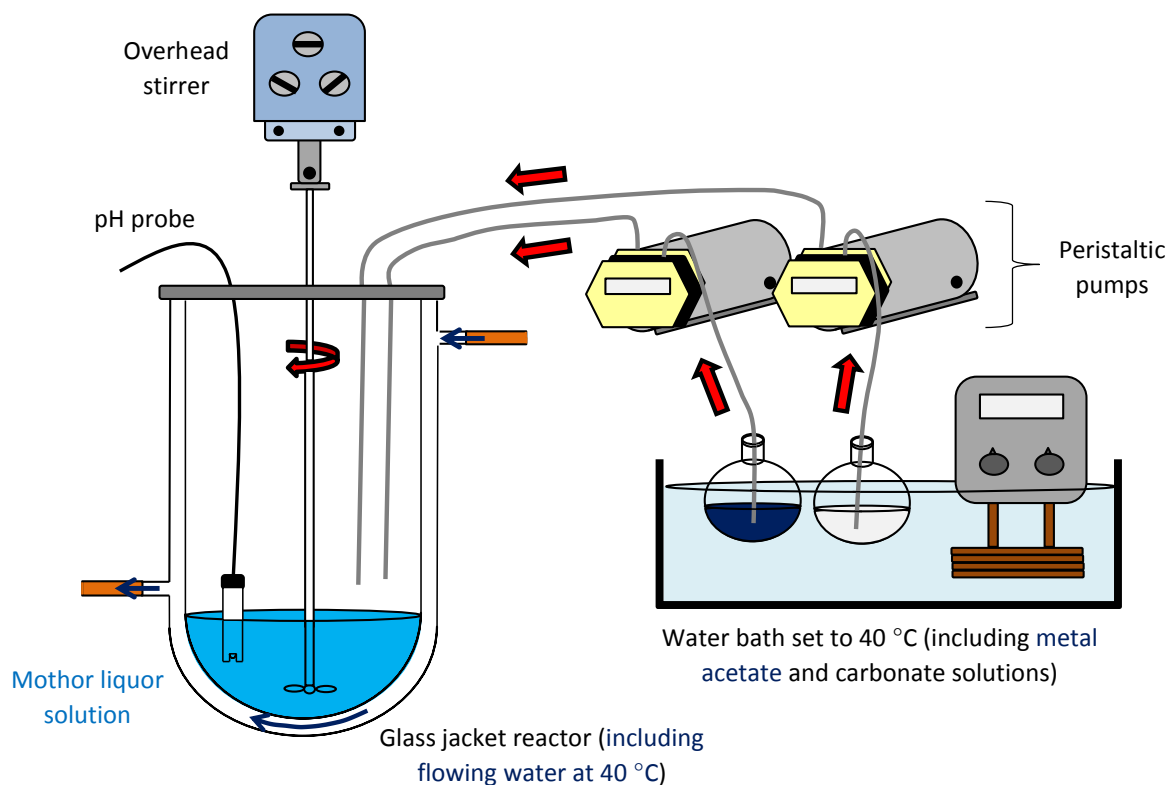


**Figure 2.2.** Set-up for co-precipitation.

The materials were dried overnight at 40 °C in a vacuum oven in order to again prevent ageing of the precursors into the malachite phase. Experiments regarding the co-precipitation procedure were conducted for approximately 3.5 hours, which resulted in the synthesis of approximately 7.5 g of solid.

## 2.4. Characterisation

In this section the techniques used for the extensive characterisation of catalyst materials is outlined, including details of the experimental conditions. All gases used were supplied by BOC of high purity grade. The degree of error (or the error margin) associated with relevant analytical techniques is also provided herein and was obtained by standard deviation after running various samples multiple times. The information derived from each technique regarding specific properties (structural, thermal, chemical, physical, morphological and elemental) were used in combination to build up a detailed understanding of the microstructural features of prepared materials. This is essential for studying 'structure-activity' relationships in the field of catalysis.

### 2.4.1. Powder X-ray diffraction (XRD)

X-ray diffraction (XRD) is based on the elastic scattering of monochromatic X-ray photons by atoms ordered in a crystalline structure<sup>(1,4-5)</sup>. The scattered monochromatic X-rays which are in phase give constructive interference and satisfy the Bragg relation (**Figure 2.3.** and **Equation 2.1.**).

**Equation 2.1.** 
$$n\lambda = 2d_{hkl}\sin\theta$$

Whereby  $n$  = the order of the reflection (an integer),  $\lambda$  = the X-ray wavelength,  $d$  = the distance between two lattice planes and  $\theta$  = the angle between the incoming X-rays and the normal to the reflecting lattice plane. Therefore, from measuring the angles under which constructively interfering X-rays leave the crystal the Bragg relation gives the corresponding lattice spacings which are characteristic of a given compound.

For a powdered sample, the XRD pattern is measured using a stationary X-ray source and a moveable detector, which scans the intensity of the diffracted radiation as a function of the angle,  $2\theta$  between the incoming and diffracted beams. Diffraction lines form on the XRD pattern because a small fraction of the powder will be oriented such that by chance a certain crystal plane is at the correct angle,  $\theta$  with the incident beam for constructive interference. Rotation of a sample during measurement can be used in combination to enhance the number of particles that contribute to

diffraction. However, whilst XRD is a powerful tool for phase analysis it also has an important limitation. Clear diffraction peaks are only observed when the sample possesses sufficient long range order, and is therefore not suitable for the detailed study of amorphous materials. The advantage of this limitation though is that the width of the diffraction peaks carries information on the dimensions of the reflecting planes. As crystallite sizes decrease, the peaks broaden due to incomplete destructive interference in scattering directions where the X-rays are out of phase. The Scherrer formula relates this line width to the crystallite size ([Equation 2.2.](#)).

**Equation 2.2.** 
$$L = \frac{K\lambda}{\beta \cos \theta}$$

Whereby  $L$  = is a measure of the crystallite size in the direction perpendicular to the reflecting plane,  $K$  = a constant (taken as 1),  $\lambda$  = the X-ray wavelength,  $\beta$  = the peak width and  $\theta$  = the angle between the beam and the normal on the reflecting plane. Therefore XRD can be readily used for deriving crystallite sizes. However, it should be noted that the error associated with the measurement significantly increases as the peaks become ill-defined. Particles generally < 5 nm cannot be detected and measured as the peaks are so broad they merge into the background signal.

XRD can also be used to study catalysts under *in-situ* conditions to yield important information on the kinetics of solid state reactions. This includes activation of catalysts from processes such as reduction or oxidation which can also be extended to investigations under reaction conditions. In this context though it is important to appreciate that XRD is a bulk technique. X-rays have wavelengths in the angstrom range making them sufficiently energetic to penetrate solids. Therefore

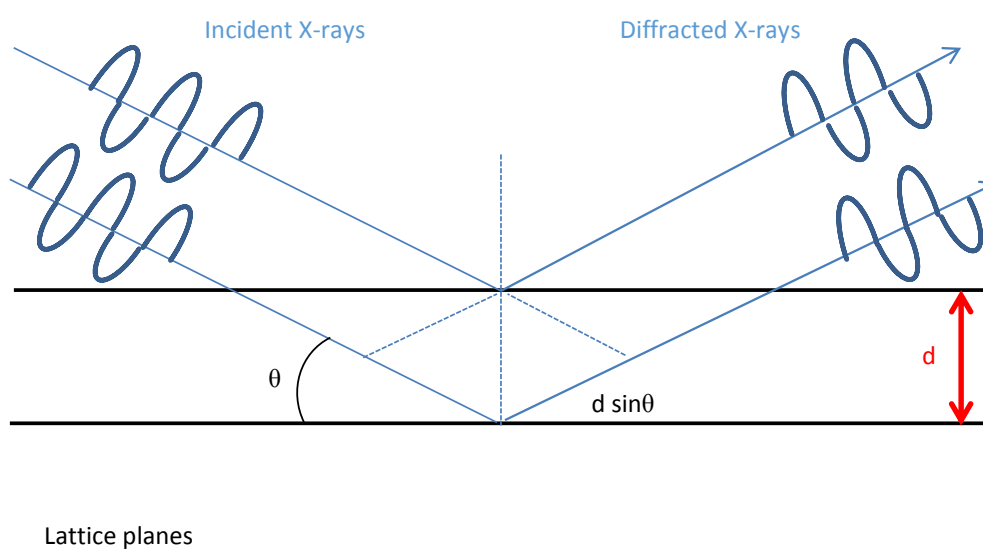


**Figure 2.3.** X-rays scattered by atoms in an ordered lattice satisfying the Bragg relation and interfering constructively. The angles of maximum intensity enable the spacings between the lattice planes to be calculated which allows for phase identification.

the surface region where catalytic activity resides is virtually invisible to XRD.

XRD Analysis was performed on a ( $\theta$ - $\theta$ ) PANalytical X'pert Pro powder diffractometer with a Ni filtered  $\text{CuK}\alpha$  radiation source operating at 40 keV and 40 mA. Patterns were recorded over the range  $10$ - $80^\circ 2\theta$  using a step size of  $0.016^\circ$ . Analysis was performed using a back filled sample holder or with the sample dispersed on a silicon wafer when limited sample was available. An *in-situ* Anton Parr XRK900 cell (internal volume  $\sim 0.5$  L) was also used to monitor the formation of  $\text{Cu}^0$  during reduction of  $\text{CuO/ZnO}$  materials. A flow of  $2\% \text{H}_2/\text{N}_2$  ( $60$  ml/min) was passed through the sample bed whilst the cell was heated to  $225^\circ\text{C}$  (ambient to  $125^\circ\text{C}$  at  $10^\circ\text{C}/\text{min}$ ,  $125$ - $225^\circ\text{C}$  at  $2^\circ\text{C}/\text{min}$ ). For both instrumentation patterns were identified using the ICDD database and crystallite sizes were determined using the Scherrer equation. The *in-situ* analysis was not carried out by the author.

#### 2.4.2. Extended X-ray absorption fine structure (EXAFS)

Extended X-ray absorption fine structure (EXAFS) is an X-ray absorption technique which gives detailed information on local structure<sup>(4)</sup>. It is based on absorbing X-rays to create photoelectrons which are scattered by nearby atoms in a lattice (Figure 2.4.). The fine features of the X-ray absorption spectrum can be used to give detailed information on the distance, number and type of neighbours of the absorbing atom. EXAFS when utilised from X-rays generated from synchrotrons is a very powerful tool in the field of catalysis, with the capacity to evaluate local structural parameters of amorphous materials which broadens its applications into material science.

Similar to the photoelectric effect, irradiating an atom with electrons of binding energy,  $E_b$  using X-rays of energy,  $h\nu$  results in absorption and ejection of electrons with kinetic energy,  $E_k = h\nu - E_b$  when  $h\nu \geq E_b$ . Consequently, the X-ray absorption spectrum shows a series of edges which correspond to the binding energies of these ejected electrons. Neighbours surrounding the atom gives rise to fine structure on the spectrum. The ejected photoelectron with both particle and wave character can be scattered back from one of these neighbouring atoms. This results in interference of the wave character of outgoing and backscattered electrons. These two waves either enhance or destroy each other to give constructive or destructive interference respectively. This depends on factors which relate to the local structure. The resulting fine structure extends several hundred eV above the absorption edge and is defined as the EXAFS region. The absorption around the edge arises from electrons with low kinetic energies and is defined as the XANES part of the spectrum. Regarding the interpretation of spectra: the intensity of wiggles increases with the number of neighbouring atoms, the number of oscillations depends inversely on interatomic distances, and the

step height is proportional to the concentration of atoms in the sample. The EXAFS function,  $\chi(k)$  is extracted from the absorption spectrum and expressed as a wavenumber. It is the sum of the scattering contributions of all atoms in neighbouring co-ordination shells ([Equation 2.3.](#)).

**Equation 2.3.** 
$$\chi(k) = \sum_j A_j(k) \sin(2kr_j + \Phi_j(k))$$

Whereby  $\chi(k)$  = the EXAFS function with wavenumber  $k$ ,  $j$  = the label of the coordination shells around the electron emitting atom,  $A_j(k)$  = the amplitude/scattering intensity due to the  $j^{\text{th}}$  coordination shell,  $r_j$  = the distance between the central atom and atoms in the  $j^{\text{th}}$  shell and  $\Phi(k)$  = the total phase shift, equal to the phase shift of the backscattering atom plus twice that of the absorbing atom. Thus each coordination shell contributes a sine function multiplied by an amplitude, whereby EXAFS analysis essentially boils down to recognising all sine contributions to  $\chi(k)$  from Fourier analysis.

Cu and Zn k-edge XAFS studies were carried out on the B18 beamline at the Diamond Light Source in Harwell. Measurements were performed using a QEXAFS set-up with a fast scanning Si (111) double crystal monochromator. The time resolution of the spectra reported herein was 1 min/spectrum ( $k_{\text{max}} = 14$ ). On average three scans were acquired to improve the signal to noise level of data. All *ex-situ* samples were diluted with cellulose and pressed into pellets to optimise the effective edge-step of the XAFS data, and measured in transmission mode using ion chamber detectors. All transmission XAFS spectra were acquired concurrently with the appropriate reference coil (Cu or Zn) placed between  $I_t$  and  $I_{\text{ref}}$ . XAS data processing and EXAFS analysis were performed using IFEFFIT with the Horae package (Athen and Artemis). The amplitude reduction factor,  $s_0^2$  was derived from EXAFS

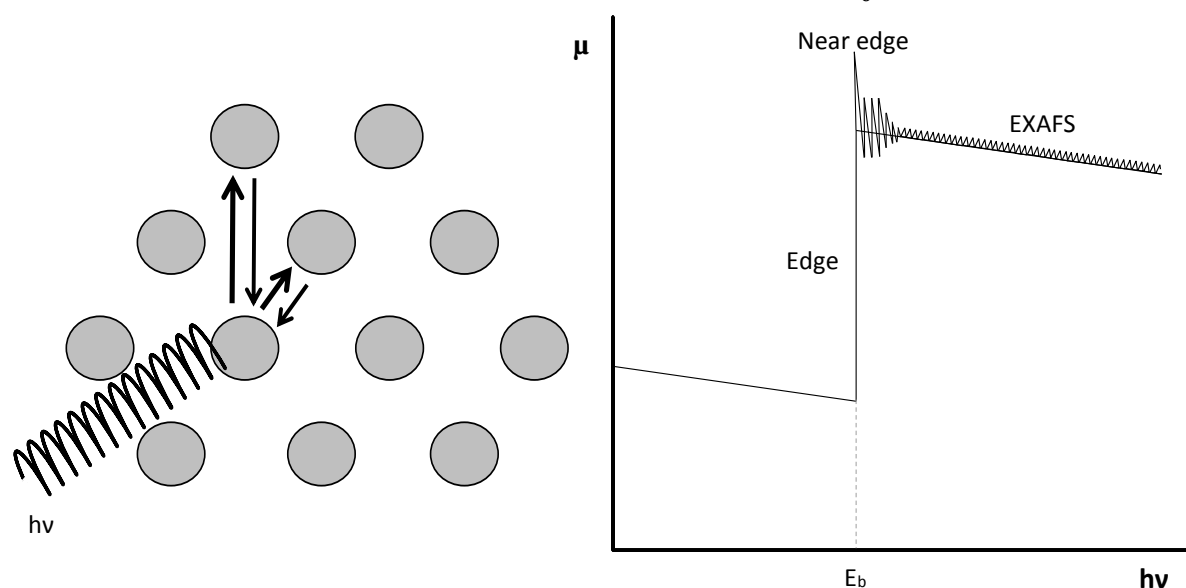


**Figure 2.4.** Adsorption of X-rays as a function of photon energy,  $E = h\nu$  by atoms in a lattice. Right: the fine structure represents the EXAFS function.

data analysis of known Cu reference compound, CuO. With the exception of sample preparation this work was not carried out by the author.

### 2.4.3. Pair distribution function (PDF)

The pair distribution function (PDF) is used to investigate the short, medium and long-range order of materials. This makes it a powerful technique regarding analysis of the local structure of amorphous materials, and can therefore be used as a complimentary technique to EXAFS. This also allows the deviation of the short range order from the average structure in crystalline materials to be recognised. It describes a probability of finding any two atoms at given atom distances,  $r$  (Figure 2.5.). The technique is complimentary to the Rietveld method, which models the average structure from the intensities of Bragg reflections in a diffraction pattern. However, the PDF is also calculated from scattering intensities which regards deviations from ideal symmetry such as thermal displacement parameters. A PDF can therefore discriminate between short range order and random atomic displacements. The experimental PDF,  $G(r)$  are directly obtained from the diffraction data by Fourier transforming the normalised total structure factor  $S(Q)$ , whereby  $Q = 4\pi(\sin\theta)/\lambda$ .  $S(Q)$  is the measured intensity corrected for factors such as background, multiple scattering and adsorption. Fourier termination errors, resolution and counting statistics all effect the quality of PDF findings.

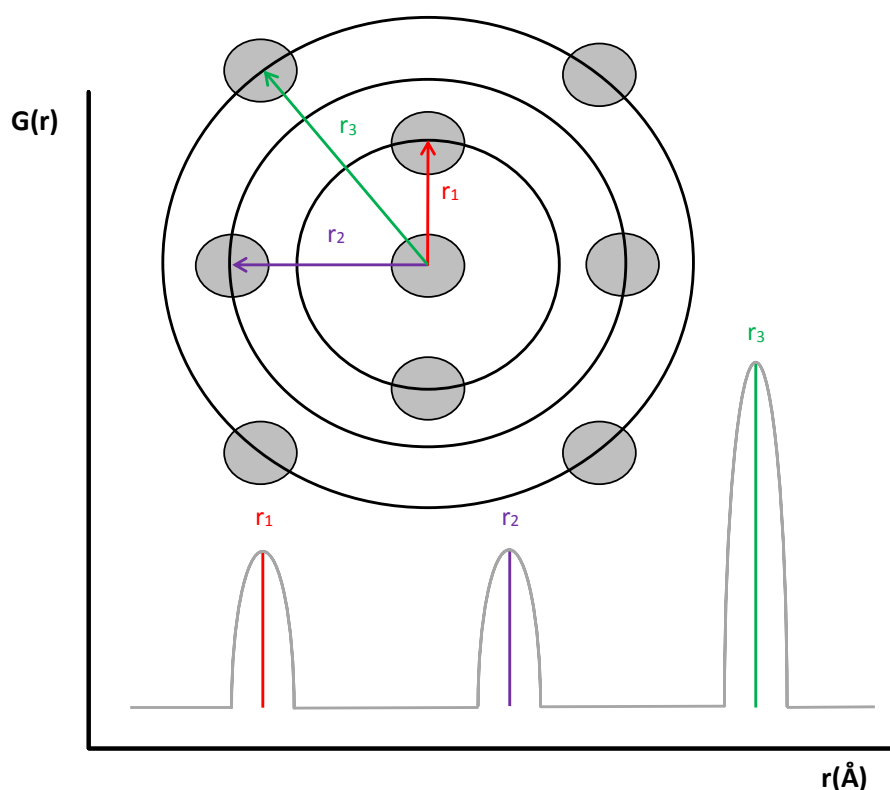


**Figure 2.5.** Principle of the PDF. Inter-atomic distances,  $r_i$  cause maxima in the PDF  $G(r)$ . The area below the peaks correspond to the number of neighbours, scaled by the scattering power of the respective atoms.

Termination errors are minimised by using larger values of  $Q$ , which itself is limited by the instrument setting for the highest diffraction angle and X-ray wavelength source. In terms of radiation source,  $Q$  increases in the order:  $\text{Ag} > \text{Mo} > \text{Cu}$ . Therefore, a Ag source gives the highest  $Q$  values, however, the flux of X-rays from a Ag tube is low and the detector efficiency is lower resulting in loss of intensity in comparison to Mo. The measurement time needed to collect sufficient counting statistics for high  $Q$  values is also long. It generally exceeds one day per scan.

Synchrotron PDF data were collected on the 11-ID-B beamline at the Advanced Photon Source at Argonne national laboratory. Powder samples were packed into kapton capillaries with an internal diameter of 1 mm. Room temperature powder XRD data were collected at a wavelength of 0.2114 Å using the Rapid Acquisition PDF method. The scattering data ( $0.5 \leq Q \leq 22 \text{ \AA}^{-1}$ ) was processed into PDF using the program GudrunX. This work was not carried out by the author.

#### 2.4.4. Thermogravimetric analysis (TGA), differential thermal analysis (DTA) and evolved gas analysis (EGA)

Thermogravimetric analysis (TGA) is an extremely powerful tool for studying phases which partially decompose upon thermal treatment. This applies to hydroxycarbonate and acetate phases in particular which are investigated in this work. The technique simply measures the sample mass as a function of temperature or time, and can be performed under a range of gas atmospheres (air,  $\text{N}_2$  and 10%  $\text{H}_2/\text{Ar}$ ). Each unique phase gives a fingerprint TGA profile and total mass loss, which provides qualitative and quantitative information respectively. The TGA profile assists in identifying suitable calcination temperatures. Moreover, certain phases have the potential to incorporate additional elements into their lattice and these changes to thermal behaviour can be studied from monitoring temperature shifts in the decomposition steps. The observed total mass loss of unknown phases can be compared against theoretical total mass losses calculated for known phases making it a powerful tool for phase identification. This therefore complements findings derived from XRD, IR and Raman analysis.

Techniques associated with TGA are differential thermal analysis (DTA) and evolved gas analysis (EGA). DTA measures the change in temperature during the thermal treatment providing information on the nature of the decomposition (exothermic, thermo-neutral or endothermic). EGA is essentially TGA coupled to a mass spectrometer (MS), whereby  $m/z$  values of the evolved fragments is determined. This allows the chemical species to be identified which is associated with each decomposition step. When all three techniques are used a detailed understanding of the overall decomposition process is derived.

TGA was performed using a Setaram Labsys 1600 in conjunction to DTA. 10-60 mg of the sample was loaded into alumina crucibles, heated to 600 °C (at 1 or 10 °C/min) in a flow of synthetic air or N<sub>2</sub> (50 ml/min) and held for 10 minutes before cooling. For each specified run, a blank run was first carried out and the results were subtracted from the relevant data to remove buoyancy effects. Selected samples were analysed for EGA using CatLab instrumentation at Diamond Light Source in Harwell. EGA analysis was not carried out by the author. The main difference with EGA was that the gas flowed directly through the sample cell as opposed to just over the top of the crucible as was apparent for TGA/DTA.

#### 2.4.5. Temperature programmed reduction (TPR) and temperature programmed desorption (TPD)

Temperature programmed reduction (TPR) consists of heating a sample slowly in a dilute H<sub>2</sub> flow, and records the consumption of H<sub>2</sub> that reacts with oxygen present in the sample as a function of temperature<sup>(4)</sup>. Consequently, water is generated and therefore a cold trap is required to prevent it from reaching the thermal conductivity detector (TCD). This technique detects the different reducible species present in the sample. In the case of Cu/ZnO/Al<sub>2</sub>O<sub>3</sub> systems this reduction is associated with the activation of the catalyst to generate the Cu<sup>0</sup> active species from CuO. TPR was performed using a Thermo TPDRO 1100 series using 50 mg of calcined sample and heated to 400 °C at 10 °C/min under flowing 10% H<sub>2</sub>/Ar (50 ml/min).

Temperature programmed desorption (TPD) involves saturating a sample (adsorbent) in a chemical species (adsorbate), and then monitoring the temperature at which this species evolves from the surface of the sample in order to assess the binding strength of the chemisorption. Materials with acidic sites are investigated using basic chemical species such as NH<sub>3</sub> (NH<sub>3</sub>-TPD) whilst materials with basic sites are investigated using acidic chemical species such as CO<sub>2</sub> (CO<sub>2</sub>-TPD). In some cases materials have both acidic and basic surface sites making it useful to carry out both TPD techniques. Desorption occurring at higher temperatures indicates stronger chemisorption, whilst the peak areas correlate to the quantity of adsorbate. It is also important to consider both Brønsted and Lewis types of acidity and basicity. CO<sub>2</sub>-TPD was used in this work to analyse catalysts with various loadings of alkali metals using a Quantachrome ChemBET Chemisorption analyser equipped with a TCD. Calcined samples (100 mg) were reduced under 10% H<sub>2</sub>/Ar (30 ml/min) to 140 °C at 10 °C/min and then to 225 °C at 1 °C/min. The materials were held at this temperature for 20 minutes to ensure complete reduction to the final state catalysts took place, before cooling back down to ambient temperature under flowing He (80 ml/min). The catalysts were exposed to an excess quantity of CO<sub>2</sub>

(80 ml/min) for 30 minutes before the desorption was performed, by increasing the temperature from 25 to 600 °C at a rate of 10 °C/min, and held at 600 °C for 20 minutes under the flow of helium.

#### 2.4.6. Infrared spectroscopy

Vibrations (stretching and bending) in molecules or in solid lattices are excited by the absorption of photons with energy in the range 25-496 meV<sup>(1,4)</sup>. This energy lies in the infrared (IR) region of the electromagnetic spectrum. The absorption of IR radiation is used to determine the molecular bonding present in the sample. This arises because functional groups undergo vibrations by absorbing IR radiation at specific wavelengths. However, not all vibrations can be observed. A general selection rule for the absorption of an IR photon is that the dipole moment of the molecule must change during the vibration. The intensity of the IR band is proportional to this change in dipole moment. The group frequency concept states that functional groups in molecules may be treated as independent oscillators. The bond strength of functional groups can be determined using the band positions in the resulting IR spectra, as derived from Hooke's law (Equation 2.4.).

Equation 2.4. 
$$\nu = \frac{1}{2\pi c} \sqrt{\frac{k}{\mu}} \quad \text{with} \quad \mu = \frac{m_A m_B}{m_A + m_B}$$

Whereby  $\nu$  = the wavenumber of the vibration ( $\text{cm}^{-1}$ ),  $c$  = the speed of light =  $2.998 \times 10^8$  (m/s),  $k$  = the force constant of the bond (dyne/m) and  $\mu$  = the reduced mass (g) with  $m_i$  = the mass of vibrating atom,  $i$  (g). Therefore, functional groups with lighter atoms and/or stronger bonds absorb IR radiation of higher wavenumber. This technique is useful for identifying phases of catalyst materials and has proven very useful in the study of minerals in particular. Point group theory is a successful technique in predicting the IR spectrum of a molecule from identifying its symmetry group<sup>(6)</sup>. It is important to consider briefly here the  $\text{CO}_3^{2-}$  ion which is present in hydroxycarbonate phases. The free ion has  $D_{3h}$  symmetry, which exhibits four vibrational modes: symmetric stretching ( $\nu_1$ ), an out of plane bend ( $\nu_2$ ), a doubly degenerate asymmetric stretch ( $\nu_3$ ) and another doubly degenerate bending mode ( $\nu_4$ ). These occur at 1063 (R), 879 (IR), 1415 (IR, R) and 680 (IR, R)  $\text{cm}^{-1}$ , respectively with the transitions which are infrared (IR) and Raman (R) active indicated<sup>(7-8)</sup>. Thus vibrational spectroscopy provides a sensitive test for structural distortion of the  $\text{CO}_3^{2-}$  ion present in hydroxycarbonates. It should be noted that vibrations which are infrared inactive can become activated from a reduction in symmetry of the  $\text{CO}_3^{2-}$  ion, which can also split degenerate modes into several components.

Several forms of IR spectroscopy can be used with the transmission and diffuse reflection forms utilised in this work (Figure 2.6.). The fundamental difference is that transmission applies IR radiation directly through the sample, whilst diffuse reflection is reflected off the surface of the sample, and therefore are bulk and surface analytical techniques respectively.

FT-IR Analysis was performed on a Jasco 660 plus spectrometer in transmission mode over the range 400-4000  $\text{cm}^{-1}$ . Samples were first pressed with KBr (FT-IR Grade, Sigma Aldrich) to generate a thin optically transparent disk with ~1 wt.% of the investigated sample. Alternatively, a Shimadzu IR Affinity-1 spectrometer was used. Samples were pressed directly onto the sample stage without requiring the use of KBr. *In-situ* DRIFTS analysis was carried out on a Tensor 27 spectrometer. Samples were loaded into the sample holder with ~50 wt.% KBr. Scans were recorded every 2 °C using a ramp rate of 2 °C/min under flowing air (50 ml/min). Regarding all three spectrometers a background scan using KBr was always performed before each scan and subtracted from the spectra.

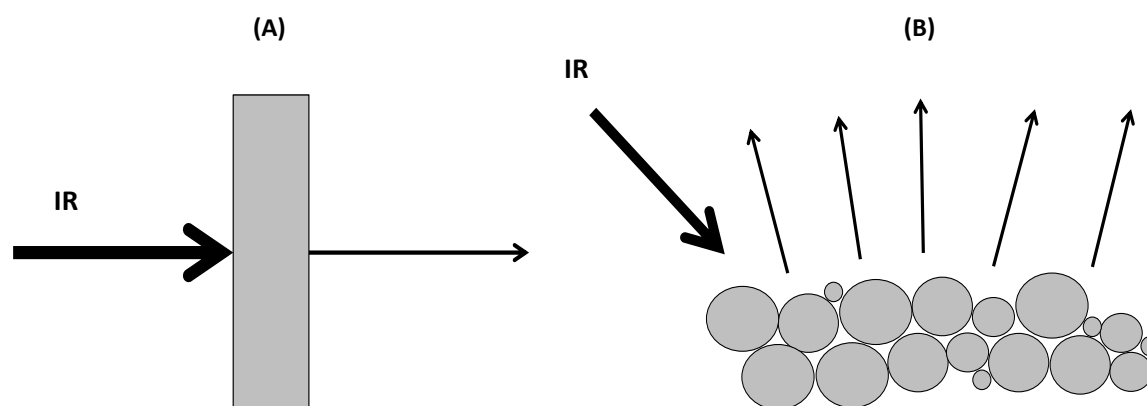


Figure 2.6. Two forms of infrared spectroscopy: (A) Transmission and (B) Diffuse reflection.

#### 2.4.7. Raman spectroscopy

In infrared spectroscopy a molecule absorbs photons with the same frequency as its vibrations. In contrast Raman spectroscopy is based on the inelastic scattering of photons (Figure 2.7.)<sup>(1,4,9)</sup>. A sample is irradiated with monochromatic light of frequency,  $\nu_0$  whereby the majority of the photons undergo Rayleigh (elastic) scattering. The molecule is excited to an unstable state (a virtual energy state) with energy,  $h\nu_0$  above the ground state, from which it decays back down to the ground state. Therefore no energy is exchanged between the molecule and the photon. However, when the excited molecule decays to the first vibrational energy level with frequency,  $\nu_{\text{vib}}$  it removes an amount of energy equal to  $h\nu_{\text{vib}}$  away from the photon. Therefore, the scattered light exhibits intensity at the frequency  $\nu_0 - \nu_{\text{vib}}$ . This Raman peak is called the Stokes band which is usually the side recorded for Raman scattering. The reverse process, occurring the opposite side to the Rayleigh

band, forms anti-Stokes bands. This occurs when decay down to the ground state leaves the sample in a lower vibrational energy state, with the net energy transferred to the photon. The relative intensities of the two processes depends on the population of various states in the molecule, but generally at room temperature anti-Stokes is of lower intensity. Like IR spectroscopy, not all vibrations are observable. A vibration is only Raman active if it changes the polarisability of the molecule, which generally requires the molecule to change shape. IR and Raman spectroscopy therefore complement each other since together both selection rules are obeyed and all the chemical bonds of a sample can be analysed. Whilst Raman has the disadvantage that certain samples are weakly active or give fluorescence, the resulting spectra is generally much simpler to interpret than IR from the reduced number of bands present. Moreover, Raman in conjunction with IR is essential for phase analysis. IR can be misleading as the abundant phase of a sample dominates the spectra<sup>(5)</sup>. Raman is extremely useful for verifying the presence of minority phases whose IR bands are masked.

Raman Spectroscopy was performed using a Renishaw inVia microscope with a green argon ion laser ( $\lambda = 514 \text{ nm}$ ). Samples were prepared by pressing onto a Raman inactive aluminium plate. Before samples could be analysed, the laser was first calibrated using an internal Si reference, and then the samples were brought into focus by adjusting the sample holder height. Typically 10 seconds of exposure and 10 accumulations were used in each scan. Only 5% laser power was used in order to

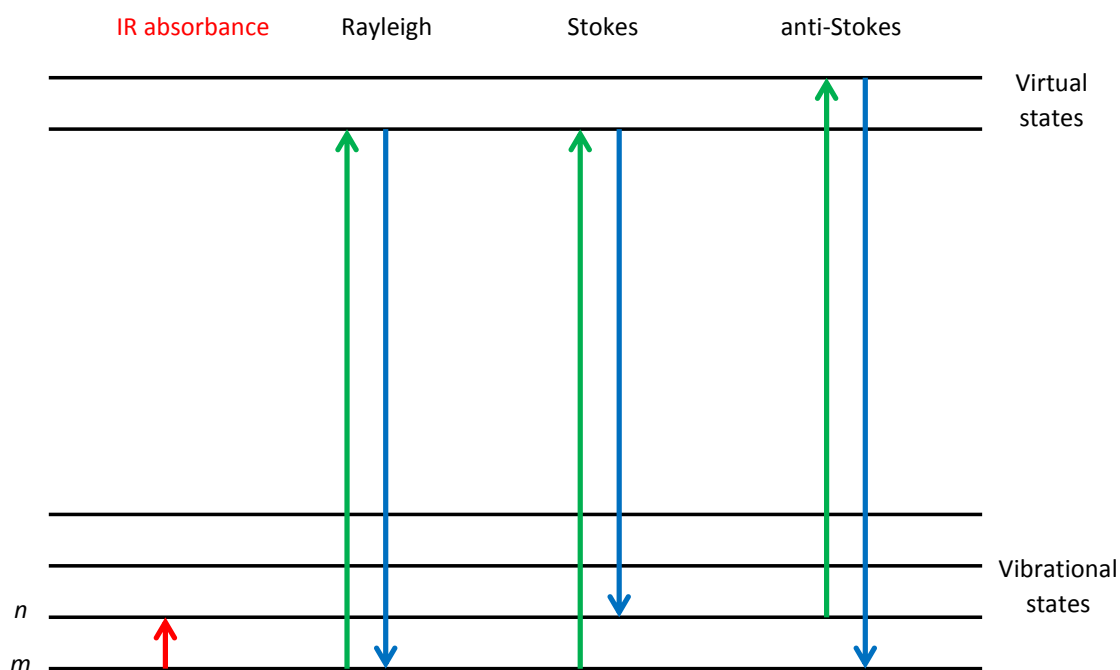


Figure 2.7. Transitions between energy levels in IR and Raman spectroscopy.

prevent modification of heat sensitive materials. Cosmic rays were also removed from each analysis.

#### 2.4.8. Diffuse reflectance ultra violet-visible spectroscopy (DRUVS)

Similar to IR spectroscopy, diffuse reflectance ultra violet-visible spectroscopy (DRUVS) involves transitions between energy states from the absorption of photons. However in DRUVS, photons with higher energy, from the visible and ultra-violet part of the electromagnetic spectrum, are absorbed. This absorbance induces electronic transitions from the ground state to an excited state. Various samples can be studied by this technique, which includes conjugated organic compounds or charge transfer complexes. However, in relation to this work, analysis was used to investigate samples with  $\text{Cu}^{2+}$  centres since transition metal ions with d electrons can also be excited to higher electronic states. The electronic excitation of d electrons explains why transition materials are coloured. The frequency of light absorbed depends on the energy gap between the ground and excited states, whereby the splitting of energy levels is dictated by the crystal field splitting. This depends on the oxidation state of the metal ion as well as the number and type of surrounding ligands which gives information on the co-ordination geometry and local structure. The technique is also a useful method for determining the concentration of absorbing species in solution using the Beer Lambert law. However, in this work the technique was not used to analyse liquid samples.

DRUVS was carried performed on a Varian Cary 4000 UV-Vis spectrometer. Samples were pressed into the sample holder with ~50 wt.%  $\text{BaSO}_4$  (99.998%, Sigma Aldrich) and analysed using a monochromatic source ( $\lambda = 500 \text{ nm}$ ). Scans were taken at 100 nm/minute. A background scan using  $\text{BaSO}_4$  was always performed before each scan and subtracted from the spectra.

#### 2.4.9. Brunauer Emmett Teller (BET) and density functional theory (DFT) Monte Carlo analysis

Surface area analysis is an extremely important aspect of catalyst and materials characterisation and is often calculated using the Brunauer Emmett and Teller (BET) method<sup>(5,10-11)</sup>. This first requires obtaining an adsorption isotherm. The technique most commonly used is  $\text{N}_2$  adsorption at 77 K, whereby the volume of  $\text{N}_2$  physisorbed on the adsorbent surface is plotted against its relative pressure. Physisorption arises from van der Waals forces and these weak forces between the adsorbate gas molecules and the adsorbent surface require the analysis to be carried out at the temperature of liquid  $\text{N}_2$ . BET simply involves determining the amount of  $\text{N}_2$  (adsorbate gas) corresponding to a monolayer coverage at the surface,  $V_m$  (Equation 2.5.).

**Equation 2.5.**

$$\frac{P}{V(P_0 - P)} = \frac{1}{V_m C} + \frac{(C - 1)}{V_m C} \times \frac{P}{P_0}$$

Whereby  $P$  = the specific pressure (pascals),  $P_0$  = the saturation pressure (pascals),  $V$  = the gas volume (ml),  $V_m$  = the monolayer gas volume (ml) and  $C$  = the dimensionless BET constant. This equation is a linear expression with the form  $y = mx + c$ . Usually at least three values of  $V$  are measured from the adsorption isotherm in the  $P/P_0$  range 0.06-0.35. Thus  $P/V(P_0 - P)$  ( $y$ ) can be plotted against  $P/P_0$  ( $x$ ) to yield a straight line. A straight line will not be obtained outside this range as at lower or higher pressure ranges insufficient adsorption or condensation takes place respectively. The accuracy of the analysis also significantly increases when more than 3 data points are used. From the equation, the slope of the linear graph ( $m$ ) gives  $(C-1)/V_m C$  with the intercept ( $c$ ) equal to  $1/V_m C$ . This gives  $V_m = 1/(m+c)$  with  $C = (m/c)$ . Therefore, taking into account the effective cross sectional area of one  $N_2$  molecule ( $0.162 \text{ nm}^2$ ) and the sample mass (g), the surface area ( $\text{m}^2 \text{ g}^{-1}$ ) is readily obtained. The BET ( $C$ ) constant is related to the heats of adsorption of the monolayer and the subsequent layers. Large  $C$  values reflect high adsorption energies for the first layer in comparison to subsequent layers, whereas small values reflect small differences in adsorption compared with condensation. As a general rule of thumb, the  $C$  value must lie between 50-200 to give a reasonable calculation of the monolayer volume, and is therefore an indicator of the accuracy of the analysis. These intermediate values give an easily distinguishable transition from monolayer to multilayer adsorption. It should also be noted that the BET theory is based on a number of assumptions. This includes the following: (1) a clean, homogeneous surface is present, (2) there are no lateral interactions between molecules, (3) the uppermost layer is in equilibrium with the vapour phase, (5) the first layer relates to the heat of adsorption, whilst higher layers relate to heat of condensation and (6) at saturation pressure, the number of layers becomes infinite. If these assumptions are not satisfied during experimental measurements a linear BET plot will not be obtained, which also results in BET surface area values not being obtained.

In the context of this work, it is also important to examine pore volume and pore size distribution in order to derive additional information of the physical properties of various materials. Whilst there are again many methods available such as the t-plot and BJH, there is now considerable interest in the application of density functional theory (DFT) from physisorption in model pore structures<sup>(10-11)</sup>. It is now possible to predict the behaviour of simple fluids in model micropores of defined size and shape. The approach consists of the construction of a grand potential functional of the average local density and of a minimization of this, with respect to local density, to obtain equilibrium density profile and thermodynamic properties. Most simulation studies have been carried out using  $N_2$  adsorption at 77 K and as the work has progressed more accurate analysis has been obtained. From computing model isotherms for various adsorbents (e.g. silica, carbon and zeolites) the analysis can

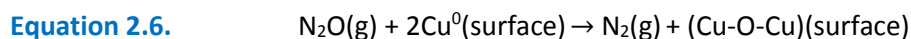
be tailor made for each unique sample. Overall the method has no theoretical limitations regarding pore size, whereby the applicability ranges between ultra-micropores to macropores.

In this work BET analysis was performed using a Micromeritics Gemini 2360 surface analyser. A five point analysis was performed using N<sub>2</sub> as the adsorbate gas. Samples were degassed for 60 minutes at 105 °C prior to analysis. Surface areas were calculated with a reasonably high level of inaccuracy due to technique limitations, variable amounts of sample used and the thermal instability of specific materials. In order to overcome these limitations and to obtain data of higher accuracy selected samples were also analysed using a Quantachrome Autosorb-1. 200 mg of each sample was degassed under vacuum. This enabled lower degas temperatures to be utilised, which was required for heat sensitive materials. In each case an 80 point (40 adsorption and 40 desorption points) isotherm was obtained using N<sub>2</sub> at 77 K. Surface area analysis was carried out using an 8 point BET plot. The pore volume and size distribution was calculated from the entire adsorption isotherm using the DFT Monte-Carlo model. The N<sub>2</sub>-silica adsorption branch at 77 K was the kernel file chosen.

#### 2.4.10. Copper surface area analysis

Copper surface area analysis is an extremely powerful tool for screening materials against their potential catalyst activities, since the copper surface area is linearly proportional to methanol synthesis activity<sup>(12)</sup>. Samples were first calcined to 300 °C for 2 hours under static air using a ramp rate of 10 °C/min, unless otherwise stated. The calcined materials which were then going to be analysed the following day were ground into fine powders and placed overnight in an oven set to 110 °C. This was to ensure that any residual water or solvent was removed, since the mass of the sample is essential for calculating the final surface areas. The analysis was carried out on a Quantachrome ChemBET Chemisorption analyser (**Figure 2.8.**). Approximately 100 mg of sample was packed into a quartz glass U-tube using quartz wool, and purged with high purity He for 5 minutes to remove any adsorbed surface species. Since surface Cu<sup>0</sup> is required for this analysis the CuO component must be first reduced which results in a mass loss. Consequently, the sample mass was accurately recorded before and after each analysis was complete in order to take this mass loss into account. Therefore for each sample, two Cu SA values were recorded. For the purposes of accurately examining final state catalysts only the Cu surface area which took into consideration the mass loss from reduction was considered in this work. The sample was reduced under 10% H<sub>2</sub>/Ar (30 ml/min) to 140 °C at 10 °C/min, before being heated to 225 °C at 1 °C/min. A reduced ramp rate was required during the reduction in order to minimise the extent of Cu sintering. The sample was then held at this temperature for 20 minutes to ensure complete reduction. Residual H<sub>2</sub> was flushed from the system by switching the gas line back over to He (80 ml/min), whilst holding the sample at 220 °C

for another 10 minutes. The He line went through a He purifier to remove any impurities such as oxygen which would be detrimental to the accuracy of this analysis, especially at these elevated temperatures. The temperature was then reduced down to 65 °C for pulsing with N<sub>2</sub>O (AA Grade). A programme of 12 pulses of 113 µl N<sub>2</sub>O with a 5 minute stabilisation time between each one was used, followed by 3 pulses of N<sub>2</sub> for calibration. The overall chemical process relies on the decomposition of nitrous oxide on copper (**Equation 2.6.**).



The unreacted N<sub>2</sub>O was trapped before reaching the detector using a molecular sieve 5A (pelleted, 1.6 mm, Sigma Aldrich) trap which was tested and trailed before analysis. It is clear that the process relies only on oxidation of the Cu surface, with the resulting Cu surface area determined using the amount of N<sub>2</sub> emitted and the catalyst mass (**Equation 2.7.**).

**Equation 2.7.** 
$$\text{Cu surface area (m}^2 \text{ g}^{-1}) = \frac{\text{N}_2 \text{ volume (ml)} \times N_A \times 2}{\text{catalyst mass (g)} \times 24000 \text{ (ml)} \times (1.0 \times 10^{19} \text{ (atoms/m}^2\text{)})}$$

Whereby N<sub>A</sub> = Avogadro constant = 6.022 x 10<sup>23</sup> (atoms). The key assumptions are that the amount of N<sub>2</sub> emitted amounts to half a monolayer coverage of oxygen and that the surface density of Cu is 1.47 x 10<sup>19</sup> (atoms/m<sup>2</sup>). The volume of N<sub>2</sub> produced was quantified using a thermal conductivity

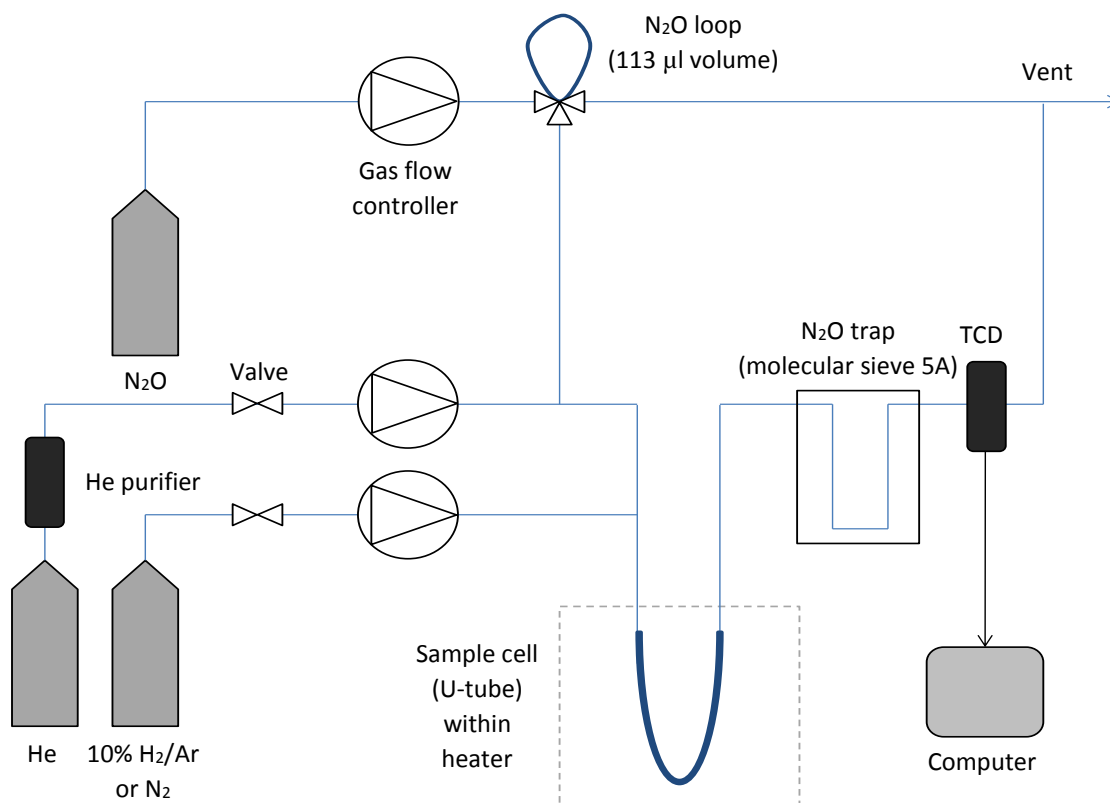


**Figure 2.8.** Schematic of pulse reactive chemisorption set-up for copper surface area analysis.

detector (TCD). Cu surface area analysis was also conducted on selected materials at Johnson Matthey, but this was not done by the author. Whilst the methodology is similar, the fundamental difference is that the analysis was carried out using reactive frontal chromatography. This involves using a flow technique for the decomposition of N<sub>2</sub>O in comparison to the pulse technique utilised in Cardiff. Each sample after calcination (500 mg) was crushed and pelleted to give particle sizes 0.621 mm in diameter. For analysis 2.5% N<sub>2</sub>O/He at 68 ml/min was passed over each catalyst.

#### 2.4.11. Helium pycnometry

Helium pycnometry is used to obtain information on the true density or real density of solids. Since He can enter even the smallest voids or pores, it is used to measure the unknown volume of a material of a known weight. The result is often referred to as a skeletal density. The pycnometer is a vessel with a precisely known volume and involves being filled before weighing. Density is simply calculated from mass / volume. In this particular case, samples were placed in the pycnometer and filled up with He. The density of the sample can then be determined from knowing the density of He, the weight of the pycnometer filled only with He, the weight of the pycnometer filled with sample and He and the weight of the sample.

Selected samples were submitted to MCA Services in Cambs for analysis and was not carried out by the author. The error margin reported was 0.03% of the reading plus 0.03% of the sample capacity.

#### 2.4.12. Scanning electron microscopy (SEM), transmission electron microscopy (TEM) and scanning transmission electron microscopy (STEM)

Electron microscopy is a suitable technique for determining the size and morphology of particles, ranging from several hundred micrometres down to the atomic level<sup>(1,4)</sup>. It can also reveal information on the composition and internal structure of the particles. For scanning electron microscopy (SEM) a source of electrons is focused into a beam with a very fine spot size ~5 nm, with energy ranging between a few hundred eV to 50 keV. This beam is rastered over the surface of the sample by deflection coils. As the electrons strike and penetrate the surface several interactions occur with the emitted electrons and X-rays collected on a cathode ray tube (CRT) and an energy dispersive X-ray (EDX) detector respectively. When a high energy primary electron interacts with an atom it undergoes either inelastic scattering with atomic electrons or elastic scattering with the atomic nucleus. Secondary electrons with energies less than 50 eV arise when the primary electron transfers enough of its energy to another electron in order for it to emit. Backscattered electrons are the high energy electrons which are elastically scattered and possess the same energy as the primary electrons. Backscattering probability increases when the atomic number of the specimen increases

and provides images with useful contrast where the atomic number range widely varies. Furthermore, the primary electron can collide with and eject a core electron from an atom in the sample. The excited atom will decay back down to its ground state by either emitting a characteristic X-ray photon or an Auger electron both of which can be used for quantitative and qualitative (elemental mapping) chemical characterisation. For EDX analysis, the incident X-ray is converted into an electron with kinetic energy by means of the photoelectric effect. The detector dissipates this energy by creating electron-hole pairs in the semiconductor whereby the number of these pairs is reflected in the pulse height of the current that is measured if a voltage is applied over the detector. In TEM a primary electron beam of energy 100 keV or higher passes through a condenser to produce parallel rays which impinge on the sample. The greatest advantages of TEM is the high magnification ranging from 50 to  $10^6$ , and its ability to provide both image and diffraction information from a single sample. Switching between imaging and observing the diffraction pattern is possible from simply changing the strength of the intermediate lens. The higher the operating voltage of the TEM the greater its spatial resolution, with voltages up to 400 keV generating point-to-point resolutions better than 0.2 nm. However one shortcoming relates to the limited depth resolution, whereby scattering information originating from a three-dimensional sample is projected onto a two-dimensional detector. The scanning transmission electron microscope (STEM) combines both the SEM and TEM modes of operation and is thus an extremely powerful tool in the field of catalysis.

SEM-EDX analysis was performed using a Carl Zeiss EVO-40 with samples mounted on 12.5 mm carbon disks supported on aluminum stubs. Analysis was used in order to extract useful topology, morphology and chemical composition data from the samples. The analysis was performed under the following operating conditions: under vacuum the secondary electron detector was used with the EHT set to 25 kV and the I-probe set to 1000 pA. The z-axis of the sample holder was set to 25 mm and the electron beam was then focused before carrying out analysis. For EDX analysis calibration was first carried out using a cobalt standard. The I-probe was increased to 10,000 with the working distance set to 9 mm and the live time set to 120 seconds. In order to obtain representable data for each sample, scans were carried out from at least 5 different particulates with the average taken. TEM and STEM-ADF analysis was performed on a JEM-2100 and was not carried out by the author. Samples were prepared by dispersing the catalyst powder in deionised water before allowing a drop of the suspension to evaporate on a holey carbon microscope grid.

#### **2.4.13. Microwave plasma atomic emission spectroscopy (MP-AES)**

Microwave plasma atomic emission spectroscopy (MP-AES) is an analytical technique used for the accurate quantification and verification of trace metals<sup>(13)</sup>. The principle of AES essentially relates to

exciting atoms in order to promote electrons into higher electronic states, which emit photons with energy characteristic of a specific element when they relax back down to the ground state. The wavelengths of radiation emitted therefore provides qualitative information of the elements present, whilst the intensity of the wavelengths provides quantitative information. The emission source in this case was a microwave plasma sustained with nitrogen gas.

In this procedure an aqueous solution is delivered into an analytical nebulizer using peristaltic pumps, whereby it is converted into a very fine mist and introduced inside the plasma flame. The sample collides with the electrons and charged ions in the plasma, which strips each element down into atoms, and then charged ions. Characteristic wavelengths of elements are then emitted when electrons return back down to the ground electronic states. A series of transfer lenses are used to focus the emitted light onto a diffraction grating. This separates the combined photons (all with varying energies of a specific wavelength) into the component wavelengths in the optical spectrometer. In this case, the separated colours fall upon an array of semiconductor photo-detectors termed charge coupled devices (CCD). CCD detectors allow for multi-element measurements providing sub-parts-per-billion (ppb) detection limits for many elements. The intensities of all wavelengths are measured simultaneously allowing for fast analysis. For quantification of specific elements, the intensity of each line from emission is compared against intensities of known concentrations. This requires preparation of calibration standards which must be analysed before the sample solutions. The concentrations of sample solutions is then computed by interpolation along the calibration lines. It should also be noted that wavelengths of certain elements can overlap. Therefore it is appropriate to analyse at 2-3 wavelengths emitted from each element being analysed in order to verify the findings.

MP-AES was performed using a 4100 MP-AES manufactured by Agilent Technologies in order to confirm and quantify specific elements present down to parts-per-million (ppm) levels in various solid samples and effluents. For analysis of solid samples: materials of known mass were digested in  $\text{HNO}_3$  ( $\geq 99.999\%$  trace metals basis, Sigma Aldrich). Residual solid was removed using PTFE filter membranes. Sample solutions were then accurately produced of known volume using a specific solution, also referred to as the matrix (in this case 10% volume  $\text{HNO}_3/\text{H}_2\text{O}$ ). Blanks and calibration standards were also accurately prepared of known concentration and volume using the exact same matrix. The blank, standards and solutions were then consecutively analysed in turn. Three emitted wavelengths were analysed for each element with an average taken of the findings. Data produced for the sample solutions was only accepted if the determined concentration was in the calibration range. In some instances this required diluting the sample solutions down, whereby the true

concentration could be calculated from the determined dilution factor. The analysis of effluents was largely similar, but with the exclusion of the digestion step which enabled solutions to be prepared without using HNO<sub>3</sub>. For the analysis of residual sodium levels, extreme care was taken to use reagents with Na levels ≤ 0.1 ppm, which is within the error limits of the technique. A series of high purity standards (TraceCERT, 1000 mg/L in 2% HNO<sub>3</sub>, Sigma Aldrich) were used for preparation of the calibration solutions including Cu, Zn, Al and Na.

#### 2.4.14. Inductively coupled plasma mass spectrometry (ICP-MS)

Inductively coupled plasma mass spectrometry (ICP-MS) is a state of the art technique used for elemental analysis. It has excellent detection capability, with the ability to obtain isotope information. The ICP source converts the atoms in the sample into ions which are then separated and detected by the mass spectrometer. The sample is typically introduced into the plasma as an aerosol using a nebuliser, whereby it is completely desolvated, and the elements are first converted into gaseous atoms and then ionized towards the end of the plasma. To generate the plasma, argon gas flows through the concentric channels of the ICP torch. Power is supplied to a load coil from a generator to produce an oscillating electromagnetic field at the end of the torch. When a spark is applied to the argon flowing through the torch, the atoms become ions which get caught in the electromagnetic field to produce an argon plasma from colliding with other argon atoms. Once the elements are converted into ions, they are then passed through a vacuum before entering the low pressure region of the mass spectrometer ( $< 1 \times 10^{-5}$  torr). Electrostatic lenses are used to focus the ion source to collimate an ion beam. Once the ions enter the mass spectrometer they are separated by their mass-to-charge ratio. The most commonly used type of mass spectrometer is the quadrupole mass filter, consisting of 4 rods to establish an electrostatic filter. A detector is then used to translate the number of ions striking the detector into an electric signal, that can be measured and related to the number of atoms of particular elements in a sample from calibration standards.

Selected samples were submitted to Warwick Analytical Service for analysis and was not carried out by the author. The error margin reported for each element was ±0.01 wt.%.

## 2.5. Catalyst testing

As previously mentioned, catalyst testing for methanol synthesis and the LTS reaction was carried out at Johnson Matthey in Billingham. Very limited time on test reactors was available and therefore catalysts prepared from SAS and co-precipitation were screened prior to testing using copper surface

area analysis. This is because activity for methanol synthesis is strongly related to the copper surface area<sup>(12)</sup>, which was covered in more detail in **Chapter One**. All tested samples were calcined (300 °C at 1 °C/min for 4 h in static air) at Johnson Matthey before being pelleted and ground to give particle sizes 0.621 mm in diameter. Justification for why specific catalysts were selected for testing as well as the reasoning for the specific calcination conditions chosen will be given in subsequent chapters.

### 2.5.1. Methanol synthesis

Testing for methanol synthesis was performed by Johnson Matthey using a single stream, six bed flow reactor. The reactor set-up was similar to the LTS reactor, but with the exclusion of the steam vaporiser line. The schematics for this general reactor set-up is presented but has been reported elsewhere (**Figure 2.9.**)<sup>(14)</sup>. For each catalyst precursor, 500 mg was charged into a reactor bed and then reduced using a gas composition of 2% H<sub>2</sub>/N<sub>2</sub> with a flow of 60 ml/min. The pressure for reduction was 10 bar. The materials were heated under these conditions to 90 °C at 2 °C/min, then to 135 °C at 1 °C/min, and then finally to 225 °C at 0.5 °C/min. Materials were held at 225 °C for 1 hour to ensure complete reduction to the final state catalysts took place.

For testing each catalyst was subjected to a synthesised composition of syn-gas (**Table 2.2.**) at 60 ml/min. The pressure for testing was 25 bar. In order to examine catalyst stability as well as the activity a specific programme was chosen: the initial temperature was 190 °C and after 12 hours online the temperature was increased by 15 °C, using a ramp rate of 1 °C/min to 205 °C. This cycle was repeated up to 250 °C, whereby after 12 hours at this temperature it was reduced back down to 190 °C for a final 12 hours, to examine the extent of deactivation. In-line gas analysis was performed using IR which detected carbon monoxide, carbon dioxide, water and methanol. Whilst knockout pots were present downstream of the reactor beds to collect the resulting effluents, the selectivity of the catalysts was not investigated. Testing was not performed by the author.

**Table 2.2.** Composition of syn-gas used for methanol synthesis testing.

Gas	Composition (mole %)
Carbon Monoxide	6
Carbon Dioxide	9.2
Hydrogen	67
Nitrogen	17.8

### 2.5.2. Low temperature water gas shift (LTS) reaction

Testing for the LTS reaction was performed at Johnson Matthey using a single stream, six-bed flow reactor (**Figure 2.9.**). The reduction conditions used for all catalysts was similar to that used for

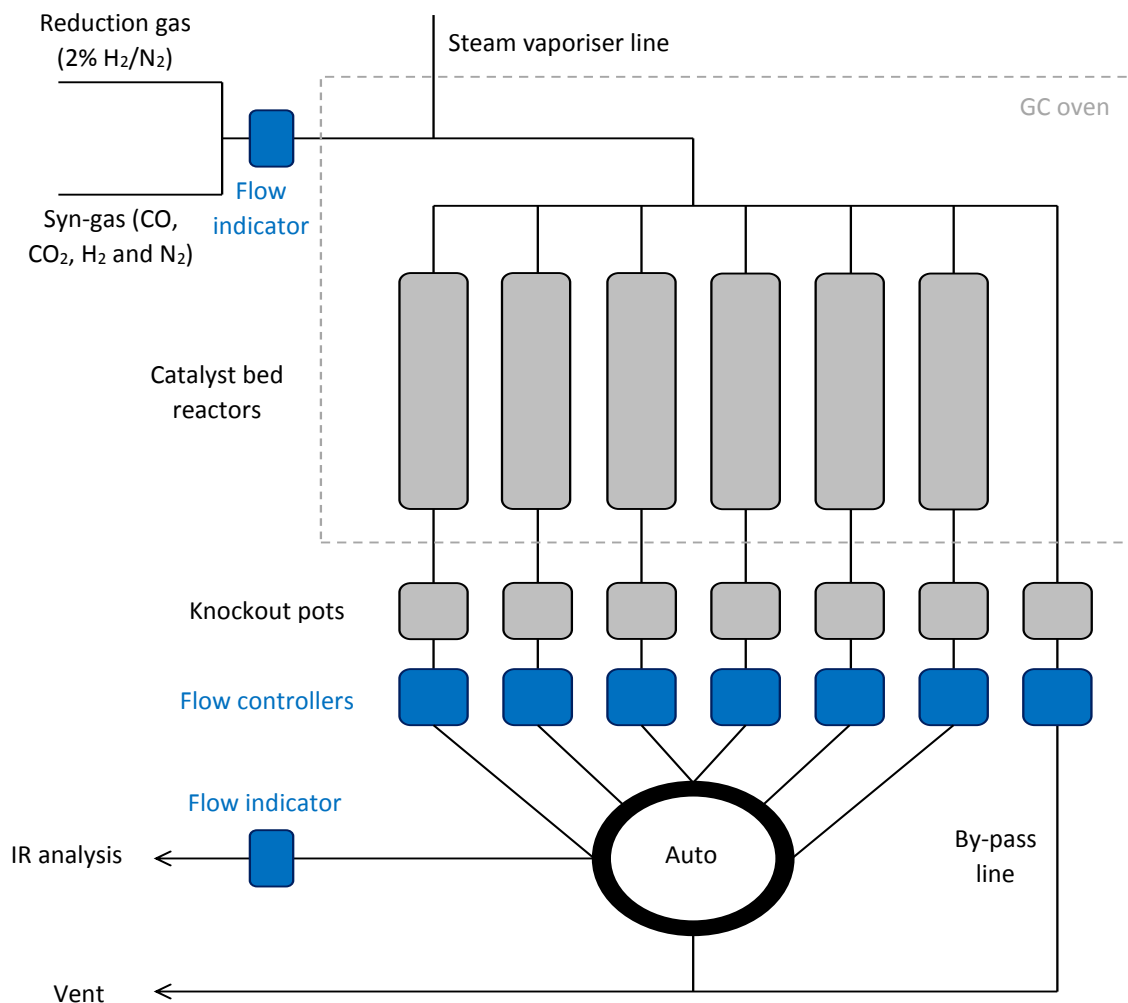


Figure 2.9. Schematic of LTS reactor set-up at Johnson Matthey<sup>(14)</sup>.

Table 2.3. Composition of syn-gas used for LTS testing.

Gas	Composition (mole %)
Carbon Monoxide	4
Carbon Dioxide	16
Hydrogen	55
Nitrogen	25

methanol synthesis. For each catalyst precursor, 500 mg was charged into a reactor bed and then reduced using a gas composition of 2% H<sub>2</sub>/N<sub>2</sub> with a flow of 42 ml/min. The pressure for reduction was 10 bar. The materials were heated under these conditions to 150 °C at 0.75 °C/min, and then to 220 °C at 0.5 °C/min. The resulting catalysts were then held at 220 °C for 1.5 hours to ensure complete reduction had taken place.

For testing, each catalyst was subjected to a synthesised composition of syn-gas (Table 2.3.). In order to investigate the catalyst activity in terms of mass and space velocity the flow of syn-gas was varied between 500-1250 ml/min. This reactant gas stream was passed through vaporised water to give a water composition of 50 vol.%. Reaction conditions were at 220 °C and 27.5 bar. The duration of testing was 138 hours. In-line gas analysis was performed using IR to measure CO conversion. Relative activities were calculated by altering the flow of each catalyst bed in order to achieve 70% CO conversion. The total system flow is maintained during the by-pass line, whereby the ratio of flows used for each catalyst reactor was used to calculate the standard catalyst activities. Selectivity was determined by the methanol ppm content within the knockout pots downstream of the reactors. Testing was not performed by the author.

## 2.6. References

- 1 G. Cao, *Nanostructures and Nanomaterials: Synthesis, Properties and Applications*, Imperial College Press, 2004.
- 2 M. Behrens, F. Studt, I. Kasatkin, S. Kuhl, M. Havecker, F. Abild-Pedersen, S. Zander, F. Girgsdies, P. Kurr, B. Kniep, M. Tovar, R. W. Fischer, J. K. Norskov and R. Schlögl, *Science*, 2012, **336**, 893-897.
- 3 C. Baltès, S. Vukojevic and F. Schuth, *Journal of Catalysis*, 2008, **258**, 334-344.
- 4 J. W. Niemantsverdriet, *Spectroscopy in Catalysis: An introduction*, Second Edition, Wiley-VCH, 2000.
- 5 G. C. Bond, *Heterogeneous Catalysis: Principles and Applications*, Second Edition, Oxford Science Publications, 1987.
- 6 A. Vincent, *Molecular Symmetry and Group Theory*, Second Edition, J. Wiley and Sons Ltd, 2001.
- 7 R. L. Frost, W. N. Martens, D. L. Wain and M. C. Hales, *Spectrochimica Acta Part A*, 2008, **70**, 1120-1126.
- 8 K. Nakamoto, *Infrared and Raman Spectra of Inorganic and Coordination Compounds Part A: Theory and Applications in Inorganic Chemistry*, Sixth Edition, J. Wiley and Sons Ltd, 2009.
- 9 E. Smith and G. Dent, *Modern Raman Spectroscopy: A practical approach*, J. Wiley and Sons Ltd, 2005.

- 10 G. Leofanti, M. Padovan, G. Tozzola and B. Venturelli, *Catalysis Today*, 1998, **41**, 207-219.
- 11 F. Rouquerol, J. Rouquerol and K. Sing, *Adsorption by Powders and Porous Solids: Principles, Methodology and Applications*, Academic Press, 1999.
- 12 G. C. Chinen, K. C. Waugh and D. A. Whan, *Applied Catalysis*, 1986, **25**, 101-107.
- 13 M. Cullen, *Atomic Spectroscopy in Elemental Analysis*, Blackwell Publishing, 2004.
- 14 S. A. Kondrat, PhD Thesis, Cardiff University, 2011.

## 3.0. Optimization of precipitation synthesis routes to georgeite hydroxycarbonate catalyst precursors

### 3.1. Introduction

As discussed in **Section 1.3.1.**, the hydroxycarbonate mineral malachite has been widely reported as the optimum catalyst precursor for the preparation of established industrial Cu/ZnO/Al<sub>2</sub>O<sub>3</sub> catalysts. An aqueous co-precipitation route is utilised in industry to prepare malachite, and hence significant research has been carried out to optimise the relevant synthesis parameters to produce catalysts with optimum performance. It is well known that formation of intimately mixed copper, zinc oxide and alumina phases to generate strained, nanoscale copper crystallites, in a highly porous framework is a fundamental requirement of an optimum catalyst. Furthermore, the presence of residual sodium loadings, a direct consequence from using sodium carbonate in the preparation, is a known poison to the catalytic performance and hence it is plausible that the full potential of such catalysts has yet to be exploited.

In direct contrast, the amorphous hydroxycarbonate mineral georgeite has been rarely cited in the literature, and its potential as an alternative precursor has not yet been fully investigated. However, recent work carried out by Kondrat has demonstrated that georgeite can be readily prepared synthetically using supercritical CO<sub>2</sub> anti-solvent (SAS) precipitation, and has demonstrated its potential as an alternative catalyst precursor<sup>(1)</sup>. The work therefore discussed in **Chapter Three** focuses on optimising key experimental parameters of the SAS precipitation route with the intention of producing optimum georgeite precursors. Furthermore, it is shown that georgeite can also be prepared by co-precipitation, and again relevant key parameters of this route were optimized. Both precipitation routes avoided the use of alkali reagents to prevent catalyst deactivation. This work allowed suitable georgeite materials to be selected, which were trialled and tested against established industrial standards at Johnson Matthey, for both methanol synthesis and the LTS reaction.

### 3.2. Optimization of the content of water used as a co-solvent in binary copper-zinc SAS systems

Varying the volumetric ratio between water and ethanol in the starting metal acetate solution significantly alters the resulting precipitate from the SAS process. Changes are observed in the phase type or mixture, the structural and physical properties as well as the chemical composition, which in

turn can affect yields. Studies carried out by Hutchings and co-workers have investigated the water content in the production of hopcalite precursors using metal acetates in SAS precipitation<sup>(2)</sup>, whilst Kondrat has carried out similar studies regarding the synthesis of georgeite<sup>(4)</sup>. It was concluded from both studies that the absence of water results in the formation of disordered hydroxyacetates, whilst water addition resulted in the formation of hydroxycarbonates. Thus, the presence of water in the system is essential for the formation of georgeite, and in fact is universally present in amorphous minerals<sup>(3)</sup>. Whilst water contents of 0, 5 and 10% by volume have been investigated in the attempts to synthesise georgeite it is clear that further investigation would be beneficial in order to fully optimise the water content in the starting solution. Moreover, this work would allow for a better understanding of this particular system and contribute towards the rational design of alternative catalyst materials prepared by SAS precipitation. Copper acetate monohydrate (4 mg/ml) and zinc acetate dihydrate (2.13 mg/ml) salts were dissolved in ethanol containing 0.5, 1, 15, 20 and 30% water by volume to give a nominal Cu/Zn molar ratio of 2/1. Precipitates made from solutions using 0, 5 and 10% water by volume were also replicated from Kondrat's work for comparison.

### 3.2.1. Results and discussion

In order to identify the phase or phases produced from using various water contents as well as to determine changes in the molecular structure from the SAS process, vibrational spectroscopy analytical techniques were carried out on the resulting precipitates. The FT-IR findings confirmed the

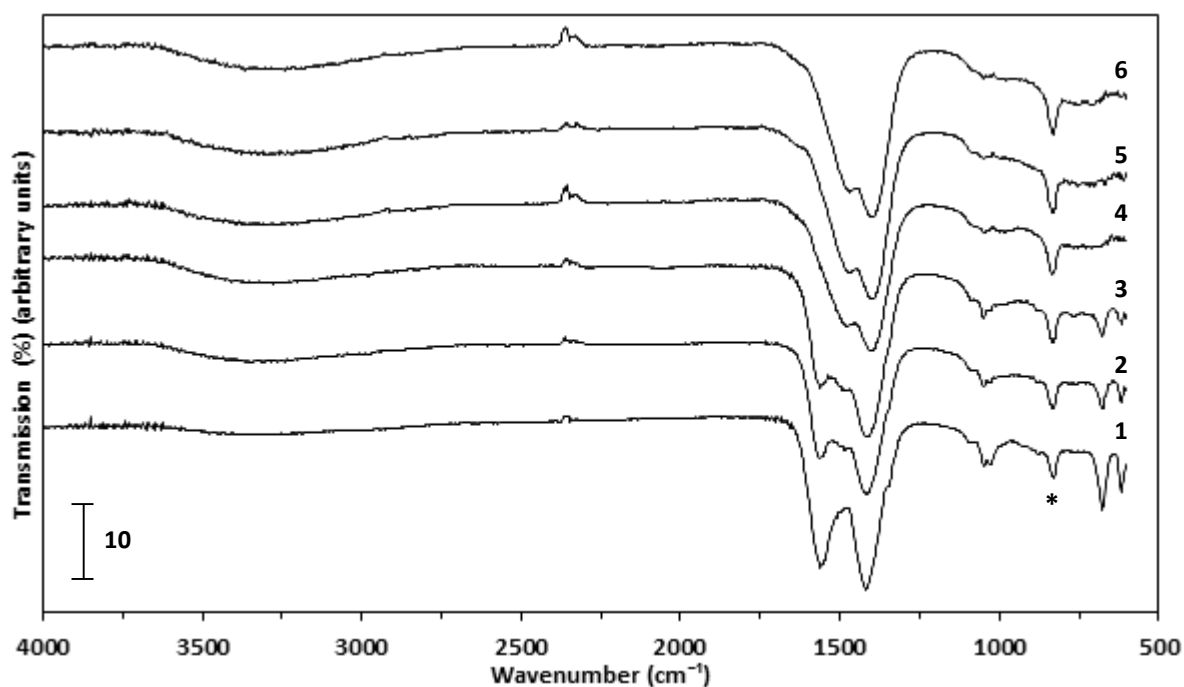


**Figure 3.1.** FT-IR spectra of the SAS prepared materials formed using different solvent mixtures: (1) 0 vol.% H<sub>2</sub>O/EtOH (2) 0.5 vol.% H<sub>2</sub>O/EtOH (3) 1 vol.% H<sub>2</sub>O/EtOH (4) 5 vol.% H<sub>2</sub>O/EtOH (5) 10 vol.% H<sub>2</sub>O/EtOH (6) 30 vol.% H<sub>2</sub>O/EtOH. \* Carbonate  $\nu_2$  band (835 cm<sup>-1</sup>) marked for clarity.

predominant phase to be the disordered hydroxyacetate when no water was incorporated into the system, but confirmed zincian georgeite as the predominant phase when water contents  $\geq 5\%$  were utilised (**Figure 3.1.**). Interestingly, the materials prepared using 0.5-1% water clearly showed a phase mixture as bands for both phases were apparent. FT-IR analysis was also carried out on the starting copper and zinc acetates for comparison (**Figure S1.**), with a complete assignment of all the bands for zincian georgeite, the CuZn hydroxyacetate and starting materials carried out in accordance to the literature<sup>(4-7)</sup> (**Table S1.**). A comparison of the FT-IR findings with the literature also confirms that it is indeed the georgeite phase produced when using these higher water contents<sup>(8-10)</sup>. The broad band centred at  $3289\text{ cm}^{-1}$  is associated with the O-H stretch, whilst peaks associated with the carbonate are present as the intense doublet at  $1475$  and  $1404\text{ cm}^{-1}$  for the  $\nu_3$  asymmetric stretch, the weakly visible peak at  $1048\text{ cm}^{-1}$  for the  $\nu_1$  symmetric stretch and the peak at  $835\text{ cm}^{-1}$  for the  $\nu_2$  bending mode.

The CuZn hydroxyacetate phase, in contrast, displays bands at  $1561$  and  $1420\text{ cm}^{-1}$  which are assigned to the  $\text{COO}^-$  asymmetric and symmetric stretches, respectively, whilst bands positioned at  $1053$  and  $1043\text{ cm}^{-1}$  are associated with  $\delta(\text{C-H})$  modes. The bands are broader in comparison to the starting materials, and there is a reduction in the number of peaks. In particular, further splitting of the  $\text{COO}^-$  bands is apparent for the as received copper acetate. Kondrat also highlighted a change in the wavenumber gap between the  $\text{COO}^-$  bands and reported a reduction of  $\sim 10\text{ cm}^{-1}$  after SAS precipitation but without using zinc<sup>(1)</sup>. Interestingly, this gap was determined to be  $141\text{ cm}^{-1}$  for the CuZn hydroxyacetate, and  $159$  and  $115\text{ cm}^{-1}$  for the starting copper and zinc acetates respectively. As shown the SAS prepared material also displays an additional band at  $832\text{ cm}^{-1}$  which is the carbonate  $\nu_2$  bending mode. Whilst no water was used, trace amounts of zincian georgeite were formed and this is attributed to the small amounts of water present from the hydrated starting metal salts. In related studies Reverchon, and co-workers also reported the presence of zinc carbonate using DMSO and NMP solvents in the SAS precipitation of zinc acetate from FT-IR peaks at  $1500$  and  $835\text{ cm}^{-1}$ <sup>(11)</sup>.

Raman analysis was carried out to obtain additional information on the SAS prepared materials regarding phase identification and structure (**Figure 3.2.**), with all peaks assigned in accordance to the literature<sup>(5-7)</sup> (**Table S2.**). The spectra for the zincian georgeite phase only displays bands for carbonate at  $1091\text{ cm}^{-1}$  for the  $\nu_1$  symmetric stretch, and a doublet at  $771$  and  $724\text{ cm}^{-1}$  for the  $\nu_4$  bending mode. However bands are also present at  $2934$  and  $938\text{ cm}^{-1}$  and these are assigned to  $\nu(\text{C-H})$  and  $\nu(\text{C-C})$  modes, respectively. This is most clearly shown for the sample made using 5% water which also demonstrates a broad band present from  $1624$ - $1313\text{ cm}^{-1}$ . This lies in the region of the  $\text{COO}^-$  symmetric stretch and  $\delta(\text{C-H})$  modes. Whilst only the band at  $2934\text{ cm}^{-1}$  remains weakly visible

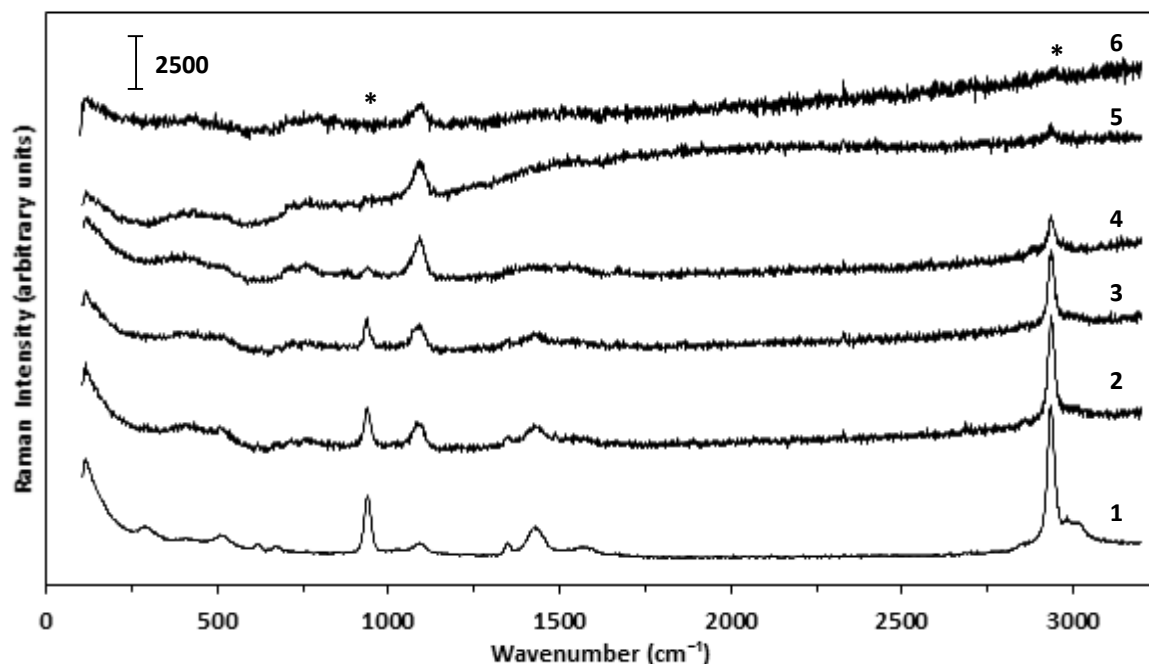


**Figure 3.2.** Raman spectra of the SAS prepared materials formed using various solvent mixtures: (1) 0 vol.% H<sub>2</sub>O/EtOH (2) 0.5 vol.% H<sub>2</sub>O/EtOH (3) 1 vol.% H<sub>2</sub>O/EtOH (4) 5 vol.% H<sub>2</sub>O/EtOH (5) 10 vol.% H<sub>2</sub>O/EtOH (6) 30 vol.% H<sub>2</sub>O/EtOH. \* Acetate bands (938 and 2934 cm<sup>-1</sup>) which remain at higher water contents are marked for clarity.

with water contents  $\geq 10\%$ , it is clear that some residual acetate remains even at these higher water contents. The preparation of the starting metal acetate solution however generates a well dispersed precipitate when water contents  $\geq 5\%$  are used, which could be attributed to hydrolysis of the dissolved metal acetate ions. This precipitate is so finely dispersed it passes through the filtration set-up used and gets incorporated into the resulting precipitate. In order to investigate this further, this precipitate was retained for Raman analysis and compared against the starting acetate materials, confirming that it was indeed an acetate phase ([Figure S2.](#)). For the SAS prepared materials the peaks associated with the acetate phase did not shift with water content, and surprisingly, were identical to the starting solution precipitate. The wavenumber for the  $\nu(\text{C-C})$  mode in particular is most useful since it has been correlated to the carboxylate structure in copper complexes from studies by Quiles and Burneau<sup>(6)</sup>. This wavenumber for the as received copper acetate was 949 cm<sup>-1</sup>, but was 938 cm<sup>-1</sup> for all the other copper acetates examined. This strongly matches the bi-dentate and pseudo-bridging acetate modes respectively. Such findings were also reported by Kondrat<sup>(1)</sup>, with these results suggesting that this change in co-ordination mode may be attributed to the incorporation of OH<sup>-</sup> anions into the structure.

XRD analysis of the SAS prepared materials was also carried out ([Figure 3.3.](#)) and compared against the starting acetate materials and the precipitate retained from the metal acetate solution ([Figure S3.](#)). It is clear that all the SAS prepared materials are amorphous regardless of the water content used, whilst in contrast the as received acetates are highly crystalline. The SAS synthesis parameters

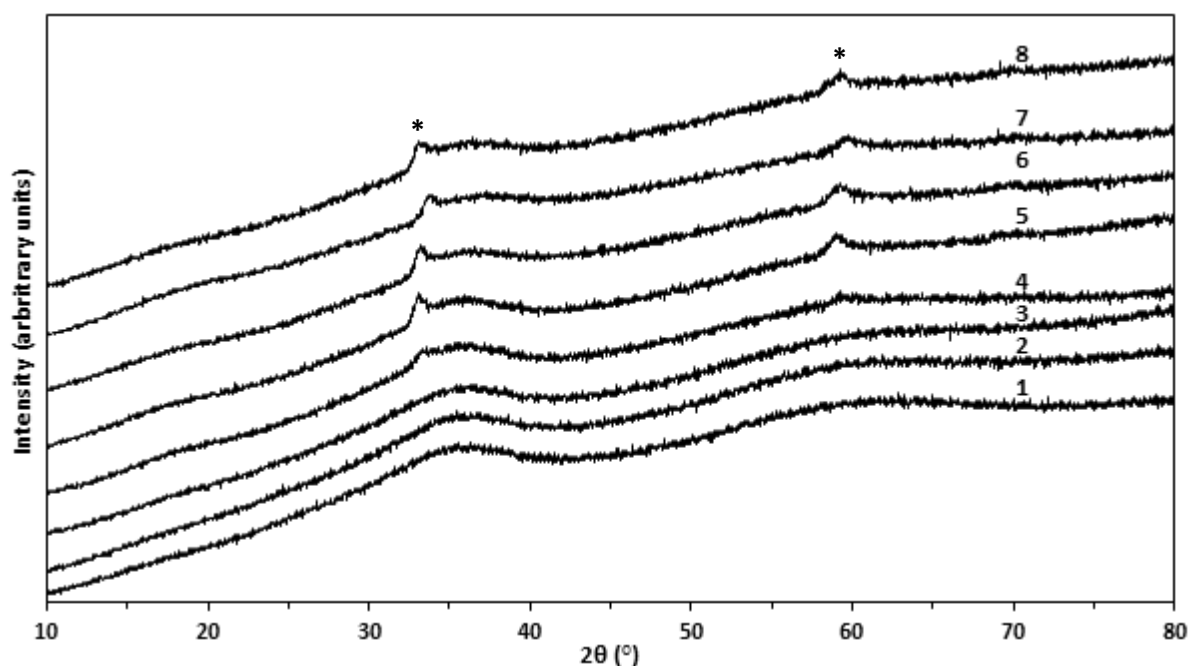


**Figure 3.3.** XRD patterns of the SAS prepared materials formed using various solvent mixtures: (1) 0 vol.% H<sub>2</sub>O/EtOH (2) 0.5 vol.% H<sub>2</sub>O/EtOH (3) 1 vol.% H<sub>2</sub>O/EtOH (4) 5 vol.% H<sub>2</sub>O/EtOH (5) 10 vol.% H<sub>2</sub>O/EtOH (6) 15 vol.% H<sub>2</sub>O/EtOH (7) 20 vol.% H<sub>2</sub>O/EtOH (8) 30 vol.% H<sub>2</sub>O/EtOH. \* Reflections (33.1 and 59.1 °) associated with acetate precipitate obtained from the starting metal acetate solution.

used would be expected to generate amorphous precipitates as a result of achieving significantly high levels of super-saturation, leading to greater nucleation to growth ratios and subsequently preventing crystal growth. However, georgeite is an amorphous mineral and so this XRD pattern would be expected for this phase regardless. It can also be seen though that two reflections at 33.1 and 59.1 ° are present from using water contents  $\geq 5\%$ . The XRD pattern of the precipitate retained from the metal acetate solution displays far fewer reflections in comparison to the starting materials, but the two most intense reflections also lie at 33.1 and 59.1 °. This concludes that this acetate is being incorporated into the resulting SAS precipitates.

The effect of water content on the chemical composition of the SAS prepared precipitates was examined using EDX analysis ([Table 3.1.](#)). A clear trend is apparent which essentially divides the materials into three groups. Without water addition, the nominal Cu/Zn molar ratio of 2/1 is not achieved and a higher zinc content is apparent giving a 1.4/1 ratio. This can be attributed to the high degree of solubility of the copper acetate phase in the EtOH/scCO<sub>2</sub> phase, meaning that complete precipitation of the metal does not occur. The aqueous ions present in solution fail to fully precipitate out and/or the resulting precipitate is leached of copper over time during the synthesis. However, addition of just 0.5% water to the system achieves the desired Cu/Zn molar ratio and this was apparent with water contents up to 15%. When no water is added to the starting solution, it can only come from the hydrated metal acetate salts used, which in total is 0.0197 moles. Addition of

**Table 3.1.** EDX analysis of the SAS prepared materials formed using various solvent mixtures.

Water content (%)	Atomic (%) <sup>a</sup>		Determined Cu/Zn molar ratio
	Cu	Zn	
0	58	42	1.4/1
0.5	67	33	2/1
1	67	33	2/1
5	67	33	2/1
10	67	33	2/1
15	68	32	2.1/1
20	71	29	2.4/1
30	75	25	3.1/1

<sup>a</sup> Standard deviation  $\pm 1$  atomic%.

0.5% water adds a further 0.1388 moles, giving a total of 0.1585 moles of water to 8.52 moles of EtOH, the minimum ratio required to achieve full metal precipitation. It suggests that the copper species present in the SAS system is less soluble in a H<sub>2</sub>O/EtOH/scCO<sub>2</sub> phase, so that the addition of water facilitates complete metal precipitation. As the water content is increased above 15%, the Cu/Zn ratio increases above 2/1 and interestingly the relationship between water content and the Cu/Zn molar ratio becomes linear. Since water is not very miscible in scCO<sub>2</sub> it would be expected that such large water contents would result in the breakdown of the homogeneous H<sub>2</sub>O/EtOH/scCO<sub>2</sub> phase present in the SAS system, with a simultaneous reduction in the anti-solvating power of scCO<sub>2</sub>. Consequently, it would be expected that incomplete precipitation of both copper and zinc would occur as opposed to just leaching of zinc.

In order to verify the conclusions drawn from the EDX findings as well as to determine absolute yields, the effluents produced downstream where the system is depressurised were collected for each precipitate and analysed for Cu and Zn concentrations down to ppm levels using MP-AES analysis (Table 3.2.). It is clear that these findings are in agreement with the EDX results. With no additional water added, the copper yield determined was only 79% but was 99% for zinc. This concludes that the reduced Cu/Zn molar ratio for this precipitate is primarily attributed to incomplete copper precipitation. In order to overcome this, the anti-solvent strength of the scCO<sub>2</sub> needs to be enhanced by increasing the pressure of the system. However, the precipitates which achieved the correct Cu/Zn molar ratio had overall yields of 100%, showing that total metal precipitation did occur. This illustrates the practicality of this process from a green perspective. For water contents above 15%, the yield decreases again and this is more apparent for zinc. With 30% water content the overall yield drastically drops below 70%. Since significant levels of both metals is present in the effluent, this further clarifies that a reduction in the scCO<sub>2</sub> anti-solvating power is associated with using these higher water contents.

**Table 3.2.** MP-AES analysis of SAS effluents obtained from using various solvent mixtures to determine yields.

Water content (%)	Effluent concentration (mg/L)		Yield (%) <sup>c</sup>		
	Cu <sup>a</sup>	Zn <sup>b</sup>	Cu	Zn	Total
0	264	8	79	99	89
0.5	0	0.1	100	100	100
1	0	0.2	100	100	100
5	0	0.3	100	100	100
10	0	0.5	100	100	100
20	16	68	99	89	94
30	128	332	90	48	69

Calibration standards prepared using ethanol as solvent.

<sup>a</sup> Standard deviation  $\pm 0.04$  mg/L.

<sup>b</sup> Standard deviation  $\pm 0.08$  mg/L.

<sup>c</sup> Yields calculated assuming initial copper and zinc concentrations were 1275 and 635 mg/L respectively based on metal acetate concentrations used.

The thermal behaviour of the precipitates was studied by TGA/DTA in order to trial the applicability of each one as a suitable precursor to the industrial catalyst (**Figure 3.4.**). TGA/DTA studies have already been carried out by Hutchings and co-workers on the as received copper acetate<sup>(12)</sup>. The thermal decomposition of metal acetates is complex and also highly exothermic. A phenomenon known as ‘auto-reduction’ occurs as the acetate ligand decomposes producing CO. Easily reducible elements like copper reduce down to the metallic state, and in a supply of oxygen can then gradually re-oxidise with temperature. However, this process is not expected for less reducible elements like zinc whereby metal oxides are consistently formed. The ‘auto-reduction’ process was examined on the precipitates prepared using 0-1% water to determine how the behaviour changed with increasing amounts of the georgeite phase present. Since copper acetate decomposition is dependent on the sample mass<sup>(1)</sup>, attempts were made to keep it constant. The mass loss for each sample was recorded after total acetate decomposition and after the observed mass gain (**Table 3.3.**). It is clear in comparison to the zincian georgeite TGA profile that the acetate decomposition dominates the thermal behaviour of precipitates using 0.5-1% water. The mass gain from ‘auto-reduction’ increased as the amount of the acetate phase in the precipitate increased. Interestingly, the final mass loss is reduced by 5% when 0.5-1% water is used, and this is attributed to the higher content of the georgeite phase present in these samples. Moreover, whilst analysis of the DTA profiles shows these materials to be exothermic, the profile of the precipitate using 0% water was moderately different in terms of the temperature of the exothermic steps as well as their relative intensities. The initial exothermic peak shifts from 222 to 234 °C when the water content increases from 0% to 1%, suggesting an enhanced thermal stability from increasing georgeite content. With water contents  $\geq 5\%$ , the TGA profile is characteristic of zincian georgeite, which will be discussed in

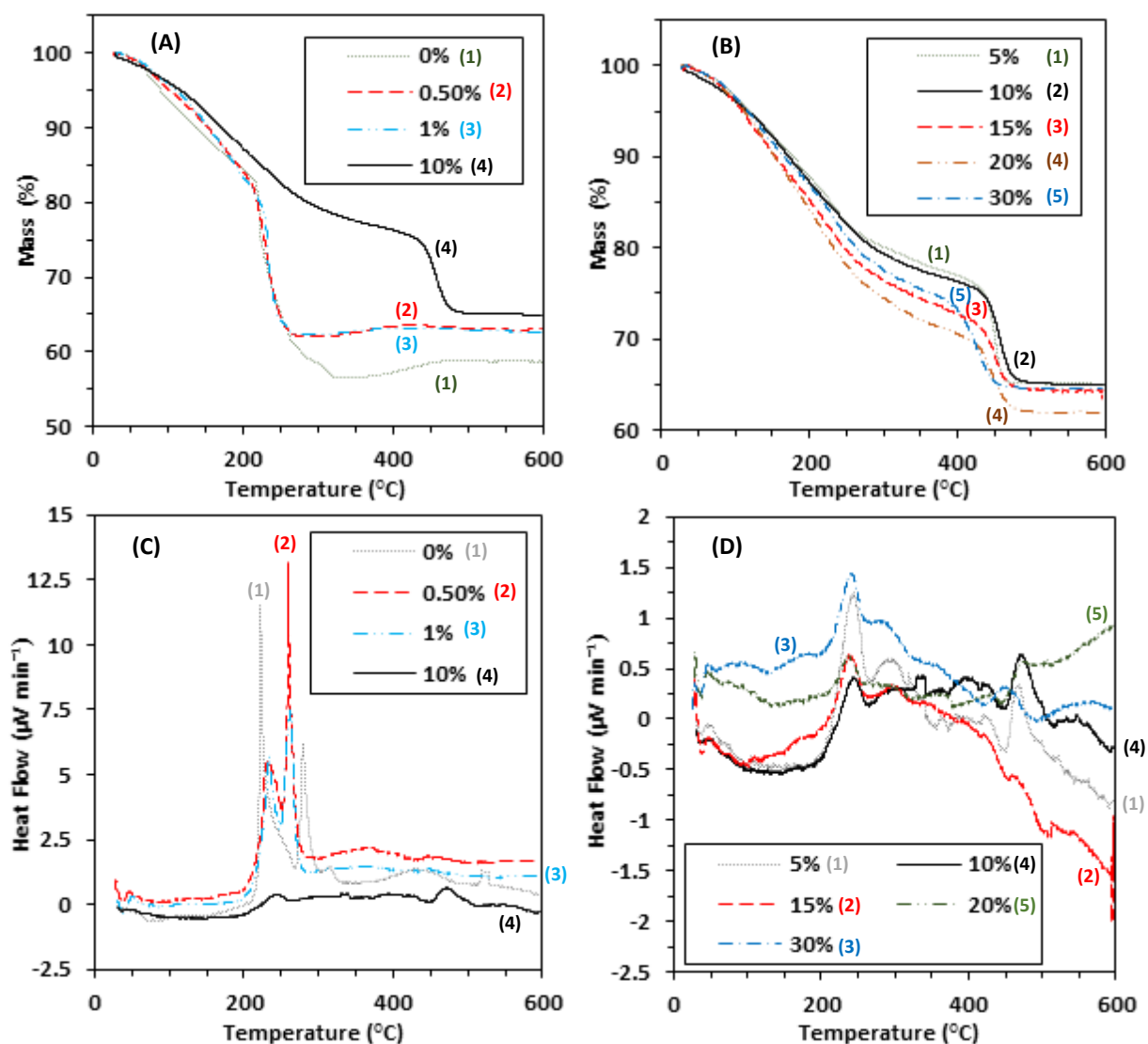


**Figure 3.4.** TGA/DTA of the SAS prepared materials formed using various solvent mixtures, with water contents indicated in legends above: (A) TGA of materials prepared using 0-1 vol.% H<sub>2</sub>O/EtOH mixtures, with 10 vol.% H<sub>2</sub>O/EtOH included for clarity (B) TGA of materials prepared using 5-30 vol.% H<sub>2</sub>O/EtOH mixtures (C) DTA of materials prepared using 0-1 vol.% H<sub>2</sub>O/EtOH mixtures, with 10 vol.% H<sub>2</sub>O/EtOH included for clarity (D) DTA of materials prepared using 5-30 vol.% H<sub>2</sub>O/EtOH mixtures. Numbered keys are also provided for clarity.

**Table 3.3.** Effect of water content (0-1%) on observed TGA mass losses.

Water content (%)	Sample mass (mg)	Mass loss from decomposition (%)	Final mass loss (%)	Mass gain (%)
0	11.9	43.5	41.1	2.4
0.5	13.5	38	36.4	1.6
1	11.6	37.7	36.8	0.9

greater detail in **Chapter Four**. In brief, the thermal decomposition process occurs in several steps with loss of hydroxyl and low temperature carbonate groups occurring up to 300 °C, whilst loss of the high temperature carbonate (HT-CO<sub>3</sub>) species is clearly seen at temperatures > 420 °C. All of these materials give a final mass loss of 33-36%, leaving 13-15% residual mass after reaching 300 °C. The acetate precipitates in comparison have no residual mass after 300 °C. Interestingly, the temperature of the HT-CO<sub>3</sub> decomposition shifts to lower temperature as the water content is increased from 20 to 30%. This species begins to decompose at 400 °C using 30% water, but remains stable up to 430 °C for water contents 5-20%. The temperature of the HT-CO<sub>3</sub> mass loss increases as the thermal stability of the material increases. The reduction observed in the 30% material is attributed to a breakdown of the homogenous phase present in the SAS system during precipitation. This produces precipitates with poor mixing between the metals and hence Cu and Zn phase segregation. Comparison of the DTA profiles shows all the zincian georgeite materials to be essentially thermo-neutral, although a weak exothermic peak is seen at 245 °C. Even for the 5% material which is expected to have the highest acetate content of these materials, no intense peaks were observed.

XRD analysis was carried out on the SAS prepared materials after calcination to examine the structural changes. All materials were calcined using the standard set of conditions: 300 °C using a ramp rate of 10 °C/min and held for 2 hours in static air. Whilst all the precursors were amorphous (**Figure 3.3.**) the precipitates with water contents 0-1% displayed strong crystallinity after calcination

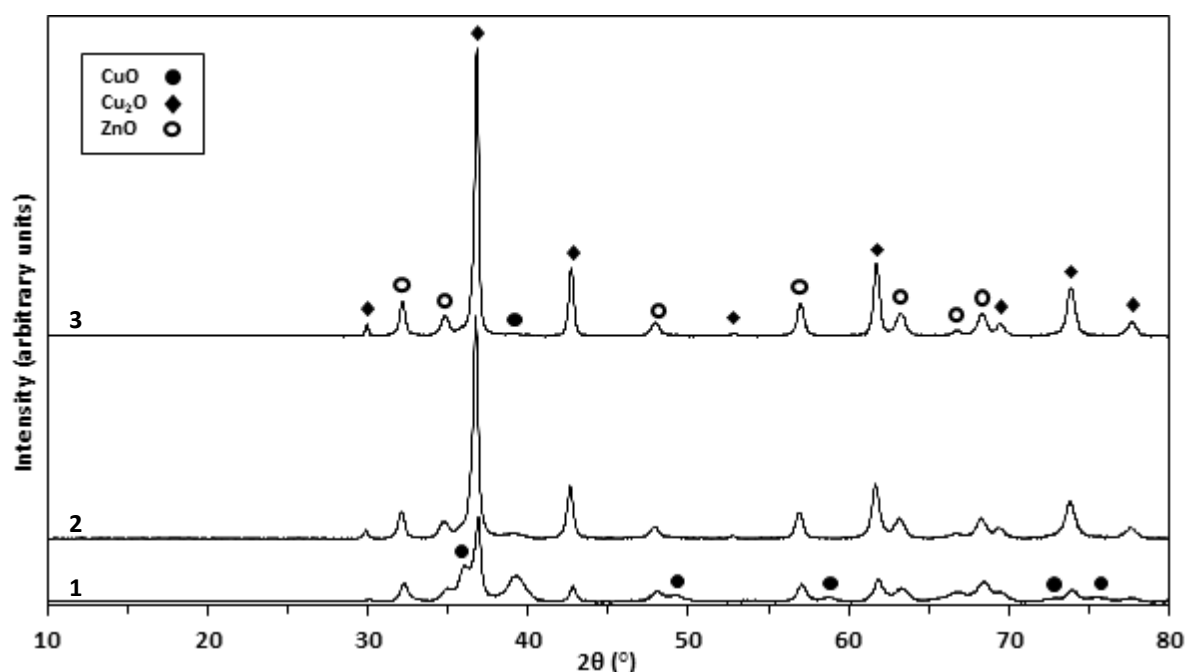


**Figure 3.5.** XRD patterns of calcined materials which were prepared by SAS precipitation using different water contents as indicated: (1) 1 vol.% H<sub>2</sub>O/EtOH (2) 0.5 vol.% H<sub>2</sub>O/EtOH (3) 0 vol.% H<sub>2</sub>O/EtOH.

**Table 3.4.** XRD crystallite sizes and semi-quantitative analysis of Cu<sub>2</sub>O, CuO and ZnO phases after calcination of SAS prepared materials formed using 0-1 vol.% H<sub>2</sub>O/EtOH mixtures.

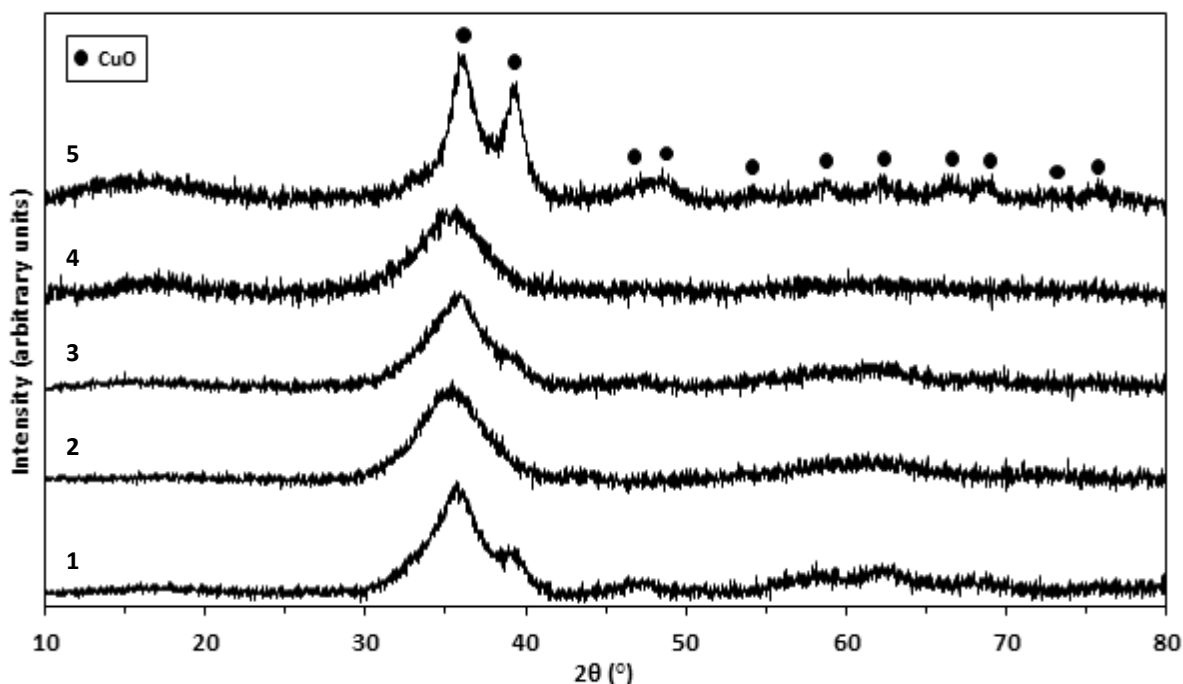
Water content (%)	Crystallite size (nm)			Relative intensity ratio (%)		
	Cu <sub>2</sub> O <sup>a</sup>	CuO <sup>b</sup>	ZnO <sup>c</sup>	Cu <sub>2</sub> O	CuO	ZnO
0	26.6	6.5	14.4	77	10	13
0.5	19	-	11.9	70	12	17
1	19.5	-	10.9	35	37	28

<sup>a</sup> Determined using the (200) Cu<sub>2</sub>O reflection.

<sup>b</sup> Determined using the (111) CuO reflection.

<sup>c</sup> Determined using the (110) ZnO reflection.

(Figure 3.5.). The reflections sharpened and increased in intensity as the water content decreased, which is indicative of an increase in crystallite size and hence reduction in surface area. Crystallite sizes were measured using the Scherrer equation, with semi-quantitative phase analysis also determined (Table 3.4.). It is clear that the Cu<sup>+</sup>/Cu<sup>2+</sup> ratio increases as the water content decreases as a result of enhanced 'auto-reduction'. Interestingly, no metallic copper reflections were identified suggesting that the copper in the samples had not been fully reduced, or most likely that the labile metallic copper metal produced had re-oxidised during the thermal process. In either case, it is apparent that the Cu<sub>2</sub>O crystals were stabilized with subsequent re-oxidation to CuO not occurring. The Cu<sub>2</sub>O crystallite size is dependent on the water content, with sizes ranging between 19 to 27 nm. Interestingly, ZnO crystallite sizes were always smaller indicating that it is thermally more stable and less prone to sintering.

**Figure 3.6.** XRD patterns of calcined materials which were prepared by SAS precipitation using different solvent mixtures: (1) 5 vol.% H<sub>2</sub>O/EtOH (2) 10 vol.% H<sub>2</sub>O/EtOH (3) 15 vol.% H<sub>2</sub>O/EtOH (4) 20 vol.% H<sub>2</sub>O/EtOH (5) 30 vol.% H<sub>2</sub>O/EtOH.

In clear contrast, the XRD patterns of the precipitates which used water contents of 5-30% remained largely amorphous after thermal treatment (**Figure 3.6.**). The highest degree of crystallinity was obtained from using 30% water content, but even in this case only the CuO (111) and (-111) reflections were distinct, with all other peaks still largely broad and ill-defined. Interestingly, phase analysis did not identify the ZnO phase present, suggesting the crystallite sizes were smaller just like for the low water content samples. However, overlap of the most intense (101) reflection with the CuO (-111) reflection cannot be ruled out. The sample using 5% water content was the only other material to display a low degree of crystallinity, but reflections were broader in comparison to the 30% material.

To further examine the thermal decomposition process, surface areas of all SAS prepared materials were measured before and after calcination using the BET method (**Table 3.5.**). Prior to calcination, the samples prepared using 0.5-1% water contents produced the highest BET surface areas in the range 152-162 m<sup>2</sup> g<sup>-1</sup>. Unfortunately, successful analysis could not be performed on the material prepared using 0% water, whereby it is possible that the assumptions for the theory broke down on this particular surface (**Section 2.4.9.**). With higher water contents between 5-20%, the BET surface area almost decreased up to 50%, ranging from 87-104 m<sup>2</sup> g<sup>-1</sup>. Taking all the errors of the analysis into account, it is clear that the BET surface area significantly decreases between 1-5% water content but then remains relatively constant up to 20% water content. This surface area trend is in agreement with the work carried out by Hutchings and co-workers, albeit they reported that no precipitate was obtained using water contents  $\geq 15\%$ <sup>(2)</sup>. The reduction in BET surface area with water content was attributed to the reduced miscibility of scCO<sub>2</sub> in water. Evidently this trend continues with water contents up to 30%, whereby this precursor had the lowest BET surface area of 65 m<sup>2</sup> g<sup>-1</sup>.

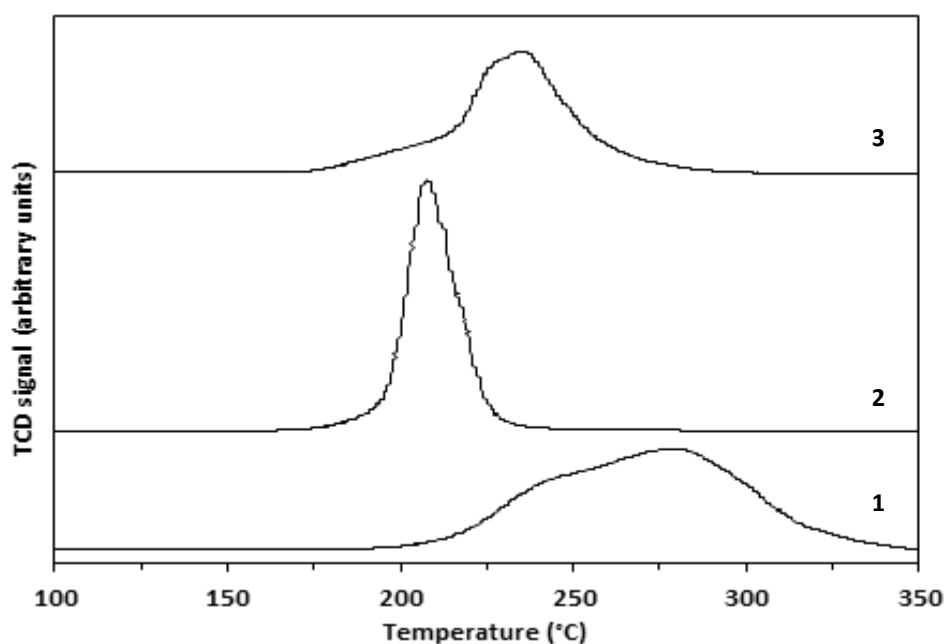
The BET surface area trend for the calcined materials is in strong agreement with the DTA and XRD findings (**Figure 3.4(C).** and **Figure 3.6.**). The highly exothermic decomposition of the acetate materials (0-1% water) resulted in highly crystalline materials, with large crystallite sizes and hence low BET surface areas. Using  $\geq 5\%$  water content in the SAS preparation allows the behaviour of the thermal decomposition process to be dictated by the zincian georgeite phase, which is almost thermo-neutral and remains largely amorphous. Consequently, the BET surface areas after calcination only reduce slightly, although interestingly with 10% water content the observed decrease was within the standard deviation error range. This indicates that the BET surface area almost remains the same after calcination.

**Table 3.5.** BET surface areas of SAS prepared materials formed using various solvent mixtures before and after calcination. C values provided to indicate degree of accuracy for each analysis.

Water content (%)	Precursor surface area		Calcined surface area	
	(m <sup>2</sup> g <sup>-1</sup> ) <sup>a</sup>	C value	(m <sup>2</sup> g <sup>-1</sup> ) <sup>a</sup>	C value
0	-	-	19	443
0.5	162	30	20	104
1	152	29	27	281
5	87	65	67	367
10	97	79	85	89
15	99	85	76	368
20	104	129	77	298
30	65	75	48	472

<sup>a</sup> Standard deviation  $\pm 6$  m<sup>2</sup> g<sup>-1</sup>.

The TPR profiles of the calcined samples prepared using 1 and 10% water content were recorded and compared against a CuO reference in order to decipher differences in the ‘catalyst activation’ process from acetate and georgeite derived materials (**Figure 3.7.**). From using 10% water, a single symmetric peak centred at 208 °C was obtained which is attributed to rapid reduction of CuO to Cu<sup>0</sup>. Reduction of the acetate derived sample is more complex, displaying a shoulder between 179-215 °C and two overlapping peaks centred at 227 and 237 °C. TPR studies by Fierro and co-workers report the ZnO role as promoter in the reduction, with copper oxides in the bulk state reducing at higher temperatures than surface layers directly in contact with ZnO<sup>(13)</sup>. This would justify why significantly higher temperatures are required to reduce the CuO reference. Furthermore a peak could arise from the reduction of Cu<sup>+</sup> to Cu<sup>0</sup>, whereby Cu<sub>2</sub>O is largely present in the calcined acetate sample. This

**Figure 3.7.** TPR of calcined materials prepared from SAS precipitation using various solvent mixtures: (1) as received CuO reference (2) 10 vol.% H<sub>2</sub>O/EtOH (3) 1 vol.% H<sub>2</sub>O/EtOH.

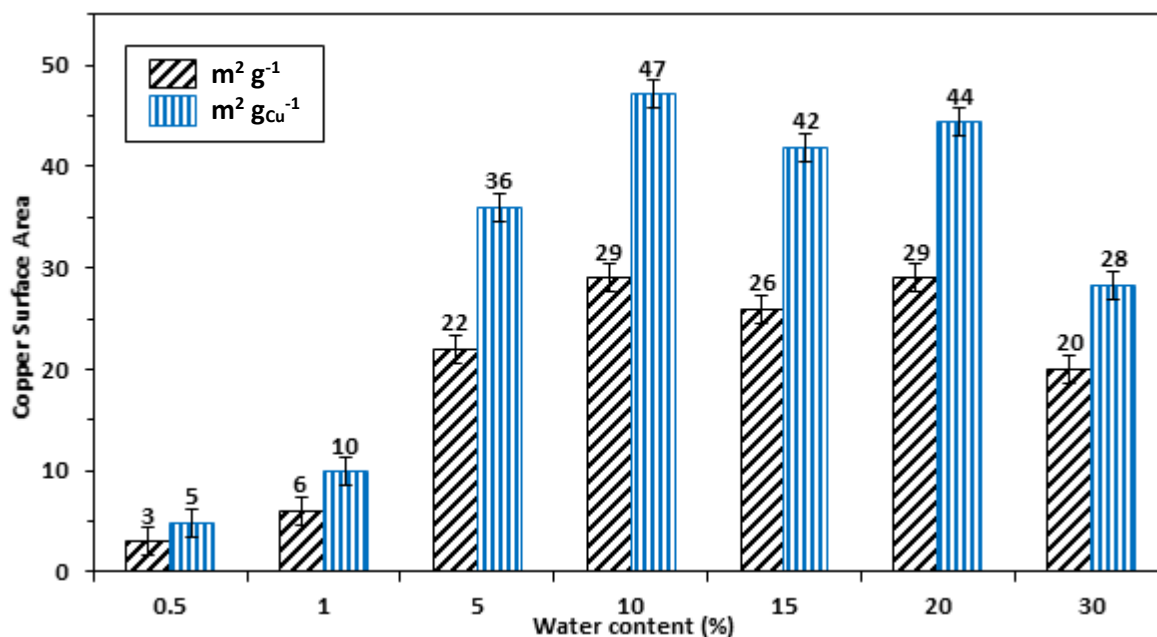


**Figure 3.8.** Copper surface area analysis of Cu/ZnO catalysts prepared from SAS precipitation using various H<sub>2</sub>O/EtOH solvent mixtures, with water vol. contents indicated. Note, catalyst prepared using 0 vol.% not presented (see text). Normalised copper surface areas calculated using EDX findings and assuming only Cu and ZnO phases present prior to analysis.

could explain the multiple number of peaks present for this material, which overall requires a higher reduction temperature because of the presence of segregated copper oxide and zinc oxide phases.

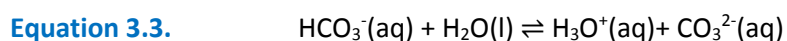
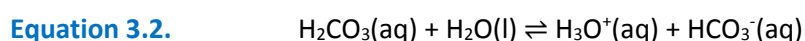
The copper surface areas of the final state catalysts after reduction were recorded for catalyst screening (**Figure 3.8.**). Since the EDX findings determined that the Cu/Zn molar ratio was not consistent for all the samples, copper surface areas normalised by copper content are also provided. It is clear that the acetate derived catalysts display the lowest copper surface areas. It decreases as the acetate/georgeite phase ratio increases. This is indicative of the catalyst derived using 0% water whose precursor contained the highest amount of acetate. This produced the lowest copper surface area, which measured  $< 1 \text{ m}^2 \text{g}^{-1}$  (not shown). These materials display poor dispersion of the metallic copper phase which is attributed to the presence of segregated phases and hence large crystallites.

The change in copper surface area with water content in the range 5-30% does not vary considerably, although was  $\sim 2\text{-}4 \text{ m}^2 \text{g}^{-1}$  higher between 10-20%. This trend is further emphasised in the observed normalised copper surface areas. This indicates that the metallic copper phase is utilised most effectively in these catalysts. The high level of mixing between the Cu and ZnO phases facilitates and stabilises the formation, dispersion and dilution of optimum nanoscale Cu<sup>0</sup> crystals.

### 3.2.2. Conclusions from water content optimization

The specific volume of water used in relation to ethanol has significant implications on the physical, chemical and structural properties of SAS prepared precipitates, and hence is a powerful synthetic

parameter in the preparation of georgeite precursors. Whilst a precipitation phenomenon is occurring, it is fundamentally important to also appreciate the *in-situ* reaction taking place which is essential for hydroxycarbonate formation. As already described by Kondrat the addition of water leads to formation of the georgeite phase through an ‘anionic ligand exchange’ reaction<sup>(1)</sup>. **Equations 3.1.-3.3.** illustrate the generation of carbonate anions, which then displace the acetate ligands to form the thermodynamically favoured hydroxycarbonate.



According to le Chatelier’s principle, an increase in water will shift the equilibrium for each step to the right and favour georgeite formation. Unfortunately, the SAS system is limited by the reduced miscibility of scCO<sub>2</sub> in H<sub>2</sub>O/EtOH mixtures with increasing water content. It is therefore clear the optimum water content (5-15 vol.%) reflects a compromise between the acetate/georgeite ratio in the resulting precipitate and the degree of miscibility between scCO<sub>2</sub> and the resulting metal solution. Negligible water contents (0-1%) produce well mixed hydroxyacetates, with BET surface areas > 150 m<sup>2</sup> g<sup>-1</sup>, as a result of the solution and anti-solvent being highly miscible. The surface tension disappears before jet break-up of the metal solution resulting in gas-like mixing during particle nucleation and growth<sup>(14)</sup>. However, the undesired thermal behaviour of the acetates makes them unfavourable candidates as catalysts precursors. For high water contents (20-30%) the reduced miscibility with scCO<sub>2</sub> is expected to result in a breakdown of the single, homogeneous phase present in the SAS system required for optimum nanoparticulate formation. It is clear further studies are required to examine the changes in phase behaviour for this particular system with water content. Direct observation using a glass window would be an effective methodology. However, it is speculated that a scCO<sub>2</sub> rich phase and a H<sub>2</sub>O rich phase would be present at high water contents with the degree of mixing primarily limited by the surface tension. Nucleation and growth would be expected to facilitate at the contact point of the phases, with scCO<sub>2</sub> slowly diffusing into the H<sub>2</sub>O rich phase, resulting in expansion and further nucleation and growth. With increasing water content, the surface tension increases which would reduce the mole fraction of scCO<sub>2</sub> present in the H<sub>2</sub>O rich phase. This results in a lower degree of expansion of the resulting phase and a reduction in the level of super-saturation produced. Consequently, the smaller nucleation to growth ratios form larger particulates and inferior Cu-Zn mixing. This is reflected in the sample prepared using 30% water which crystallised after calcination as a result of poor mixing between Cu and Zn in the precursor.

The Zn ppm level in the resulting effluents also increased with water content. With the solubility of zinc acetate considerably higher in water than copper acetate, this indicates that there is a subsequent reduction in the ability of scCO<sub>2</sub> to act as an anti-solvent with increasing water content.

### 3.3. Optimization of the binary Cu/Zn molar ratio of SAS prepared zincian georgeite

In **Section 1.3.1.** it was explained that the Cu/Zn molar ratio dictates the type of phase or phase mixture produced during the preparation of crystalline hydroxycarbonates from the industrial co-precipitation route. Studies have shown that a molar ratio close to 2/1 leads to the formation of the optimum monophasic zincian malachite precursor. This arises from a combination of nano- and meso-structuring effects<sup>(15)</sup>.

It is clear that examining changes to the zincian georgeite phase from varying the Cu/Zn molar ratio could result in further optimization of the precursor. Identification of additional phases from using Cu-rich or Zn-rich compositions would also enable a better understanding of the SAS system, as well as to expand on the potential applications of the synthetic process. Copper acetate and zinc acetate salts were dissolved in ethanol containing 5 or 10% water by volume, to give nominal Cu/Zn molar ratios of 4/1, 3/1 and 1/1, whilst keeping the total number of moles of metal constant (0.0149 moles) in 500 ml of total solvent. Precipitates prepared using just copper acetate or zinc acetate were also produced for comparison, with all the findings compared against the 2/1 molar ratio already discussed.

#### 3.3.1. Results and discussion

Initial work primarily focused on identifying phases potentially produced in addition to zincian georgeite. Precipitates prepared using the Cu/Zn molar ratio of 1/1 with 5 or 10% water were compared against the 2/1 molar ratio, as well as the copper only precipitate using a combination of FT-IR, Raman and XRD analytical techniques (**Figure 3.9.**).

When no zinc is included in the SAS procedure, the resulting precipitate is georgeite as reported by Kondrat<sup>(1)</sup>. It is clear the vibrational spectra for georgeite is almost identical to zincian georgeite even when zinc contents up to a 1/1 molar ratio are used. The FT-IR and Raman bands for georgeite were therefore assigned in relation to zincian georgeite (**Table S1.** and **Table S2.**). Subtle differences were, however, identified with the incorporation of zinc shifting certain carbonate peaks to higher wavenumbers. For instance, the  $\nu_2$  mode in the FT-IR spectra shifted from 831 to 835 cm<sup>-1</sup> whilst the  $\nu_1$  symmetric stretch in the Raman spectra shifted from 1086 to 1091 cm<sup>-1</sup> as the Zn content

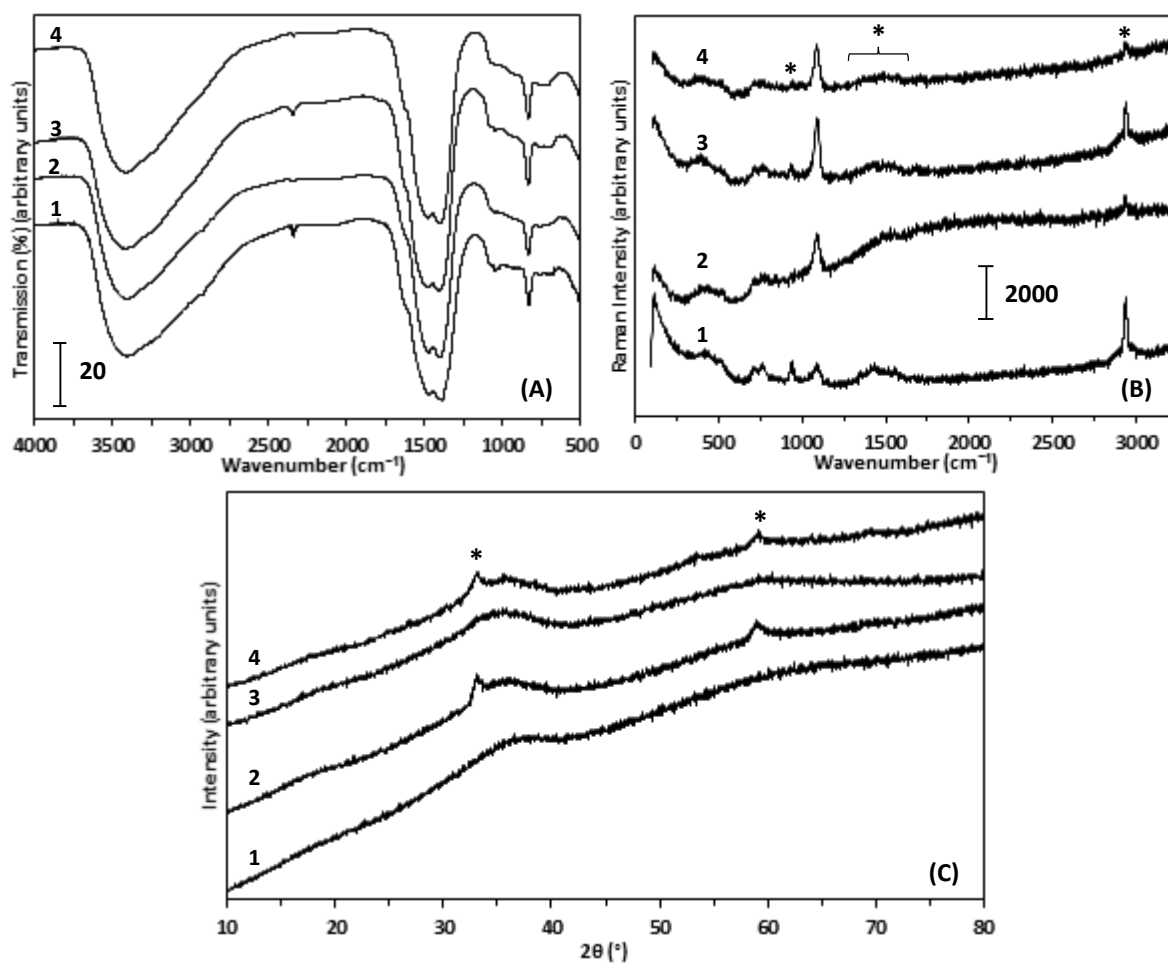
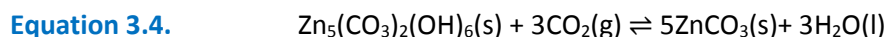


**Figure 3.9.** (A) FT-IR spectra (B) Raman spectra and (C) XRD patterns for the SAS prepared materials formed using different Cu/Zn molar ratios and water contents: (1) 100% Cu (5 vol.% H<sub>2</sub>O) (2) 2/1 (10 vol.% H<sub>2</sub>O) (3) 1/1 (5 vol.% H<sub>2</sub>O) (4) 1/1 (10 vol.% H<sub>2</sub>O). \* Peaks/reflections associated with acetate phase.

increased from 0 to 33 at.%. The shift to higher wavenumbers with zinc addition is attributed to an increase in strength of the carbonate bonds. Interestingly, no further peak shifts were observed as the Cu/Zn molar ratio was reduced further from 2/1 to 1/1. Moreover, the absence of additional peaks suggested that no additional phases were produced, with the exception of the acetate phase as indicated for clarity. This was supported by the XRD findings which did not identify any additional crystalline phases.

In order to examine this further, the precipitate prepared from the SAS procedure using zinc acetate in 10% water was analysed in order to identify the phase produced when no copper was present. It should be noted that Kondrat identified smithsonite (ZnCO<sub>3</sub>) as an additional phase produced from SAS precipitation when more vigorous conditions (60 °C, 150 bar) were used, in attempts to ‘age’ zincian georgeite into zincian malachite<sup>(1)</sup>. The aurichalcite phase, which is structurally related to hydrozincite, also begins to form as the Cu/Zn ratio is reduced below 2/1 in the co-precipitation procedure. However, aurichalcite and hydrozincite phases are not produced in the SAS process as

explained from the high partial pressure of scCO<sub>2</sub> utilised. As expressed in **Equation 3.4.**, the CO<sub>2</sub> partial pressure controls the formation of these Zn phases, as reported by Frost and co-workers<sup>(16-18)</sup>.



At CO<sub>2</sub> partial pressures above 10<sup>-1.4</sup>, the equilibrium shifts to the right and smithsonite is formed in favour of hydrozincite. With this taken into consideration, the zinc precipitate prepared from the conditions used by Kondrat and an as received basic zinc carbonate material suspected to be hydrozincite were also used as reference materials. Raman analysis carried out on these three materials proved to be difficult as a result of fluorescence, however, the SAS precipitate formed under standard conditions produced a peak at 1101 cm<sup>-1</sup>, whilst the as received material provided a peak at 1065 cm<sup>-1</sup> (**Figure S4.**). The peak position for the SAS precipitate did not shift from using the more vigorous conditions. A direct comparison could be made with the Raman analysis carried out by Frost and co-workers, whereby intense peaks at 1092 and 1062 cm<sup>-1</sup> were determined for synthetic smithsonite and hydrozincite, respectively<sup>(17-18)</sup>.

Identification of the exact phases present in these materials was determined by XRD analysis, which showed all the materials to be highly crystalline (**Figure S5.**). These findings verified that smithsonite is produced under more vigorous SAS conditions (i.e. at pressures > 110 bar) and reflections were significantly more intense than those present in the other zinc materials. However, residual amounts of an additional phase can clearly be seen, with these reflections clearly matching the phase produced under the standard SAS conditions. Phase analysis was inconclusive in matching an exact phase to this precipitate, although residual amounts of the smithsonite phase could be identified. Moreover, reflections for the hydrozincite phase did not provide a match as was expected. The ICDD database however did provide an additional zinc carbonate phase which was Zn<sub>4</sub>(CO<sub>3</sub>)(OH)<sub>6</sub>·H<sub>2</sub>O. Interestingly, a phase match was obtained, however, multiple peaks were still left unassigned even assuming a phase mixture with smithsonite. For the as received basic zinc carbonate phase, analysis concluded it was hydrozincite which provided broader peaks more ill-defined in comparison to the SAS prepared materials.

In order to investigate the unidentified SAS precipitate further, TGA/DTA was carried out to obtain a decomposition profile and to determine the final mass loss of the material (**Figure S6.**). The analysis was also carried out on the smithsonite and hydrozincite references for comparison and also to verify the XRD findings. The theoretical mass loss for each zinc carbonate phase identified by XRD was calculated (**Table 3.6.**), which could then be compared against the experimental total mass loss for each material. For the precipitate prepared using the intense SAS conditions used by Kondrat,

**Table 3.6.** Zinc carbonate phases identified from ICDD database with TGA theoretical total mass losses.

Phase	Molecular formula	Theoretical total mass loss (%) <sup>a</sup>
Hydrozincite	Zn <sub>5</sub> (CO <sub>3</sub> ) <sub>2</sub> (OH) <sub>6</sub>	25.88
Smithsonite	ZnCO <sub>3</sub>	35.1
Zinc carbonate hydroxide hydrate	Zn <sub>4</sub> (CO <sub>3</sub> )(OH) <sub>6</sub> .H <sub>2</sub> O	26.28

<sup>a</sup> Calculated from assumption of final product being ZnO.

the observed total mass loss was 37.8% which closely matches the 35.1% mass loss expected for a pure smithsonite phase. The slightly higher than expected mass loss is attributed to the presence of the residual phase identified from XRD. Interestingly, the TGA profile showed three mass loss steps in total. The final decomposition step begins at 298 °C, which is similar to the findings of Frost and Hales who reported that the thermal decomposition of smithsonite occurs at 293 °C<sup>(18)</sup>. For the SAS precipitate prepared under standard conditions, the total mass loss was 43.9% which confirmed that it was none of the identified zinc carbonate phases. The TGA profile is similar to the SAS smithsonite material, whereby three mass loss steps are seen occurring. In fact the small final weight loss, which occurs around the same temperature interval of 300 °C, could be attributed to the presence of residual smithsonite. The main decomposition step occurs between 148-245 °C, which accounts for 28% of the mass loss. The TGA results overall are in agreement with the XRD findings, whereby the two SAS prepared precipitates consist of a phase mixture of smithsonite and an unknown phase, with the content of smithsonite increasing as the scCO<sub>2</sub> pressure is increased from 110 to 150 bar. The as received zinc carbonate material in comparison had a final mass loss 27.2% which closely matches the theoretical mass loss of 25.88% for hydrozincite. The TGA profile is identical to the TGA profile reported by Kanari and co-workers for synthetic hydrozincite<sup>(19)</sup>, and hence also validates the Raman and XRD findings.

With a better understanding of the phases produced using copper and/or zinc in the SAS system, attention focused on optimizing the Cu/Zn molar ratio for zincian georgeite. Precursors were prepared with Cu/Zn molar ratios ranging between 4/1 and 1/1, whilst the effect of water content was also examined for the 1/1 molar ratio. EDX analysis was first used to determine if the correct metal ratios were achieved in the resulting precipitates (**Table 3.7.**). For the Cu/Zn molar ratios of 4/1 and 3/1 this was successfully achieved. However for the Cu/Zn molar ratio of 1/1 the determined ratio was slightly lower than expected, even when taking the error of the analysis into account. This can be explained by the increase in zinc content used. As mentioned in **Section 3.2.**, during the preparation of metal acetate solutions with water contents  $\geq 5\%$ , a finely dispersed acetate precipitate is formed. An increase in the amount of zinc acetate in the starting solution resulted in

**Table 3.7.** EDX analysis of SAS prepared zincian georgeite precursors formed using various Cu/Zn molar ratios with 5-10 vol.% H<sub>2</sub>O/EtOH mixtures.

Water content (%)	Theoretical atomic (%)		Determined atomic (%) <sup>a</sup>		Determined Cu/Zn molar ratio
	Cu	Zn	Cu	Zn	
10	80	20	80	20	4/1
10	75	25	74	26	2.9/1
10	50	50	48	52	0.9/1
5	50	50	48	52	0.9/1

Precipitated CuZn acetate obtained from starting metal acetate solution was 62% copper to 38% zinc according to EDX analysis.

<sup>a</sup> Standard deviation  $\pm 1$  at.%.

an increased amount of this acetate precipitate. In fact the precipitate did not form when Cu/Zn molar ratios  $\geq 3/1$ , suggesting it is facilitated by the presence of zinc. EDX analysis was carried out on the precipitate retained from the 1/1 metal acetate solution using 5 vol.% H<sub>2</sub>O. The content of Cu and Zn was determined as 62 and 38 at.%, respectively, thus concluding that a fraction of copper, and to a lesser extent zinc, was being lost before SAS precipitation took place.

To examine if additional metal content was being lost during SAS precipitation from using higher zinc contents, the SAS effluents from the 1/1 metal solutions were collected and analysed for Cu and Zn ppm levels using MP-AES analysis. The zinc concentration was 0 ppm using 5% water and  $\leq 1$  ppm using 10% water, whilst for copper both effluents had a concentration of 0 ppm. This concluded that the SAS process was not responsible for the copper content in the 1/1 precipitates being lower than the nominal amount.

TGA was carried out to study the thermal behaviour of the SAS precipitates with varying Cu/Zn molar ratios (Figure 3.10.). The TGA profiles of all the samples were characteristic of zincian georgeite, with the 2/1 zincian georgeite findings (Figure 3.4.) again presented for comparison. All materials gave a final mass loss of 33-35%, leaving 13-15% residual mass after reaching 300 °C. These findings are in agreement with the vibrational spectroscopy and XRD analysis (Figure 3.9.), which indicate that no additional phases are present other than the amorphous hydroxycarbonate and residual acetate.

The zinc precipitate prepared by SAS using the same conditions had a final mass loss of 43.9% (Figure S6.) and therefore, if residual amounts were present in the 1/1 zincian georgeite samples the TGA final mass losses would have been expected to be higher. Interestingly, a clear trend is also apparent in the TGA findings. The final mass loss step attributed to HT-CO<sub>3</sub> decomposition shifts to higher temperature with increasing Zn content. For the 4/1 sample this decomposition begins at 417 °C, but with increasing zinc content shifts to 436 °C for the 2/1 material. Finally, for the 1/1 material

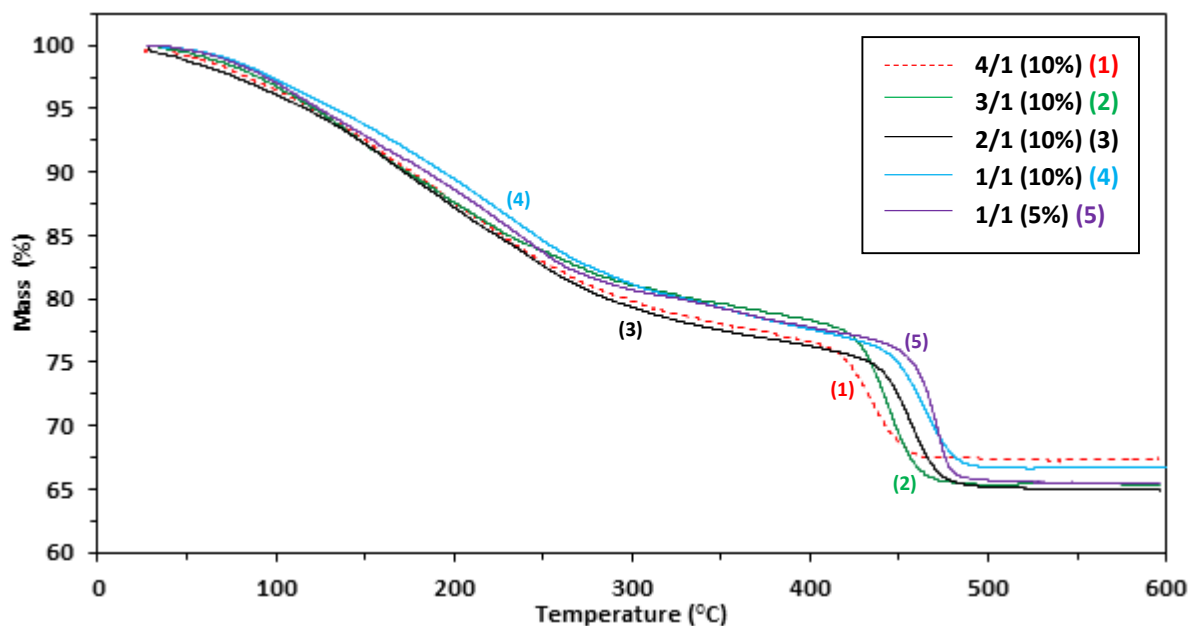


**Figure 3.10.** TGA of SAS prepared zincian georgeite precursors formed using various Cu/Zn molar ratios with 5-10 vol.% H<sub>2</sub>O/EtOH mixtures. A numbered key is also provided for clarity.

this decomposition does not occur until 445 °C, whereby in comparison all of the HT-CO<sub>3</sub> has been removed from the 4/1 zincian georgeite at this temperature. These findings therefore provide evidence that Zn is being incorporated into the georgeite phase and enhances its thermal stability. In other words, with increasing Zn content the decomposition of the hydroxycarbonate is suppressed. Spencer reported similar findings, and attributed the enhanced thermal stability to increased covalent metal-oxygen bonding<sup>(10)</sup>.

The SAS prepared precipitates were calcined and then analysed using XRD to examine the degree of crystallinity produced from the thermal process (**Figure 3.11.**). The precipitates prepared using 1/1 molar ratios remained amorphous after calcination. This was expected from the TGA findings which indicated the retention of HT-CO<sub>3</sub> at this calcination temperature. However, the (111) reflection is weakly visible from using 5% water as was determined for the 2/1 molar ratio. It appears the amorphous nature is retained up to Cu/Zn molar ratios of 3/1. With a 4/1 ratio the strongly defined crystalline peaks emerge, with phase analysis determining that all these reflections were associated with CuO. Therefore, with no ZnO reflections detected it suggests that the ZnO crystallites are smaller than the CuO crystallites.

To examine this further surface areas of the SAS prepared materials before and after calcination was determined using BET analysis (**Table 3.8.**). For a fixed water content of 10%, it is clear that the BET surface areas of the precursors does not drastically vary with the Cu/Zn molar ratio. BET surface areas in the range 102-91 m<sup>2</sup> g<sup>-1</sup> are produced from using all the binary Cu/Zn molar ratios investigated. Whilst it has been shown that subtle changes in the water content can significantly

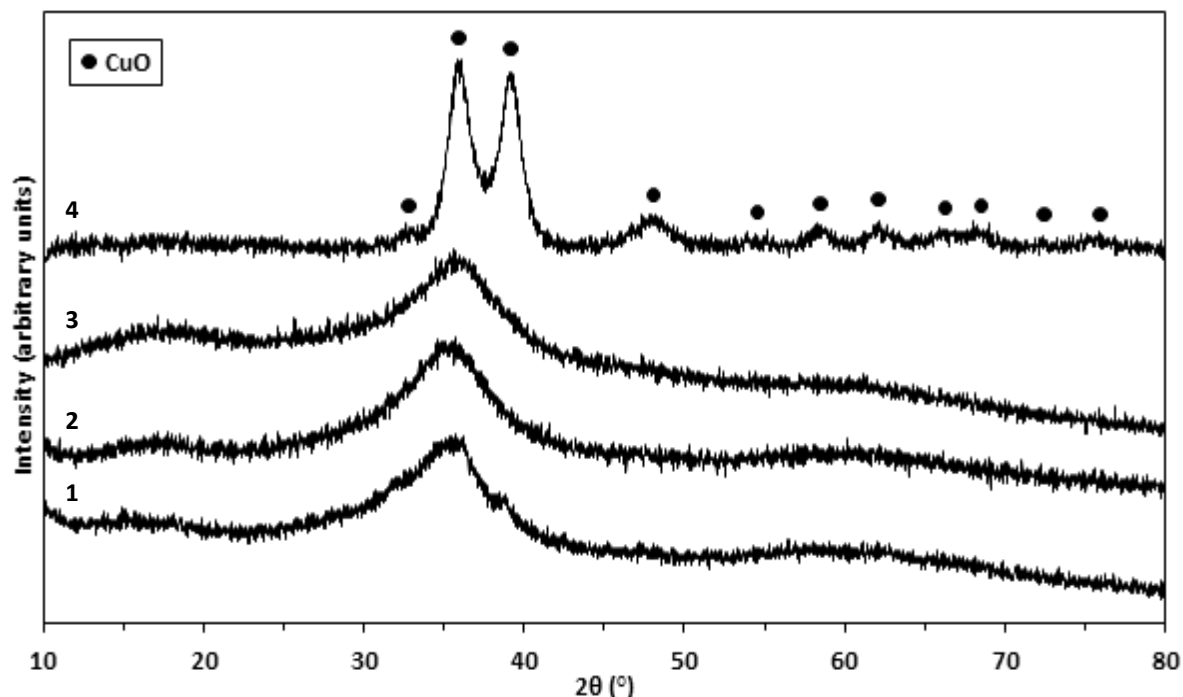


**Figure 3.11.** XRD patterns for the calcined SAS prepared materials formed using different Cu/Zn molar ratios and water contents: (1) 1/1 (5 vol.% H<sub>2</sub>O) (2) 1/1 (10 vol.% H<sub>2</sub>O) (3) 3/1 (10 vol.% H<sub>2</sub>O) (4) 4/1 (10 vol.% H<sub>2</sub>O).

alter the physical properties of the resulting precipitate (**Table 3.5.**), slight alterations in the concentrations of copper and zinc acetate does not have the same influence. Interestingly, from reducing the water content to 5%, the 1/1 precipitate had a slightly lower BET surface area as was determined for the 2/1 precipitate, albeit it is within the error range of the analysis.

After calcination the determined BET surface areas illustrate some interesting results. Surprisingly the surface area appears to increase with an increase in copper content, although these results do not include the findings for the 2/1 zincian georgeite precipitate, which for comparison has a surface area of 85 m<sup>2</sup> g<sup>-1</sup> (**Table 3.5.**). In order to explain these findings it is important to appreciate the following: for high copper contents (Cu/Zn molar ratios of 4/1 or 3/1) the surface area reduced by 26-31 m<sup>2</sup> g<sup>-1</sup>, whilst for low copper contents (Cu/Zn molar ratio of 1/1) the surface area reduced by 38-44 m<sup>2</sup> g<sup>-1</sup>. The TGA findings also determined that the carbonate decomposition was suppressed with increasing zinc content, whilst all materials were calcined the same at 300 °C. Therefore it is clear that a Cu/Zn molar ratio of 1/1 will give a lower BET surface area because it will retain a higher amount of residual material under these calcination conditions. This is concluded from the fact the 1/1 materials appeared dark green after calcination whilst the other samples were black, which indicated that some additional low temperature species had been retained. It is therefore proposed that loss of this residual content is required in order to increase the surface area after calcination, and this is discussed in much greater detail in **Chapter Four**. For high copper contents a higher degree of porosity is expected from a greater loss of carbonate, which will subsequently enhance

**Table 3.8.** BET surface areas of SAS prepared zincian georgeite precursors using various Cu/Zn molar ratios and solvent mixtures before and after calcination. C values provided to indicate degree of accuracy for each analysis.

Water content (%)	Cu/Zn molar ratio	Precursor surface area		Calcined surface area	
		(m <sup>2</sup> g <sup>-1</sup> ) <sup>a</sup>	C value	(m <sup>2</sup> g <sup>-1</sup> ) <sup>a</sup>	C value
10	4/1	102	153	76	100
10	3/1	91	127	60	240
10	1/1	97	36	53	382
5	1/1	85	62	47	832

<sup>a</sup> Standard deviation  $\pm 6$  m<sup>2</sup> g<sup>-1</sup>.

the surface area. However, when low zinc contents are used the thermal stability and degree of copper dispersion is reduced, and therefore copper sintering is more severe as was deduced from the XRD findings (Figure 3.11).

The calcined materials were reduced with the copper surface areas of the resulting catalysts determined and compared against the 2/1 catalyst for catalyst screening (Figure 3.12.). Since the copper content varies between samples, copper surface areas normalised to copper content are again provided. It is clear that the optimum Cu/Zn ratio is 2/1, as it produced the highest copper surface area of 29 m<sup>2</sup> g<sup>-1</sup>. Surprisingly, all the other catalysts had broadly similar copper surface areas and were  $\sim 7$  m<sup>2</sup> g<sup>-1</sup> lower compared to the optimum catalyst. However, this trend drastically changes when the normalised copper surface areas are considered. The 1/1 catalyst made using 10% water provides the highest copper surface area per mass of copper used which is attributed to

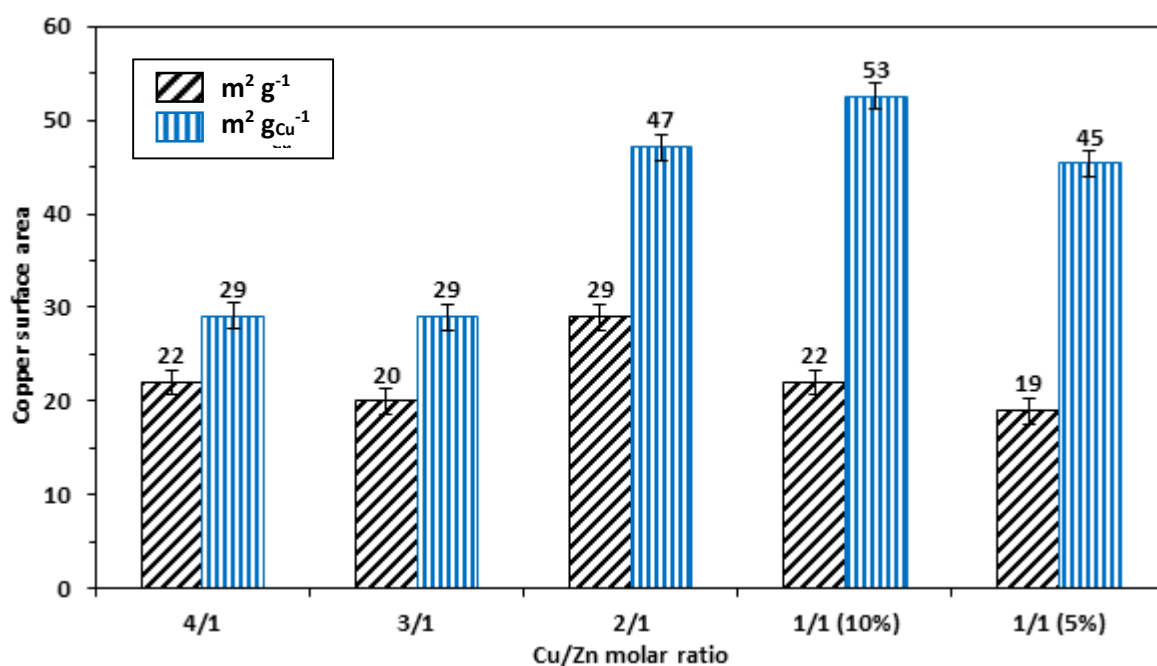


**Figure 3.12.** Copper surface area analysis of Cu/ZnO catalysts prepared from SAS precipitation using various Cu/Zn with 5-10 vol.% H<sub>2</sub>O/EtOH mixtures. Normalised copper surface areas calculated using EDX findings and assuming only Cu and ZnO phases present prior to analysis.

optimum mixing on an atomic level between Cu and ZnO phases. This in turn provides optimum dispersion and dilution of the copper crystallites, which emphasises that it is being utilised most effectively in this catalyst. This is in agreement with Behrens who reported that the optimum Cu/Zn molar ratio is 1/1 from a nano-structuring perspective<sup>(15)</sup>. Interestingly, using 5% water content the normalised copper surface area is  $\sim 8 \text{ m}^2 \text{ g}^{-1}$  lower which was also determined for the 2/1 catalyst (Figure 3.8.), and could be attributed from a higher acetate content in the precursor. For the catalysts with 4/1 and 3/1 ratios it is clear that the reduced copper dispersion is reflected in the normalised copper surface area findings. Copper is being poorly utilised which is highly undesirable for an industrial and a commercial perspective. Taking into consideration the error margin of this technique, as presented with error bars, the copper surface areas are the same for these two catalysts. This was expected since the copper atomic contents are similar.

### 3.3.2. Conclusions from optimization of the Cu/Zn molar ratio

From varying the Cu/Zn molar ratio between zinc atomic contents of 0-50%, it was concluded that this parameter was insignificant in terms of influencing phase formation within this particular SAS system. Whilst the addition of zinc results in a phase change from georgeite to zincian georgeite, no additional phases associated with the SAS process could be identified. This suggests that at least 50 at.% zinc could be incorporated into the georgeite phase, in contrast to just 28 at.% for zincian malachite prepared by conventional co-precipitation<sup>(15)</sup>. For the synthesis methodology of the latter, the zinc content is restricted by the formation of aurichalcite at higher zinc contents, which is highly undesirable from a meso-structuring perspective. Thus the SAS system is highly advantageous as it excludes this meso-structuring limitation which enables zinc contents required for maximum Cu dispersion to be utilised. Moreover, the process allows for the production of a single hydroxycarbonate precursor enabling a simpler and greater understanding, and hence rationalisation, of the catalytic structure-activity relationship implemented.

The zinc content in this range examined also bears little influence on the physical properties of the resulting precipitate. However, since it enhances the thermal stability of the phase, it significantly influences the physicochemical properties of the material in the subsequent thermal processing steps. It seems precursors prepared with a 1/1 molar ratio require temperatures  $> 300 \text{ }^\circ\text{C}$  to remove all residual low temperature hydroxycarbonate material, and this clearly warrants further investigation. This could enable copper surface areas greater than  $29 \text{ m}^2 \text{ g}^{-1}$  to be achieved as determined for the 2/1 ratio. However, whilst copper is indeed utilised most effectively in a 1/1

ratio, a drawback arises from loss of metal content in the starting metal solution, due to the enhanced formation of an acetate precipitate.

### 3.4. Incorporation of aluminium into SAS prepared zincian georgeite

Investigating binary Cu/ZnO systems as model catalysts yields valuable information to assist in the complex understanding of 'real' industrial catalytic materials. Ultimately however, the incorporation of aluminium into the zincian georgeite phase is essential if it is ever going to be considered as an alternative industrial precursor. Subsequent thermal treatment generates the Al<sub>2</sub>O<sub>3</sub> phase. This refractory metal oxide significantly enhances catalyst stability, and hence lifetime, by severely limiting Cu sintering under the harsh industrial reaction conditions implemented<sup>(20-21)</sup>.

One particular challenge regarding the SAS precipitation set-up relates to the limited solubility of aluminium salts in organic solvents required for this process. However, Al acetylacetonate (acac) and Al L-Lactate salts were identified as potential candidates. Furthermore, Johnson Matthey also provided an Al boehmite sol to investigate. The clear difference with the sol is that it does not dissolve in the prepared metal solution and therefore a SAS precipitation phenomenon does not occur. Instead it exists highly suspended in the solution and gets incorporated into the resulting precipitate as precipitation of the copper and zinc species occurs. Attempts were therefore made to incorporate Al into zincian georgeite by SAS precipitation using these Al reagents with the standard Cu/Zn/Al molar ratio of 6/3/1 targeted. In addition, for the Al boehmite reagent, the 3.3/1.7/5 molar ratio was also targeted since higher Al contents are required for the harsh LTS reaction conditions.

Copper acetate (3.56 mg/ml), zinc acetate (1.96 mg/ml) and aluminium salts (0.87-0.96 mg/ml) were dissolved in ethanol containing 10% water by volume to give in this instance a nominal Cu/Zn/Al molar ratio of 6/3/1. When using Al boehmite (0.232 mg/ml) the procedure was similar except 0.25 vol.% of the water was replaced with nitric acid in order to stabilise the dispersed sol.

## 3.4.1. Results and discussion

FT-IR spectroscopy was used to determine phases present in the resulting SAS precipitates, and was compared against the binary 2/1 standard to determine any additional structural changes made to the precursor (**Figure 3.13.**). Furthermore, in order to aid in the interpretation of the spectra FT-IR analysis was also carried out on just the Al reagents before and after SAS precipitation (**Figure S7.**). Since KBr was used in the preparation for FT-IR analysis all spectra display bands centred around 3400 and 1627  $\text{cm}^{-1}$ . This is attributed to physisorbed water<sup>(22)</sup> due to the hygroscopic nature of the compound. It is clear that for all Al reagents examined the georgeite phase has been retained as bands associated with the hydroxycarbonate are present in all the FT-IR spectra. In fact using  $\text{Al}(\text{acac})_3$  resulted in no clear differences in comparison to the binary 2/1 material. However, subtle changes are seen at wavenumbers  $< 600 \text{ cm}^{-1}$  which is associated with vibrations in the metal-oxygen framework. Interestingly, a slight shift in the carbonate peaks to higher wavenumbers is seen with  $\text{Al}(\text{acac})_3$  addition, as was observed with the incorporation of zinc into the phase (**Section 3.3.**). For zincian georgeite the doublet for the  $\nu_3$  stretch lies at 1475 and 1404  $\text{cm}^{-1}$ , with the  $\nu_2$  mode positioned at 835  $\text{cm}^{-1}$ .  $\text{Al}(\text{acac})_3$  addition shifts these peaks to 1476, 1411 and 838  $\text{cm}^{-1}$  respectively, which again implies an increase in the strength of the carbonate bonds. A comparison of the spectra of just  $\text{Al}(\text{acac})_3$  before and after SAS precipitation also indicates that a phase change has taken place as the bands associated with the acac ligand, such as C-H vibrations at 2960-2920  $\text{cm}^{-1}$  and C=O vibrations at 1381-1584  $\text{cm}^{-1}$ , are not retained. Kondrat reported identical findings and assigned the

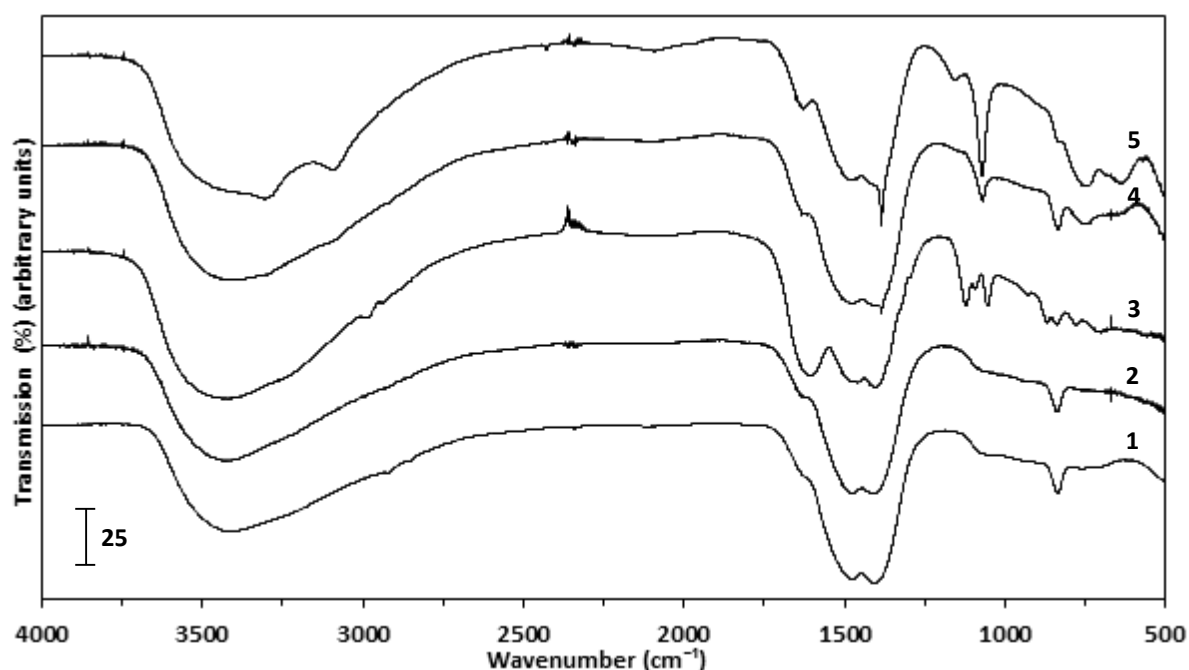


**Figure 3.13.** FT-IR spectra of SAS prepared georgeite precursors formed using various aluminium reagents: (1) binary zincian georgeite standard (2/1) included for clarity (2) aluminium acetylacetonate (6/3/1) (3) aluminium L-lactate (6/3/1) (4) aluminium boehmite (6/3/1) (5) aluminium boehmite (3.3/1.7/5).

bands around 1200-1700  $\text{cm}^{-1}$  and at 833  $\text{cm}^{-1}$  in the resulting precipitate to carbonate ligands<sup>(1)</sup> after comparisons were made to spectra reported by Robinson and Mol<sup>(23)</sup>. However, aluminium carbonates are well known to be unstable compounds and readily decompose to aluminium hydroxides. These findings therefore suggest that after SAS precipitation the resulting aluminium gets incorporated into the georgeite phase which stabilises this species. Alternatively, an aluminium hydroxide phase could independently precipitate out which co-exist with the zincian georgeite phase. This would require the resulting IR peaks to be masked by the zincian georgeite bands.

Additional bands are clearly seen in the georgeite spectra from using Al L-lactate. A comparison of these bands to the as received salt concludes that they are associated with the lactate ligand. This was unexpected and implies that lactate formation is kinetically or thermodynamically favoured to carbonate formation. The spectra of the as-received salt is complex but it is clear that not all bands are present after SAS precipitation, with bands in the range 1320-1250  $\text{cm}^{-1}$  missing, indicating a structural change. The potential overlap of bands for lactate and carbonate made comparisons with the 2/1 standard difficult and no conclusions were drawn regarding changes to carbonate band positions. It is, however, worth mentioning that SAS precipitation of just Al L-lactate did not result in a precipitate which could be collected for analysis. Since it can be determined that aluminium is present in the georgeite precursor from using this reagent, it is clear that SAS precipitation of this reagent results in the formation of nanoparticles, which are either smaller or do not agglomerate. This means that the nanoparticles pass straight through the pores of the frit normally used to collect the precipitate and go straight to vent. With the addition of Cu and Zn to the system the resulting Al nanoparticles must get incorporated or encapsulated into the resulting georgeite precipitate.

The Al boehmite sol reagent also produced additional bands in the georgeite spectra, which increased in intensity as the content was increased. A comparison with the spectra of the as received material before and after SAS precipitation clearly shows that the sol is completely unaffected by the SAS process and that these bands are associated with the Al boehmite phase. This is verified by the findings of Popovic and co-workers who also provide assignment of all bands for the Al boehmite phase<sup>(24)</sup>. In brief, bands for the symmetric and asymmetric O-H stretches are present at 3295 and 3092  $\text{cm}^{-1}$ , respectively, with peaks for  $\delta$  and  $\gamma$  O-H modes also present at 1157, 1068 and 746  $\text{cm}^{-1}$ . Bands at lower wavenumber in the fingerprint region are associated with  $\text{AlO}_6$  stretching modes. Analysis of the georgeite carbonate peaks was again difficult as a result of overlap with boehmite peaks, however no change in wavenumber was observed for bands centred at 1475 and 835  $\text{cm}^{-1}$ . This implies that none of the aluminium sol was incorporated into the georgeite phase and co-exists with the hydroxycarbonate as independent phases.

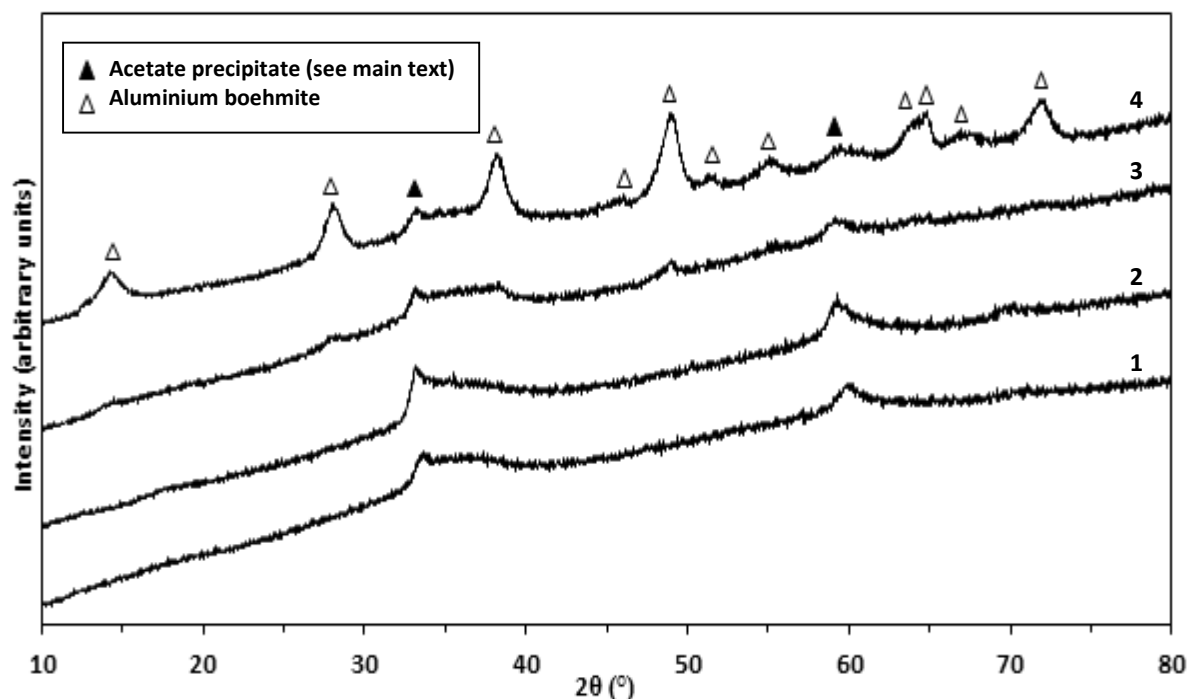


**Figure 3.14.** XRD patterns of SAS prepared georgeite precursors formed using various aluminium reagents: (1) aluminium acetylacetonate (6/3/1) (2) aluminium L-lactate (6/3/1) (3) aluminium boehmite (6/3/1) (4) aluminium boehmite (3.3/1.7/5).

XRD analysis was carried out to investigate the precipitates further as well as the Al reagents before and after SAS precipitation (**Figure 3.14.** and **Figure S8.**). The XRD patterns of the georgeite precipitates were the same as those seen previously for zincian georgeite. The materials were largely amorphous, with only two crystalline reflections present which are associated with the acetate precipitate, which forms in the starting metal solution and gets incorporated into the resulting precipitate. However, for the samples prepared using Al boehmite additional reflections of strong crystallinity are seen, which phase analysis confirmed was the crystal structure for Al boehmite. Johnson Matthey have also confirmed that the crystallite sizes for this phase ranges from 70-90 nm. XRD analysis of both the Al acac and L-lactate reagent salts determined that both were highly crystalline. However, XRD analysis could not be performed on the Al L-lactate salt after SAS precipitation for comparison, as previously discussed for the FT-IR findings (**Figure 3.13.**). For the acac salt the XRD analysis clearly shows that after SAS precipitation the resulting precipitate is completely amorphous, as already demonstrated for the as received copper/zinc acetate salts (**Figure 3.3.**). In contrast, comparison of the XRD patterns of the Al boehmite before and after SAS precipitation further demonstrates that the sol is totally unaffected by the SAS process. The XRD findings overall verify and complement the findings deduced from the FT-IR analysis.

EDX analysis was used to verify the presence of aluminium in all the georgeite precursors, as well as to determine if the desired Cu/Zn/Al molar ratios had been achieved (**Table 3.9.**). It can be seen that

**Table 3.9.** EDX analysis of SAS prepared georgeite precursors formed using various aluminium reagents.

Aluminium reagent	Theoretical Cu/Zn/Al molar ratio	Atomic (%) <sup>a</sup>			Determined Cu/Zn/Al molar ratio
		Cu	Zn	Al	
Boehmite	6/3/1	51	25	24	5.1/2.5/2.4
Boehmite	3.4/1.6/5	22	11	67	2.2/1.1/6.7
Acetylacetonate	6/3/1	53	28	19	5.3/2.8/1.9
L-lactate	6/3/1	57	25	18	5.7/2.5/1.8

<sup>a</sup> Standard deviation  $\pm 3\%$ .

the nominal Cu/Zn/Al molar ratios were not achieved, although these initial results are promising and the experimentally determined ratios are not considerably far from the correct ratios. For the precipitates made from Al boehmite it is clear that the Cu/Zn molar ratio is very close to 2/1.

However, the aluminium atomic content was 14-17% higher than it should have been which suggests that too much of the sol was used in the preparation, and that this component just simply needs fine tuning in order to achieve the correct molar ratio. Interestingly, after taking multiple scans from different particulates of the precipitate, it was found that the error margin for the analysis was slightly higher ( $\pm 3\%$ ) than that determined for the binary materials ( $\pm 1\%$ ). This suggests that the degree of homogenous dispersion of the metal components is reduced in this material. This is attributed to the use of the sol which generates two discrete phases.

For the precipitates prepared using Al salts, it is clear that an excess of aluminium is also present in these samples in the range 8-9%. However, the desired Cu/Zn molar ratio of 2/1 has also not been achieved and therefore this is not just simply a result of using excess Al reagent. For the precipitate prepared using Al acac the zinc atomic content is 28%. This is close to the nominal value of 30%, but there is a clear deficiency in the atomic copper content. Kondrat in very similar studies investigated aluminium incorporation into georgeite using the acac salt and also identified copper deficiency, whereby it was suggested that the acac salt inhibited complete precipitation of the copper phase<sup>(1)</sup>. These findings, however, at least indicate the presence of aluminium in this material which could not be determined from the FT-IR and XRD analysis. The L-lactate salt, in contrast, showed a copper content close to the desired amount but with a slight deficiency in zinc. The findings clearly illustrate that addition of the Al salts to the SAS procedure has significantly affected the precipitation process, whereby incomplete metal precipitation is apparent. Since the two salts give different findings it demonstrates that the choice of salt drastically influences the precipitation dynamics of the metal components, with the acac salt for instance showing hindrance to copper precipitation.

The georgeite precursors which used Al boehmite and acac reagents were investigated further. In order to verify the conclusions drawn from the EDX findings, the effluents generated from the synthesis procedure were collected and analysed for Cu, Zn and Al concentrations down to ppm

levels (Table 3.10.). For the boehmite material, it is clear that no metals present in the effluent confirms that complete precipitation of the metals took place, and the addition of the sol to the starting metal solution did not influence the precipitation phenomenon. For the acac effluent the EDX findings are also verified. Negligible quantities of zinc and aluminium were present but there is a detectable amount of copper present. This was also indicated by the colour of the effluent being blue indicating that copper was present. However, the 98% yield calculated for copper is still significantly high to account for this. However, this can be explained from the utilisation of starting metal solutions with very dilute concentrations (< 4 mg/ml Cu acetate) meaning even a subtle loss in metal content can significantly affect the determined metal molar ratio. Since the acac precursor had presented promising results with in-depth analysis suggesting aluminium could possibly have been incorporated into the georgeite phase, attempts were made to try and overcome the inhibition of copper precipitation. Studies by Reverchon and co-workers have shown that higher pressures are required as additional solute is introduced into the SAS system since the mixture critical point (MCP) shifts to higher pressures<sup>(14)</sup>. If the system operates outside the MCP then precipitation occurs under sub-critical conditions instead, as there is not complete miscibility between the solvent and anti-solvent. It therefore suggests that in order to achieve the required metal molar ratio, pressures > 110 bar may be required. Moreover, it was concluded in Section 3.2. that the variation in the water content can significantly influence the metal molar ratio in binary Cu/Zn SAS systems. With this all taken into consideration, EDX analysis was carried out on ternary georgeite precipitates prepared using various water contents (5-20%) and pressures (110 bar and 150 bar) with the Al acac salt (Table S3.). Unfortunately, the attempts were futile in obtaining the nominal Cu/Zn/Al molar ratio of 6/3/1. It is apparent in each case that the Zn content always remains close to 30% but the Cu atomic content is always ~5-8% lower than it should be. A trend, however, could be identified regarding the water content, whereby an increase from 5 to 20 vol.% resulted in an increase in the copper atomic content of the material by 3%. However, taking into consideration the error margin of the EDX

**Table 3.10.** MP-AES analysis of SAS effluents obtained from using various aluminium reagents to determine yields. Nominal Cu/Zn/Al ratio was 6/3/1.

Aluminium reagent	Effluent concentration (mg/L)			Yield (%) <sup>d</sup>			
	Cu <sup>a</sup>	Zn <sup>b</sup>	Al <sup>c</sup>	Cu	Zn	Al	Total
Boehmite	0	0.4	0	100	100	100	100
Acetylacetonate	25.1	0.3	0.7	98	100	99	99

Calibration standards prepared using ethanol as solvent.

<sup>a</sup> Standard deviation  $\pm 0.04$  mg/L.

<sup>b</sup> Standard deviation  $\pm 0.08$  mg/L.

<sup>c</sup> Standard deviation  $\pm 0.08$  mg/L.

<sup>d</sup> Yields calculated assuming initial copper, zinc and aluminium concentrations were 1135, 973 and 80 mg/L, respectively, based on metal reagent concentrations used.

analysis ( $\pm 3$  atomic %), this finding could be inconclusive.

TGA/DTA was used to examine the thermal decomposition process for each georgeite precursor after aluminium was confirmed present in all the materials (**Figure 3.15.** and **Table 3.11.**). The TGA of zincian georgeite (2/1) is also presented for clarity, in order to directly compare the influence that each aluminium species has on the resulting decomposition. For the materials prepared using Al boehmite, inspection of the TGA profiles against the binary standard shows that disruption of the HT-CO<sub>3</sub> species takes place. In previous sections it has been demonstrated that this carbonate species plays a particular role in generating optimum catalysts. For the binary standard, this HT-CO<sub>3</sub> species completely decomposes by 473 °C, whilst for the 6/3/1 material this is evident at 453 °C. With the higher content of the boehmite used in the 3.3/1.7/5 material, this decomposition step is not even apparent. The boehmite sol is clearly influencing the structure and/or thermal behaviour of the co-existing georgeite phase, which is attributed to the unstable nature of this mineral. Inspection of the DTA also shows that with boehmite addition, the entire decomposition is largely endothermic which rules out the possibility of exothermic processes removing the HT-CO<sub>3</sub> species. The TGA findings were also used to compare against the theoretical total mass loss calculated for both Al boehmite containing precursors, to justify that in each case the precipitate consists of separate zincian georgeite and Al boehmite phases. It is clear that the comparisons are in fairly good agreement, even when several assumptions were made. The EDX findings were used to determine that the wt.% of the sol in these materials was 11.72 and 46.06%, with the remainder assumed to be 2/1 zincian georgeite. A TGA of the Al sol determined that it has a total mass loss of 21.6%, whilst the TGA of the 2/1 zincian georgeite material has a total mass loss of 35.7%. Therefore, the contributions from both phases to the total mass loss can be determined which reconciles with the theoretical mass loss.

The TGA and DTA profile for the precursor prepared using Al(acac)<sub>3</sub> indicates that it has significant potential to be an optimum catalyst precursor. With the FT-IR analysis suggesting that the Al may be getting incorporated into the georgeite phase, these temperature programmed studies provide further evidence of this occurring. In **Section 3.3**, it was demonstrated that the decomposition temperature of the HT-CO<sub>3</sub> species increased as the zinc content increased, suggesting incorporation of higher amounts of zinc into the georgeite phase. The HT-CO<sub>3</sub> species completely decomposes by 473 °C for the 2/1 precursor and at 485 °C for the 1/1 precursor. With the addition of Al(acac)<sub>3</sub>, this decomposition step has shifted significantly to 530 °C. Therefore a 19 at.% addition in Zn increased this decomposition temperature by 12 °C, but a 19 at.% increase in Al increased it by 57 °C. This enhanced thermal stability could be attributed to the presence of Al<sup>3+</sup> cations in the georgeite phase.

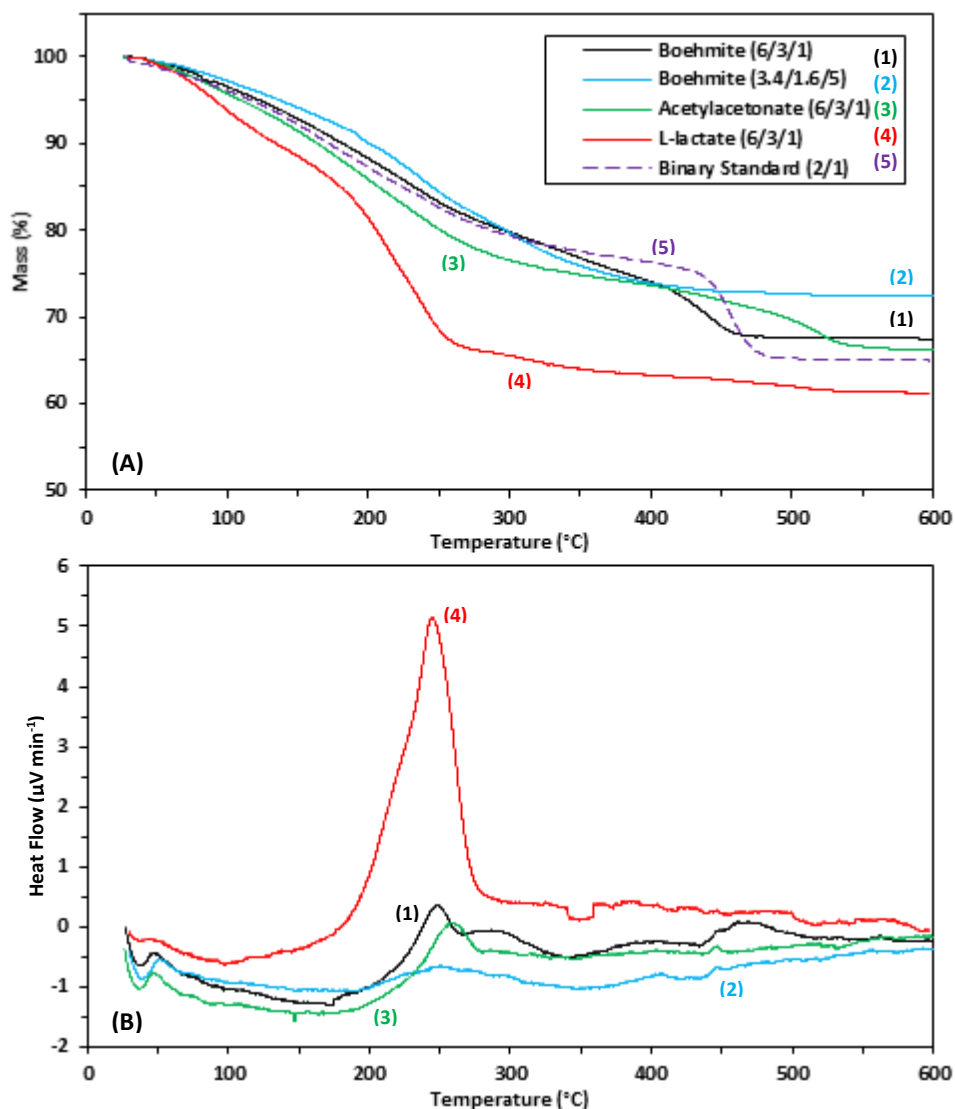


**Figure 3.15.** (A) TGA and (B) DTA of the SAS prepared georgeite precursors formed using various Al reagents and molar metal ratios as indicated. The zincian georgeite (2/1) precursor is provided in the TGA findings for comparison. A numbered key is also provided for clarity, which is associated with both (A) and (B).

**Table 3.11.** Comparison of TGA theoretical and experimental mass losses for ternary georgeite precursors.

Aluminium reagent used	Residual mass remaining at 300 °C (%)	Experimental total mass loss (%)	Theoretical total mass loss (%) <sup>a</sup>	Theoretical / experimental total mass loss (%)
Boehmite	12.2	32.5	34.01	104.6
Boehmite*	7.4	27.7	29.2	105.4
Acetylacetonate	10.5	34	36.5	107.4
L-lactate	4.4	38.9	36.47	93.8

<sup>a</sup> Calculated from assumptions discussed in the text.

\* The nominal Cu/Zn/Al molar ratio was 3.3/1.7/5 and was 6/3/1 for all other materials.

$\text{Al}^{3+}$  has a greater charge density to  $\text{Zn}^{2+}$  resulting in increased covalent metal-oxygen bonding, which implies that it could be a more effective thermal stability promoter. Furthermore, the theoretical total mass loss determined is also in good agreement with the observed experimental total mass loss. To calculate the theoretical mass loss the molecular formula of the precursor is required and it must be assumed that total decomposition leads to the formation of  $(\text{CuO})_x/(\text{ZnO})_y/(\text{Al}_2\text{O}_3)_z$ , whereby  $x$ ,  $y$  and  $z$  relate to the metal molar ratio. Determination of the molecular formula of zincian georgeite is covered in **Chapter Four** and will not be discussed in detail here. However, with aluminium incorporation the molecular formula is expected to be  $(\text{Cu}_x\text{Zn}_y\text{Al}_z)_5(\text{CO}_3)_3(\text{OH})_4 \cdot 3\text{H}_2\text{O}$ , and for the desired Cu/Zn/Al molar ratio of 6/3/1 it is clear  $x = 0.6$ ,  $y = 0.3$  and  $z = 0.1$ . With these assumptions, the total mass loss is calculated to be 36.09%. However, it is clear from the EDX findings that this nominal metal ratio was not achieved and instead it was found that  $x = 0.53$ ,  $y = 0.28$  and  $z = 0.19$ . Therefore, from the EDX findings and assuming complete decomposition to the metal oxides the theoretical total mass loss determined is 36.5%.

In contrast, the TGA and DTA profile for the precursor prepared using Al L-lactate suggests that this is an unsuitable candidate for a catalyst precursor. The DTA shows a highly exothermic decomposition step occurring at 245 °C, which contributes to the significant mass loss observed up to this temperature in the TGA. This is expected to leave no more than 4.4% residual mass after calcination to 300 °C with no HT- $\text{CO}_3$  species present. It is therefore clear that an additional phase is present, as this thermal behaviour is not seen for the zincian georgeite phase. Interestingly, the FT-IR findings did show that peaks associated with the L-lactate phase were retained in this precursor

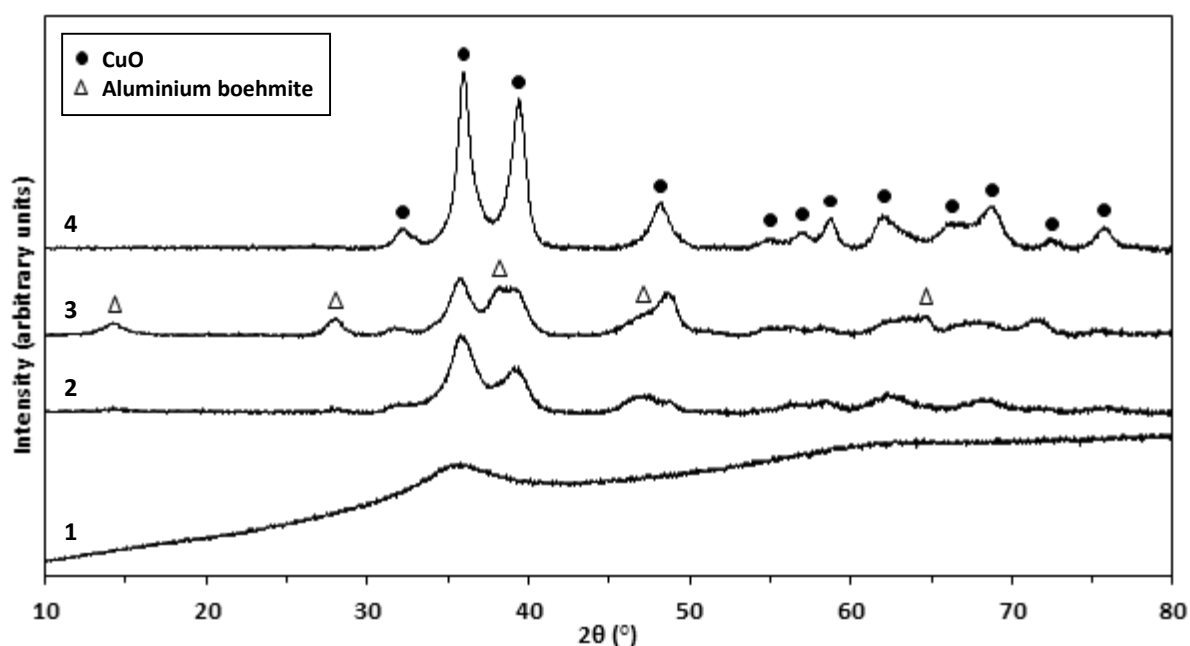


**Figure 3.16.** XRD patterns of the georgeite materials prepared from SAS precipitation using various aluminium reagents after calcination: (1) aluminium acetylacetonate (6/3/1) (2) aluminium boehmite (6/3/1) (3) aluminium boehmite (3.3/1.7/5) (4) aluminium L-lactate (6/3/1).

(Figure 3.13.). A TGA performed on the starting Al L-lactate reagent also showed a highly exothermic decomposition which verifies these FT-IR findings. Clearly the L-lactate phase is present in this precursor, with the undesirable decomposition dominating the overall thermal behaviour.

Regardless, the theoretical total mass loss was still calculated similarly to the acac material. Using the EDX findings, whereby  $x = 0.57$ ,  $y = 0.25$  and  $z = 0.18$  it is still seen to be in good agreement with the observed total mass loss.

To examine the thermal decomposition process further, evaluation of the georgeite precursors after calcination was carried out using XRD analysis (Figure 3.16.). It is clear that the findings compliment and verify the TGA/DTA findings. The presence of Al boehmite reflections is an indication that this phase does not decompose under the standard calcination conditions used. In fact, the TGA of the sol showed that total decomposition does not occur until 470 °C, which would result in substantial sintering of the copper component. This means that the final state catalyst will not have the  $\text{Al}_2\text{O}_3$  phase present but instead is expected to be Al boehmite. Phase analysis also identified reflections for CuO in contrast to the 2/1 analogue which, as already shown, remains amorphous after calcination. This would imply that the CuO crystallites are larger in the Al containing material. No ZnO reflections were observed as seen previously, although the (101) reflection could be overlapping with the (-111) CuO reflection at 36.2 °. With the TGA findings illustrating decreasing amounts of  $\text{HT-CO}_3$  with increased Al boehmite content, it is possible that this correlates to the presence of larger CuO crystallites after the calcination step. This is emphasised in the other two samples analysed. The acac precursor is shown to still be amorphous after calcination and was the only Al precursor to induce a thermal promotional effect on the  $\text{HT-CO}_3$  species. In contrast, the L-lactate precursor displays high crystallinity after calcination with no  $\text{HT-CO}_3$  retained. Loss of  $\text{HT-CO}_3$  and CuO sintering are both associated with the highly exothermic decomposition process. Interestingly, phase analysis again determined no reflections present for ZnO suggesting this exothermic process was not vigorous enough to facilitate substantial ZnO sintering. The CuO crystallite size determined for the calcined material made using Al L-lactate was 7.4 nm using the (111) reflection.

The findings derived from the Al boehmite materials warranted further investigation. The calcined material with the nominal ratio of 6/3/1 was further analysed using STEM-ADF elemental mapping in order to determine the degree of dispersion of the three metal components (Figure 3.17.). It is clear than at magnifications zoomed down to several hundred nanometers the Al is not homogeneously dispersed like the other two metals. Some regions are Al rich, whilst other areas contain no Al for several tens of nanometers. With the XRD findings displaying CuO reflections after calcination, it is clear that Cu sintering is more pronounced when the sol is present. This can only be attributed to the

loss of HT-CO<sub>3</sub> as seen from TGA, or a reduction in the degree of mixing between Cu and Zn in the georgeite phase. Since the sol should not be disrupting the precipitation phenomenon it is most plausible that the high dispersion of the sol in the unstable, amorphous georgeite phase induces structural changes in the hydroxycarbonate causing loss of HT-CO<sub>3</sub>. This intensifies as the content of the sol is increased. This implies that the role of HT-CO<sub>3</sub> is to assist ZnO by restraining the resulting CuO crystallites from agglomerating by also acting as a thermally rigid spacer.

BET was carried out to determine surface areas of the aluminium containing georgeite materials before and after calcination and used to compare against the EDX, TGA/DTA and XRD findings (Table 3.12.). It was seen in Section 3.3., that varying the Cu/Zn molar ratio did not have a profound effect on the BET surface area of the resulting precursor. However, this is not apparent with Al addition which results in a significant increase in the BET surface area. BET surface areas in the range

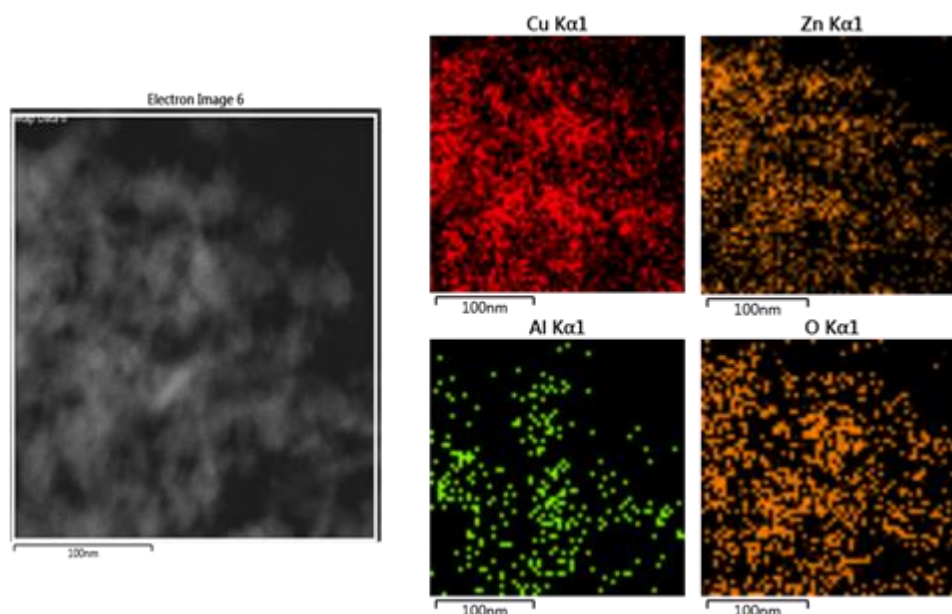


Figure 3.17. STEM-ADF (left column) and STEM-XEDS images of Cu-K $\alpha$ , Zn-K $\alpha$ , Al-K $\alpha$  and O-K $\alpha$  signals (middle and right columns) of calcined georgeite prepared by SAS precipitation using aluminium boehmite. The nominal Cu/Zn/Al molar ratio was 6/3/1.

Table 3.12. BET surface areas of SAS prepared georgeite precursors formed using various aluminium reagents before and after calcination. C values are provided to indicate degree of accuracy for each analysis.

Aluminium reagent	Cu/Zn/Al molar ratio	Precursor surface area		Calcined surface area	
		(m <sup>2</sup> g <sup>-1</sup> ) <sup>a</sup>	C value	(m <sup>2</sup> g <sup>-1</sup> ) <sup>a</sup>	C value
Boehmite	6/3/1	92	430	90	174
Boehmite	3.3/1.7/5	128	182	115	673
Acetylacetonate	6/3/1	158	93	81	230
L-lactate	6/3/1	114	266	-	-

<sup>a</sup> Standard deviation  $\pm 6$  m<sup>2</sup> g<sup>-1</sup>.

114-158 m<sup>2</sup> g<sup>-1</sup> were obtained using the Al salt reagents, in comparison to 97 m<sup>2</sup> g<sup>-1</sup> obtained for the binary 2/1 zincian georgeite material. Interestingly, whilst an increase in BET surface area was also observed using Al boehmite it is clear that it was less apparent, with the 6/3/1 material being similar to the binary hydroxycarbonate. Moreover, the 3.3/1.7/5 material, which has a significantly higher Al content, only produced a BET surface area of 128 m<sup>2</sup> g<sup>-1</sup>. This is likely a result of the poor dispersion of the sol in the precursor (**Figure 3.17.**), and possibly because no Al is incorporated into the georgeite phase.

After calcination there is a decrease in the BET surface area for each material, as was observed for the binary materials previously investigated. The findings, however, suggest that the boehmite reagent is most effective in minimising this reduction. This results in the 6/3/1 boehmite material having a similar BET surface area to the acac material in the range 81-90 m<sup>2</sup> g<sup>-1</sup> after calcination. This was not expected from the conclusions drawn from the previous findings. However, it is actually not possible to directly compare the BET surface areas of these materials since the EDX analysis showed that they all display different Cu/Zn/Al ratios. The copper and zinc atomic content in the 6/3/1 materials is similar but the boehmite has a slightly higher content of Al present. Moreover, the colour of the acac material after calcination was dark green in comparison to the boehmite sample which was black. This suggests retention of residual amounts of low temperature hydroxyl and carbonate species, which after removal from using a slightly higher calcination temperature could generate a higher BET surface area. In **Section 3.3.**, similar observations and conclusions were made. For the calcined Al L-lactate material, no surface area could be obtained. This is possibly a result in the breakdown in the assumptions used by the BET model on this particular surface (**Section 2.4.9.**). Regardless from the TGA/DTA and XRD findings, it is likely a very low surface area was formed, which has already been attributed to the exothermic decomposition of the residual lactate phase retained after SAS precipitation.

Copper surface area analysis was carried out on the ternary catalysts after subsequent reduction of the calcined materials, with normalised copper surface areas also determined from the EDX findings (**Figure 3.18.**). The catalyst which used Al(acac)<sub>3</sub>, displayed the highest copper surface area of 27 m<sup>2</sup> g<sup>-1</sup> which, within the error limits of the analysis, is similar to that determined for the optimum 2/1 catalyst prepared using 10% water. Interestingly, despite XRD showing clear reflections for CuO the 6/3/1 catalyst prepared using Al boehmite still produced a high surface area of 23 m<sup>2</sup> g<sup>-1</sup>, which is comparable to the 1/1 catalyst prepared using 10% water. In contrast, the catalysts prepared using the higher content of Al boehmite and Al L-Lactate displayed lower copper surface areas. Regarding

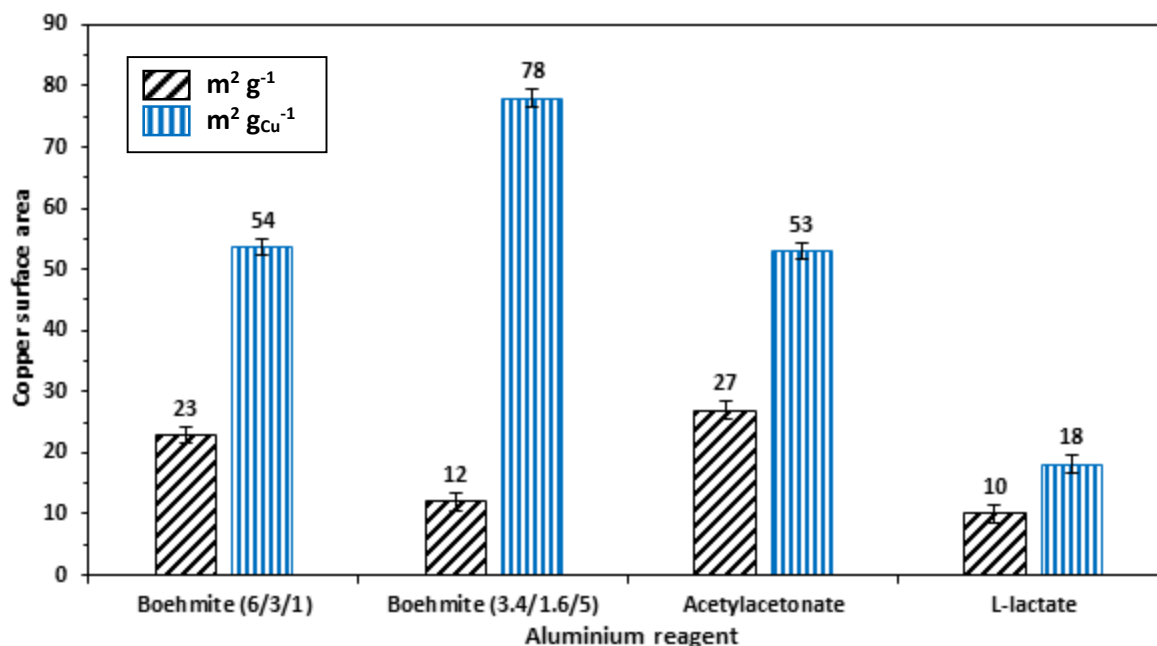


**Figure 3.18.** Copper surface area analysis of Cu/ZnO/Al<sub>2</sub>O<sub>3</sub> catalysts prepared from SAS precipitation using various aluminium reagents with metal molar ratios indicated. Normalised copper surface areas calculated using EDX findings and assuming only Cu, ZnO and Al<sub>2</sub>O<sub>3</sub> phases present prior to analysis with the exception of the boehmite materials whereby the aluminium boehmite phase is still present.

the 3.4/1.6/5 catalyst, this is clearly explained by a lower copper content present in this catalyst. For the L-lactate derived catalyst, this finding is in agreement to the previous findings, whereby the high degree of mixing and dispersion of the Cu component produced from SAS is evidently lost within the subsequent calcination step. This therefore concludes that Al L-lactate is an unsuitable reagent to use in the preparation of Cu/ZnO/Al<sub>2</sub>O<sub>3</sub> catalysts.

The 3.4/1.6/5 catalyst produced the optimum normalised copper surface area of 78  $\text{m}^2 \text{g}^{-1}$  which is the highest value determined from all catalysts evaluated. This was expected from the higher Al boehmite content which, in addition to ZnO, further dilutes and disperses the Cu component. It is, however, interesting that the 6/3/1 catalysts prepared using Al boehmite and Al(acac)<sub>3</sub> displayed similar normalised copper surface areas of 53-54  $\text{m}^2 \text{g}^{-1}$ . The normalised copper surface areas, however, should not be treated decisively since they are calculated using the EDX findings which were found to deviate slightly between different scans, particularly for the boehmite materials. Moreover, the optimum calcination conditions are likely to vary between samples as indicated from the different thermal behaviours illustrated in the TGA/DTA profiles. Since the acac derived catalyst was still green after calcination, it suggests that this catalyst in particular could be optimised further. Regardless, it is clear that both the boehmite and acac derived catalysts display huge potential and are thus identified as suitable candidates for catalyst testing.

### 3.4.2. Conclusions from aluminium incorporation into SAS prepared zincian georgeite

The choice of aluminium reagent in the preparation of ternary georgeite precursors by SAS precipitation will ultimately be reflected in the performance of the resulting Cu/Zn/Al<sub>2</sub>O<sub>3</sub> catalyst. This is a result of changes inflicted in the structure, chemical composition and subsequent thermal behaviour of the precursor, which combine to govern the construction of the final state system. Whilst aluminium incorporation into the georgeite precursor was achieved using all three reagents the Al(acac)<sub>3</sub> salt, and to a lesser extent, the Al boehmite sol are identified as promising candidates. This is because the high level of dispersion and dilution of the metal components in the precursor, which is characteristic of the SAS procedure, is retained to a much higher degree throughout the entire synthesis procedure to yield catalysts with higher copper surface areas.

In related work, Behrens and co-workers have investigated the incorporation of Al into the 2/1 zincian malachite precursor and reported that 3.3 at.% is the optimal content<sup>(25)</sup>. They report that Al is a promoter in the Cu/ZnO/Al<sub>2</sub>O<sub>3</sub> system through both geometric and electronic effects. It is therefore important to discuss these effects in context to the findings reported herein.

1.) The structural/geometric effect: For the preparation of crystalline hydroxycarbonates by co-precipitation, the content of both Zn and Al affects phase formation of the resulting precipitate. It is seen that 3.3 at.% is the maximum amount of Al which can be incorporated into the malachite lattice which further promotes Cu dispersion and dilution. Higher Al contents are detrimental as it results in formation of the hydrotalcite phase, which has an unfavourable mesostructure and withdraws Zn<sup>2+</sup> and Al<sup>2+</sup> cations out of the co-existing malachite phase. In this current work, much higher Al contents ( $\geq 18$  at.%) were used and there is evidence for incorporation of Al into the georgeite phase using Al(acac)<sub>3</sub> with no subsequent by-phase formation. It is currently not known how much Al can be incorporated into the georgeite phase, and in **Section 3.3.** the same conclusions were made regarding Zn incorporation. This clearly warrants further investigation regarding both Zn and Al incorporation, with georgeite formation by SAS precipitation not apparently restricted by formation of additional phases with undesirable mesostructures.

2.) The electronic effect: The intrinsic activity of the catalyst increases as the amount of Al<sub>Zn</sub> increases. This arises from the partial doping of Al into the ZnO phase by substitution of Zn<sup>2+</sup> with Al<sup>3+</sup> cations, whereby Al<sub>Zn</sub> refers to the fraction of Al in ZnO:Al. This fine tunes the reducibility of the ZnO phase, which under reducing conditions, generates ZnO<sub>x</sub> ( $x < 1$ ) moieties that migrate onto the Cu surface to facilitate formation of optimum active sites. Consequently, the higher super-saturation levels achieved in SAS compared to co-precipitation enables access to more intimately mixed metal

precursors which could encourage higher contents of Al to be doped into ZnO in the subsequent thermal steps. This outlines the clear distinction between using  $\text{Al}(\text{acac})_3$  and the Al boehmite reagents. Homogeneous aluminium incorporation is not apparent when using the sol and therefore the amount of  $\text{Al}_{\text{Zn}}$  in the resulting catalyst is expected to be minimal, if present at all. Therefore, it is clear that preparation of ternary georgeite precursors by SAS precipitation using  $\text{Al}(\text{acac})_3$  is an exciting concept in the study of  $\text{Cu}/\text{ZnO}/\text{Al}_2\text{O}_3$  catalysts.

### 3.5. Synthesis of zincian georgeite by co-precipitation

Whilst SAS precipitation provides an alternative route to co-precipitation for the preparation of catalyst precursors, several limitations using this methodology are clearly evident. The high energy consumption associated with cycling pressures operating up to 110 bar in combination with the low solubility of metal acetates/acac salts in organic solvents is clearly avoided in the aqueous co-precipitation procedure. From a commercial perspective, catalysts must be cheap to manufacture on an industrial scale in order to be sustainable and with a co-precipitation set-up already in operation, principally a smooth transition can be facilitated if the same technique is applied in the preparation of georgeite precursors.

Spencer and co-workers were first to report that zincian georgeite can be prepared by co-precipitation<sup>(10)</sup>. However, this process remains challenging since reagents including nitrates, halides, sulphates and alkali metals must be avoided if the synthesis is to be rendered completely green and free of catalytic poisons. Moreover, the preparation parameters must be finely tuned as the initial metastable georgeite precipitate readily ages into the thermodynamically stable malachite precursor under the current industrial conditions utilised.

The work presented herein overcomes such challenges, whereby it is demonstrated that zincian georgeite precursors can be readily produced by co-precipitation free of alkali-metal reagents, which otherwise hinders optimum catalytic performance levels being achieved. Emphasis was also placed on limiting the production of environmentally harmful waste streams by avoiding use of nitrate reagents. This was achieved using the current industrial co-precipitation set-up with optimised synthesis parameters but with slight modifications made: A solution of copper acetate (70 mg/ml) and zinc acetate (38.482 mg/ml), which gives a nominal Cu/Zn molar ratio of 2/1 and a total metal concentration of 0.526 M, was simultaneously added to a 0.55 M solution of precipitation reagent at constant pH = 6.5-7 and temperature = 40 °C. The lower temperature used and the shortening of the ageing time to 15 minutes was to prevent ageing into zincian malachite. The concentration chosen

for copper acetate was close to its solubility limit in water at ambient temperature (72 mg/ml). The effect of precipitation reagent type on the physicochemical properties of the precursor material was investigated using ammonium carbonate, ammonium bicarbonate and sodium carbonate. Sodium carbonate was specifically chosen to examine and directly compare catalysts with and without residual alkali-metal loadings to shed new light on the deactivation process. This was investigated further by preparing zincian georgeite precursors with and without incorporation of a washing step after filtration using all three precipitation reagents. For the washing step, 1 L of deionised water at ambient temperature was used on the resulting precipitate. These zincian georgeite precursors are discussed and directly compared against the zincian malachite (2/1) precursor prepared using the industrial co-precipitation methodology, as well as zincian georgeite (2/1) prepared by SAS precipitation.

### 3.5.1. Results and discussion

To confirm that the zincian georgeite hydroxycarbonate was being produced using this modified co-precipitation procedure, FT-IR and XRD analysis was carried out on the resulting precipitates prepared using  $(\text{NH}_4)_2\text{CO}_3$ ,  $(\text{NH}_4)\text{HCO}_3$  and  $\text{Na}_2\text{CO}_3$  (**Figure 3.19.**). In each case, it is clear that the amorphous precursor has indeed been synthesised. The FT-IR assignments for zincian georgeite were discussed earlier (**Section 3.2.** and **Table S1.**) and so will not be repeated here. The crystalline reflections at  $33.1$  and  $59.1^\circ$  in the XRD patterns of the SAS prepared zincian georgeite materials are absent in these XRD findings as was to be expected. However, it is clear that an acetate by-phase is still present, at least in the precursors prepared using ammonium reagents. Careful inspection of the FT-IR spectra shows bands at  $617$  and  $678\text{ cm}^{-1}$ , which are assigned as  $\pi(\text{COO})^-$  and  $\alpha(\text{COO})^-$  modes, respectively. This was investigated further by performing Raman analysis on the precursor prepared using  $(\text{NH}_4)_2\text{CO}_3$  with and without a washing step included (**Figure S9.**). The intensity of all the Raman bands is higher in comparison to the materials prepared by SAS precipitation, as a result of the lower density of the samples prepared supercritically. It is clear that acetate bands are present at  $939$  and  $2940\text{ cm}^{-1}$  with a broad band ranging between  $1336$ - $1645\text{ cm}^{-1}$ . Assignments of these bands was also discussed earlier (**Section 3.2.** and **Table S2.**) although it is worth mentioning again that the band for  $\nu(\text{C-C})$  at  $939\text{ cm}^{-1}$  indicates the pseudo-bridging acetate mode<sup>(6)</sup>. It is most likely that this acetate species is the ammonium acetate by-product. If the reaction had not gone to full completion it could also possibly be residual copper and zinc acetate starting material. However, the strong crystalline reflections of these materials is absent in the XRD findings making it less likely. Regardless it is clear that even with the washing step included this acetate by-phase remains.

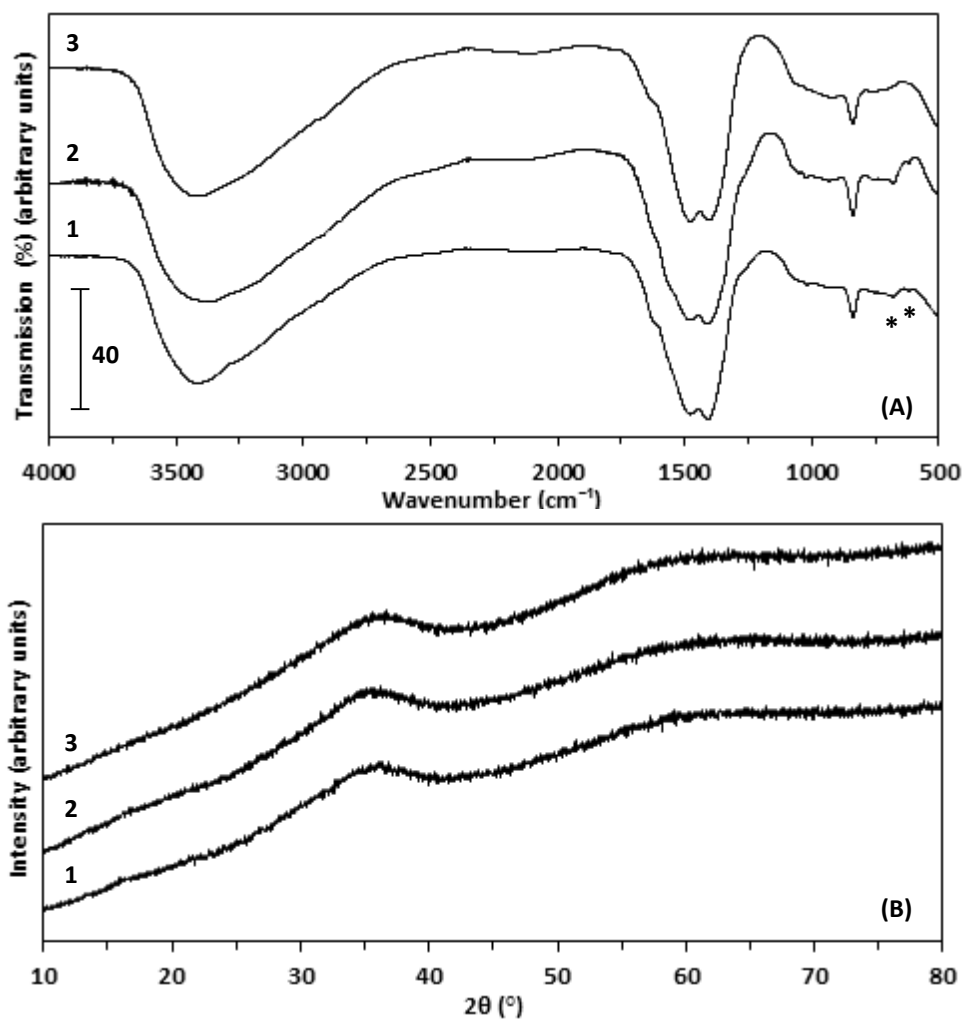


**Figure 3.19.** (A) FT-IR spectra and (B) XRD patterns of 2/1 zincian georgeite precursors prepared by co-precipitation using: (1) ammonium carbonate (2) ammonium bicarbonate and (3) sodium carbonate. \* FT-IR bands for acetate by-phase (617 and 678  $\text{cm}^{-1}$ ) marked for clarity.

Moreover, these findings conclude that no additional hydroxycarbonate phases are present as was determined in the SAS precipitation work.

EDX analysis was used to determine if the desired chemical composition was present in each precursor to give the nominal Cu/Zn molar ratio of 2/1 ([Table 3.13](#)). Whilst the precipitate prepared using  $\text{Na}_2\text{CO}_3$  achieved the correct metal composition, it was determined that using ammonium precipitation reagents produced precursors which were slightly Cu deficient, giving Cu/Zn molar ratios of 1.8/1. Simson and co-workers in related studies investigated the preparation of mixed malachite/rosasite/aurichalcite precursors by co-precipitation using  $(\text{NH}_4)_2\text{CO}_3$  and reported similar findings<sup>(26)</sup>. They explained the reduced Cu content by a “leaching” effect caused by the formation of copper-ammine complexes during the precipitation reaction. At pH 7, the release of  $\text{NH}_3$  from  $(\text{NH}_4)_2\text{CO}_3$  cannot be suppressed, which results in a characteristic blue complex compound soluble in the mother liquor. This subsequently reduces the yield of the precursor, which if significant enough

**Table 3.13.** EDX analysis of zincian georgeite precursors prepared by co-precipitation using various precipitation reagents. The nominal Cu/Zn molar ratio was 2/1.

Precipitation Reagent	Atomic (%) <sup>a</sup>		Determined Cu/Zn molar ratio
	Cu	Zn	
(NH <sub>4</sub> ) <sub>2</sub> CO <sub>3</sub>	64	36	1.8/1
(NH <sub>4</sub> )HCO <sub>3</sub>	64	36	1.8/1
Na <sub>2</sub> CO <sub>3</sub>	67	33	2/1

<sup>a</sup> Standard deviation  $\pm 1\%$ .

**Table 3.14.** MP-AES analysis of co-precipitation effluents obtained from using ammonium carbonate or ammonium bicarbonate in order to estimate yields. The nominal Cu/Zn/Al ratio was 2/1.

Precipitation reagent	Effluent Concentration (mg/L)		Yield (%) <sup>c</sup>		
	Cu <sup>a</sup>	Zn <sup>b</sup>	Cu	Zn	Total
(NH <sub>4</sub> ) <sub>2</sub> CO <sub>3</sub>	430.5	0	92.5	100	96
(NH <sub>4</sub> )HCO <sub>3</sub>	222.5	0	96.1	100	98

Calibration standards prepared using deionised water as solvent.

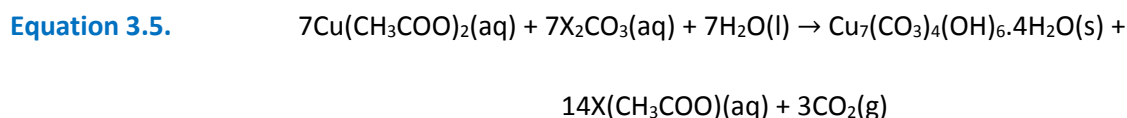
<sup>a</sup> Standard deviation  $\pm 0.05$  mg/L.

<sup>b</sup> Standard deviation  $\pm 0.07$  mg/L.

<sup>c</sup> Yields calculated assuming initial copper and zinc concentrations were 5713 and 2938 mg/L respectively based on metal salt concentrations used. Total volume of mother liquor solution was 0.39 L.

deems the synthesis route unsustainable and hence undesirable. To get an approximation as to the amount of metal leached during this procedure, the resulting blue effluents were collected after filtration and analysed using MP-AES in order to determine the metal concentrations (**Table 3.14.**). However, whilst the technique is accurate to ppm levels, yields were calculated based on initial acetate salt concentrations prepared using measuring apparatus of low accuracy and therefore the findings are only to provide a rough indication. The results, however, conclude with absolute certainty that no Zn is leached, which verifies the conclusions that only Cu is effected by the presence of ammonia. Furthermore, the (NH<sub>4</sub>)HCO<sub>3</sub> precipitation reagent was specifically investigated to see if the Cu yield could be increased by simply halving the stoichiometric amount of NH<sub>3</sub> present in the mother liquor. Whilst the EDX findings conclude this not to be the case, the MS-AES findings do illustrate a subtle increase in Cu yield. It can be concluded, however, that at least 8 % of copper used in this particular system is lost from the use of (NH<sub>4</sub>)<sub>2</sub>CO<sub>3</sub>.

At this point it is important to appreciate these fundamental chemical processes occurring within the mother liquor solution in order to derive a better understanding and overview of the synthesis procedure. This in turn could contribute towards the rational design of hydroxycarbonate preparation. The simplest reaction that can occur regards the preparation of georgeite from reaction between copper acetate and a water soluble carbonate reagent (**Equation 3.5.**).

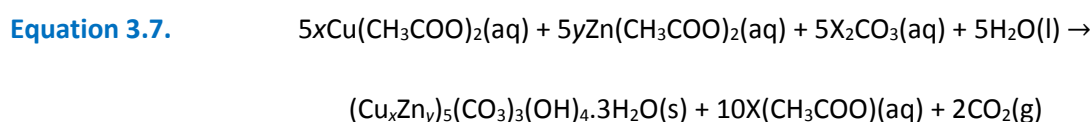


Whereby X = Na, K or NH<sub>4</sub> (i.e. any chemical species that forms a 1+ charged cation in solution).

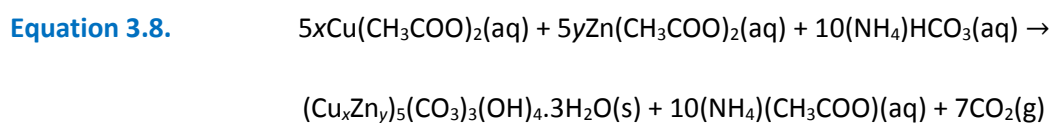
However, georgeite is highly unstable and rapidly ages into malachite, even at 40 °C (**Equation 3.6.**).



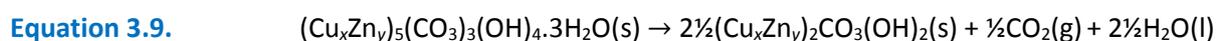
If the addition of zinc to the system is now considered, as is apparent for this particular study, the hydroxycarbonate formed is zincian georgeite (**Equation 3.7.**).



Whereby X = Na, K or NH<sub>4</sub> and in this particular case x = 0.67 and y = 0.33. However, a slightly different reaction proceeds when using the (NH<sub>4</sub>)HCO<sub>3</sub> precipitation reagent (**Equation 3.8.**).



It is seen that the stoichiometry between the acetate and precipitation reagents is 1:1 except in the case when (NH<sub>4</sub>)HCO<sub>3</sub> is used, whereby it is 1:2, respectively. The incorporation of zinc into the georgeite phase stabilises the hydroxycarbonate, and thus under these synthesis conditions (temperature = 40 °C and ageing time = 15 minutes) the ageing transformation into zincian malachite is prevented (**Equation 3.9.**).



The molecular formulas for georgeite and zincian georgeite will be discussed in more detail in **Chapter Four**. It should also be noted that these equations display overall reaction schemes and hence do not contain the individual fundamental steps of the presumed pathways of formation. However, several literature papers have reported that the sequence of solid formation begins with the initial precipitation of amorphous copper hydroxide<sup>(4,26)</sup>. This is attributed to the more acidic character of Cu<sup>2+</sup> in comparison to Zn<sup>2+</sup>. The copper hydroxide phase reacts with Zn<sup>2+</sup> and CO<sub>3</sub><sup>2-</sup> to produce zincian georgeite. However, such conclusions have been drawn from studies of the conventional metal nitrate/sodium carbonate system and so must be carefully considered here.

When  $(\text{NH}_4)_2\text{CO}_3$  or  $(\text{NH}_4)\text{HCO}_3$  is used, the formation of the copper-ammine complex must also be considered. This coordination chemistry has been well documented for decades with Hathaway and Tomlinson reporting that a complex equilibria is set up when ammonia solution is added to an aqueous  $\text{Cu}^{2+}$  solution<sup>(27)</sup> (Equation 3.10.).



The coordinated water is replaced by ammonia ligands in successive steps, but there is a negligible tendency to take up more than four ammonia groups (i.e.  $n = 4$ ) as a result of the formation constants for  $n = 5$  and  $6$  being so small. Therefore, as the concentration of  $(\text{NH}_4)_2\text{CO}_3$  or  $(\text{NH}_4)\text{HCO}_3$  increases the equilibrium shifts to the right and competes more strongly against Cu incorporation into the resulting zincian georgeite precipitate (Equations 3.7. and 3.8.).

With a better understanding of some of the key principles regarding the preparation of georgeite precursors using the modified co-precipitation route, attention focused on optimising certain aspects of the synthesis procedure, and in particular studying the deactivation role of residual sodium. The precipitates prepared using the three carbonate reagents were each split into two parts whereby half had no additional washing step included whilst the other half did. These precursors were then calcined before being digested in diluted aqua regia solvent and analysed using MP-AES to determine sodium loadings (Table 3.15.). Furthermore, the zincian malachite precursor prepared at Johnson Matthey using the conventional co-precipitation route was also analysed for direct comparison. It is clear that even when using Na-free reagents there is always residual amounts present in the precursors. It comes from the starting materials which can never be fully depleted of

**Table 3.15.** MP-AES analysis of digested calcined materials prepared using co-precipitation to determine sodium loadings. Various washing treatments and precipitation reagents were used as indicated.

Precipitation reagent	Washing treatment	Determined Na concentration (mg/L) <sup>a</sup>	Na weight (%)	mg(Na) kg <sub>(CuO/ZnO)</sub> <sup>-1b</sup>
$(\text{NH}_4)_2\text{CO}_3$	Yes	0.6	0.015	147.5
$(\text{NH}_4)_2\text{CO}_3$	None	0.8	0.021	207.5
$(\text{NH}_4)\text{HCO}_3$	Yes	0.6	0.015	147.5
$(\text{NH}_4)\text{HCO}_3$	None	1.4	0.034	340
$\text{Na}_2\text{CO}_3$	Yes	23.5	0.589	5885
$\text{Na}_2\text{CO}_3$	None	281.3	7.033	70325
JM Standard <sup>c</sup>	Yes	2.8	0.07	695

Calibration standards prepared using 20 vol.% aqua regia/deionised water as solvent.

<sup>a</sup> Standard deviation  $\pm 0.2$  mg/L.

<sup>b</sup> Sodium weights calculated knowing 40 mg of each sample digested in 10 ml of solvent.

<sup>c</sup> Johnson Matthey zincian malachite (2/1) prepared by standard co-precipitation using sodium carbonate.

Na. However, using higher purity grades can minimise the content present. Regardless, using  $(\text{NH}_4)_2\text{CO}_3$  or  $(\text{NH}_4)\text{HCO}_3$  with a washing step produced precursors with the lowest Na levels analysed at around  $148 \text{ mg}_{(\text{Na})}\text{kg}_{(\text{CuO/ZnO})}$ . This is a significant reduction from  $695 \text{ mg}_{(\text{Na})}\text{kg}_{(\text{CuO/ZnO})}$  typically expected for a standard industrial precursor. The industrial precursor would also have had a washing step using deionised water around 60-70 °C. This clearly illustrates that using Na-free reagents allows access to lower residual loadings not possible, regardless of the utilisation of a washing step, when using  $\text{Na}_2\text{CO}_3$ . The use of  $\text{Na}_2\text{CO}_3$  in the preparation of zincian georgeite shows loadings  $> 5000 \text{ mg}_{(\text{Na})}\text{kg}_{(\text{CuO/ZnO})}$  after washing, which is expected to result in a highly deactivated catalyst. Clearly, washing with water at higher temperatures is required to effectively remove more residual Na, however this risks ageing of the precursor into zincian malachite.

TGA/DTA was used to examine the effect of washing (with and without) and ramp rate (1 and 5 °C/min) on the decomposition of zincian georgeite precursors prepared using  $(\text{NH}_4)_2\text{CO}_3$  (**Figure 3.20**). The unwashed precursor prepared using  $\text{Na}_2\text{CO}_3$  is also provided for comparison, which was heated at a ramp rate of 5 °C/min. When using  $(\text{NH}_4)_2\text{CO}_3$  significant changes in the decomposition process occur from altering both variables. With no washing, the TGA profile is unrecognisable as to what is expected for this precursor, with loss of all residual material and  $\text{HT-CO}_3$  from a highly exothermic decomposition occurring between 200-280 °C. This is expected to be detrimental to the resulting catalysts produced. This significant alteration to the thermal decomposition of the amorphous hydroxycarbonate is attributed to the coexisting ammonium acetate by-phase retained, whereby washing reduces the amount retained and lower ramp rates ease the exothermic process. Ammonium acetate decomposes to acetamide on heating, and this transformation may attribute to the sharp endothermic peak that precedes the exothermic decomposition in the temperature range 200-225 °C. With washing included, both the TGA and DTA profiles are more characteristic of zincian georgeite, although clearly some by-phase remains as was indicated by Raman analysis (**Figure S9**). This is best seen when using a ramp rate of 5 °C/min, whereby a mild exothermic peak lies at 257 °C. This is at the same temperature for the strong exothermic peak observed when washing was absent. For comparison, the analogous SAS prepared zincian georgeite shows a very weak exothermic peak at a slightly lower temperature of 245 °C. In terms of quantification, the washed precursors gave total mass losses between 31-32%, which is slightly lower than the range 33-36% observed for the SAS prepared materials. However, the amount of residual mass remaining after 300 °C is 13% which was in the range found using SAS precipitation. This slightly lower total mass loss observed for the co-precipitated precursors could be attributed to a reduced occluded amount of water retained within the amorphous structure, or a slightly lower content of low temperature hydroxyl and

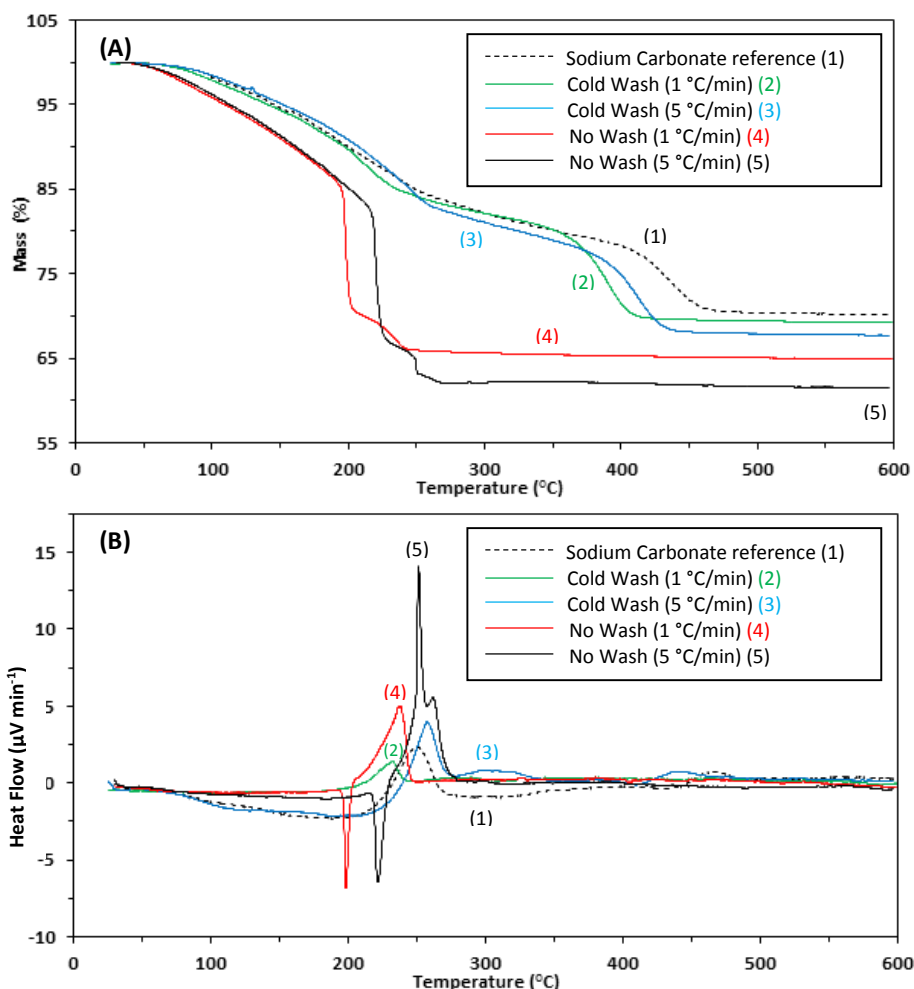


**Figure 3.20.** (A) TGA and (B) DTA of zincian georgeite precursors prepared by co-precipitation using ammonium carbonate to investigate the effect of washing treatment and ramp rate on the thermal decomposition process. The unwashed precursor prepared using sodium carbonate using a ramp rate of 5 °C/min is included for comparison. A numbered key is also provided for clarity.

carbonate groups. The most significant distinction though regards the decomposition temperature of the HT-CO<sub>3</sub>. As already mentioned in **Section 3.4.**, this species fully decomposed by 473 °C for SAS prepared 2/1 zincian georgeite, however when using the same ramp rate this is evident at 430 °C for the washed co-precipitated material. This is likely a result of poorer mixing between Cu and Zn within the precursor. In comparison, the unwashed materials give total mass losses in the range 35-38%, whereby the higher by-phase content could be attributing to this greater mass loss. Similar TGA/DTA findings were also found in investigating the precursor prepared using (NH<sub>4</sub>)HCO<sub>3</sub> as precipitation reagent (**Figure S10.**).

Interestingly, inspection of the TGA/DTA profile for the precursor prepared using Na<sub>2</sub>CO<sub>3</sub> was similar to that expected for zincian georgeite, even without washing treatment. Therefore, the role of deactivation is clearly different to using ammonium (bi)carbonate. This material had a total mass loss of 30%, which again is lower than that shown from SAS precipitation. However, the residual

mass content after 300 °C is only 12%, which means a lower content of HT-CO<sub>3</sub> is also present. This HT-CO<sub>3</sub> fully decomposed at 458 °C, which is higher than from using (NH<sub>4</sub>)<sub>2</sub>CO<sub>3</sub> as is clearly evident in the TGA findings. This strongly illustrates that the precipitation reagent plays a significant role on both the physicochemical and thermal properties of the resulting precipitate. TGA/DTA was also carried out on the washed precursor prepared using Na<sub>2</sub>CO<sub>3</sub>, but there was no significant change in comparison except that the mild exothermic peak at 252 °C disappeared.

The washed and non-washed precipitates prepared using all three precipitation reagents were calcined under standard conditions and analysed using XRD (Figure 3.21.). The washed materials remain largely amorphous after calcination, as was determined using the SAS precipitation route (Figure 3.6.), although very weak, ill-defined reflections can be seen. In direct contrast, the unwashed materials are strongly crystalline after thermal treatment. For the materials prepared using ammonium (bi)carbonate, phase analysis indicated that only CuO and ZnO phases were present. This suggests that the ammonium by-phase is removed after the calcination step. Interestingly, crystallite sizes determined for ZnO (10.2-18.1 nm) were always larger than for CuO (6.9-8.8 nm) despite being less susceptible to sintering (Table 3.16.). However, crystallite sizes for both phases were determined using a single reflection whereby analysis of multiple reflections is required for representable size comparisons.

For the non-washed material prepared using Na<sub>2</sub>CO<sub>3</sub>, a large number of additional reflections were

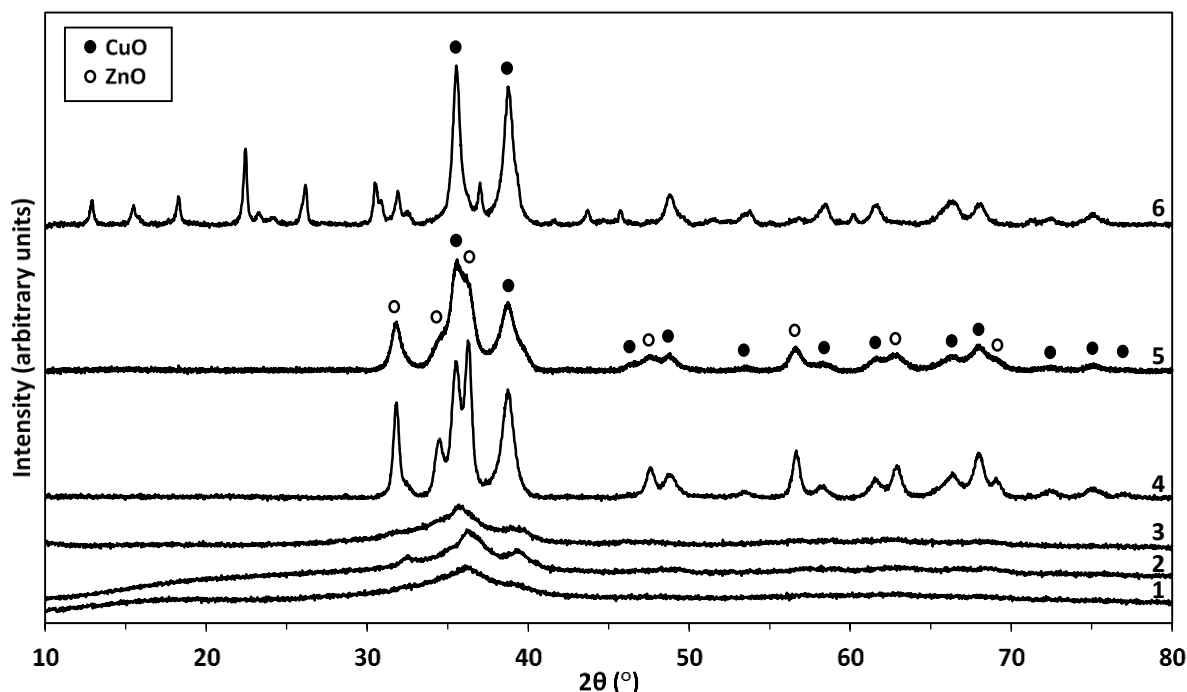


**Figure 3.21.** XRD patterns for the calcined zincian georgeite materials prepared by co-precipitation using: (1) (NH<sub>4</sub>)<sub>2</sub>CO<sub>3</sub> (washed) (2) (NH<sub>4</sub>)HCO<sub>3</sub> (washed) (3) Na<sub>2</sub>CO<sub>3</sub> (washed) (4) (NH<sub>4</sub>)<sub>2</sub>CO<sub>3</sub> (no wash) (5) (NH<sub>4</sub>)HCO<sub>3</sub> (no wash) (6) Na<sub>2</sub>CO<sub>3</sub> (no wash).

present. Sharp CuO reflections were identified by phase analysis, whereby the crystallite size was the largest determined at 10.1 nm. This XRD pattern was very challenging to analyse because no additional phases could be strongly matched using phase analysis. Attempts were made using phase files for a range of sodium compounds including acetate, carbonate, oxalate, hydroxide, the oxides and even chalconatronite. Difficulties arose as a result of the large number of reflections associated with each phase. Furthermore, reflections for ZnO did not appear present. Since certain materials are capable of incorporating water into their structure to form hydrates, which drastically alters their XRD patterns, a similar occurrence is possible here. Sodium acetate was expected to be the main by-phase present, and it is seen with the starting materials that acetate salts readily incorporate water into their crystal structure.

Surface areas of the samples were measured before and after calcination using BET analysis to further analyse the effect of precipitation reagent type and washing treatment (**Table 3.16.**). For the precursors, the BET surface areas were low using ammonium (bi)carbonate ( $16\text{--}17\text{ m}^2\text{ g}^{-1}$ ) and drastically higher using sodium carbonate ( $52\text{ m}^2\text{ g}^{-1}$ ). For clarity, SAS prepared zincian georgeite precursors give BET surface areas ranging  $90\text{--}100\text{ m}^2\text{ g}^{-1}$ . Comparison of the BET surface areas after calcination showed that for all materials washing results in higher surface areas, as was expected after analysing the XRD findings (**Figure 3.21.**). However, this is really only apparent when using sodium carbonate since use of the ammonium reagents showed little difference in surface area from the use of washing. It is also important to note that the SAS materials all produced lower BET surface areas after calcination, whilst that is not apparent here. In order to investigate this further, selected materials prepared using sodium and ammonium carbonate were again analysed using the

**Table 3.16.** BET surface areas and crystallite sizes of precursors prepared by co-precipitation before and after calcination treatment. C values provided to indicate degree of accuracy for each analysis. Analysis obtained from Gemini instrumentation.

Precipitation reagent	Washing Treatment	Calcination treatment	BET S.A. ( $\text{m}^2\text{ g}^{-1}$ ) <sup>a</sup>	C value	CuO cry. size (nm) <sup>b</sup>	ZnO cry. size (nm) <sup>b</sup>
(NH <sub>4</sub> ) <sub>2</sub> CO <sub>3</sub>	None	None	16	39	-	-
(NH <sub>4</sub> )HCO <sub>3</sub>	None	None	17	38	-	-
Na <sub>2</sub> CO <sub>3</sub>	None	None	52	47	-	-
(NH <sub>4</sub> ) <sub>2</sub> CO <sub>3</sub>	Yes	Yes	31	449	-	-
(NH <sub>4</sub> )HCO <sub>3</sub>	Yes	Yes	27	328	-	-
Na <sub>2</sub> CO <sub>3</sub>	Yes	Yes	48	544	-	-
(NH <sub>4</sub> ) <sub>2</sub> CO <sub>3</sub>	None	Yes	22	117	8.8	18.1
(NH <sub>4</sub> )HCO <sub>3</sub>	None	Yes	26	198	6.9	10.2
Na <sub>2</sub> CO <sub>3</sub>	None	Yes	10	1583	10.1	-

<sup>a</sup> Standard deviation  $\pm 6\text{ m}^2\text{ g}^{-1}$ .

<sup>b</sup> XRD crystallite sizes determined using the Scherrer equation.

Autosorb-1 in order to obtain surface areas of greater accuracy, as well as to obtain pore size distributions and total pore volumes, using the BET and DFT Monte-Carlo methods respectively (Table 3.17. and Figure 3.22.). As mentioned in Section 2.4.9., the Autosorb-1 also differs from the Gemini apparatus by allowing samples to be pre-treated under vacuum, allowing lower temperatures to be used, which can significantly alter the physical properties of the heat sensitive precursors. This is clearly apparent for the precursor prepared using ammonium carbonate, whereby the BET surface area is actually  $35 \text{ m}^2 \text{ g}^{-1}$  and not  $16 \text{ m}^2 \text{ g}^{-1}$ . This now illustrates that the surface area decreases after calcination regardless of washing treatment. However, with the exception of the precursors both instrumentation gave similar surface areas and trends for all the materials analysed.

At this point it is important to discuss the Autosorb-1 findings together with the TGA/DTA and XRD findings. For the precursor prepared using  $\text{NH}_4\text{CO}_3$ , the co-existing by-phase decomposes highly exothermically during calcination, which subsequently results in loss of  $\text{HT-CO}_3$ . This is responsible for crystallisation of the material. With washing, the by-phase content is reduced,  $\text{HT-CO}_3$  is retained and hence the material remains largely amorphous after calcination. However, the surface areas and porosities are similar in both cases with a slightly higher surface area produced from washing. However, the one material has  $\text{HT-CO}_3$  present whilst the other does not and therefore the findings of the Autosorb-1 reflect contributions from both metal oxide sintering, as well as loss of the residual carbonate.

Using  $\text{Na}_2\text{CO}_3$  produces precursors with much higher BET surface areas than using  $\text{NH}_4\text{CO}_3$  or  $(\text{NH}_4)\text{HCO}_3$ . The  $\text{HT-CO}_3$  also decomposes at higher temperature, which indicates a greater degree of mixing and dilution of the metal components. This clearly indicates that the use of ammonia disrupts the precipitation process, most likely from the simultaneous formation of the copper ammine complex. In other words, the presence of sodium does not hinder the precipitation step, and in fact superior precursors are obtained. Interestingly, the co-existing by-phase reacts differently in this precursor, whereby no highly exothermic processes occur during the calcination step and therefore the  $\text{HT-CO}_3$  is retained even without washing treatment. However, the XRD still shows strong crystallinity for this material. Studies on related catalysts systems which investigated sodium deactivation through doping experiments have also reported that crystallisation increases with higher sodium loadings after calcination<sup>(28-30)</sup>. It is thus apparent that even with  $\text{HT-CO}_3$  present, this cannot be prevented. Furthermore, the BET surface area is significantly lower and the CuO crystallite size larger in comparison to unwashed materials prepared using  $\text{NH}_4\text{CO}_3$ . In fact the use of washing is much more influential when using  $\text{Na}_2\text{CO}_3$ , as surface areas can drastically drop from 56 to  $16 \text{ m}^2 \text{ g}^{-1}$

**Table 3.17.** BET surface areas and pore volumes of precursors prepared by co-precipitation before and after calcination treatment. C values provided to indicate degree of accuracy for each analysis. Analysis obtained from Autosorb-1 instrumentation.

Precipitation reagent	Washing treatment	Calcination treatment	Surface area ( $\text{m}^2 \text{g}^{-1}$ ) <sup>a</sup>	C value	Total pore volume ( $\text{cm}^3 \text{g}^{-1}$ ) <sup>b</sup>
$(\text{NH}_4)_2\text{CO}_3$	Yes	None	35	28.5	0.3
$(\text{NH}_4)_2\text{CO}_3$	Yes	Yes	30	32	0.3
$(\text{NH}_4)_2\text{CO}_3$	None	Yes	28	28	0.3
$\text{Na}_2\text{CO}_3$	Yes	Yes	56	70	0.7
$\text{Na}_2\text{CO}_3$	None	Yes	16	16	0.15

<sup>a</sup> Standard deviation  $\pm 0.5 \text{ m}^2 \text{g}^{-1}$ .

<sup>b</sup> Standard deviation  $\pm 0.1 \text{ cm}^3 \text{g}^{-1}$ .

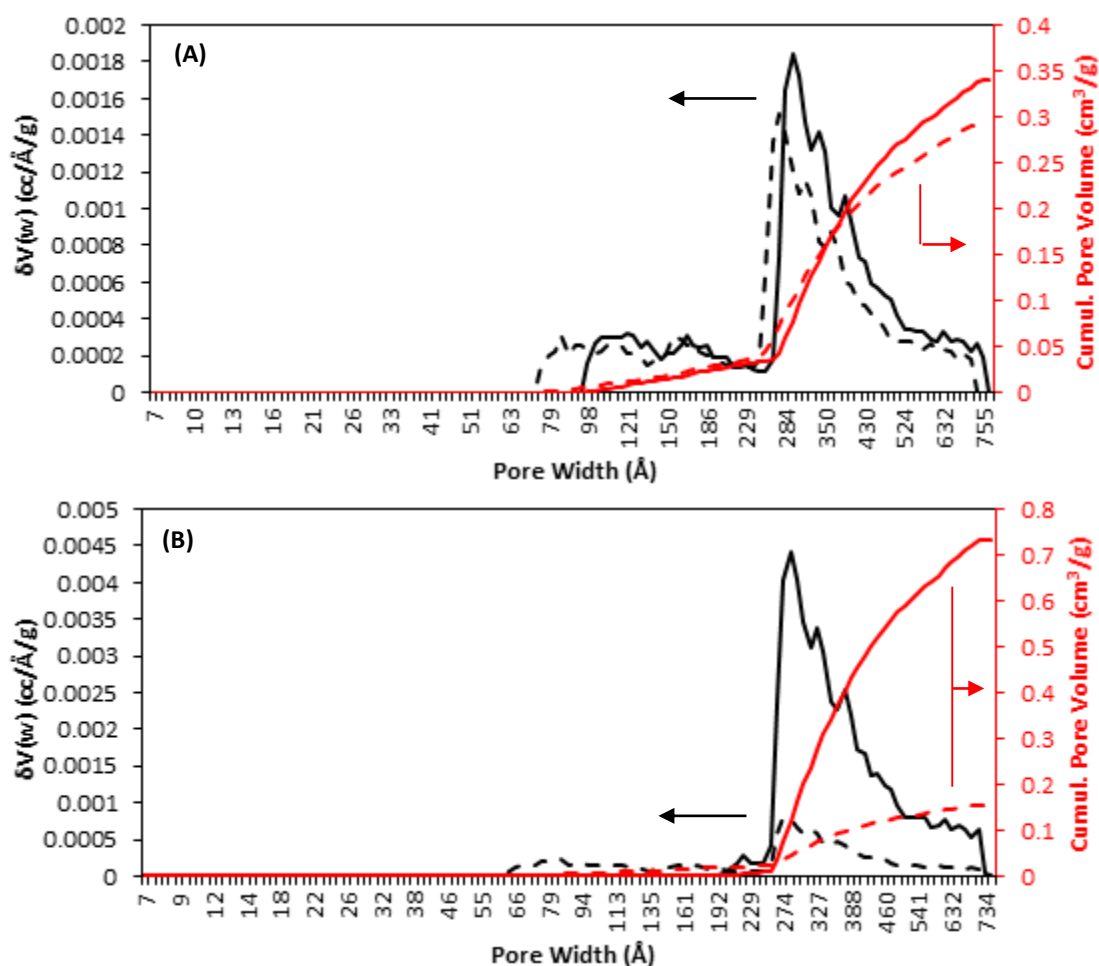


**Figure 3.22.** DFT Monte-Carlo pore size distribution and cumulative pore volume for calcined materials prepared from zincian georgeite precursors using: (A) ammonium carbonate (B) sodium carbonate. Solid lines represent samples which were washed prior to calcination with hashed lines representing samples not washed. Arrows are also provided for clarity.

and pore volumes from 0.7 to 0.15 cm<sup>3</sup> g<sup>-1</sup> without it. Clearly the deactivation from residual sodium comes from the subsequent thermal steps, and proceeds by a completely different mechanism in comparison to when ammonium by-phases are present. Furthermore, the ammonium by-phase appears to be removed after the calcination step, whilst the unidentified sodium by-phase remains. It is not known how the sodium by-phase effects the hydroxycarbonate during the calcination process to significantly alter the physical properties and any further interpretation would be highly speculative.

Further investigation was carried out by performing copper surface area analysis on all of the resulting catalysts, with normalised copper surface areas also calculated using the EDX findings (Figure 3.23). For direct comparison, analysis was also performed on a catalyst derived from the 2/1 zincian malachite precursor which was determined to be 18 m<sup>2</sup> g<sup>-1</sup>. This is in strong agreement with Behrens who reported a similar value for the exact same catalyst<sup>(15)</sup>. The trend for the copper surface area values is in large agreement with the trend for the BET findings. Higher values were determined from the catalysts that had been washed prior to calcination, whereby this is most significant for the catalyst prepared using Na<sub>2</sub>CO<sub>3</sub>. It is not known if the presence of sodium assisted further in the decrease of the surface area during the reduction step. However, the most significant conclusions drawn from these findings relates to the fact that catalysts can be prepared from georgeite precursors which match or even surpass copper surface areas achieved in industrial

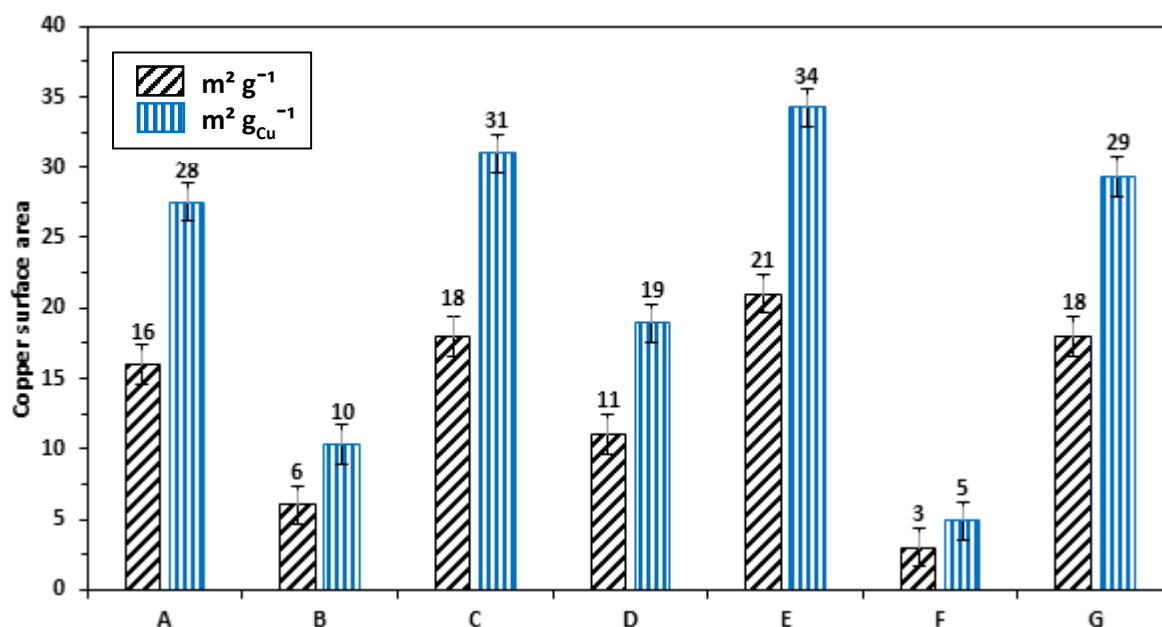


**Figure 3.23.** Copper surface area analysis of Cu/ZnO catalysts prepared from co-precipitation using various precipitation reagents and washing treatments. Normalised copper surface areas calculated using EDX findings and assuming only Cu and ZnO phases present prior to analysis. Catalysts: Ammonium carbonate (A) washed and (B) not washed. Ammonium bicarbonate (C) washed and (D) not washed. Sodium carbonate (E) washed and (F) not washed. (G) JM zincian malachite standard.

catalysts prepared from malachite precursors. The normalised copper surface areas also illustrate that the dispersion of copper is also rivalled. It is tempting to relate these observations to the sodium loadings determined for each catalyst, however, the catalyst prepared using  $\text{Na}_2\text{CO}_3$  had the highest sodium loading out of all the catalysts that were washed. This catalyst had the highest copper surface area of  $21 \text{ m}^2 \text{ g}^{-1}$  from a sodium weight of 0.589%. Without washing, the copper surface area reduced to  $3 \text{ m}^2 \text{ g}^{-1}$  from a sodium weight of 7%. However, related studies by Lee and co-workers have reported similar findings whereby the copper surface area is significantly altered from varying the sodium weight between 0.1 and 4%<sup>(28)</sup>. In other words, high copper surface areas can still be produced if the sodium weight is kept well below 1%. It is also likely that the higher surface area and porosity produced after calcination enabled this catalyst to compete against the catalysts prepared from ammonium (bi)carbonate.

Selected catalyst were investigated further by  $\text{CO}_2$ -TPD since  $\text{CO}_2$  is a reactant and product molecule in methanol synthesis and the LTS reaction, respectively (Figure 3.24.). This could therefore shed new light on the understanding of these reactions. In particular, since  $\text{CO}_2$  is an acidic molecule used to study basic materials it was anticipated that with higher amounts of sodium, the desorption behaviour would drastically change. The 2/1 catalyst prepared from SAS precipitation was also investigated for comparison, with all the data normalised to catalyst mass. The hashed vertical line on the TPD profiles is positioned at  $220 \text{ }^\circ\text{C}$  which is the frequent temperature used for industrial testing. Therefore, adsorbed  $\text{CO}_2$  species associated with peaks below this temperature are expected

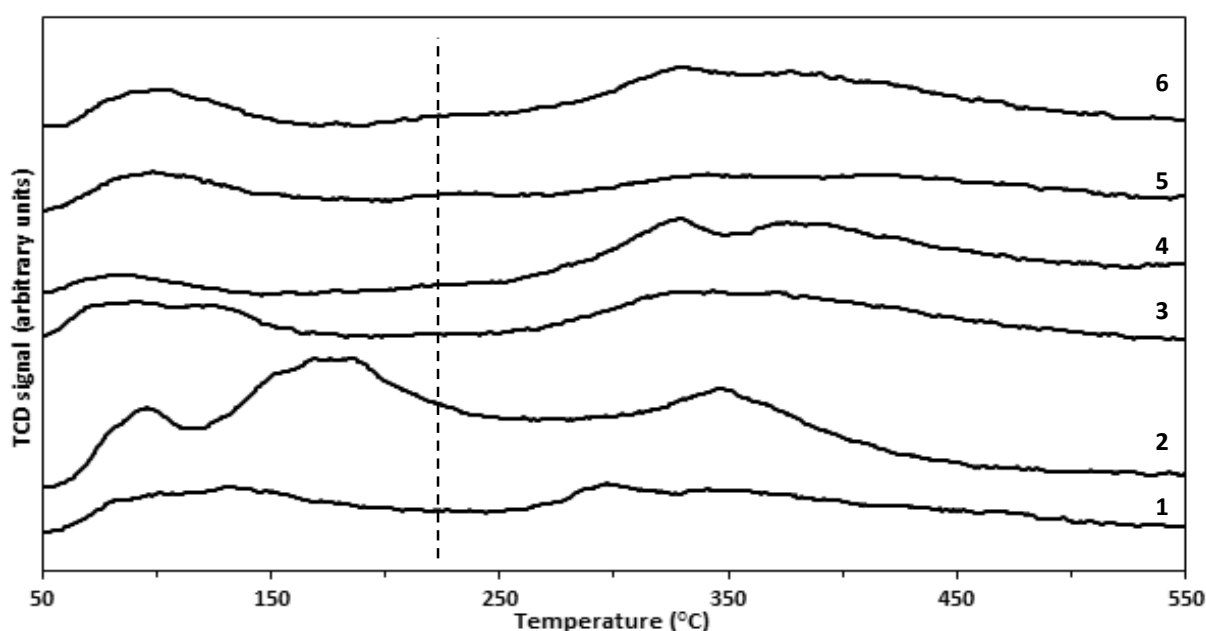


**Figure 3.24.**  $\text{CO}_2$ -TPD profiles of Cu/ZnO catalysts prepared from co-precipitation using various precipitation reagents and washing treatments: Sodium carbonate (1) washed and (2) not washed. Ammonium carbonate (3) washed and (4) not washed. Standards: (5) JM zincian malachite and (6) SAS prepared from zincian goergeite (2/1). Hashed line at  $220 \text{ }^\circ\text{C}$  indicates temperature used for LTS testing carried out at JM.

to play a more significant role, since CO<sub>2</sub> which remains adsorbed on the sites at higher temperature will be difficult to desorb under reaction conditions. The majority of the profiles display a low temperature peak centred at 96 °C, and a much broader peak at higher temperature which actually consists of a doublet centred at 331 and 380 °C. These findings strongly match the CO<sub>2</sub>-TPD profiles obtained by Lee and co-workers, although they report peaks at 170 and 477 °C for their catalysts with low sodium loadings<sup>(28)</sup>. They assign the low temperature peak to desorption from metallic copper and the high temperature peak to desorption from ZnO. It would be expected that the site where CO<sub>2</sub> is removed at ~96 °C is exceptionally labile under reaction conditions. For the catalysts prepared using Na<sub>2</sub>CO<sub>3</sub> the profiles are slightly different. The non-washed catalyst contains an additional peak at 178 °C. This peak is likely a result of the higher sodium loading, whereby the alkali metal strongly binds the acidic CO<sub>2</sub> molecule and requires additional energy for desorption. With the washing step included, this peak is absent although interestingly a low intensity peak appears at 132 °C. For the SAS prepared and JM catalysts, the profiles are similar. It suggests that the TPD profiles only show clear differences when comparisons are made between catalysts with significantly different sodium loadings. These conclusions are again in agreement with Lee and co-workers.

### 3.5.2. Conclusions from co-precipitation studies on zincian georgeite

This work has demonstrated that zincian georgeite precursors can be readily made by co-precipitation free of nitrate and alkali-metal reagents, which are detrimental both from an environmental and industrial perspective. Furthermore, it is shown that these precursors have the capacity to compete with the zincian malachite precursor, whereby similar copper surface areas can be obtained. This was achieved simply by modifying certain parameters of the optimised industrial co-precipitation route. This clearly has significant implications regarding how this precursor is perceived in the context of hydroxycarbonate preparation and subsequent catalyst optimisation.

Zincian georgeite precursors can be prepared from both sodium and ammonium carbonates, with the washing procedure a key step in the preparation of optimum catalyst systems. This is because the co-existing by-phase is detrimental to the physicochemical properties, since deactivation occurs during the thermal treatment steps. This hinders the ability to fully exploit the potential of the co-precipitation route. The mechanism for deactivation depends on the by-phase present and for sodium this is still not well understood. Precursors prepared by sodium carbonate are superior to those prepared from ammonium carbonates, but ultimately the final state catalysts have similar copper surface areas. It is therefore plausible that the higher sodium content plays a pivotal role in the reduction of the copper surface area. It is also anticipated that such catalysts will also be inferior to those prepared using ammonium carbonates as a result of enhanced catalyst deactivation. The

desorption properties of CO<sub>2</sub> during the reaction process will also likely be influenced by the content of alkali-metal. Overall, this work has paved the way forward for further investigations with additional optimisation of the procedure still possible. The benchmark has been set as whilst copper surface areas up to 18 m<sup>2</sup> g<sup>-1</sup> can be achieved at present from co-precipitation, the SAS process in comparison produces copper surface areas up to 29 m<sup>2</sup> g<sup>-1</sup>.

### 3.6. Catalyst testing of georgeite materials

The work carried out in **Sections 3.2-3.5.** enabled suitable georgeite precursors to be selected for testing at Johnson Matthey in Billingham for methanol synthesis and the LTS reaction. Precursors were prepared by both SAS and co-precipitation and scaled up to produce ~20 g of each material. The precursors were calcined at Johnson Matthey with the conditions used similar to those implemented in previous sections: 1 °C/min to 300 °C and held for 4 hours in static air. A low ramp rate was decided after observation of the TGA findings in **Section 3.5.** (**Figure 3.20.**). The materials were also characterised to verify previous findings. The resulting catalysts were trialled and tested against established industrial catalysts for both reactions. Such catalysts have been successfully prepared from routes that were patented in the 1960's and 1970's<sup>(31-32)</sup>.

#### 3.6.1. Results and discussion

In total six georgeite precursors were prepared for testing, and additional characterisation with the synthesis details of each material provided (**Table 3.18.**). In brief, the effect of water content (10 and 5%), Cu/Zn molar ratio (2/1 and 1/1) and aluminium addition was investigated for the SAS prepared

**Table 3.18.** Synthesis details, EDX analysis and calcination details of selected georgeite precursors scaled up for analysis and testing at JM in Billingham.

Synthesis method	Water content (%)	Nominal metal molar ratio	Atomic (%) <sup>a</sup>			Mass loss on calcination (%)	Colour after calcination
			Cu	Zn	Al		
SAS	10	2/1	67	33	-	24	Black
SAS	5	2/1	67	33	-	23.9	Dark brown
SAS	5	1/1	48	52	-	23.2	Dark green
SAS <sup>b</sup>	5	6/3/1	59	29	12	28.4	Dark brown
CP <sup>c</sup>	-	2/1	68	32	-	15.4	Green
CP <sup>d</sup>	-	2/1	65	35	-	17.2	Green

<sup>a</sup> EDX standard deviation ±1%.

<sup>b</sup> Prepared using aluminium boehmite. EDX standard deviation ±3%.

<sup>c</sup> Prepared using 15 mg/ml copper acetate and 8.246 mg/ml zinc acetate with washing step included.

<sup>d</sup> Prepared using 70 mg/ml copper acetate and 38.482 mg/ml zinc acetate with washing step included.

Materials, whilst the effect of starting reagent concentrations (using 15 and 70 mg/ml copper acetate) was investigated for materials prepared by co-precipitation using  $(\text{NH}_4)_2\text{CO}_3$ . The precursors were analysed using EDX analysis in order to determine metal molar compositions. The results are in strong agreement with the previous findings. A slight Cu deficiency was found for the SAS 1/1 precursor, which was also apparent for the precursor prepared by co-precipitation using concentrated starting reagents. Interestingly though, by using more dilute concentrations in the co-precipitation procedure, whereby there is less ammonia present in the mother liquor solution, precursors with the correct Cu/Zn molar ratio can be produced from this route. This supports the theory that higher concentrations of  $(\text{NH}_4)_2\text{CO}_3$  results in greater Cu deficiencies in the resulting precursor (**Equation 3.10**). For the SAS precursor prepared with aluminium the observations learned from the earlier findings enabled the correct Cu/Zn/Al molar ratio of 6/3/1 to be achieved from fine-tuning the Al boehmite content.

The mass loss and resulting colour of the materials was recorded after calcination. From the TGA findings, a mass loss ~18-21% was expected for all materials. However, this analysis does not consider holding these materials for 4 hours at 300 °C where additional loss could be expected. The majority of the samples were dark in colour suggesting variations in the amount of retained residual content. Surprisingly, for the co-precipitated materials mass losses were close to 18% as predicted from previous TGA findings, but the samples were green meaning a higher content of residual material had been retained. All the materials were crushed and sieved to give pellets of particle size 0.621 mm in diameter.

The calcined materials were analysed further by XRD, which showed that the samples remained largely amorphous after the calcination procedure. However, ill-defined CuO reflections were identified from the material prepared by co-precipitation using concentrated reagents (**Figure S11**). The SAS 6/3/1 material displayed the sharpest CuO reflections as well as reflections for the Al boehmite phase. The residual HT- $\text{CO}_3$  retained after calcination is attributed to the amorphous nature being preserved. These findings are also in agreement with the previous work.

Since all six samples had been prepared using sodium-free reagents of high purity grade, the sodium loadings were determined using MP-AES analysis and compared against the binary zincian malachite precursor (**Table 3.19**). It should be noted that analysis was carried out on the materials after calcination. The sodium loadings of the final state catalysts could then be calculated from the mass losses determined after the reduction step. All of the calcined materials had exceptionally low sodium levels in the range 11-32  $\text{mg}_{(\text{Na})}\text{kg}_{(\text{CuO/ZnO})}$ . For comparison, the sodium loading determined in **Section 3.5** for the calcined zincian malachite material was 695  $\text{mg}_{(\text{Na})}\text{kg}_{(\text{CuO/ZnO})}$ . There is clearly a

**Table 3.19.** MP-AES analysis to determine sodium loadings of calcined and reduced samples.

Catalyst synthesis details	Determined Na loading (mg/L) <sup>a</sup>	mg <sub>(Na)</sub> kg <sub>(CuO/ZnO)</sub> <sup>-1</sup>	Mass loss on reduction (%) <sup>b</sup>	mg <sub>(Na)</sub> kg <sub>(Cu/ZnO)</sub> <sup>-1</sup>
SAS 10% 2/1	0.6	32	27.25	44
SAS 5% 2/1	0.5	25	27.8	34.6
SAS 5% 1/1	0.49	24.5	24.88	32.6
SAS 5% 6/3/1	0.31	15.5	22.06	19.9
CP (15 mg/ml)	0.33	16.5	32.15	24.3
CP (70 mg/ml)	0.22	11	31.72	16.1

Calibration standards prepared using 20 vol.% aqua regia/deionised water as solvent.

<sup>a</sup> Standard deviation  $\pm 0.02$  mg/L. Analysis carried out on calcined materials after they were digested.

<sup>b</sup> Determined from Cu surface area analysis carried out at JM.

significant difference in these sodium loadings. In related work, Kondrat reported sodium loadings of 82 mg<sub>(Na)</sub>kg<sub>(CuO/ZnO)</sub> for SAS prepared 2/1 zincian georgeite, and 590 mg<sub>(Na)</sub>kg<sub>(CuO/ZnO)</sub> for the zincian malachite reference after calcination using AAS<sup>(1)</sup>. The findings are therefore in rough agreement considering the different analytical techniques used, and the comparison further emphasises the large difference in sodium levels between the georgeite and malachite materials. It should be noted that potassium loading were also investigated. Loadings in the range 1-4 mg<sub>(K)</sub>kg<sub>(CuO/ZnO)</sub> were determined for the calcined georgeite samples and 7 mg<sub>(K)</sub>kg<sub>(CuO/ZnO)</sub> was determined for the calcined zincian malachite reference. Since no potassium reagents were used in the synthesis of any of these samples, these loadings are similar.

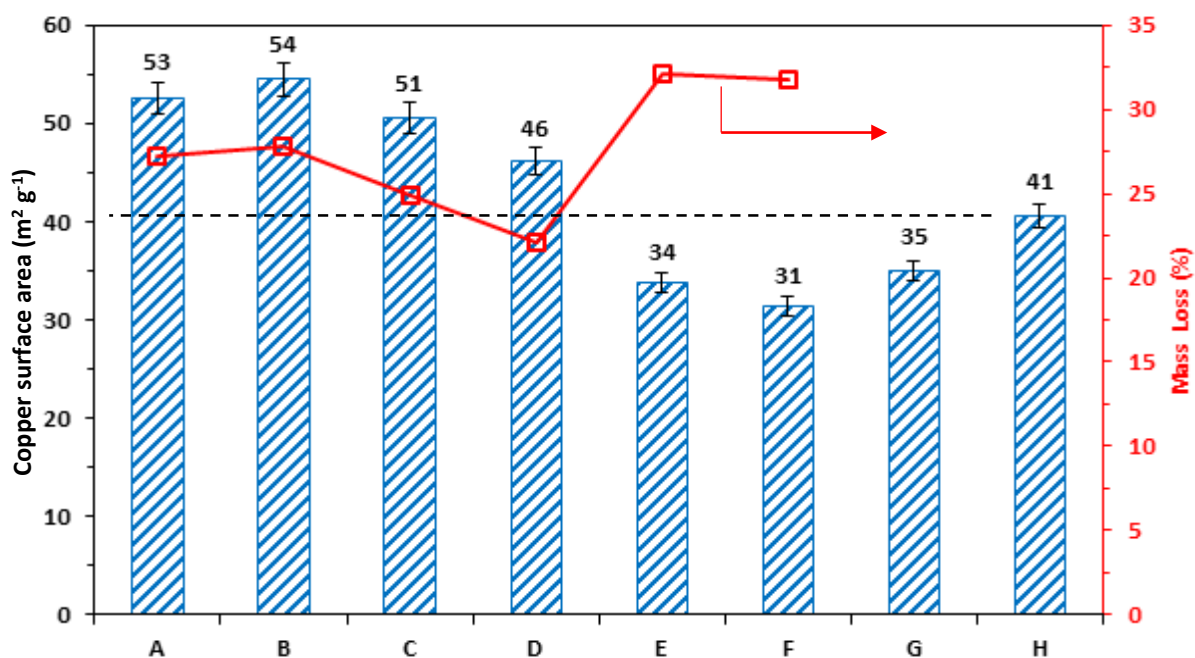


**Figure 3.25.** Copper surface area analysis from reactive frontal chromatography with subsequent mass loss for catalysts: (A) SAS 10% H<sub>2</sub>O (2/1) (B) SAS 5% H<sub>2</sub>O (2/1) (C) SAS 5% H<sub>2</sub>O (1/1) (D) SAS 5% H<sub>2</sub>O (6/3/1) (E) CP 15 mg/ml Cu(OAc)<sub>2</sub> (2/1) (F) CP 70 mg/ml Cu(OAc)<sub>2</sub> (2/1). Standards: (G) CP malachite (2/1) (H) JM 51-2 methanol synthesis industrial catalyst. An arrow is also provided for clarity.

Copper surface area analysis was performed on all six catalysts using reactive frontal chromatography and compared against the catalyst derived from co-precipitated zincian malachite, as well as the 51-2 methanol synthesis industrial standard (**Figure 3.25.**). The findings largely agree with the analysis reported in previous sections. The binary SAS prepared catalysts have the same value within the error limits of the analysis, ranging between 51-54 m<sup>2</sup> g<sup>-1</sup>. This was encouraging since the 51-2 standard has a value of 41 m<sup>2</sup> g<sup>-1</sup> in comparison. This standard can be directly compared against the SAS 6/3/1 catalyst since they have the same metal composition. The incorporation of Al sol into the catalyst resulted in a slight reduction in copper surface area to 46 m<sup>2</sup> g<sup>-1</sup>, but was still higher than the standard. These findings provide further evidence that higher copper surface areas are produced using the SAS precipitation route. For the catalysts prepared by co-precipitation lower values in the range 31-34 m<sup>2</sup> g<sup>-1</sup> were determined. The concentration of (NH<sub>4</sub>)<sub>2</sub>CO<sub>3</sub> used in preparation most likely influenced this value in the resulting catalysts. It was also useful to verify the findings in **Section 3.5.**, as it's clear these copper surface areas rival that produced from the zincian malachite derived catalyst. It could be argued that the optimum calcination conditions were not used for this precursor. The subsequent mass loss resulting from the reduction step is also provided for each catalyst. This includes loss of residual carbonate in addition to the reduction of CuO. The findings overall reflect the mass losses observed from calcination, whereby higher contents of residual material retained after calcination resulted in higher mass losses after reduction.

All of the catalysts prepared from SAS precipitation and one catalyst prepared from co-precipitation were tested for methanol synthesis, and compared against the established 51-2 methanol synthesis industrial catalyst (**Figure 3.26.**). As stated previously, the 51-2 catalyst has a metal composition of 6/3/1 and so can be directly compared against the SAS 6/3/1 catalyst, albeit the former contains the Al<sub>2</sub>O<sub>3</sub> phase whilst the latter contains the Al boehmite sol. This industrial catalyst also has a sodium loading similar to that determined for the zincian malachite reference.

For methanol synthesis both the activity and the stability of the catalysts was examined. The initial testing began at 190 °C and after 18 hours the temperature was increased by 15 °C and held for another 18 hours. The purpose was to analyse the stability of the catalysts at each set temperature. This sequence continued up to 250 °C, whereby after 18 hours, the temperature was reduced back down to 190 °C for a final 18 hours to evaluate the final stabilities. This was achieved by comparing the initial and final activities both at 190 °C. The time on line activity for all catalysts is presented up to 235 °C (**Figure 3.26(1).**). The MeOH space time yields determined at the end of each set temperature is also summarised (**Table S4.**). Catalyst activities decreased between 235 and 250 °C as

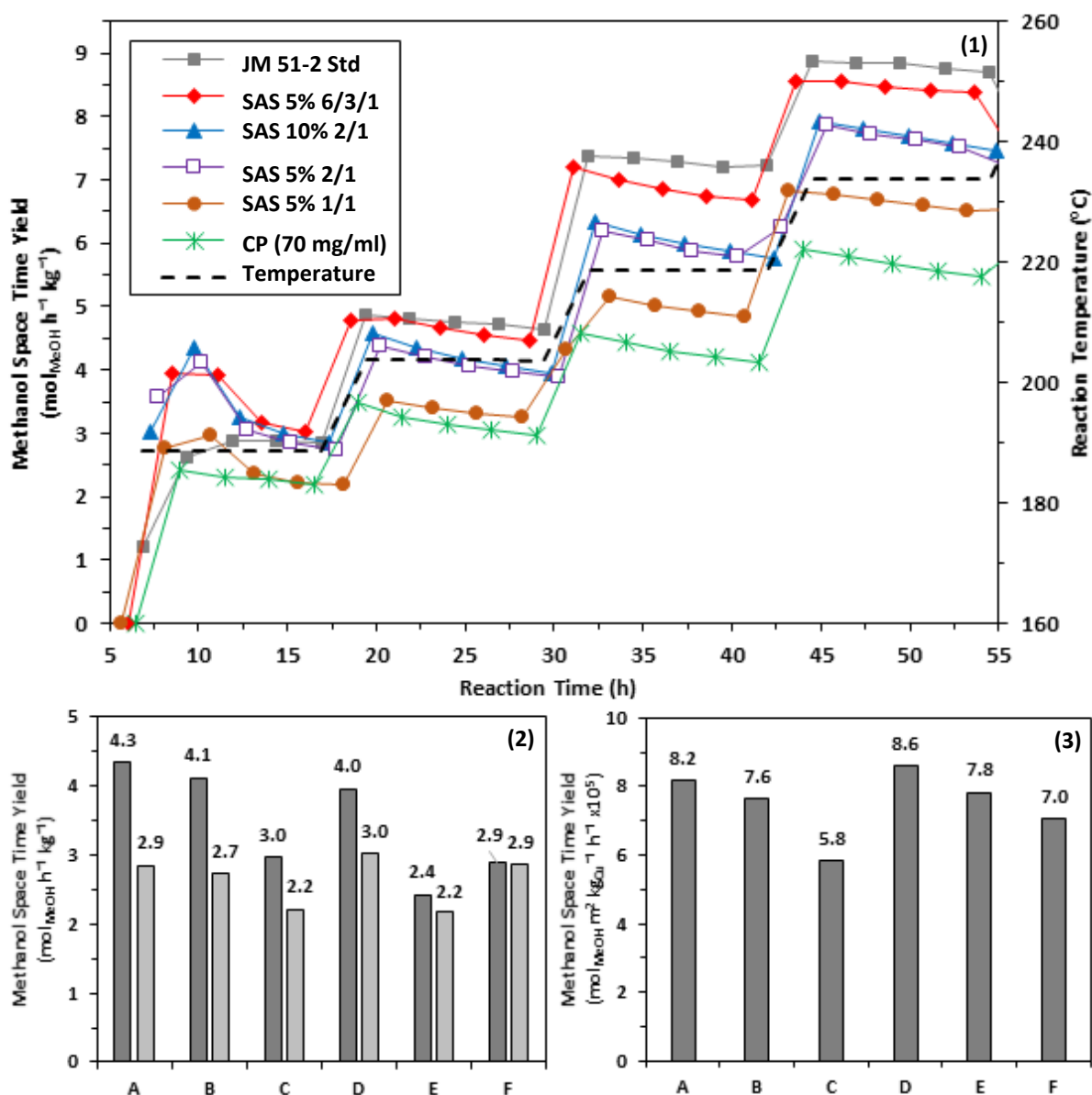


**Figure 3.26.** Catalyst testing for methanol synthesis: (1) Time on line activity with catalyst stability also examined. Reaction temperature was increased 15 °C every 18 hours between 190-235 °C. (2) Initial methanol productivity (dark grey) and stabilised activity (light grey) after 10 and 18 hours on line respectively at 190 °C (3) Initial copper surface area normalised methanol productivity. Catalysts: (A) SAS 10% H<sub>2</sub>O (2/1) (B) SAS 5% H<sub>2</sub>O (2/1) (C) SAS 5% H<sub>2</sub>O (1/1) (D) SAS 5% H<sub>2</sub>O (6/3/1) (E) CP (2/1) (F) JM 51-2 industrial catalyst.

a result of methanol condensation in the lines. The 51-2 standard and the SAS 6/3/1 catalyst displayed the highest overall activity and stability for methanol synthesis at temperatures  $\geq 205$  °C. It is apparent that the SAS catalyst matched the activity of 51-2 at the start of this temperature, but the catalyst deactivated faster, and was seen to lag behind the industrial standard for the remainder of the testing. After testing was complete, the standard had deactivated by 16% based on initial activity whilst the SAS catalyst had deactivated by 33%. Since all the other catalysts demonstrated lower stabilities this promotion in catalyst stability and lifetime is attributed to the incorporation of Al into the catalyst, in agreement with the literature<sup>(20-21,25,33-36)</sup>. Interestingly, since both catalysts

used different Al reagents, it is possible that the difference in stability is attributed to this phase type. Comparison of the two binary 2/1 SAS catalysts demonstrated that the effect of water content is negligible. These catalysts which also displayed very similar copper surface areas had almost identical time on line profiles. Using 5% water would have increased the acetate content in the precursor, which was expected to result in a reduced copper surface area. However, the lower ramp rate used in the calcination procedure and the processing of these materials into pellets are factors which could have resulted in similar surface areas in the final state catalysts. Surprisingly, whilst the copper surface area of the SAS 1/1 catalyst was similar in comparison to the SAS 2/1 catalysts the activity was significantly lower. Behrens and co-workers have reported that the active site for methanol synthesis consists of Cu steps decorated with Zn atoms, whereby Zn strengthens binding of the intermediates, and in particular, serves as an adsorption site for oxygen-bound species<sup>(33)</sup>. This catalyst was therefore expected to be more active in contrast to these findings. It is plausible that active site blocking was a problem for this catalyst resulting in reduced activity. In relation to the Behrens findings, the stronger binding of oxygen containing intermediate species from higher Zn contents could be attributed to this site blocking. The catalyst prepared from co-precipitation displayed the lowest activity out of all catalysts tested. This was expected as it had the lowest determined copper surface area.

The time on line findings show for the first 10 hours at 190 °C the catalyst activities did not follow the same trend to the rest of the testing already discussed. This was outlined more clearly by comparing initial activities against stabilised activities (**Figure 3.26(2)**). The SAS 6/3/1 catalyst and SAS 2/1 catalysts have significantly higher initial activities in the range 4.1-4.3 mol<sub>MeOH</sub> h<sup>-1</sup> kg<sup>-1</sup>, in comparison to the 51-2 standard which was 2.9 mol<sub>MeOH</sub> h<sup>-1</sup> kg<sup>-1</sup>. This was also reflected in the intrinsic catalyst activities determined for initial activities (**Figure 3.26(3)**). In fact all prepared catalysts illustrated higher initial intrinsic activities in comparison to the 51-2 standard, with the exception of the SAS 1/1 catalyst. This means they have a higher 'quality' of Cu surface, which implies either the active sites present are higher in activity or there is a higher density of these sites. Interestingly, the SAS 6/3/1 catalyst had the highest initial intrinsic activity, and evidently this is apparent for the entire testing procedure in relation to the other georgeite derived catalysts. This is again in direct contrast to findings reported by Behrens and co-workers who reported that the intrinsic activity decreases when Al is incorporated into the catalyst<sup>(25)</sup>. This further illustrates differences between the two catalyst systems.

Whilst the georgeite derived catalysts display the highest initial activities at 190 °C, ultimately the 51-2 standard illustrates the highest overall activity. It is therefore apparent that deactivation is the

fundamental cause of preventing the full potential of these catalysts from being exploited. Interestingly, the degree of deactivation is not the same for each catalyst in this initial 18 hours (**Figure 3.26(2)**). Deactivation was lower for the SAS 6/3/1 and 1/1 catalysts ( $0.8\text{--}1 \text{ mol}_{\text{MeOH}} \text{ h}^{-1} \text{ kg}^{-1}$ ) in comparison to the SAS 2/1 catalysts ( $1.4 \text{ mol}_{\text{MeOH}} \text{ h}^{-1} \text{ kg}^{-1}$ ), which might be expected from the higher Zn and Al contents used. However, the 2/1 catalyst prepared by co-precipitation displayed the lowest degree of deactivation ( $0.2 \text{ mol}_{\text{MeOH}} \text{ h}^{-1} \text{ kg}^{-1}$ ). It also had the lowest activity which is possibly linked to this deactivation rate. Deactivation is usually attributed to sintering of Cu crystallites and at temperatures  $\geq 205 \text{ }^\circ\text{C}$  investigated, this mechanism would have accelerated. However, this does not explain these observed trends for initial deactivation rates at  $190 \text{ }^\circ\text{C}$ . In related work, Sehested and co-workers studied the deactivation process in binary Cu/ZnO catalysts under methanol synthesis and LTS testing conditions using DFT calculations<sup>(37)</sup>. They report that sintering depends on several factors, including the syn-gas composition. In particular, the abundance and diffusion rates of Cu-X species is critical, whereby CuCO and Cu<sub>2</sub>HCOO species are predominant for Cu transport. Therefore, it is plausible that the catalysts displaying highest activity are more susceptible to deactivation from a greater abundance of Cu transport species, facilitating agglomeration and sintering.

Kondrat also tested georgeite derived catalysts for methanol synthesis, whereby the same trends in terms of activity and stability in relation to the 51-2 standard were apparent<sup>(41)</sup>. Interestingly, it was concluded that reduced sodium loadings did not result in any improvement in terms of either activity, stability or selectivity. Furthermore for the SAS prepared catalysts, copper surface areas did not correlate to the methanol synthesis activities. The findings presented herein are in agreement and verifies these conclusions. Whilst no selectivity data was determined in this study, Kondrat reports georgeite derived catalysts all have methanol selectivity  $> 99\%$ <sup>(41)</sup>. This is also obtained from standard malachite derived catalysts as reported by Spencer<sup>(38)</sup>.

All of the georgeite derived catalysts were tested for the LTS reaction, and compared against the established 83-0 industrial catalyst (**Figure 3.27.**). The reaction conditions are more aggressive in comparison to methanol synthesis, since high partial pressures of steam are utilised. Consequently, this industrial standard has a typical composition of 33% CuO, 34% ZnO and 33% Al<sub>2</sub>O<sub>3</sub><sup>(39-40)</sup>. The copper surface area is also not measured by JM since it is not deemed an essential component of an optimum catalyst, and therefore, intrinsic activities could not be compared.

In complete contrast to the methanol synthesis findings, all the catalysts displayed remarkable activity and stability in comparison to the 83-0 standard. The SAS prepared catalysts all had initial CO conversions  $\sim 96\%$ . After 135 hours online, the degree of deactivation was negligible and was 1.3-

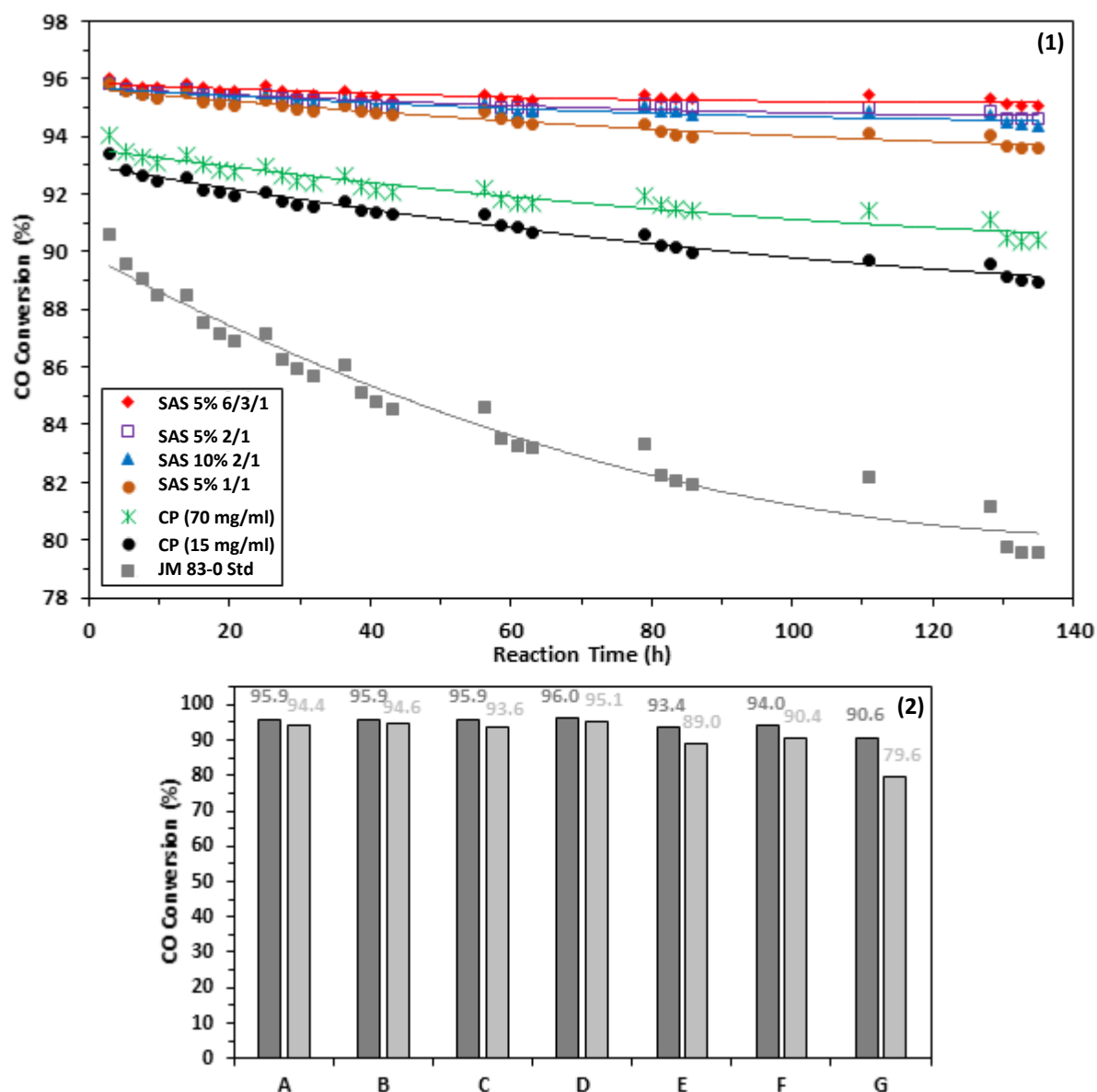


**Figure 3.27.** Catalyst testing for the LTS reaction: (1) Time on line activity (2) Initial CO conversion (dark grey) and stabilised activity (light grey) after 135 hours on line. Catalysts: (A) SAS 10% H<sub>2</sub>O (2/1) (B) SAS 5% H<sub>2</sub>O (2/1) (C) SAS 5% H<sub>2</sub>O (1/1) (D) SAS 5% H<sub>2</sub>O (6/3/1) (E) CP 15 mg/ml Cu(OAc)<sub>2</sub> (2/1) (F) CP 70 mg/ml Cu(OAc)<sub>2</sub> (2/1) (G) JM 83-0 LTS industrial catalyst.

1.5% for the 2/1 catalysts, 2.3% for the 1/1 catalyst and 0.9% for the 6/3/1 catalyst. This demonstrates that Al incorporation is not essential for an optimum LTS catalyst. In fact, the 83-0 standard with ~33% Al<sub>2</sub>O<sub>3</sub> content deactivated by 11% in the same timeframe, with the initial activity only 90.6%. This was highly unexpected since the LTS reaction conditions are harsher to those used in methanol synthesis. The LTS reaction temperature was 220 °C, whilst for methanol synthesis it started at 190 °C, where severe deactivation was apparent. This further illustrates that the reaction temperature is not the only factor which influences the rate of sintering. It is clear that the two reactions have alternative mechanisms for catalyst deactivation. Furthermore, for LTS the SAS 1/1 catalyst deactivated more than the SAS 2/1 catalysts, which was also not apparent in methanol

synthesis. Overall this suggests that the content of Zn and Al, which are widely cited as stabilisers in preventing Cu sintering<sup>(39-41)</sup>, are less influential in suppressing deactivation rates in this reaction.

The most significant finding is attributed to the performances displayed by the catalysts prepared by co-precipitation. These binary catalysts were also superior to the 83-0 standard, having initial CO conversions of 93.4-94%, and still only deactivating by 3.6-4.4% after 135 hours on line. This is astonishing since well cited literature reports that construction of catalysts from amorphous precursors is expected to result in reduced performance levels<sup>(4,42-43)</sup>. Moreover, this was again achieved without Al being incorporated into these catalysts. Whilst they do not achieve the same level of performance seen with the SAS catalysts, they are prepared from energy sustainable production routes which makes them a realistic alternative and attractive option to industry.

The enhanced catalyst performance of the georgeite derived catalysts in comparison to the 83-0 standard for the LTS reaction is at least partly attributed to the sodium loadings. The 83-0 standard after calcination would have a sodium loading in the range 590 mg<sub>(Na)</sub>kg<sub>(CuO/ZnO)</sub> seen for the binary zincian malachite material. In comparison, loadings in the range 11-32 mg<sub>(Na)</sub>kg<sub>(CuO/ZnO)</sub> were determined for the georgeite derived catalysts. The deactivation of Cu/ZnO/Al<sub>2</sub>O<sub>3</sub> catalysts by residual alkali-metal levels for the LTS reaction has been documented<sup>(30)</sup> and in **Section 3.5**. this was investigated in more detail. It is plausible from these findings that residual sodium could reduce intrinsic catalyst activities by binding CO<sub>2</sub> product molecules more strongly to the surface thus blocking potential active sites. The SAS prepared catalysts, therefore, display optimum performance as a result of having low sodium loadings combined the high large copper surface areas. Interestingly, these catalysts also deactivated to a lesser extent than those prepared by co-precipitation. This could be reflected in the chemical memory of the catalyst<sup>(15,25,33-34)</sup>. Since this is a structure sensitive reaction, differences in the preparation methodology might prove pivotal in influencing the behaviour of the final state catalyst.

The catalyst activities were examined further by monitoring CO conversion, as a function of both mass and space velocity (**Figure 3.28.**). These tests were carried out after the catalysts had stabilised for 96 hours. Total gas flow rates were varied in the range 34-136 L/h. This enabled the activity of the catalysts to be monitored as a function of both mass and volume, with the latter more important from a commercial perspective. As the gas flow is increased, the respective mass and space velocities also increase. This results in a shorter residence or contact time with the catalyst, with a subsequent decrease in CO conversion. As was observed with the time on line findings, the activity with respect to catalyst mass is far superior for the georgeite derived catalysts, in comparison to the 83-0 standard. With respect to catalyst volume, the georgeite catalysts are still more active in

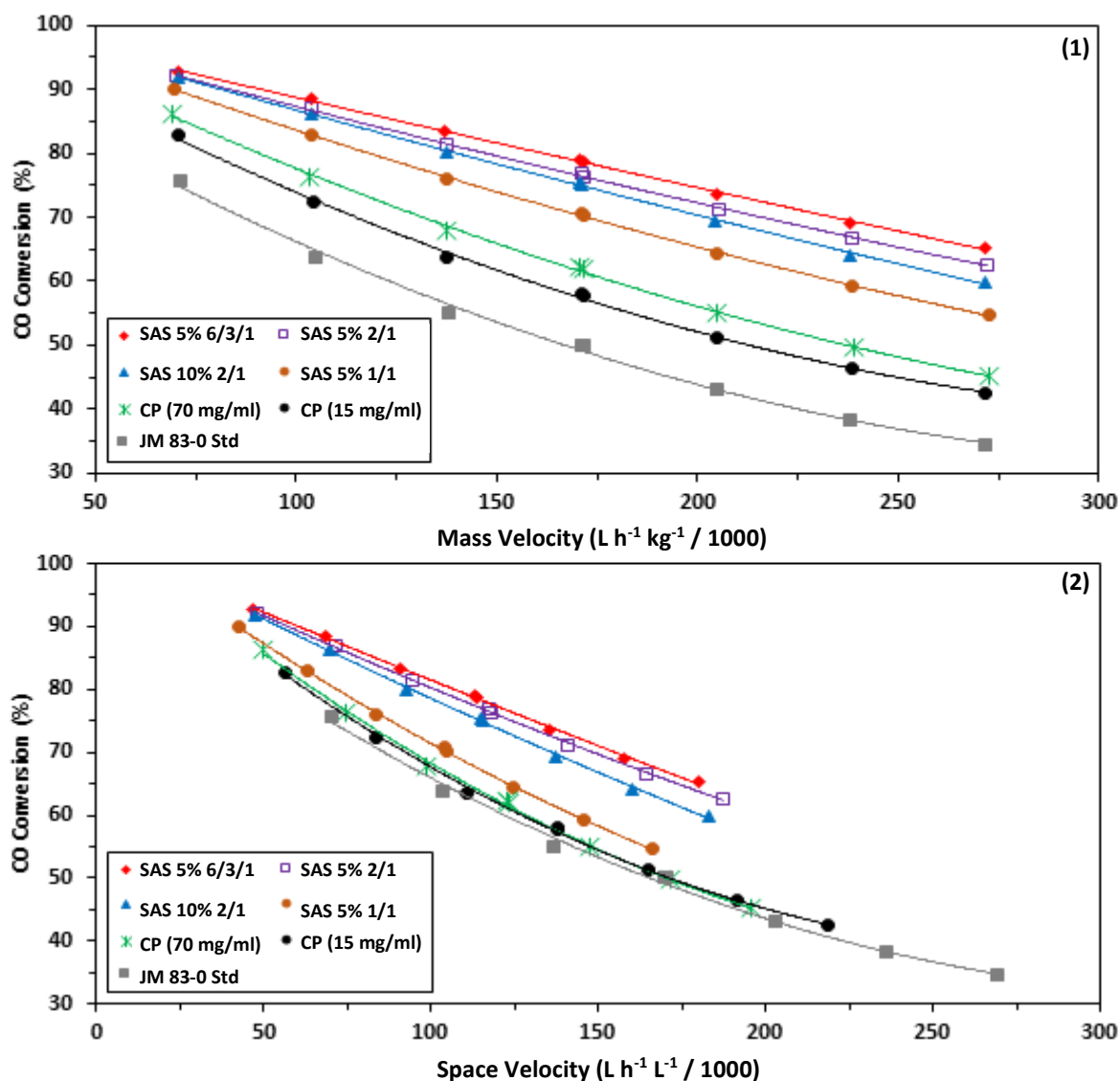


Figure 3.28. CO conversion for the LTS reaction with respect to (1) mass velocity and (2) space velocity.

comparison, although the co-precipitated catalysts are only marginally better than the industrial standard. However, it is important to note that the mass and space velocities were calculated based on the mass and volume of the calcined materials once they were loaded into the reactor. This is before the reduction step when the catalysts are activated. The georgeite precursors retain high contents of residual mass after the calcination step, and so it is possible that they reduce to a greater extent, in terms of both mass and volume after reduction in comparison to the industrial standard. However, additional analysis on the 83-0 standard is required in order to confirm this. If the georgeite catalysts do reduce to a greater extent in terms of mass and volume after reduction it would widen the gap further between these catalysts in these velocity studies. It is also clear that the relationship between CO conversion and mass or space velocity is linear for the SAS prepared catalysts but this is not apparent for the other catalysts prepared by co-precipitation. A linear relationship implies that the activity is directly proportional to the gas flow rate with no additional

factors to consider. However regarding the catalysts prepared by co-precipitation a slight variation in this relationship means that as the velocities decrease the CO conversion increases, but at a slightly faster rate. These slight differences in behaviour are most likely a result of differences in catalyst activities.

The selectivity of the catalysts for the LTS reaction was also determined by analysis of the effluents recovered from knock out pots downstream of the reactors. Methanol synthesis is the primary side reaction, and therefore, methanol concentrations down to ppm levels were determined after 67.5 and 91.5 hours on line (Table S5.). The methanol concentration relative to CO conversion gives an indication of the catalyst selectivity, but cannot be taken as a direct selectivity value since the presence of CO<sub>2</sub> in the initial gas stream can allow for methanol formation not associated with CO conversion. Regardless, a strong correlation is seen, whereby higher CO conversions result in an increase in methanol formation. This is expected since higher CO<sub>2</sub> levels produced from more efficient LTS catalysts will thermodynamically favour methanol synthesis by shifting the equilibrium towards this by-product. However, despite this, the selectivity of all catalysts examined is > 99%, with all these findings for LTS testing in agreement with related studies carried out by Kondrat<sup>(1)</sup>.

### 3.5.2. Conclusions from catalyst testing

The potential of the georgeite phase as a catalyst precursor for the construction of optimum Cu/ZnO/Al<sub>2</sub>O<sub>3</sub> catalysts has now been illustrated in this work and cannot be dismissed as a replacement for crystalline hydroxycarbonates. The behaviour of such catalysts is significantly different to those derived from crystalline precursors after comparisons were made against the industrial standards and relevant literature studies. This will substantially alter the way this mineral is perceived in the context of hydroxycarbonate preparation, whereby for over 50 years it has been highly stressed to an unprecedented degree that an ageing step is essential to generate optimum crystalline hydroxycarbonates from an amorphous phase, with inferior physicochemical properties<sup>(4,10,15,25,34,38,42-50)</sup>.

The performances of these catalysts for methanol synthesis and the LTS reaction were in complete contrast in terms of their stability. For methanol synthesis, georgeite derived catalysts prepared by both SAS and co-precipitation have higher intrinsic activities and are therefore superior to malachite derived catalysts. However, this is only apparent for the initial 10 hours of testing with deactivation a fundamental problem. Incorporation of an Al phase into the catalyst is essential whilst the influence of sodium levels is negligible. For the LTS reaction, georgeite derived catalysts prepared by both precipitation routes are superior to the industrial catalyst in terms of both activity and stability.

Since the rate of deactivation is negligible, this implies that Al incorporation is not essential. However, this may only be apparent when ultra-low sodium loadings are present. It is thus clear that the deactivation mechanism is different in these two reactions and not influenced solely by temperature. This observation will also alter the way these reactions are perceived in relation to Cu/ZnO/Al<sub>2</sub>O<sub>3</sub> catalysts.

Whilst at present malachite remains the precursor of choice for methanol synthesis, it is important to appreciate that the same degree of work regarding hydroxycarbonate optimization has not been carried out for georgeite. It is indeed possible that the amorphous mineral is still the optimum precursor for both reactions. Clearly, future work should investigate catalysts derived from ternary georgeite precursors and the SAS material prepared using Al(acac)<sub>3</sub> is an interesting prospect. This work will be challenging because ultimately georgeite precursors are always at a slight disadvantage to malachite precursors. Kondrat reported that from a binary zincian malachite precursor the mass loss after reduction is 26.8%<sup>(1)</sup>. Zincian georgeite precursors, by comparison, retain higher contents of residual mass after calcination. Consequently, after reduction the observed mass losses were seen to range between 27-32%. With 500 mg of each calcined material used for testing, this will result in a catalyst mass of 366 mg from using zincian malachite and between 365-340 mg from using zincian georgeite after reduction. It is therefore clear that there is less catalyst present when using georgeite precursors, even though the same mass is loaded into the reactors, and this should also be taken into consideration in subsequent studies.

### 3.7. References

- 1 S. A. Kondrat, PhD Thesis, Cardiff University, 2011.
- 2 Z. R. Tang, S. A. Kondrat, C. Dickinson, J. K. Bartley, A. F. Carley, S. H. Taylor, T. E. Davies, M. Allix, M. J. Rosseinsky, J. B. Claridge, Z. Xu, S. Romani, M. J. Crudace and G. J. Hutchings, *Catal. Sci. Technol.*, 2011, **1**, 740-746.
- 3 A. F. Rogers, *The Journal of Geology*, 1917, **25**, 515-541.
- 4 B. Bems, M. Schur, A. Dassenoy, H. Junkes, D. Herein and R. Schlögl, *Chem. Eur. J.*, 2003, **9**, 2039-2052.
- 5 R. L. Frost, D. L. Wain, W. N. Martens and B. J. Reddy, *Spectrochimica Acta Part A*, 2007, **66**, 1068-1074.

### Chapter Three

- 6 F. Quiles and A. Burneau, *Vibrational Spectroscopy*, 1998, **16**, 105-117.
- 7 T. Ishioka, Y. Shibata, M. Takahashi, I. Kanesaka, Y. Kitagawa and K. T. Nakamura, *Spectrochimica Acta Part A*, 1998, **54**, 1827-1836.
- 8 P. J. Bridge, J. Just and M. H. Hey, *Mineralogical Magazine*, 1979, **43**, 97-98.
- 9 A. M. Pollard, R. G. Thomas and P. A. Williams, *Mineralogical Magazine*, 1991, **55**, 163-166.
- 10 A. M. Pollard, M. S. Spencer, R. G. Thomas, P. A. Williams, J. Holt and J. R. Jennings, *Applied Catalysis A: General*, 1992, **85**, 1-11.
- 11 E. Reverchon, G. Della Porta, D. Sannino and P. Ciambelli, *Powder Technology*, 1999, **102**, 127-134.
- 12 S. A. Kondrat, T. E. Davies, Z. Zu, P. Boldrin, J. K. Bartley, A. F. Carley, S. H. Taylor, M. J. Rosseinsky and G. J. Hutchings, *Journal of Catalysis*, 2011, **281**, 279-289.
- 13 G. Fierro, M. L. Jacono, M. Inversi, P. Porta, F. Cioci and R. Lavecchia, *Applied Catalysis A: General*, 1996, **137**, 327-348.
- 14 E. Reverchon, I. D. Marco and E. Torino, *J. of Supercritical Fluids*, 2007, **43**, 126-138.
- 15 M. Behrens, *Journal of Catalysis*, 2009, **267**, 24-29.
- 16 R. L. Frost, W. N. Martens, D. L. Wain and M. C. Hales, *Spectrochimica Acta Part A*, 2008, **70**, 1120-1126.
- 17 M. C. Hales and R. L. Frost, *Polyhedron*, 2007, **26**, 4955-4962.
- 18 M. C. Hales and R. L. Frost, *J. of Thermal Analysis and Calorimetry*, 2008, **91**, 855-860.
- 19 N. Kanari, D. Mishra, I. Gaballah and B. Dupre, *Thermochimica Acta*, 2004, **410**, 93-100.
- 20 M. V. Twigg and M. S. Spencer, *Topics in Catalysis*, 2003, **22**, 191-203.
- 21 K. C. Waugh, *Catal. Lett.*, 2012, **142**, 1153-1166.
- 22 I. Melian-Cabrera, M. Lopez Granados and J. L. G. Fierro, *Phys. Chem. Chem. Phys.*, 2002, **4**, 3122-3127.
- 23 W. R. A. M. Robinson and J. C. Mol, *Applied Catalysis*, 1990, **60**, 73-86.
- 24 S. Music, D. Dragcevic and S. Popovic, *Materials Letters*, 1999, **40**, 269-274.

- 25 M. Behrens, S. Zander, P. Kurr, N. Jacobsen, J. Senker, G. Koch, T. Ressler, R. W. Fischer and R. Schlögl, *Journal of the American Chemical Society*, 2013, **135**, 6061-6068.
- 26 G. Simson, E. Prasetyo, S. Reiner and O. Hinrichsen, *Applied Catalysis A: General*, 2013, **450**, 1-12.
- 27 B. J. Hathaway and A. A. G. Tomlinson, *Coordin. Chem. Rev.*, 1970, **5**, 1-43.
- 28 K. Jun, W. Shen, K. S. Rama Rao and K. Lee, *Applied Catalysis A: General*, 1998, **174**, 231-238.
- 29 J. Wu, S. Luo, J. Toyir, M. Saito, M. Takeuchi and T. Watanabe, *Catalysis Today*, 1998, **45**, 215-220.
- 30 P. Kowalik, W. Prochniak and T. Borowiecki, *Catalysis Today*, 2011, **176**, 144-148.
- 31 B. M. Collins, The Patent Office London, 1975, 1405012.
- 32 P. Snowden, United States Patent Documents, 1978, 4129523.
- 33 M. Behrens, F. Studt, I. Kasatkin, S. Kuhl, M. Havecker, F. Abild-Pedersen, S. Zander, F. Girgsdies, P. Kurr, B. Knief, M. Tovar, R. W. Fischer, J. K. Norskov and R. Schlögl, *Science*, 2012, **336**, 893-897.
- 34 C. Baltès, S. Vukojevic and F. Schuth, *Journal of Catalysis*, 2008, **258**, 334-344.
- 35 M. Kurtz, H. Wilmer, T. Genger, O. Hinrichsen and M. Muhler, *Catalysis Letters*, 2003, **86**, 77-80.
- 36 X. Liu, G. Q. Lu, Z. Yan and J. Beltramini, *Ind. Eng. Chem. Res.*, 2003, **42**, 6518-6530.
- 37 D. B. Rasmussen, T. V. W. Janssens, B. Temel, T. Bligaard, B. Hinnemann, S. Helveg and J. Sehested, *Journal of Catalysis*, 2012, **293**, 205-2014.
- 38 M. S. Spencer, *Topics in Catalysis*, 1999, **8**, 259-266.
- 39 C. Rhodes, G. J. Hutchings and A. M. Ward, *Catalysis Today*, 1995, **23**, 43-58.
- 40 M. V. Twigg, *Catalyst Handbook*, Second Edition, Manson Publishing, 1989.
- 41 M. J. L. Gines, N. Amadeo, M. Laborde and C. R. Apesteguia, *Applied Catalysis A: General*, 1995, **131**, 283-296.
- 42 B. L. Knief, T. Ressler, A. Rabis, F. Girgsdies, M. Baenitz, F. Steglich and R. Schlögl, *Angew. Chem. Int. Ed.*, 2004, **43**, 112-115.

### Chapter Three

- 43 D. Waller, D. Stirling, F. S. Stone and M. S. Spencer, *Faraday Discuss. Chem. Soc.*, 1989, **87**, 107-120.
- 44 E. N. Muhamad, R. Irmawati, Y. H. Taufiq-Yap, A. H. Abdullah, B. L. Kniep, F. Girgsdies and T. Ressler, *Catalysis Today*, 2008, **131**, 118-124.
- 45 S. Zander, B. Seidlhofer and M. Behrens, *Dalton Trans.*, 2012, **41**, 13413-13422.
- 46 M. Behrens and R. Schlögl, *Z. Anorg. Allg. Chem.*, 2013, **639**, 2683-2695.
- 47 A. A. Mirzaei, H. R. Shaterian, S. H. Taylor and G. J. Hutchings, *Catalysis Letters*, 2003, **87**, 103-108.
- 48 D. M. Whittle, A. A. Mirzaei, J. S. J. Hargreaves, R. W. Joyner, C. J. Kiely, S. H. Taylor and G. J. Hutchings, *Phys. Chem. Chem. Phys.*, 2002, **4**, 5915-5920.
- 49 B. L. Kniep, F. Girgsdies and T. Ressler, *Journal of Catalysis*, 2005, **236**, 34-44.
- 50 H. Jung, D. Yang, O. Joo and K. Jung, *Bull. Korean Chem. Soc.*, 2010, **31**, 1241-1246.

## 4.0. Deciphering key structural differences between georgeite and malachite hydroxycarbonates

### 4.1. Introduction

In **Section 3.6.1.**, it was demonstrated that catalysts prepared from georgeite precursors operate and behave differently to catalysts prepared from crystalline precursors for methanol synthesis and the LTS reaction. The differences in catalyst performance is governed from the choice of precursor, whereby studies on Cu/ZnO/Al<sub>2</sub>O<sub>3</sub> catalysts predominantly focus on this ‘structure-activity’ relationship. As reported by Bems and co-workers, one of the reasons for the ongoing research concerning the chemical and structural identity of these precursors is the presumed conjunction to the activity of the final catalyst, in other words the memory of the catalyst of its origin<sup>(1)</sup>. The preparation of these catalysts is a multistep procedure, whereby each step contributes to the structural characteristics of the catalyst finally obtained. These properties in turn correlate to the performance of the catalyst. Therefore, whilst zincian georgeite and zincian malachite precursors can both be used to produce the same 2/1 Cu/ZnO catalyst, it is clear that these catalysts will not be truly identical. The microstructural properties of these two distinct catalysts needs to be understood in order to interpret and rationalise their behaviours. The phase type of the precursor is also anticipated to influence the decomposition behaviour in the preceding thermal treatment steps. Thus a thorough examination of the initial precipitate, the calcined material as well as the final state catalyst is warranted for both georgeite and malachite phases. This would enable a direct comparison of the microstructural properties, which could also be traced back to the origin of each catalyst, in order to understand how both phases influence the overall synthesis procedure.

The initial step, which regards hydroxycarbonate synthesis from a precipitation technique is ultimately the most important step in the entire manufacturing process. This determines the precursor phase type or mixture, the sodium loading and the level of mixing between the metal components. Optimisation of the subsequent calcination and reduction steps is also essential to prevent sintering of the metal components. In other words, these steps predominantly focus on implementing the mildest conditions possible, in order to retain the highest level of Cu dispersion in the final catalyst. The extent of Cu dispersion cannot be improved after the precipitation step, with an enhanced degree of mixing in the final catalyst resulting in a higher copper surface area and superior Cu-ZnO:Al interactions.

The focus of this chapter is to study and directly compare zincian georgeite and zincian malachite phases after the precipitation, calcination and reduction steps, in order to identify similarities and differences in the evolution of the microstructural properties, which can be used to rationalise the catalyst behaviour. A detailed examination of the calcination step also enabled the optimum conditions to be identified which justifies the conditions used in **Chapter Three**. Georgeite and malachite phases which do not include the incorporation of zinc were also investigated for additional comparisons.

Copper acetate monohydrate (4 mg/ml) was dissolved in ethanol containing 5% water by volume. This solution was used to prepare georgeite by SAS precipitation. Unfortunately, water contents  $\geq$  5% could not be used without preventing ageing into malachite. In a second set of experiments copper acetate monohydrate (4 mg/ml) and zinc acetate dihydrate (2.13 mg/ml) were dissolved in ethanol containing 10% water by volume. This solution was used to prepare zincian georgeite also by SAS precipitation. The malachite and zincian malachite samples were provided by Johnson Matthey using the industrial co-precipitation route. Solutions (1.5 M, 5 L) of sodium carbonate and metal nitrates were simultaneously added under continuous mixing at constant pH = 6.5-6.8 and temperature = 65 °C. The initial georgeite precipitate rapidly ages into malachite, whilst an ageing time of 15-20 minutes is required to produce zincian malachite. The precipitates were filtered, washed and dried at 110 °C for 16 hours. It should be noted that these two materials were not prepared by the author. EDX analysis determined atomic contents of 67% copper and 33% zinc for the zincian georgeite and zincian malachite samples, which gives a Cu/Zn molar ratio of 2/1. All precursors investigated were also vacuum oven dried at 40 °C overnight before any analysis was implemented. This was to remove residual solvents retained from the precipitation processes which could modify the findings.

#### 4.2. Determining physicochemical properties of copper and copper-zinc hydroxycarbonate phases

Whilst the malachite precursor has been thoroughly investigated in the literature in terms of its microstructural properties<sup>(2-9)</sup>, georgeite in clear contrast has been almost completely neglected. This is attributed to its amorphous nature, the difficulty in producing it in high purity from its low stability and the large volume of papers highlighting the crucial importance of the ageing step. Its amorphous nature in particular makes it significantly difficult to characterise, which hinders evaluation of its physicochemical properties. Furthermore, the limited pool of papers published on georgeite actually contradict one another<sup>(10-11)</sup>. This is most likely attributed to difficulties obtaining it in high purity and will be discussed in more detail in the subsequent section. However, the SAS

procedure enables the synthesis of relatively pure georgeite in large quantities, which can then be characterised to an unprecedented degree. This is a result of the rapid extraction of the ethanol/water solvent by  $\text{scCO}_2$ , which effectively makes the georgeite dry from the point of precipitation, limiting contact with water which facilitates ageing to malachite. Thus, preparation of georgeite by co-precipitation is significantly challenging in comparison, albeit zincian georgeite can be readily obtained from this route as its higher stability deters the ageing process.

Consequently, a wide range of advanced characterisation techniques such as X-ray absorption spectroscopy (XAS) and pair distribution function (PDF) analysis were used to study georgeite and zincian georgeite phases for the very first time, with comparisons made against malachite and other related phases. To complement these analytical techniques, densities and molecular formulas were also derived using ICP-CHN and helium pycnometry analysis, respectively. The main purpose of the work was to obtain partial structures for the georgeite phases. Whilst the XRD patterns signal that no long range order is evident, it was anticipated that a certain degree of local structure was still present.

#### 4.2.1. Results and discussion

ICP-MS and CHN analysis was used to determine the elemental composition of the georgeite and malachite phases, in order to calculate the molecular formulas (**Table 4.1.**) Furthermore, the density of each precursor was determined from helium pycnometry analysis. The findings were compared to the literature. For georgeite prepared from SAS precipitation the analysis gave an ideal formula of  $\text{Cu}_7(\text{CO}_3)_4(\text{OH})_6 \cdot 4\text{H}_2\text{O}$ . Slight variations in elemental compositions in an amorphous phase is anticipated<sup>(12)</sup> and taking this into account the ICP-CHN analysis closely matches that reported by Bridge and co-workers for the Carr Boyd mine sample<sup>(10)</sup>. In both cases it is seen that georgeite has occluded water trapped within its structure which, as previously mentioned, is a universal feature of amorphous phases (**Chapter One**). These observations differ from previous attempts to produce georgeite synthetically, whereby Pollard and co-workers reported that the mineral is an amorphous analogue of malachite with molecular formula  $\text{Cu}_2\text{CO}_3(\text{OH})_2$ <sup>(11)</sup>. Whilst we can attribute this to the subsequent ageing into malachite in the co-precipitation process, a later study reported that zincian georgeite also has the same molecular formula as zincian malachite<sup>(13)</sup>. The SAS prepared zincian georgeite in contrast yielded a molecular formula of  $(\text{Cu}_{0.66}\text{Zn}_{0.33})_5(\text{CO}_3)_3(\text{OH})_4 \cdot 3\text{H}_2\text{O}$ . The enhanced stability from Zn incorporation into the phase would have suppressed the ageing phenomenon. It is therefore plausible that a gradual ageing process could have resulted if the material was not stored properly. Interestingly, the determined molecular formulas for the SAS prepared georgeite phases display higher  $(\text{CO}_3) : (\text{Cu} + \text{Zn})$  ratios than the malachite analogues. For georgeite and zincian

**Table 4.1.** Elemental and density analysis of relevant natural and synthetic copper and copper-zinc phases.

Sample	Elemental composition (wt.%)				Molecular formula	Density (g cm <sup>-3</sup> )
	Cu	Zn	C	H		
SAS georgeite	50.4	-	6.8	1.5	Cu <sub>7.1</sub> (CO <sub>3</sub> ) <sub>4</sub> (OH) <sub>6.3</sub> ·4.3H <sub>2</sub> O Cu <sub>7</sub> (CO <sub>3</sub> ) <sub>4</sub> (OH) <sub>6</sub> ·4H <sub>2</sub> O	3.06
Mineralogical georgeite <sup>(10)</sup>	47.3	-	5.3	2.4	Cu <sub>5</sub> (CO <sub>3</sub> ) <sub>3</sub> (OH) <sub>6</sub> ·6H <sub>2</sub> O	2.6 <sup>a</sup>
CP georgeite <sup>(11)</sup>	57.8	-	5.5	0.9	Cu <sub>2</sub> CO <sub>3</sub> (OH) <sub>2</sub>	2.4-2.8 <sup>a</sup>
SAS zincian georgeite	34.3	17.5	5.6	1.2	(Cu <sub>0.66</sub> Zn <sub>0.34</sub> ) <sub>5.2</sub> (CO <sub>3</sub> ) <sub>3</sub> (OH) <sub>4.3</sub> ·3.4H <sub>2</sub> O (Cu <sub>0.66</sub> Zn <sub>0.34</sub> ) <sub>5</sub> (CO <sub>3</sub> ) <sub>3</sub> (OH) <sub>4</sub> ·3H <sub>2</sub> O	3.03
CP malachite	55.4	-	5.4	1.0	Cu <sub>1.9</sub> CO <sub>3</sub> (OH) <sub>1.9</sub> ·0.3H <sub>2</sub> O Cu <sub>2</sub> CO <sub>3</sub> (OH) <sub>2</sub>	3.91
CP zincian malachite	38.4	17.8	5.0	0.9	(Cu <sub>1.5</sub> Zn <sub>0.7</sub> )CO <sub>3</sub> (OH) <sub>2.2</sub> (Cu <sub>0.66</sub> Zn <sub>0.34</sub> ) <sub>2</sub> CO <sub>3</sub> (OH) <sub>2</sub>	3.85
SAS Cu acetate	46.6	-	12.9	2.3	-	2.48 <sup>b</sup>

<sup>a</sup> Density determined by sink-float (SF) method. Helium pycnometry used in the current study provides a skeletal density that negates buoyancy effects.

<sup>b</sup> Density of the Cu(II)(OAc)<sub>2</sub>·H<sub>2</sub>O starting material was 1.9 g cm<sup>-3</sup> in comparison.

georgeite, the ratio is 0.57 and 0.6 respectively, in comparison to 0.5 determined for the malachite phases. Therefore, the ageing phenomenon results in the simultaneous release of CO<sub>2</sub> gas as reported by Pollard and co-workers<sup>(13)</sup> and is frequently observed in the industrial co-precipitation route. This was also described in **Section 3.5.**, whereby the determined molecular formulas have enabled new light to be shed on the co-precipitation route. Furthermore, occluded water was also found in the zincian georgeite sample, further validating the credentials of these ICP-CHN findings. The correct molecular formulas were also determined for the malachite samples supplied by JM, which verifies the phases present. However, it is important to note that for all the samples investigated residual amounts of by-phases are also present, which will cause slight deviations from true values. The georgeite materials will contain residual amounts of acetate and therefore the SAS prepared Cu acetate was also analysed for comparison. Determination of an exact formula was more difficult, although the formula Cu<sub>9</sub>(CH<sub>3</sub>COO)<sub>13</sub>(OH)<sub>5</sub> does best fit these elemental findings. Moreover, the zincian malachite precursor will contain aurichalcite as a by-phase, whilst malachite is the only sample expected to have no additional phases present.

For the SAS prepared georgeite phases, a density of 3-3.1 g cm<sup>-3</sup> was determined, which is significantly different to the average value of 2.6 g cm<sup>-3</sup> determined from previous studies<sup>(10-11)</sup>. This can be attributed to the low stability and purity of the phase examined in these reports, the different methods used in order to calculate density, as well as the distinct type of density these techniques

derive (i.e. absolute or skeletal). For the synthetic malachite samples, significantly higher densities around  $3.9 \text{ g cm}^{-3}$  were determined. In comparison, mineralogical malachite has a density in the range  $3.6\text{--}4 \text{ g cm}^{-3}$ . Clearly, the average density found for the georgeite phase in relation to malachite is lower, which is attributed to the higher content of carbonate and occluded water. The SAS prepared Cu acetate had a density of  $2.5 \text{ g cm}^{-3}$  in comparison, to  $1.9 \text{ g cm}^{-3}$  determined for the starting material, which again is attributed to the presence of occluded water in the as received hydrated material.

The amorphous XRD patterns for georgeite and zincian georgeite have already been presented and discussed in **Chapter Three (Figure 3.9)**. XRD analysis of the malachite and zincian malachite samples were carried out for comparison (**Figure 4.1**). For clarity, the aurichalcite precursor prepared by JM using the exact same synthesis procedure but with a Cu/Zn molar ratio of 1/1 is also provided. The malachite and aurichalcite phases were confirmed by phase analysis. Overall, these findings verify the extensive work carried out by Behrens and co-workers<sup>(2-3,5)</sup>. The (20-1) and (21-1) reflections for the malachite phase are indicated with grey hashed lines. The addition and incorporation of Zn into the lattice simultaneously shifts these peaks to higher  $2\theta$  values as the d-spacing of these planes reduces. This phenomenon which arises from Jahn-Teller distortions, was explained in detail in **Chapter One** and can be used to determine the composition of zinc in the malachite phase. The d-spacing determined from the (20-1) reflection was  $2.858 \text{ \AA}$  for malachite and

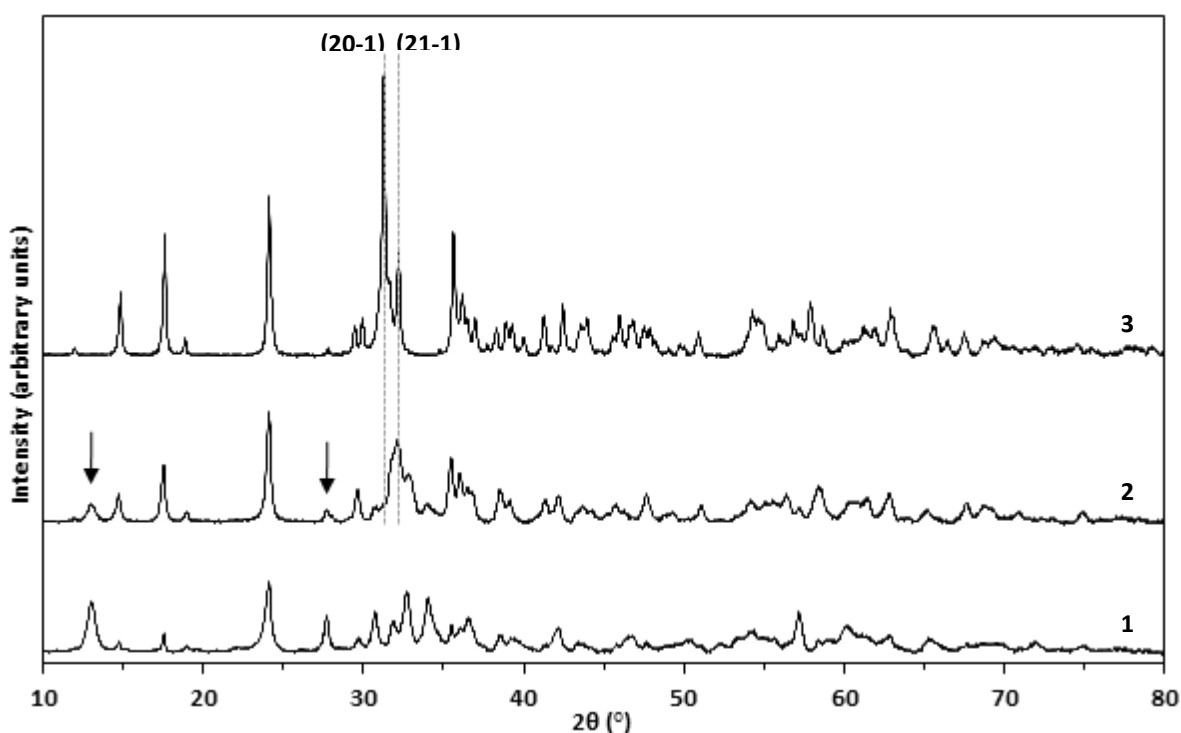


**Figure 4.1.** XRD patterns of hydroxycarbonate phases prepared at Johnson Matthey using the industrial co-precipitation route: (1) Aurichalcite (2) Zincian malachite, including aurichalcite (see main text) (3) malachite. The (20-1) and (21-1) reflections for the malachite phase are illustrated to indicate extent of peak shifts with Zn addition. The two most intense aurichalcite reflections in the 2/1 precursor are also marked with arrows.

2.776 Å for the zincian malachite 2/1 precursor, which closely matches that determined by Behrens<sup>(2)</sup>. The Zn content present in the zincian malachite 2/1 precursor is therefore 28%, which is the maximum amount which can be incorporated into the malachite lattice, before the aurichalcite by-phase begins to form. Crystallite sizes calculated using the (20-1) reflection determined a crystallite size of 60 nm for malachite, in comparison to 11 nm for the 2/1 precursor. This was expected since the malachite phase clearly displays stronger crystallinity than the binary precursors, which also implies that it has a lower surface area. The two most intense aurichalcite reflections found in the 2/1 precursor are also marked, which clearly increase in intensity of the Cu/Zn molar ratio decreases. Determining the content of the aurichalcite by-phase in the 2/1 precursor is, however, highly challenging. The relative intensity ratio and Rietveld refinement techniques gave aurichalcite contents in the range 15-25 wt.%. However, as reported in related work the aurichalcite content is overestimated using the XRD refinement technique as a result of the precursor being poorly crystalline, and the limited number of reference samples available<sup>(3)</sup>. Comparisons made with this work also indicated that the rosasite phase is not present in the 2/1 precursor, as expected from the difficulty in preparing this phase synthetically.

XAS and diffuse reflectance UV-Vis spectroscopy (DRUVS) were used to examine the local structures of the georgeite and malachite phases (**Figure 4.2.**). A comparison of the XANES data for georgeite and malachite illustrates that the position of the pre-edge and main edge features occur at the same energy (**Figure 4.2(A).**). This indicates that both phases have Cu present in a distorted octahedral environment. Linear and square planar Cu-O environments would have intense pre-edge features at 8983.5 and 8986.5 eV, respectively<sup>(14)</sup>. The main edge position centred at 8995 eV is consistent with Cu<sup>2+</sup>. The resulting Fourier Transform and fitting parameters in the range 0-3.5 Å also indicate distorted octahedral environments for both phases (**Figure 4.2(B).** and **Tables S6** and **S7.**). The primary co-ordination spheres are dominated by the four short equatorial Cu-O distances, since the two longer axial Cu-O bonds have little influence on the spectrum due to the increased thermal disorder. This is expected for a distorted octahedral environment, which also results in an increased displacement of atoms in the sample (increased  $2\sigma^2$  value). To examine these octahedral environments, further DRUVS analysis was carried out on both phases (**Figure 4.2(C).**). The Zn<sup>2+</sup> ion has a completely filled 3d<sup>10</sup> shell and does not contribute to the optical spectra, and therefore apparent bands are formed from optical d-d transitions in Cu<sup>2+</sup> ions. For georgeite, a strong band is centred at 250 nm, whilst for malachite a doublet is present centred at 257 and 319 nm. In related studies, Frost and co-workers assign the shoulder at ~300 nm to charge transfer transitions involving Cu<sup>2+</sup>-O<sup>2-</sup>-Cu<sup>2+</sup> species, whilst the effect of Zn on Cu is observed in the extreme UV spectrum ~240 nm assigned to the charge transfer of O<sup>2-</sup> → Cu<sup>2+</sup><sup>(15)</sup>. The band marked for both phases in the spectra is

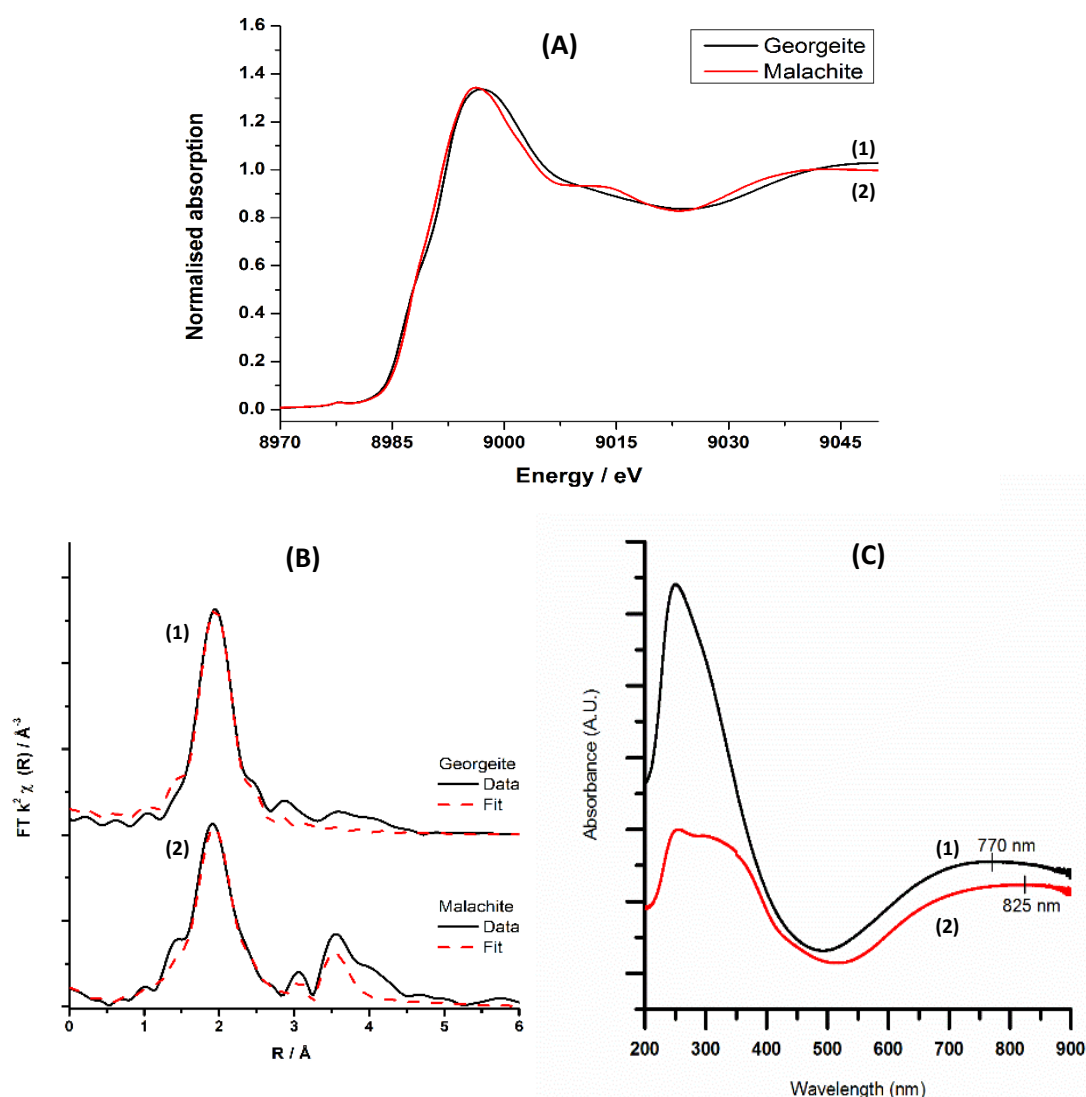


**Figure 4.2.** XAFS and DRUVS spectroscopy of (1) georgeite and (2) malachite: (A) Cu K edge XAFS spectra providing information on local structure (B) Fourier transform analysis to derive bond lengths and coordination numbers (C) DRUVS spectra, with centres of d-d transition bands marked

Complex, and is associated with all d-d transitions arising from all  $\text{Cu}^{2+}$  species. Extensive work regarding the analysis of malachite and related phases using UV-Vis-NIR analysis has already been carried out by Behrens and co-workers<sup>(4)</sup>. In this work, malachite is illustrated to contain two crystallographically distinct Cu sites in octahedral  $\text{CuO}_6$  building blocks, which are present in a 1/1 ratio. In relation to crystal field splitting, the low symmetry of the  $\text{Cu}^{2+}$  cation ( $d^9$ ) splits the doublet  $^2E$  and triplet  $^2T_2$  states into separate energy levels. Therefore, for this one hole system, 4 excitations can take place which all exceed the thermal energy,  $kT$ . The optical transitions which have been determined are:  $^2A_1^{(1)} \rightarrow ^2A_1^{(2)}$ ,  $^2A_1^{(1)} \rightarrow ^2A_2$ ,  $^2A_1^{(1)} \rightarrow ^2B_1$  and  $^2A_1^{(1)} \rightarrow ^2B_2$ . This gives a total of 8 bands superimposed on the resulting spectrum for malachite, with 4 bands contributed from each of the two  $\text{Cu}^{2+}$  species. The DRUVS findings are in agreement with the XAS findings as it shows that georgeite has d-d transitions associated with distorted octahedral centres, as determined for

malachite. However, both techniques do suggest subtle differences in co-ordination geometries between the two phases. DRUVS shows the observed optical band associated with metal centres in georgeite is located at 770 nm, whereas the combined absorption bands from the two distinct  $\text{Cu}^{2+}$  species in malachite is centred at 825 nm. Furthermore, whilst the XANES data is similar for both phases, there are clear differences in the EXAFS. This is illustrated in the Fourier transform findings at distances greater than 2 Å (**Figure 4.2(B).**). The malachite data has contributions at 3.12 and 3.31 Å, which can be correlated to the scattering effects of Cu-Cu neighbours. The fitting of the shells further out is problematic as a result of the out of phase nature of the scattering paths, and the multitude of scattering phenomena occurring at these distances. In contrast for georgeite, it is apparent that there are very few features beyond 2 Å with no evidence of Cu-Cu correlation.

Potential changes made to the local structure from incorporating Zn into the amorphous phase was also examined from analysing zincian georgeite. The DRUVS findings indicated that distorted Cu octahedral centres were still present (**Figure S12.**). The band associated with the various d-d transitions is blue-shifted relative to that of zincian malachite, as was observed for the Cu-only phases. This implies that the overall splitting of the energy levels is greater in georgeite phases, which is associated with ligand interactions with the  $\text{Cu}^{2+}$  ion. XAS analysis was also carried out, whereby georgeite samples with various Zn contents were compared (0, 20 and 33 at.%) (**Figures S13-S15.**). From the Cu K edge EXAFS findings, it is clear that the addition of Zn does not result in any discernible changes made to the Cu geometry in georgeite (**Figure S13.**). Moreover in **Section 3.3.**, it was discussed that varying the Cu/Zn molar ratio resulted in no additional phases. This is not apparent for zincian malachite, whereby at Zn contents > 28% aurichalcite formation occurs. Therefore to investigate this further the unidentified zinc precipitate prepared using identical SAS conditions, but without the inclusion of Cu, was also analysed by XAS for comparison (**Figures S14-S15.**). From the resulting Zn K edge XANES and EXAFS data there was no further evidence of this phase present in the zincian georgeite precursor. Overall, these findings are in agreement with previous XRD, FT-IR, TGA and Raman analysis, whereby it was concluded that Zn incorporation results in no disruption to the georgeite phase with no subsequent formation of by-phases.

In order to probe the short to medium range order of the materials, further PDF studies were carried out as it does not suffer from scattering path phasing phenomena apparent for EXAFS analysis (**Figure 4.3.**). The observed PDF for georgeite and zincian georgeite have almost identical short range order up to 5 Å (**Figure 4.3(A).**). Subtle differences are more apparent between 5-10 Å, with less order observed in the georgeite sample at distances > 10 Å. The extended order observed from the addition of Zn could be responsible for the enhanced stability of the zincian georgeite phase.

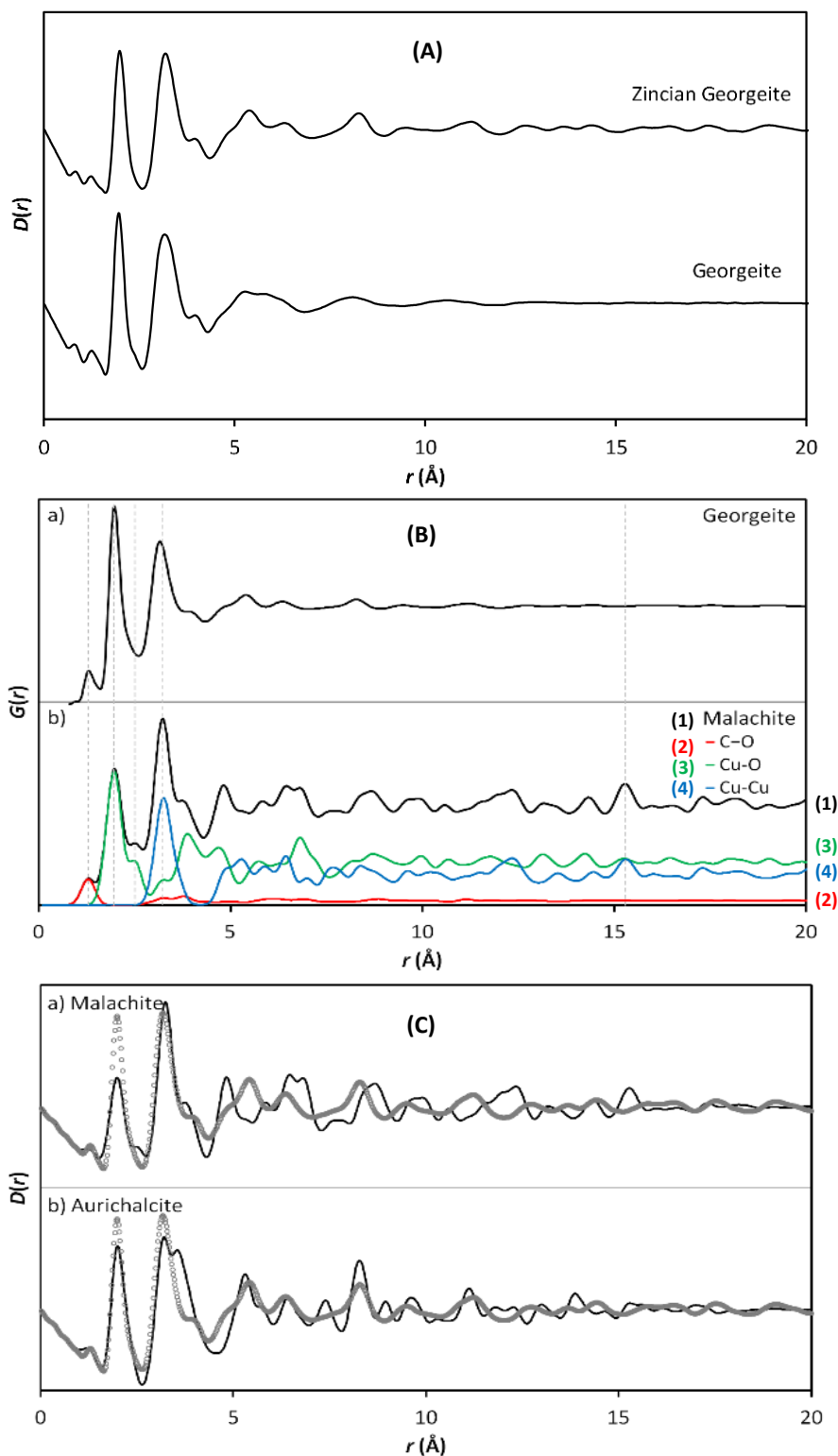


**Figure 4.3.** (A) Comparison of X-ray PDF data of georgeite and zincian georgeite. The two patterns are remarkably similar, indicating that zinc is included into the copper coordination environment without changing the local structure. (B) a) Observed X-ray PDF  $G(r)$  data of georgeite. b) Calculated X-ray PDF data of malachite, together with the partial contributions from the most strongly contributing atom pairs; C–O (2. red), Cu–O (3. green) and Cu–Cu (4. blue). A numbered key is provided for clarity. (C) Comparison of the observed georgeite PDF data (open circles) to simulations of 22 Å nanoparticles of the crystal structures of a) malachite and b) aurichalcite.

Comparisons were also made between the PDF of georgeite with a PDF of malachite calculated from the reported structure<sup>(5)</sup> (**Figure 4.3(B)**). The ordering is broadly similar, with subtle differences up to 4 Å. At longer distances it is clear that there are large differences between the structures, which demonstrates that georgeite is not simply a nano-scale form of malachite as observed with other amorphous materials such as FeS<sup>(16)</sup>. For malachite, the main individual atom-atom contributions to the calculated PDF are shown in different colours/numbers. In particular the total PDF is dominated by Cu-O and Cu-Cu features. As marked, a Cu-O peak is displayed at 1.97 Å with a distinct secondary peak at 2.44 Å associated with the Jahn-Teller distorted axial Cu-O bonds in the octahedra. In comparison, georgeite displays a Cu-O peak at 1.98 Å, which is significantly asymmetric and lacks the distinct secondary peak observed for malachite. This suggests that the Jahn Teller distortion is less pronounced in georgeite. Interestingly, inspection of the zincian georgeite PDF shows that the asymmetric shape of this peak is retained with the addition of non Jahn-Teller Zn<sup>2+</sup>, although it is slightly broader by comparison. The georgeite PDF displays a Cu-Cu peak with a bond distance of 3.14 Å which is also marked. This is typical of distances observed for edged shared octahedra seen in malachite (3.062(6) Å)<sup>(5)</sup> and aurichalcite (3.048(14), 3.174(4) Å and 3.165(14) Å)<sup>(17)</sup>. This Cu-Cu bond length is therefore longer than that observed for malachite. This Cu-Cu interaction seen in georgeite was not observed from the XAS findings, which is a result of deconstructive scattering paths. A Cu-Cu peak at 15.27 Å is also indicated for malachite. This is a result of crystallographically identical Cu ions in neighbouring unit cells. The complete absence of this peak in the georgeite PDF is a strong indication that local ordering operates well below the length scales associated with the malachite unit cell (362.7 Å<sup>3</sup>).

Attempts to refine the malachite PDF to fit the observed georgeite data were unsuccessful as it resulted in unrealistic deformation of the malachite Cu-O octahedra. Further PDF matching to other known related phases such as aurichalcite<sup>(17)</sup>, azurite<sup>(18)</sup> and rosasite<sup>(19)</sup> also showed that georgeite is a distinct phase to any previously known copper hydroxycarbonate (**Figure S16**). Moreover, attempts to match the data against PDF simulations of nanoparticles 22 Å in size from malachite and aurichalcite crystal structures were also inconclusive (**Figure 4.3(C)**).

#### 4.2.2. Conclusions from studies on the physicochemical properties of copper and copper-zinc hydroxycarbonate phases

A thorough and extensive study has been carried out for the first time, whereby a range of state of the art analytical techniques have been used to probe the chemical, physical and structural properties of georgeite. The SAS precipitation technique is capable of producing georgeite in

relatively high purity, which in conjunction to zincian georgeite, were directly compared against malachite precursors prepared from the industrial co-precipitation route.

All of the findings concluded that georgeite is a unique phase, and not an amorphous analogue of malachite as some literature defines<sup>(11,13)</sup>. The georgeite phase is lower in density, and contains occluded water with a higher carbonate content in comparison to malachite. Structural analysis regarding the short range order also concludes that the ordering in georgeite is severely restricted and operates well below the length scale of the malachite unit cell. Unfortunately, as a result of scattering path phenomena, EXAFS analysis only gives information on the primary shell of the metal ion. However the analysis is in relatively good agreement with the PDF data which determined Cu-O bond lengths of 1.94(1) Å and 1.98 Å, respectively. The PDF data was most useful as it enabled distances up to 20 Å to be investigated. Furthermore, this analysis enabled identification of a Cu-Cu bond. Whilst the EXAFS and PDF data show that ordering is similar for both georgeite and malachite up to the first shell, this is only apparent because both phases have distorted octahedra co-ordination geometries. Subtle differences between these octahedra could still be identified which was further demonstrated from the DRS findings. It is therefore concluded that georgeite and malachite are not identical, even down to the lowest scale of ordering possible.

Since the structural ordering in georgeite is so limited, a partial structure for this phase could not be constructed. The findings conclude that the copper centres are within Jahn-Teller distorted octahedral building blocks co-ordinated to six oxygen atoms. The Cu-Cu bond identified from PDF confirms that these building blocks are not completely isolated, and are most likely connected *via* common edges giving rise to small clusters. Examining the structure further would prove highly challenging. XAS and PDF were not able to determine precise lengths for each individual Cu-O bond. For malachite, this can be obtained from the XRD findings, which also enabled the number of distinct metal sites to be identified. For georgeite, this lack of information hinders the potential to carry out theoretical studies relating to the DRS findings as has already been carried out for malachite<sup>(4)</sup>. This work however is in agreement with previous findings as it further suggests that Zn is being fully incorporated into georgeite. However, it is important to appreciate that this still does not provide concentrate evidence of this phenomenon occurring.

### 4.3. Investigating the thermal decomposition behaviour of copper and copper-zinc hydroxycarbonate phases

The thermal activation step is an integral component of the catalyst synthesis procedure. Investigation is warranted in order to optimise the calcination conditions essential for generating catalysts with optimum performance. The process is complex, with many parameters influencing the resulting microstructural features of the calcined precursor including ramp rate, gas flow and type, temperature, holding time and sample mass. In particular, the phase type is anticipated to play a pivotal role in governing the thermal decomposition procedure. The focus of the work was to provide a detailed and thorough examination regarding the thermal behaviour of zincian georgeite and zincian malachite precursors. In addition, to optimising various parameters of this step attention focused specifically on what influence the phase type had on the resulting physicochemical properties. Georgeite and malachite precursors were also investigated to further analyse the resulting decomposition with respect to zinc incorporation. The work is discussed in detail in relation to literature findings.

#### 4.3.1. Results and discussion

TGA coupled with DTA and EGA was performed in order to discover more about the structures of the georgeite and malachite precursors, as well as to investigate their decomposition behaviour (**Figure 4.4.**). The TGA profile of georgeite is significantly different to that obtained for malachite, with the former having three distinct mass losses and the latter having just a single mass loss step. For georgeite, mass is immediately lost as soon as the material is heated. The first TGA mass loss up to 80 °C is a dehydration step, whereby only evolution of water is apparent. This reduction in mass is gradual in comparison to the second step. This occurs in the temperature range 80-275 °C and is associated with the simultaneous evolution of CO<sub>2</sub> and water. This is assigned as a decarbonation and dehydroxylation step. The final mass loss that occurs between 275-340 °C is an additional decarbonation step, whereby only CO<sub>2</sub> is evolved. This indicates that there are two carbonate species present in georgeite, with the carbonate decomposing at higher temperature assigned as HT-CO<sub>3</sub>. The DTA findings also illustrate that the overall decomposition is largely thermo-neutral, with a weak exothermic peak centred at 200 °C associated with the second mass loss step. In comparison for malachite, the TGA profile is in agreement with related literature findings<sup>(1,3,7)</sup>. This single mass loss occurs between 235-305 °C, and is a dehydroxylation and decarbonation step as indicated by the simultaneous evolution of water and CO<sub>2</sub> respectively. Interestingly, in comparison to georgeite the DTA profile is significantly different whereby the mass loss is strongly endothermic. This endothermic process has also been reported in related hydroxycarbonate phases<sup>(20)</sup>.

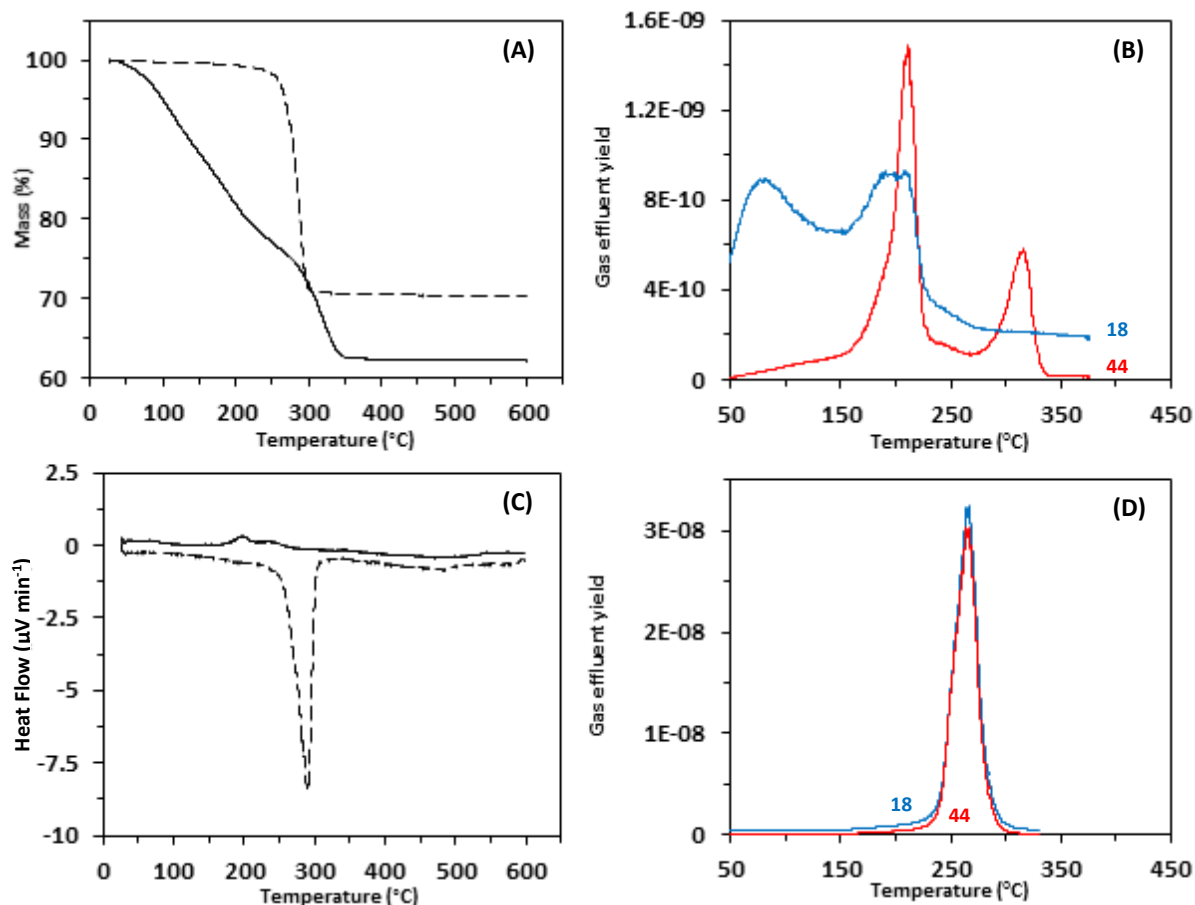


**Figure 4.4.** TGA, DTA and EGA of georgeite and malachite under 50 ml/min flowing air with a ramp rate of 1 °C/min. (A) TGA of georgeite (solid line) and malachite (hashed line) (B) EGA of georgeite (C) DTA of georgeite (solid line) and malachite (hashed line) (D) EGA of malachite. Mass spectrometry traces of  $m/z = 18$  (blue) and  $m/z = 44$  (red) were detected from EGA as shown.

In order to investigate the phases further, identical TGA/DTA/EGA studies were carried out on the zincian georgeite and zincian malachite precursors (Figure 4.5.). In comparison to the copper-only phases, similar profiles were obtained, illustrating no significant changes occurring to the phases from Zn incorporation. It is apparent though, that the incorporation of Zn shifts all the thermal decomposition steps to higher temperature as has previously been discussed (Section 3.3.). For zincian georgeite, the dehydration step is apparent up to 100 °C, as indicated clearly in the EGA findings. The simultaneous decarbonation and dehydroxylation step occurs in the temperature range 100-330 °C, whilst the final decarbonation step, attributed to the decomposition of  $\text{HT-CO}_3$ , occurs between 350-450 °C. The DTA findings again indicate that the overall decomposition of the phase is largely thermo-neutral, with a weak exothermic peak centred at 200 °C associated with the second mass loss. Above 300 °C where the final mass loss occurs, the process is weakly endothermic indicating subtle differences between these steps. For zincian malachite the simultaneous decarbonation and dehydroxylation step, which is endothermic, occurs between 260-360 °C. It is important to note, however, that the TGA/EGA profile for zincian malachite does not match that reported in certain related literature, whereby an additional decarbonation step is reported as

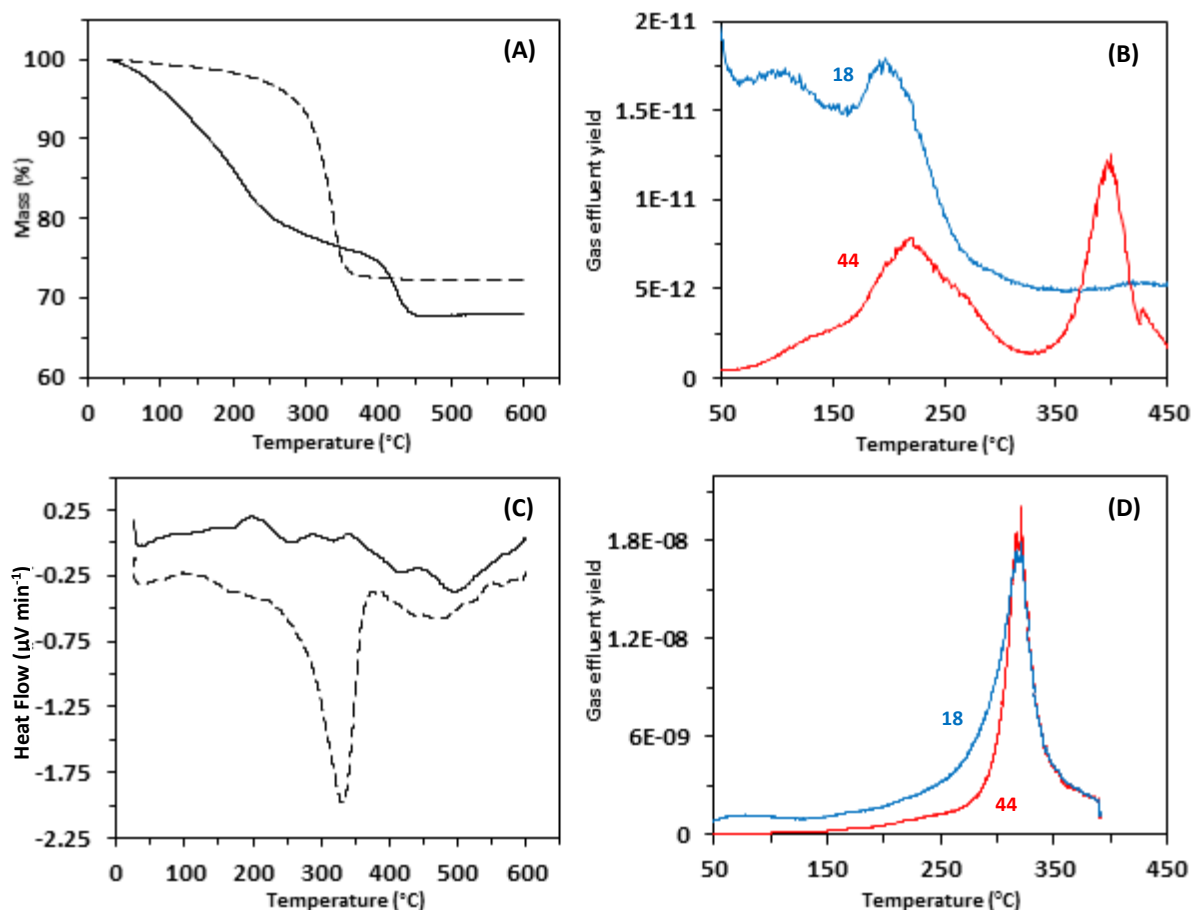


**Figure 4.5.** TGA, DTA and EGA of zincian georgeite and zincian malachite under 50 ml/min flowing air with a ramp rate of 1 °C/min. (A) TGA of zincian georgeite (solid line) and zincian malachite (hashed line) (B) EGA of zincian georgeite (C) DTA of zincian georgeite (solid line) and zincian malachite (hashed line) (D) EGA of zincian malachite. Mass spectrometry traces of  $m/z = 18$  (blue) and  $m/z = 44$  (red) were detected from EGA as shown.

shown for the georgeite phases<sup>(1,3,7,21)</sup>. This HT-CO<sub>3</sub> species is also present in aurichalcite and various related synthetic and mineralogical hydroxycarbonates. However, this is in direct contrast to findings by Bems and co-workers who reported that HT-CO<sub>3</sub> is not present in mineralogical aurichalcite<sup>(1)</sup>. Furthermore, TGA analysis carried out on the aurichalcite precursor provided by JM also displayed just a single mass loss. The factors that influence the presence of HT-CO<sub>3</sub> is therefore still not fully understood. Bems concluded that the presence of HT-CO<sub>3</sub> arises from the combination of aurichalcite and a metastable amorphous hydroxycarbonate<sup>(1)</sup>, whilst a later study from Behrens reported that HT-CO<sub>3</sub> cannot be related to amorphous phases<sup>(3)</sup>. The current TGA findings on georgeite clearly rules out both conclusions, whereby it is actually plausible that these reported precursors still have residual amounts of georgeite present which has gone undetected. Alternatively, it is possible that subtle differences in the co-precipitation procedure can drastically affect the content present. In particular, the concentration of the starting solutions might be decisive, whereby industry utilises much more concentrated solutions in comparison to what is used in the literature. This is in relation to reports that HT-CO<sub>3</sub> formation is extremely sensitive to the appearance of the NO<sub>3</sub><sup>-</sup> anion<sup>(1)</sup>.

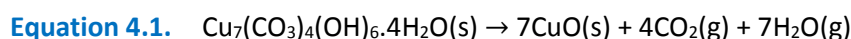
**Table 4.2.** Comparison of TGA theoretical and experimental mass losses for georgeite and malachite phases.

Phase	Residual mass remaining at 300 °C (%)	Theoretical total mass loss (%) <sup>a</sup>	Experimental total mass loss (%)	Theoretical / experimental total mass loss (%)
Georgeite	9.7	35.18	37.7	93
Zincian georgeite	9.9	35.66	35	102
Malachite	0.9	28.05	29.6	95
Zincian malachite	21	27.7	27.9	99

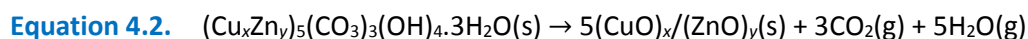
<sup>a</sup> Calculated from assumption of final product being CuO for copper only phases and (CuO)<sub>0.67</sub>/(ZnO)<sub>0.33</sub> for copper-zinc phases.

Quantitative analysis of all the TGA findings was also conducted to verify the molecular formulas derived from ICP-MS and CHN analysis (Table 4.2.). The experimental total mass losses correlate well with the calculated theoretical mass losses, which further strengthens the credentials of these findings. Subtle differences were expected, relating to the presence of by-phases and/or instrumental error. The content of residual mass remaining after 300 °C is also presented which was the standard calcination temperature used in previous work (Chapter Three). However, it should be noted that these values are guidelines only. The TGA findings were obtained using a continuous ramp in temperature and did not consider holding the materials for durations at this temperature, whereby minor additional mass loss could be expected. The data implies that the amount of residual content remaining in the georgeite phases at 300 °C is similar (9.7-9.9%). This is expected since at this point both materials only have the final decarbonation step to proceed through. In contrast, the malachite phases have significantly different amounts of retained residual content. At 300 °C, the malachite phase has essentially fully decomposed to CuO, whilst for zincian malachite 21% of the residual hydroxycarbonate phase is still present.

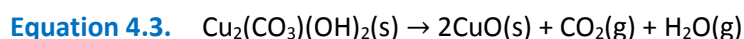
At this point it is important to reflect on the TGA/DTA/EGA findings and to discuss in more detail the relevant decomposition processes occurring in relation to the precursors. If the calcination process is allowed to proceed through to completion by heating to temperatures in excess of 450 °C, then total decomposition to the metal oxides takes place (Equations 4.1-4.4.).



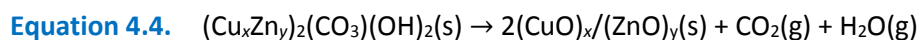
*Georgeite*



*Zincian georgeite*

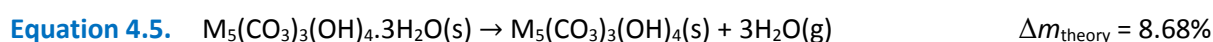


*Malachite*

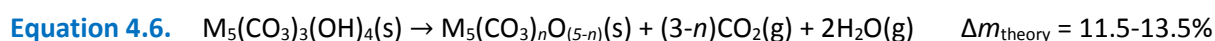


*Zincian malachite*

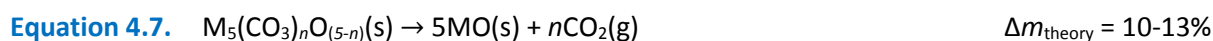
Whereby in this particular case,  $x = 0.67$  and  $y = 0.33$ . However, as already discussed, this decomposition process actually proceeds through a number of steps and calcination temperatures commonly used in the literature, including the work reported herein, are often only in the range 300-350 °C<sup>(21)</sup>. Consequently, the following decomposition pathway is proposed for zincian georgeite. The first mass loss ( $\Delta m$ ) which occurs immediately with heating is attributed to a dehydration step from loss of occluded water within the structure (**Equation 4.5.**).



Whereby in this particular case  $\text{M} = (\text{Cu}_{0.67}\text{Zn}_{0.33})$ . From this step results a colour change from sky blue to turquoise blue with the density increasing from 3.03 to 3.39 g cm<sup>-3</sup>. The second mass loss is attributed to the simultaneous decarbonation and dehydroxylation step (**Equation 4.6.**).

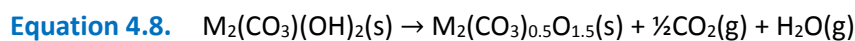


This process results in the formation of a carbonate-modified metal oxide, which has also been widely reported in related studies<sup>(7,21-22)</sup>. The actual formula is governed by the amount,  $n$  of retained HT-CO<sub>3</sub>. This value will be influenced by numerous parameters from the precipitation and calcination procedures. From the findings obtained in this work,  $n$  frequently ranges between 1.9-2.2. It has been suggested that the retained HT-CO<sub>3</sub> arises from occluded carbonate trapped at the CuO/ZnO interface<sup>(1,22-23)</sup>. However, this species is clearly evident in the TGA/EGA findings obtained for georgeite, and therefore, it can be concluded that it is associated with the amorphous phase. Interestingly, it was also apparent that the ramp rate influenced the decomposition temperature of HT-CO<sub>3</sub> (**Figure 3.20.**). Studies by Fujita and Behrens have also examined the ramp rate, whereby it was reported that higher ramp rates increase the local partial pressure of H<sub>2</sub>O resulting in faster decomposition of HT-CO<sub>3</sub> and larger CuO crystallite sizes<sup>(21-22,24)</sup>. This is related to the (evolved H<sub>2</sub>O) : (CuO + ZnO) ratio which for zincian georgeite, zincian malachite and aurichalcite is 2, 1 and 1.7 respectively. This would suggest that deactivation by H<sub>2</sub>O is most severe for the georgeite precursor, and therefore, carrying out calcination in flowing air could result in further optimisation. It should also be noted that for this second step, a colour change occurs from turquoise blue to green and then finally black indicating the presence of CuO. The third and final mass loss is attributed to the second decarbonation step with loss of HT-CO<sub>3</sub> (**Equation 4.7.**).



The loss of all residual precursor with complete formation of the metal oxide indicates that the decomposition process has gone to completion. A similar decomposition pathway is also apparent for georgeite. However, the absence of zinc reduces the thermal stability of the phase so these decomposition processes occur at lower temperature and also appear to overlap to a greater extent.

For zincian malachite, a similar two-step decomposition pathway has been proposed by Behrens<sup>(21)</sup> (**Equations 4.8-4.9**).



Whereby in this particular case  $M = (Cu_{0.67}Zn_{0.33})$ . However, as already mentioned, the TGA/EGA findings did not provide any evidence for the formation of a carbonate-modified metal oxide from this precursor. It instead suggests that residual hydroxycarbonate content co-exists with CuO/ZnO phases during this single mass loss.

Similar TGA/DTA/EGA findings were obtained for the SAS prepared Cu and CuZn acetate as well as the Cu acetate monohydrate starting material (**Figure S17**). The findings was in agreement with previous work (**Section 3.2.**), and gas effluents with high m/z values were detected indicating the presence of acetic acid and acetone. Interestingly, these effluents were not detected in the georgeite samples. Additional temperature programmed studies were also carried out, whereby air was replaced with nitrogen in order to investigate the effect of gas flow type on the decomposition process. For the hydroxycarbonate precursors, no differences were observed in contrast to the acetates, whereby nitrogen was found to switch off the exothermic decomposition in agreement with Hutchings and co-workers<sup>(25)</sup>.

With a better understanding of the thermal decomposition process for zincian georgeite and zincian malachite, attention focused on optimising various parameters of the calcination process for both precursors. Cu surface areas were measured for catalysts which had been calcined under a range of temperatures (250-550 °C) and times (2 and 6 hours) in static air (**Figure 4.6**). A fixed sample mass of 200 mg was used for each calcination to enable a fairer comparison. For both precursors, volcano-type plots were obtained for Cu surface area with respect to temperature. A similar relationship was obtained by Baltes and co-workers, who investigated the effect of calcination temperature on methanol productivity<sup>(26)</sup>. Interestingly, for zincian georgeite, little change in Cu surface area was observed in the range 250-350 °C, whereby the TGA also indicated little change in mass over the same range. It is also apparent that temperature has a stronger influence on Cu surface area than time, in agreement with similar observations made by Zhang and co-workers<sup>(27)</sup>. Similarly for zincian

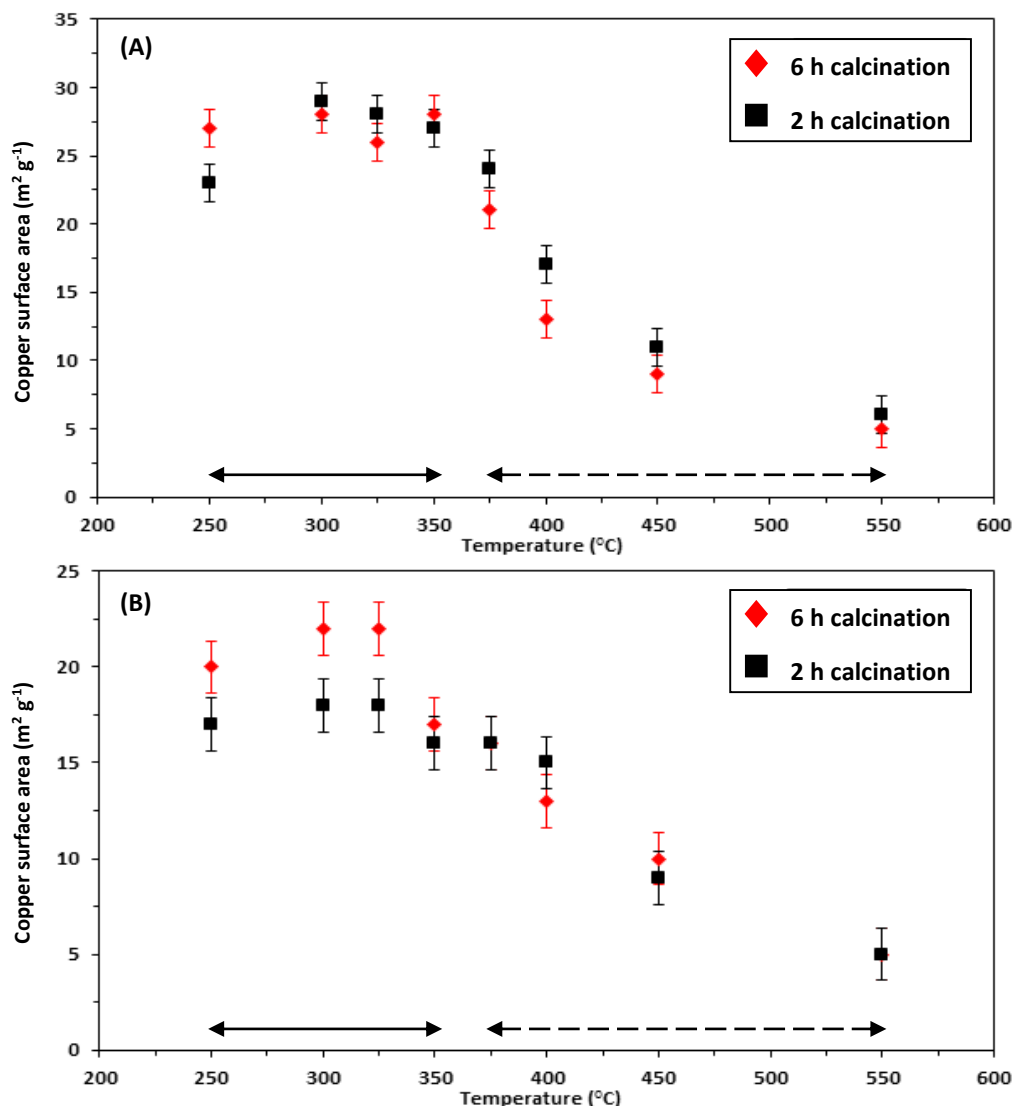


**Figure 4.6.** Copper surface area analysis of: (A) Zincian georgeite prepared by SAS precipitation (B) zincian malachite prepared by co-precipitation. Samples were calcined at various temperatures (250-550 °C) and times (2 or 6 hours) in order to determine the optimum calcination conditions for both materials. Solid arrows indicate optimum temperature range and hashed arrows indicate temperature range where sintering is clearly apparent.

malachite, the Cu surface area did not vary significantly between 250-350 °C, but the influence with time was more significant. With a 6 hour calcination time, a pronounced decrease is clearly apparent between 325-350 °C. Interestingly, this temperature range is where complete decomposition of the hydroxycarbonate occurs. At temperatures  $\geq 350$  °C, Cu surface area then appears to directly decrease with temperature. This can be explained from the complete removal of residual carbonate, which hinders sintering of the Cu crystallites. A similar trend is observed for zincian georgeite, in the temperature range 450-550 °C, again where complete decomposition of residual carbonate has already taken place. Although some of the data points are within the error limits, it also appears for both precursors that longer calcination times are favourable below the optimum temperature. Above this, temperature shorter times become more desirable in order to minimise metal sintering.

It can be seen that 300 °C is within the optimum temperature range for both precursors, which justifies why this temperature was chosen in relation to previous work (**Chapter Three**). With respect to zincian georgeite, the TGA/EGA findings indicate that at this temperature the precursor has fully decomposed to the carbonate-modified metal oxide, with only HT-CO<sub>3</sub> remaining. Therefore, this work strongly suggests that the presence of HT-CO<sub>3</sub> after calcination is essential for the production of optimum catalysts. Similar findings have been widely reported in the literature. Behrens reported that the decomposition enthalpy decreases linearly with respect to the amount of HT-CO<sub>3</sub> present<sup>(21)</sup>. Fujita reported that a reduction of HT-CO<sub>3</sub> resulted in larger CuO crystallite sizes leading to catalysts with reduced methanol formation rates<sup>(22)</sup>. Baltes stated that such residual carbonates may be responsible for the formation of highly active sites<sup>(26)</sup>. Moreover, Bems concluded that HT-CO<sub>3</sub> is a growth inhibitor for the metal oxide crystallites, by acting as glue between the components<sup>(1)</sup>. Later studies illustrated that retained HT-CO<sub>3</sub> resulted in catalysts with higher activity and were also intrinsically more active for methanol synthesis<sup>(28)</sup>. Interestingly, the content of HT-CO<sub>3</sub> is higher in aurichalcite than in zincian malachite. Millar and co-workers related this to aurichalcite being the optimum catalyst precursor, whereby HT-CO<sub>3</sub> was reported to stabilise small CuO and ZnO clusters and to bind Cu species to Zn moieties<sup>(7)</sup>. However, the (CO<sub>3</sub>) : (Cu + Zn) ratio is lower in aurichalcite in comparison to malachite (0.4 and 0.5 respectively) which rules out any potential correlation with the HT-CO<sub>3</sub> content. The studies carried out in **Chapter Three** also highlighted the importance of HT-CO<sub>3</sub>, whereby a correlation between Cu surface area and HT-CO<sub>3</sub> content and decomposition temperature was apparent.

For the zincian malachite precursor, even though no HT-CO<sub>3</sub> is present, the findings still illustrate that the optimum calcination temperature resides with residual amounts of the hydroxycarbonate still present. If this residual hydroxycarbonate was not acting similarly to HT-CO<sub>3</sub>, the Cu surface area trend may be expected to just directly decrease with temperature. Furthermore, for zincian georgeite, it can be seen that high Cu surface areas are retained up to slightly higher temperature. The Cu surface area only seems to drastically drop when HT-CO<sub>3</sub> decomposition begins. With zincian georgeite having higher Cu surface areas for each data point it was expected that it would be more prone to sintering at these higher temperatures, as a result of the higher surface energy favouring this process. This provides further evidence that HT-CO<sub>3</sub> is acting as a growth inhibitor.

It must be reminded that the higher Cu surface areas obtained in the zincian georgeite precursor is largely a result of the chosen preparation route. Precursors prepared from SAS precipitation are expected to have larger surface areas to those prepared by co-precipitation, as previously discussed (**Section 1.5.1.**). The findings conclude that Cu surface areas up to 29 m<sup>2</sup> g<sup>-1</sup> can be achieved for the

zincian georgeite precursor in comparison to  $22 \text{ m}^2 \text{ g}^{-1}$  obtained from the industrial zincian malachite precursor. Interestingly, at temperatures  $\geq 450 \text{ }^\circ\text{C}$  where no residual carbonate remains, the Cu surface areas for both precursors are identical. Cu surface areas of georgeite and malachite were also measured after calcination at  $300 \text{ }^\circ\text{C}$  for 2 hours, however, for both precursors values  $\leq 1 \text{ m}^2 \text{ g}^{-1}$  were obtained.

In order to verify the Cu surface area findings, BET surface areas of both binary precursors before and after calcination from a range of conditions were measured (Table 4.3.). The findings are in strong agreement with the Cu surface area findings, confirming the volcano-type trend. For zincian georgeite, BET surface areas in the range  $80\text{-}90 \text{ m}^2 \text{ g}^{-1}$  can be produced after calcination using the optimum temperature of  $300 \text{ }^\circ\text{C}$ . At considerably higher temperatures ( $450\text{-}550 \text{ }^\circ\text{C}$ ), the BET surface area decreases, with the lowest values recorded in the range  $16\text{-}18 \text{ m}^2 \text{ g}^{-1}$ . A similar trend was observed for the zincian malachite precursor. After calcination, optimum BET surface areas in the range  $30\text{-}40 \text{ m}^2 \text{ g}^{-1}$  were obtained, in comparison to values in the range  $7\text{-}11 \text{ m}^2 \text{ g}^{-1}$  over the exact same temperature range. This reduction in BET surface area with temperatures in excess of  $300 \text{ }^\circ\text{C}$  is associated with metal sintering. However, BET surface areas obtained using temperatures below  $300 \text{ }^\circ\text{C}$  illustrated a different trend. For both precursors, calcination at  $250 \text{ }^\circ\text{C}$  also resulted in lower BET surface areas as was apparent from the Cu surface area analysis. Zhang and co-workers obtained similar findings and concluded that full decomposition is required to obtain optimum catalysts for liquid methanol synthesis<sup>(27)</sup>. Moreover, for zincian malachite, the BET surface area appears to continuously increase up to the  $300 \text{ }^\circ\text{C}$  ( $20$  to  $41 \text{ m}^2 \text{ g}^{-1}$ ). However, for zincian georgeite the BET surface area of the precursor ( $97 \text{ m}^2 \text{ g}^{-1}$ ) is higher than after calcination to  $250 \text{ }^\circ\text{C}$  ( $59\text{-}63 \text{ m}^2 \text{ g}^{-1}$ ). At

**Table 4.3.** BET surface areas of zincian georgeite and zincian malachite. Samples were calcined under various conditions in order to determine optimum calcination conditions. C values are provided to indicate degree of accuracy for each analysis.

Calcination conditions		Zincian georgeite		Zincian malachite	
Temperature ( $^\circ\text{C}$ )	Time (h)	( $\text{m}^2 \text{ g}^{-1}$ ) <sup>a</sup>	C value	( $\text{m}^2 \text{ g}^{-1}$ ) <sup>a</sup>	C value
Precursor		97	79	20	314
250	2	59	473	24	413
	6	63	559	29	72
300	2	84	73	31	336
	6	94	228	41	329
450	2	58	45	28	364
	6	41	51	24	246
550	2	18	62	11	249
	6	16	37	7	1035

<sup>a</sup> Standard deviation  $\pm 6 \text{ m}^2 \text{ g}^{-1}$ .

this temperature the dehydration step would have run to completion, but residual contents of carbonate and hydroxyl groups associated with the second mass loss remain, as indicated by the green colour of the sample. It is plausible that complete evolution of these species is required to fully generate the optimum carbonate-modified metal oxide, possibly with a subsequent re-arrangement of HT-CO<sub>3</sub>.

In order to investigate these findings further, BET surface areas of higher accuracy as well as information regarding pore size distribution and total pore volume were obtained for all the malachite and georgeite precursors, before and calcination, using the Autosorb-1 instrumentation (Table 4.4 and Figure 4.7.). As previously discussed, the Autosorb-1 vacuum enables degassing of samples prior to analysis to be carried out at ambient temperature, which is essential for accurate analysis of heat sensitive hydroxycarbonate materials (Section 2.4.9.). All precursors were calcined using the optimum conditions for the binary precursors: 300 °C for 2 hours in static air with a ramp rate of 10 °C/min. The georgeite precursor had a BET surface area of 74 m<sup>2</sup> g<sup>-1</sup> and total pore volume of 0.6 cm<sup>3</sup> g<sup>-1</sup>, whereby after calcination using these conditions resulted in the BET surface area decreasing to 52 m<sup>2</sup> g<sup>-1</sup>, whilst the pore volume increased to 0.9 cm<sup>3</sup> g<sup>-1</sup>. The pore size distribution also narrowed after calcination, whereby pore sizes down to 50 Å were lost. Clearly, a complete reconstruction of the mesostructure from the thermal treatment took place. The lower BET surface area could be attributed to CuO sintering, whilst the increase in porosity is most likely a result of loss of all residual hydroxycarbonate species. The zincian georgeite precursor in comparison, displayed

**Table 4.4.** BET surface areas and pore volumes of georgeite and malachite phases before and after calcination using optimum conditions. Analysis obtained from Autosorb-1 instrumentation. C values are provided to indicate degree of accuracy for each analysis.

Phase	Synthesis type <sup>a</sup>	Precursor / calcined	Surface area (m <sup>2</sup> g <sup>-1</sup> ) <sup>b</sup>	C value	Total pore volume (cm <sup>3</sup> g <sup>-1</sup> ) <sup>c</sup>
Georgeite	SAS (5%)	Precursor	74	41	0.6
		Calcined	52	30	0.9
Malachite	CP	Precursor	8	16	0.04
		Calcined	43	42	0.2
Zincian georgeite	SAS (10%)	Precursor	89	34	0.6
	SAS (5%)	Precursor	102	56	0.5
	SAS (5%)	Calcined	109	59	0.5
Zincian malachite	CP	Precursor	35	28.5	0.3
		Calcined	27	50	0.3
			29	57	0.3

<sup>a</sup> Water content used provided in brackets regarding samples prepared by SAS precipitation.

<sup>b</sup> Standard deviation ±0.5 m<sup>2</sup> g<sup>-1</sup>.

<sup>c</sup> Standard deviation ±0.1 cm<sup>3</sup> g<sup>-1</sup>.

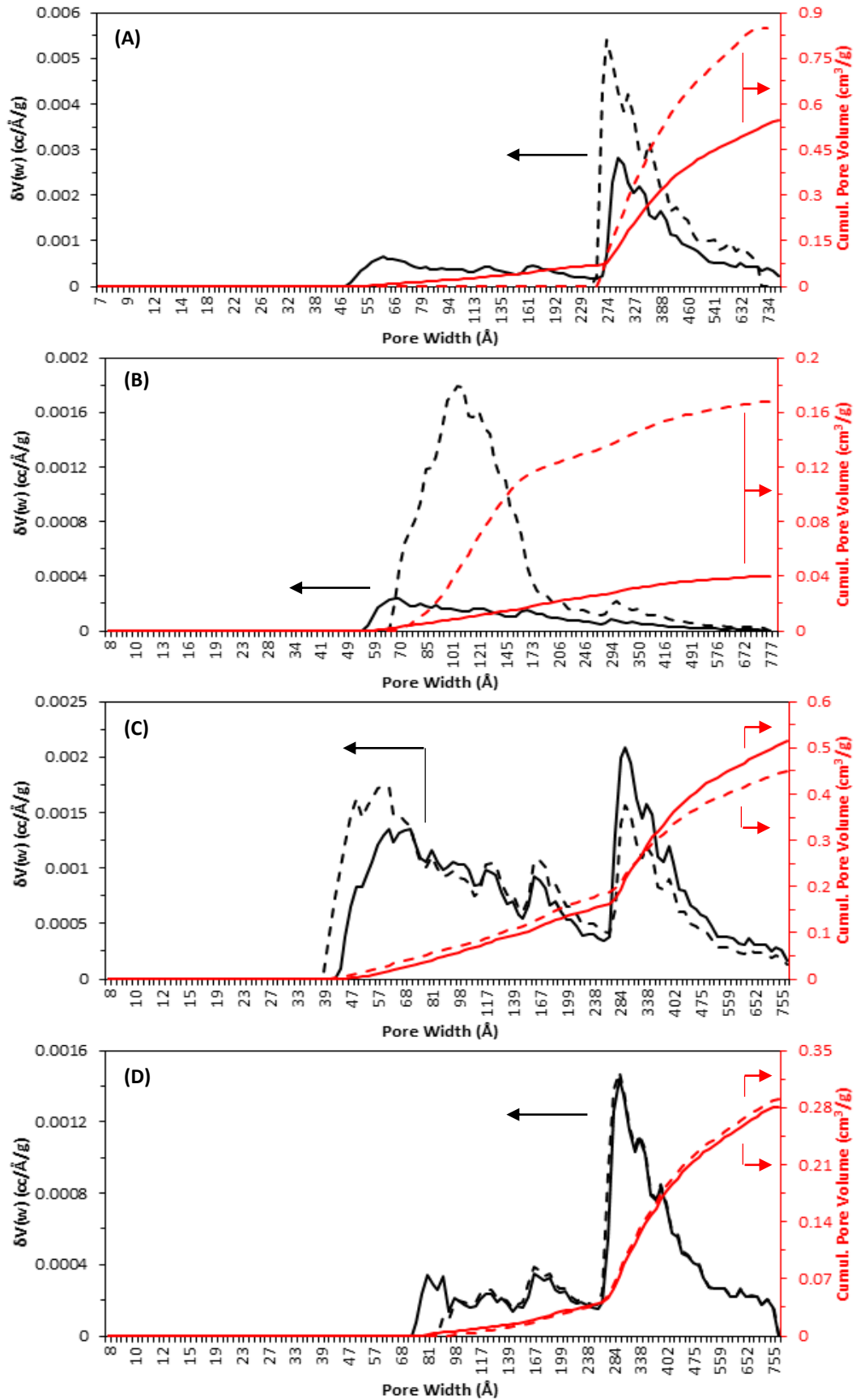


**Figure 4.7.** DFT Monte-Carlo pore size distribution and cumulative pore volume of: (A) Georgeite, (B) malachite (C) zincian georgeite (5% vol. H<sub>2</sub>O) (D) zincian malachite before and after calcination. Solid lines represent the precursors with hashed lines representing materials after calcination using optimum conditions (300 °C, 2 h). Arrows are also provided for clarity.

BET surface areas in the range 89-102 m<sup>2</sup> g<sup>-1</sup>, depending on the water content used in the SAS preparation. Moreover, the pore size distribution and total pore volume was similar to that obtained for georgeite (Figure 4.7(A). and 4.7(C).). However, clear differences are apparent after calcination. The BET surface area increased to 109 m<sup>2</sup> g<sup>-1</sup> in agreement with previous BET findings (Table 4.3.). Furthermore, in contrast to georgeite, the mesostructure of the binary precursor remained largely unchanged after calcination. Considering the error margin of the Autosorb-1 analysis, the total pore volume was the same before and after calcination as the error was ±0.1 cm<sup>3</sup> g<sup>-1</sup>. Only subtle changes were seen in the pore size distribution, meaning pore sizes down to 40 Å were retained. The clear difference in thermal behaviour regarding georgeite and zincian georgeite relates to the presence or absence of Zn and HT-CO<sub>3</sub>. Interestingly, since georgeite had a Cu surface area ≤ 1 m<sup>2</sup> g<sup>-1</sup> it illustrates that the severe sintering mechanism actually occurs in the subsequent reduction step. The analysis was also used to compare zincian georgeite precursors prepared using various synthesis routes (Table 4.4. and Figure S18(A).). The SAS prepared precursors illustrated superior BET surface areas and porosities, in comparison to the precursor prepared by co-precipitation. However, the pore size distributions were similar indicating that the same mesostructure was present in all these precursors.

For the malachite precursor, the BET surface area increased significantly from calcination from 8 to 43 m<sup>2</sup> g<sup>-1</sup>, with the total pore volume also drastically increasing from 0.04 to 0.2 cm<sup>3</sup> g<sup>-1</sup>. Since this precursor also had a Cu surface area ≤ 1 m<sup>2</sup> g<sup>-1</sup>, it further demonstrates that the sintering process is more severe in the subsequent reduction step. A complete reconstruction of the mesostructure occurred with thermal treatment, as was observed for georgeite. Furthermore, the increase in porosity is also attributed to complete removal of residual hydroxycarbonate. However, in contrast to georgeite, an improvement in BET surface area was apparent. Since the BET surface area of the malachite precursor was so low it is possible that it improved after calcination simply because the increase in BET surface area associated with removal of residual hydroxycarbonate outweighed the decrease in BET surface area associated with CuO sintering. Taking into consideration the error margin, the BET surface area of zincian malachite remained unchanged from calcination in the range 27-29 m<sup>2</sup> g<sup>-1</sup>. The thermal behaviour was identical to that observed for zincian georgeite, whereby the thermal process resulted in no significant changes to the pore size distribution or total pore volume, indicating that the mesostructure was not disrupted. The total pore volume remained the same at 0.3 cm<sup>3</sup> g<sup>-1</sup> with pore sizes down to 70 Å observed. With the BET surface area and total pore volume for zincian malachite inferior to that of Cu only georgeite after calcination, it significantly highlights the critical importance of Zn and residual carbonate in preventing sintering during the reduction process.

At this point it is important to directly compare and discuss the BET/DFT findings in relation to zincian georgeite and zincian malachite both prepared by co-precipitation (**Table 4.4.** and **Figure S18(B).**). Since it has already been illustrated that the precipitation procedure drastically effects the physical properties (**Figure S18(A).**), only a fair comparison can be made by comparing the precursors made by the same precipitation technique. Zincian georgeite was produced by the modified co-precipitation technique discussed in **Section 3.5.** using concentrated acetate solutions (Cu acetate = 70 mg/ml) and a washing step. This precursor was also one of the georgeite materials selected for testing at Johnson Matthey. It can be seen that the surface area, pore size distribution and total pore volume for both precursors is almost identical, whereby zincian georgeite actually displays a slight improvement in these properties. This is in agreement with previous Cu surface area analysis which illustrated that similar values were achieved from both precursors (**Figure 3.23.** and **3.25.**). It provides further evidence that zincian georgeite can compete against zincian malachite as an optimum catalyst precursor, and furthermore, indicates that it has a similar porous network. As mentioned previously, the optimum mesostructure has been attributed to the malachite precursor consisting of a loose network of nano-scale needles allowing greater access to Cu sites<sup>(2,5)</sup>. However, whilst a BET surface area of  $35 \text{ m}^2 \text{ g}^{-1}$  for zincian georgeite is in good agreement with the literature, zincian malachite was reported to have a BET surface area of  $57 \text{ m}^2 \text{ g}^{-1(2)}$ . This is significantly different to  $29 \text{ m}^2 \text{ g}^{-1}$  determined in this study which could be related to the HT-CO<sub>3</sub> content.

The zincian georgeite and zincian malachite structures after calcination were investigated further by TEM analysis (**Figure 4.8.**). For both materials, distorted, non-spherical CuO and ZnO nanoparticles were observed in an alternating fashion to form larger porous aggregates. Behrens and co-workers have related this non-spherical morphology to the formation of stacking faults and surface defects as a mechanism of strain relaxation<sup>(29)</sup>. The observed pores significantly varied in size and were also undefined in shape. For zincian georgeite it can be seen that pore diameters can vary between several tens of nm down to as small as 10 nm, which indicates that both macropores and mesopores are present (**Figures 4.8(A)-(B).**). The mesostructure is clearly not compact as has been previously reported<sup>(2)</sup>. These large porous aggregates are undefined in shape, which can be attributed to the amorphous nature of the material. They also agglomerate with one another to form inter-particulate macropores. For zincian malachite, pore sizes also ranged significantly down to 10 nm. However, whilst similarities were observed between both precursors at the nanoscale there are differences in the porous mesostructures. In contrast to the undefined shape of the amorphous material, the industrial precursor consists of discrete needles which vary in length and width by several tens of nanometres. Furthermore, several platelets are also observed which may be associated with the aurichalcite by-phase (**Figures 4.8(C)-(D).**).

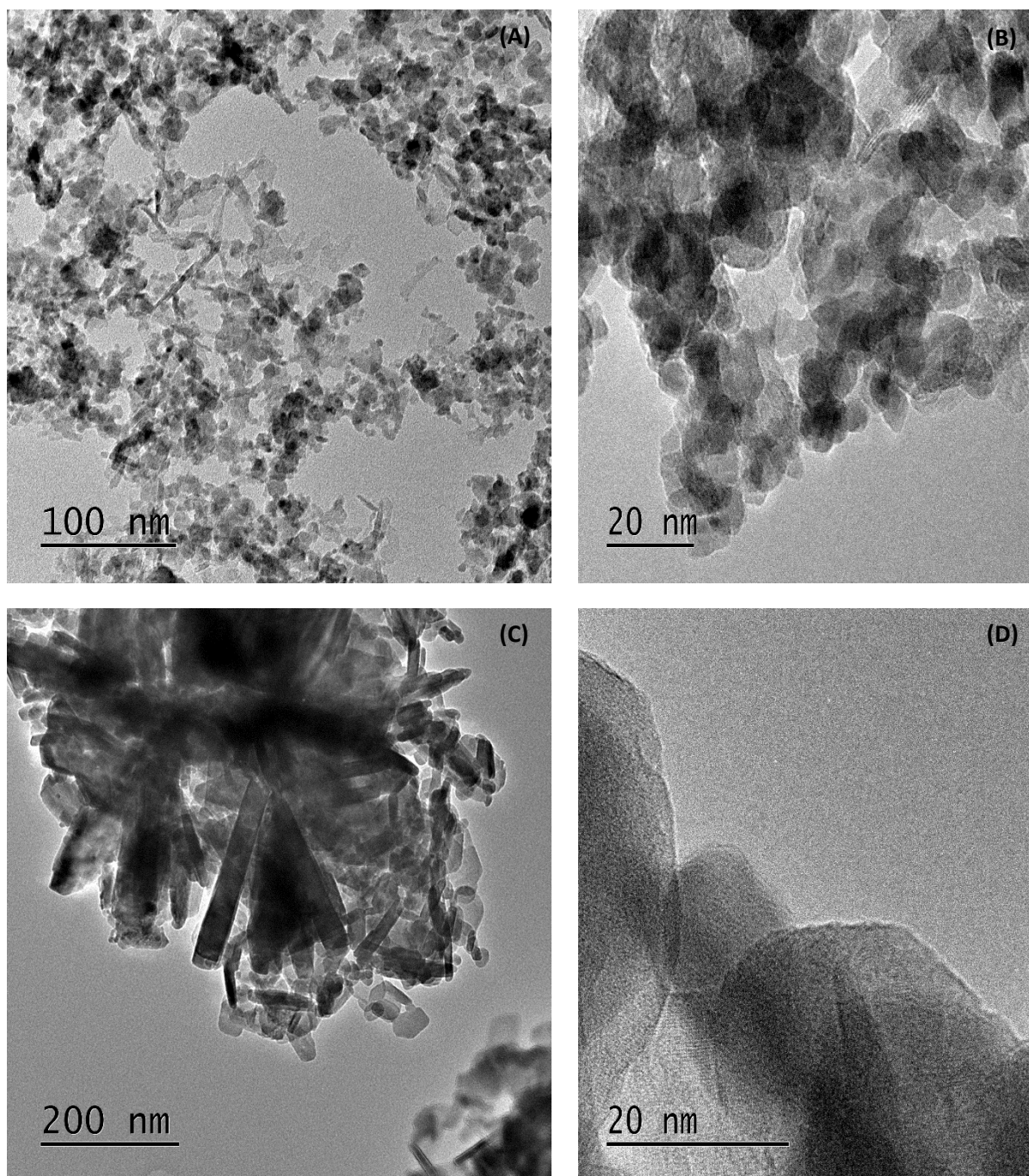


**Figure 4.8.** TEM images showing: (A and B) Zincin georgeite prepared by SAS precipitation (C and D) zincin malachite prepared by co-precipitation. The precursors were calcined using optimum conditions (300 °C, 2 h).

The binary precursors which were calcined under various temperatures (250-550 °C) and times (2 and 6 hours) for Cu surface area analysis ([Figure 4.6.](#)) were investigated further by XRD analysis in order to correlate these values to the apparent changes in structure. Therefore, the various decomposition steps associated with each precursor were also being correlated to their structural changes to yield additional information on the process. Zincin georgeite appears to remain amorphous after calcination up to the optimum temperature of 300 °C ([Figure 4.9.](#)). This could imply that the resulting carbonate-modified metal oxide is also amorphous. However, the TEM findings

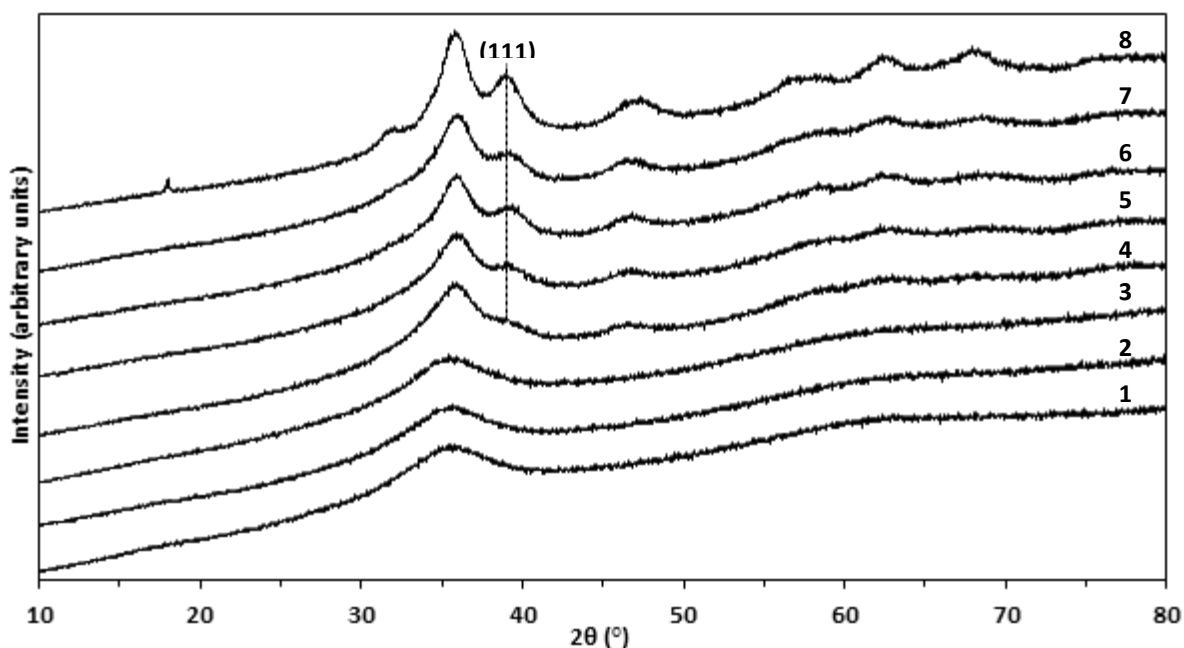


**Figure 4.9.** XRD patterns for zincian georgeite after calcination under the following conditions: (1) 250 °C for 2 h (2) 250 °C for 6 h (3) 300 °C for 2 h (4) 300 °C for 6 h (5) 325 °C for 2 h (6) 325 °C for 6 h (7) 350 °C for 2 h (8) 350 °C for 6 h. The broad (111) reflection for CuO indicated at 38.7 ° is the only peak which can be assigned.

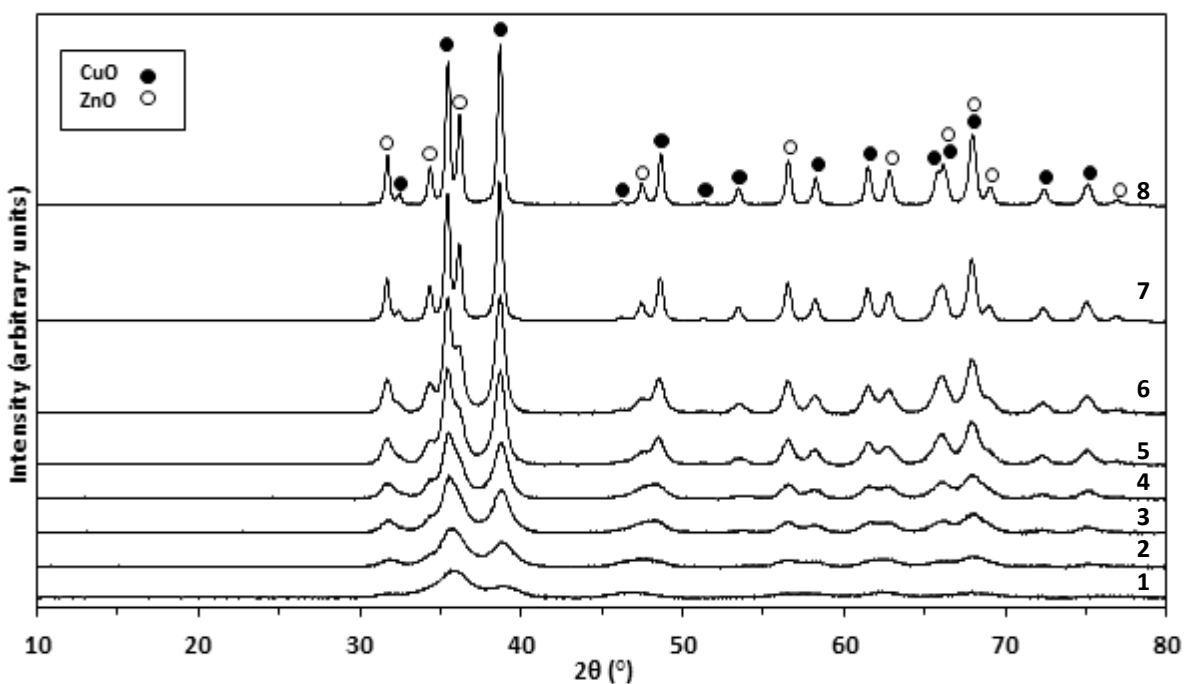


**Figure 4.10.** XRD patterns for zincian georgeite after calcination under the following conditions: (1) 375 °C for 2 h (2) 375 °C for 6 h (3) 400 °C for 2 h (4) 400 °C for 6 h (5) 450 °C for 2 h (6) 450 °C for 6 h (7) 550 °C for 2 h (8) 550 °C for 6 h.

indicated the presence of CuO and ZnO crystallites (**Figures 4.8(A)-(B).**), which means these phases at least have crystallite sizes too small to be observed. As mentioned previously in **Section 3.2.**, reflections were present at 33.1 and 59.1 ° in the precursor associated with an acetate phase. Since these reflections are not present, it suggests that this phase decomposes at temperatures  $\leq 250$  °C, as indicated from the TGA findings on acetate phases (**Figure S17.**). As the precursor is heated above

300 °C, the material slowly begins to crystallise but broad, ill-defined reflections are still only present up to 350 °C. The CuO (111) reflection is the only one which can be distinguished, as indicated. In addition, the influence of time is more evidently shown above 300 °C, whereby longer calcination times result in higher crystallinity, in agreement with the surface area findings. It was also apparent between 350-375 °C that the Cu surface area drastically began to decrease with temperature, which is when the HT-CO<sub>3</sub> begins to decompose (Figure 4.5.). The XRD findings illustrate that during this temperature range there is a sharp increase in crystallinity (Figure 4.10.). The rate of crystallisation rapidly increases above this temperature and after the HT-CO<sub>3</sub> has fully decomposed between 400-450 °C the material is highly crystalline with distinct, sharp CuO and ZnO reflections clearly present.

The XRD pattern for the zincian malachite precursor has previously been presented and discussed (Figure 4.1.). In agreement with the TGA findings, little structural change is apparent up to 250 °C (Figure 4.11.). Changes in the structure, however, can be identified at 300 °C where decomposition of the hydroxycarbonate begins. This is best illustrated in the low-angle range (10-25 °), also termed the ‘fingerprint region’<sup>(3)</sup>, where the reflections clearly begin to decrease in intensity. When the temperature increases between 325-350 °C, the hydroxycarbonate reflections are lost, indicating that all residual content has been removed. The previous findings also showed that at temperatures above 325 °C the Cu surface area began to decrease linearly. Furthermore, careful inspection of the XRD patterns shows that calcination to 325 °C resulted in the formation of the most poorly crystalline material. This is in agreement with Baltes and co-workers who reported that optimum

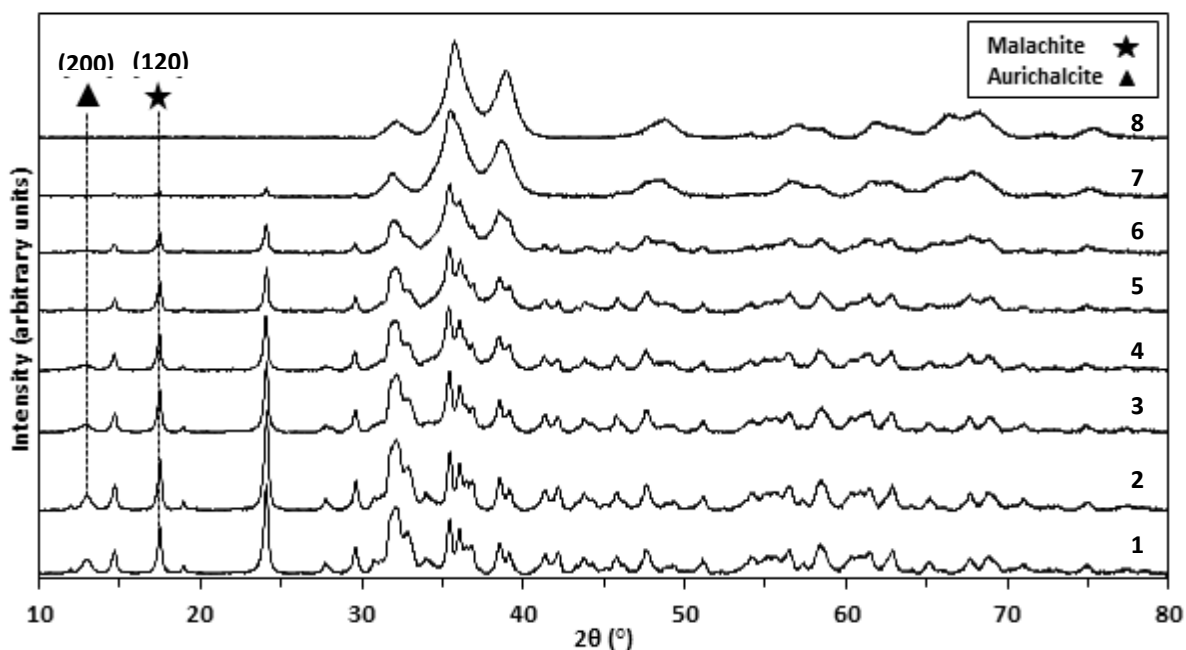


**Figure 4.11.** XRD patterns for zincian malachite after calcination under the following conditions: (1) 250 °C for 2 h (2) 250 °C for 6 h (3) 300 °C for 2 h (4) 300 °C for 6 h (5) 325 °C for 2 h (6) 325 °C for 6 h (7) 350 °C for 2 h (8) 350 °C for 6 h. The (120) and (200) reflections assigned to zincian malachite and aurichalcite phases respectively are indicated in the fingerprint region (see main text).

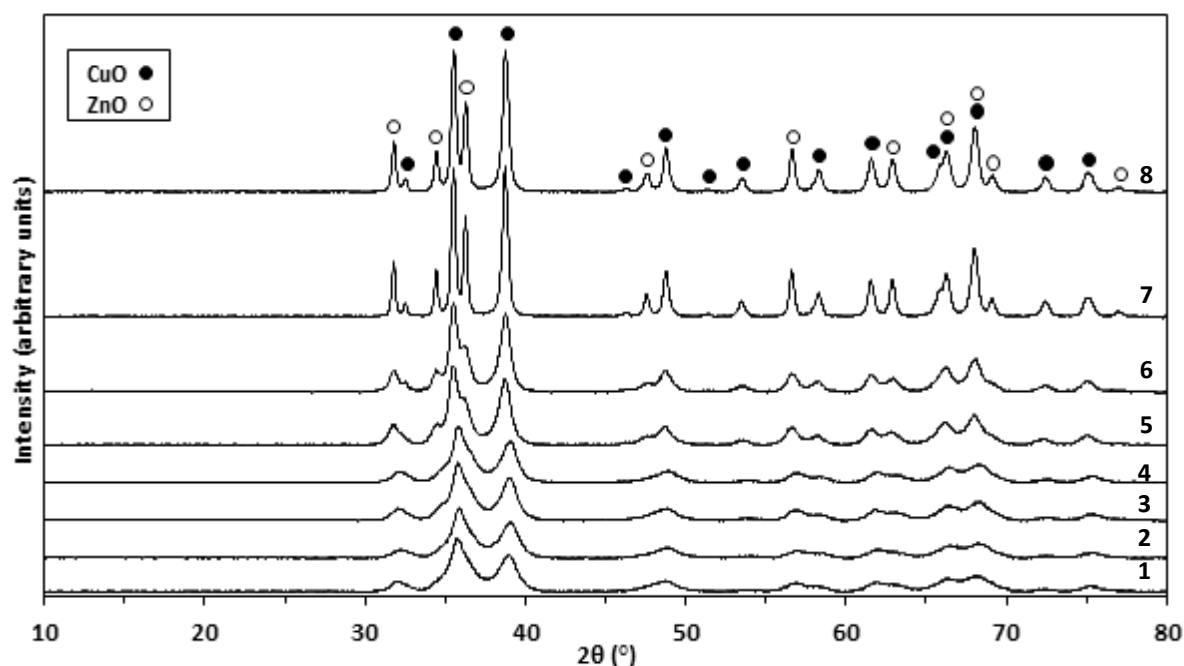


**Figure 4.12.** XRD patterns for zincian malachite after calcination under the following conditions: (1) 375 °C for 2 h (2) 375 °C for 6 h (3) 400 °C for 2 h (4) 400 °C for 6 h (5) 450 °C for 2 h (6) 450 °C for 6 h (7) 550 °C for 2 h (8) 550 °C for 6 h.

catalysts had an XRD pattern of non-decomposed hydroxycarbonate residues with poor, ill-defined reflections<sup>(26)</sup>. To investigate the decomposition of the crystalline hydroxycarbonates further, the d-spacing and crystal size was measured for various reflections present in the fingerprint region. CuO and ZnO reflections are not present in this region which avoids issues of peaks overlap.

Unfortunately, it was still not possible to analyse a zincian malachite reflection in this region which did not overlap with an aurichalcite reflection. Aurichalcite appears to decompose before zincian malachite between 300-325 °C. The (200) reflection in the precursor has a d-spacing of 6.805 Å and a crystallite size of 13.1 nm. Little change is apparent until between 250-300 °C, where the d-spacing sharply increases to 6.888 Å, whilst the crystallite size decreased to 7.8 nm. Attempts were made to carry out similar analysis on zincian malachite reflections, however, it was apparent there was influence from the overlapping aurichalcite reflections. Regardless, it is concluded at least for aurichalcite that structural changes to the hydroxycarbonate takes place during the thermal treatment. Similar to zincian georgeite, the rate of crystallinity began to increase significantly at temperatures above 350 °C once all residual hydroxycarbonate was lost (Figure 4.12.). At temperatures  $\geq 400$  °C, the XRD patterns become almost identical to those obtained from zincian georgeite. The Cu surface area findings also indicated similar values for both precursors at temperatures  $\geq 400$  °C. At 400 °C the HT-CO<sub>3</sub> content in zincian georgeite has been significantly depleted, with its capacity to act as a growth inhibitor severely inhibited. The TGA findings indicate that it fully decomposes around 420 °C. Clearly at these high temperatures the 'chemical memory' of both materials has been lost. This is because they each consist of large, segregated phases of CuO

and ZnO, meaning that they cannot be easily distinguished from one another. Interestingly though, even at 550 °C there are still very subtle differences between the XRD patterns, as illustrated by the relative intensities of the (-111) and (111) reflections for CuO at 35.5 and 38.7 ° respectively. Moreover, the BET findings indicated that differences were still apparent up to 450 °C even after complete removal of residual content. This implies that the materials are still being influenced by their origin despite loss of their chemical memory.

Crystallite sizes for CuO and ZnO were also measured from the XRD patterns for both precursors (Table 4.5.). For zincian georgeite accurate sizes could only be measured at temperatures  $\geq 375$  °C, where decomposition of HT-CO<sub>3</sub> was apparent. Similarly for zincian malachite, crystallite sizes could only be obtained once decomposition of the hydroxycarbonate took place. In agreement with the previous findings at temperatures  $\geq 400$  °C, the crystallite sizes for CuO and ZnO are similar for both materials. The data also illustrates the enhancement in crystallisation rate with temperature in particular between 450-550 °C. For instance, from the zincian georgeite precursor the CuO crystallite size increased by approximately 10-13 nm in this temperature range which was a much steeper increase than that observed at lower temperatures. Furthermore, it is also clear that the ZnO crystallite sizes were always larger than the CuO crystallites for all calcination conditions examined. However, as previously mentioned, crystallite sizes were determined using only one reflection for each phase and therefore this might deviate from true values.

**Table 4.5.** XRD crystallite sizes for CuO and ZnO phases after calcination of zincian georgeite and zincian malachite using conditions indicated. Crystallite sizes were calculated using the Scherrer equation.

Calcination conditions		Crystallite size (nm)			
Temperature (°C)	Time (h)	Zincian georgeite		Zincian malachite	
		CuO <sup>a</sup>	ZnO <sup>b</sup>	CuO <sup>a</sup>	ZnO <sup>b</sup>
350	2	-	-	5	-
	6	-	-	6.2	-
375	2	5.2	-	5.8	7.1
	6	6.4	-	6.5	7
400	2	7	8.3	7.5	8.5
	6	8.2	9.7	8	8.3
450	2	10.2	11.4	9.5	9.7
	6	11.8	13.9	10.4	12
550	2	20	22.2	20.6	30.6
	6	24.5	26.5	19.1	26.4

Each sample was 66.6% CuO and 33.3% ZnO ( $\pm 7\%$ ) as determined from the relative intensity ratios.

<sup>a</sup> Determined using the (111) CuO reflection.

<sup>b</sup> Determined using the (110) ZnO reflection.

XRD analysis was also carried out on the georgeite and malachite precursors after calcination at 300 °C for 2 hours for comparison (Figure S19.). Only narrow and intense CuO reflections were present. The crystallite sizes determined were 8 and 8.2 nm from georgeite and malachite, respectively. These findings are in agreement with the results and conclusions drawn from the binary precursors. Whilst the precursors have clear structural differences, it is seen that calcination to temperatures which remove all residual content resulted in segregated CuO materials of similar crystallite sizes. However, subtle differences were still apparent as shown for the relative intensities of the (-111) and (111) reflections.

Since the XRD findings only indicated an amorphous phase present for zincian georgeite calcined to temperatures  $\leq 300$  °C, attempts were made to obtain additional information on these materials by Raman analysis (Figure 4.13.). The analysis was carried out on the corresponding zincian malachite samples for comparison. Reference spectra for CuO and ZnO were also obtained and correlated with related literature findings to assist in peak assignments<sup>(30-31)</sup> (Figure S20.). The Raman spectrum for the zincian georgeite precursor has previously been discussed (Figure 3.2.), with the main band present at 1091  $\text{cm}^{-1}$  assigned to the carbonate  $\nu_1$  symmetric stretch. After calcination to 250-300 °C, the resulting spectra relate to the optimum carbonate-modified metal oxide. Whilst CuO bands are clearly present this was not apparent for ZnO despite being significantly more Raman active. This could be attributed to the sample having a high CuO/ZnO molar ratio of 2/1. Moreover, it could be a

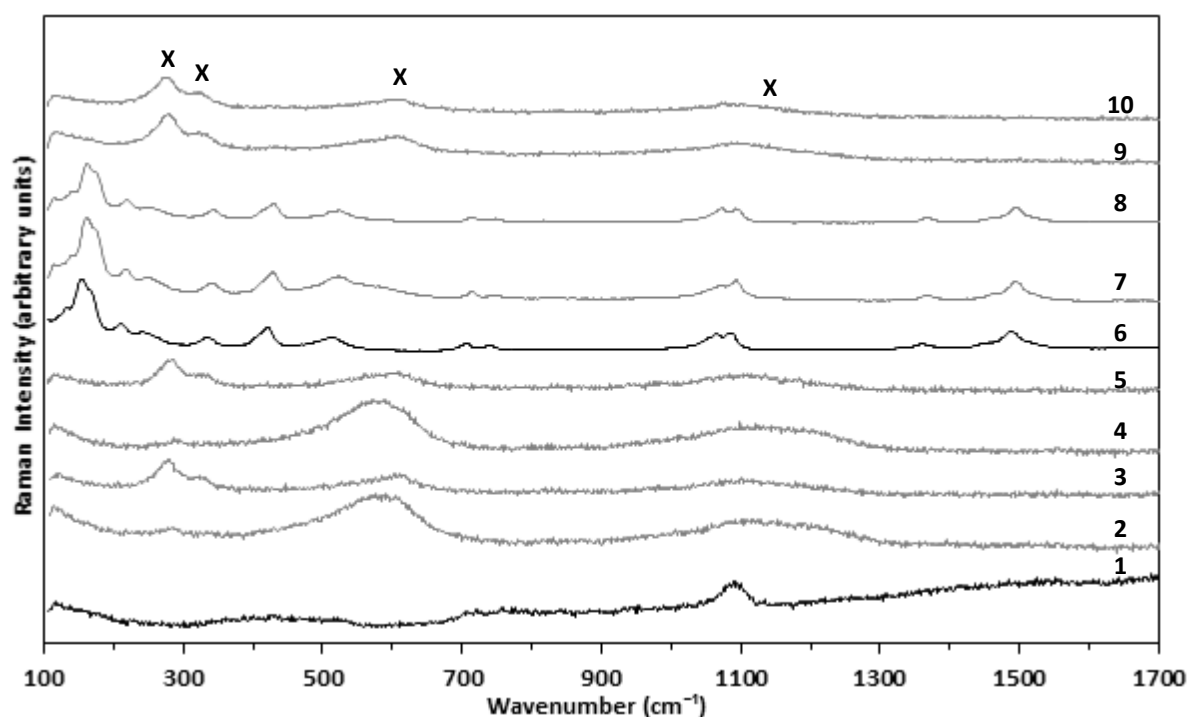


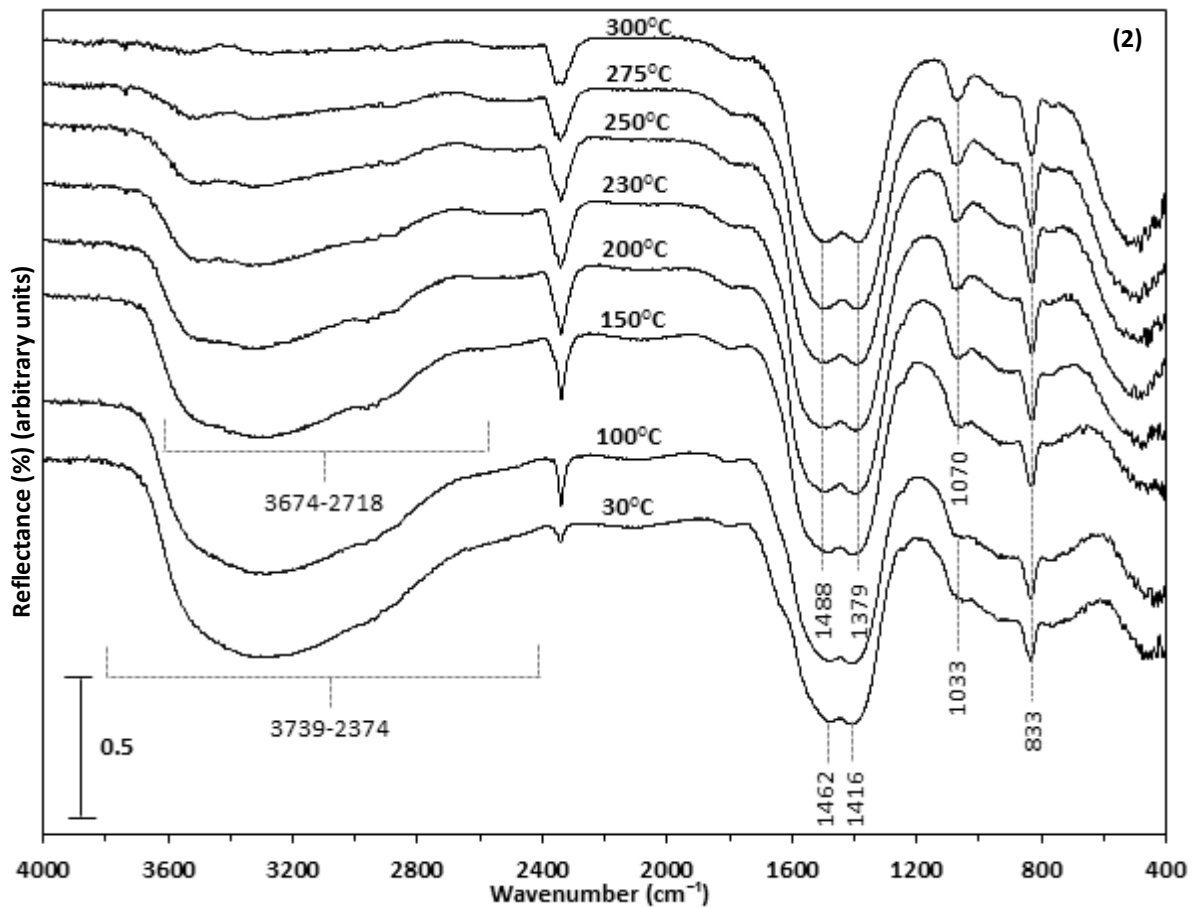
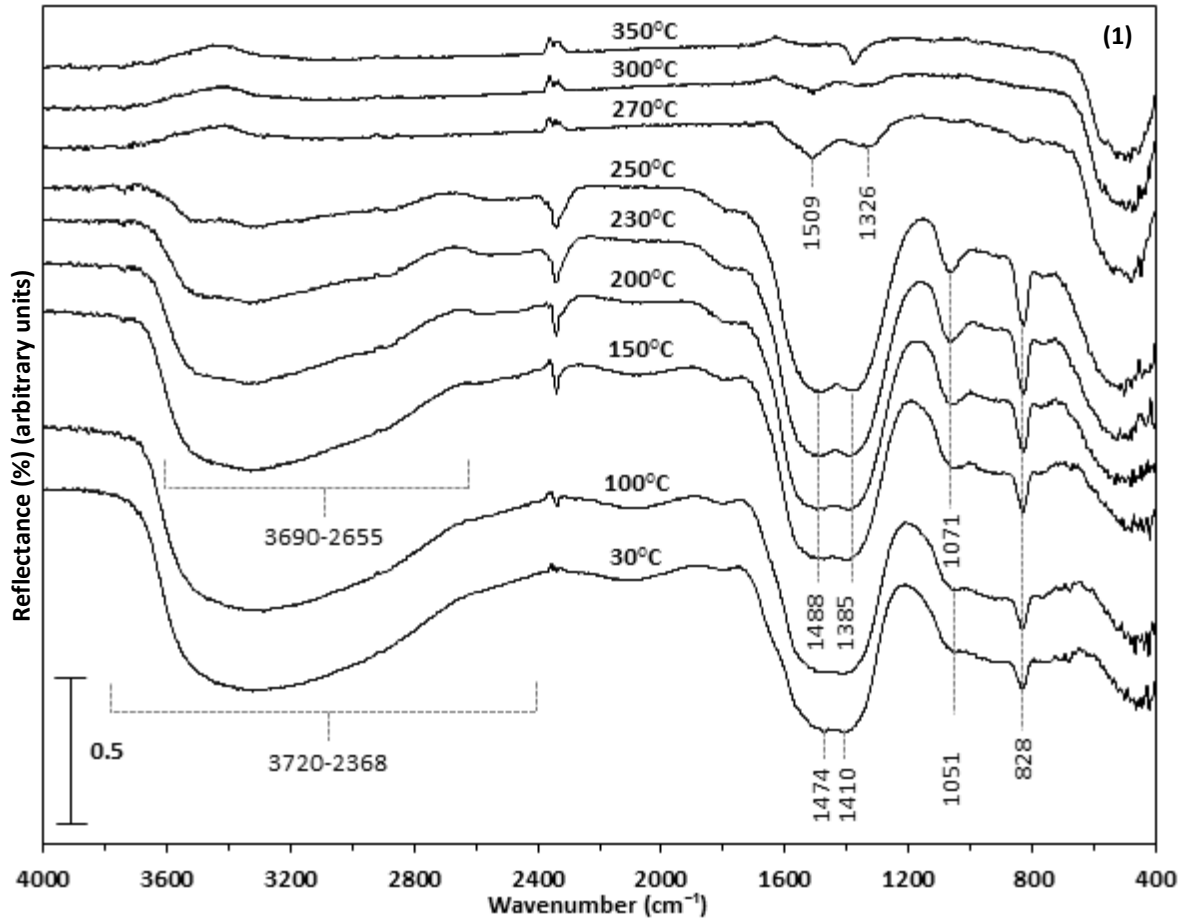
**Figure 4.13.** Raman analysis of: (1) Zincian georgeite precursor which was calcined at (2) 250 °C for 2 h (3) 250 °C for 6 h (4) 300 °C for 2 h and (5) 300 °C for 6 h. For comparison: (6) zincian malachite precursor which was calcined at (7) 250 °C for 2 h (8) 250 °C for 6 h (9) 300 °C for 2 h and (10) 300 °C for 6 h. X indicates bands associated with CuO.

result of the black CuO absorbing the scattered light from the white ZnO phase. After calcination, the carbonate band is no longer present, although it could be masked by the emerging broad peak centred at  $1115\text{ cm}^{-1}$ . Studies by Wang and co-workers have assigned this as the two-phonon scattering band ( $2B_g$ ), which is sensitive to the morphology and size of the nanostructures<sup>(30)</sup>. Interestingly, the relative intensities of all the CuO bands appears to be heavily influenced by calcination time, which could suggest that a morphological reconstruction process is occurring. This could be related to the subsequent formation of the carbonate-modified metal oxide. For zincian malachite, it is clear that bands associated with the hydroxycarbonate phase remain present up to  $250\text{ }^\circ\text{C}$ , which indicates no structural changes in agreement with previous findings. Bands associated with CuO, however, dominate the spectrum after calcination to temperature to  $300\text{ }^\circ\text{C}$  when the hydroxycarbonate begins to decompose. Samples calcined at higher temperatures illustrate similar spectra. Overall, the Raman findings conclude for both precursors that calcination under the optimum conditions results in the formation of CuO crystals  $< 5\text{ nm}$  in size, which are too small to be detected by XRD. This occurs during the initial hydroxycarbonate decomposition process, whereby the residual carbonate still remaining stabilises these highly active crystallites.

The structural changes to the zincian georgeite and zincian malachite precursors as a function of calcination temperature were further examined by PDF and XAS analysis. PDF analysis verified the TEM and Raman findings and showed that CuO species were present within the zincian georgeite sample calcined to  $300\text{ }^\circ\text{C}$  (**Figure S21.**). Interestingly, this was not apparent in the non-optimised material calcined at  $250\text{ }^\circ\text{C}$ . The  $300\text{ }^\circ\text{C}$  sample showed poorly resolved peaks in the PDF analysis that were only possible to identify when referenced to a much stronger and interpretable PDF of the  $450\text{ }^\circ\text{C}$  sample. This  $450\text{ }^\circ\text{C}$  sample was also strongly matched to a mixture of CuO and ZnO, with a 66:33 wt.% ratio (**Figure S22.**). Interestingly, Cu K edge EXAFS analysis of zincian georgeite after calcination to  $300\text{ }^\circ\text{C}$  revealed that the discernible characteristics were very similar to the original precursor (**Figure S23.**). This could suggest that the counter ion which influences Cu centre geometry in georgeite is the  $\text{HT-CO}_3$  species. Alternatively, it suggests a well dispersed CuO species, whereby previous XAFS studies have reported that supported CuO produced a Cu K edge XANES spectrum which best fitted a Jahn-Teller distorted octahedron<sup>(32)</sup>. In comparison, the zincian malachite sample calcined to  $300\text{ }^\circ\text{C}$  also illustrated CuO and ZnO phases present from Cu and Zn K edge XANES spectra in agreement with the TEM and Raman findings (**Figures S24.** and **S25.**). From a linear combination fit of XANES data 35 wt.% of the material was associated with CuO and ZnO, compared to the complete absence of these phases in the EXAFS data for the zincian georgeite material also calcined to  $300\text{ }^\circ\text{C}$  (**Table S8.**).

In order to investigate the induced structural changes of the carbonate anion with thermal treatment an *in-situ* DRIFTS study was carried out on all the georgeite and malachite precursors (Figure 4.14.). To complement these findings Raman analysis of the precursors was also carried out, but will not be discussed here further (Figure S26.). Infrared spectra of the precursors acquired at room temperature as well as during heated are provided. The temperature at which each spectrum was recorded is indicated on each line.

For the georgeite and zincian georgeite precursors, the FT-IR spectra have already been discussed (Chapter Three) with assignments made of all peaks present (Table S1.). Peak positions are slightly shifted in comparison to previous FT-IR findings, but considering the different instrumentation used the values are in very close agreement. Considering the spectra for georgeite first, a subtle change is apparent after heating to 100 °C (Figure 4.14(1)). The slight decrease in the intensity of the broad O-H band ranging between 3720-2366  $\text{cm}^{-1}$  can be seen along with complete disappearance of a weakly visible band at 1651  $\text{cm}^{-1}$ . This band at 1651  $\text{cm}^{-1}$  has been assigned as a bending mode of water by Melian-Cabrera and co-workers<sup>(33)</sup>. These observations are due to loss of physisorbed water from the hygroscopic KBr required for sample preparation. Furthermore, the EGA findings clearly show loss of water from the georgeite phase in this temperature range which is attributed to loss of occluded water present in the structure. The EGA findings also showed a simultaneous dehydroxylation and decarbonation step occurring between 150-250 °C. This invoked a change in all the carbonate bands present. Interestingly, the degree of splitting between the asymmetric  $\nu_3$  bands increases substantially from 64 to 103  $\text{cm}^{-1}$ . Similar *in-situ* DRIFT findings on related hydroxycarbonate precursors have been reported by Melian-Cabrera and co-workers who attributed these observations to a rearrangement of the carbonate<sup>(33)</sup>. Furthermore, the symmetric  $\nu_1$  band at 1051  $\text{cm}^{-1}$  increases in intensity and shifts to 1071  $\text{cm}^{-1}$ . It should be noted that this band is the dominant band present in the Raman spectrum and should not be infrared active. However, from symmetry reduction of the carbonate anion it can become activated. The increase in band intensity implies that the reduction in symmetry is increasing, whilst a shift to higher wavenumber is attributed to an increase in bond strength. The intensity of the band centred at 828  $\text{cm}^{-1}$  for the  $\nu_2$  bending mode also increases in intensity, although no shift in peak position was observed. Simultaneous to changes in carbonate, the intensity of the broad O-H band decreases until it is no longer present, indicating formation of the carbonate-modified metal oxide. Moreover, whilst assignments to bands at wavenumbers < 600  $\text{cm}^{-1}$  were not made due to complexity of the Cu-O framework it can be seen that this band also increases in intensity, which could be attributed to CuO formation. At temperatures between 250-350 °C, the EGA findings indicated decomposition of the remaining HT-CO<sub>3</sub> species. The IR spectra in this temperature range show that this decomposition is



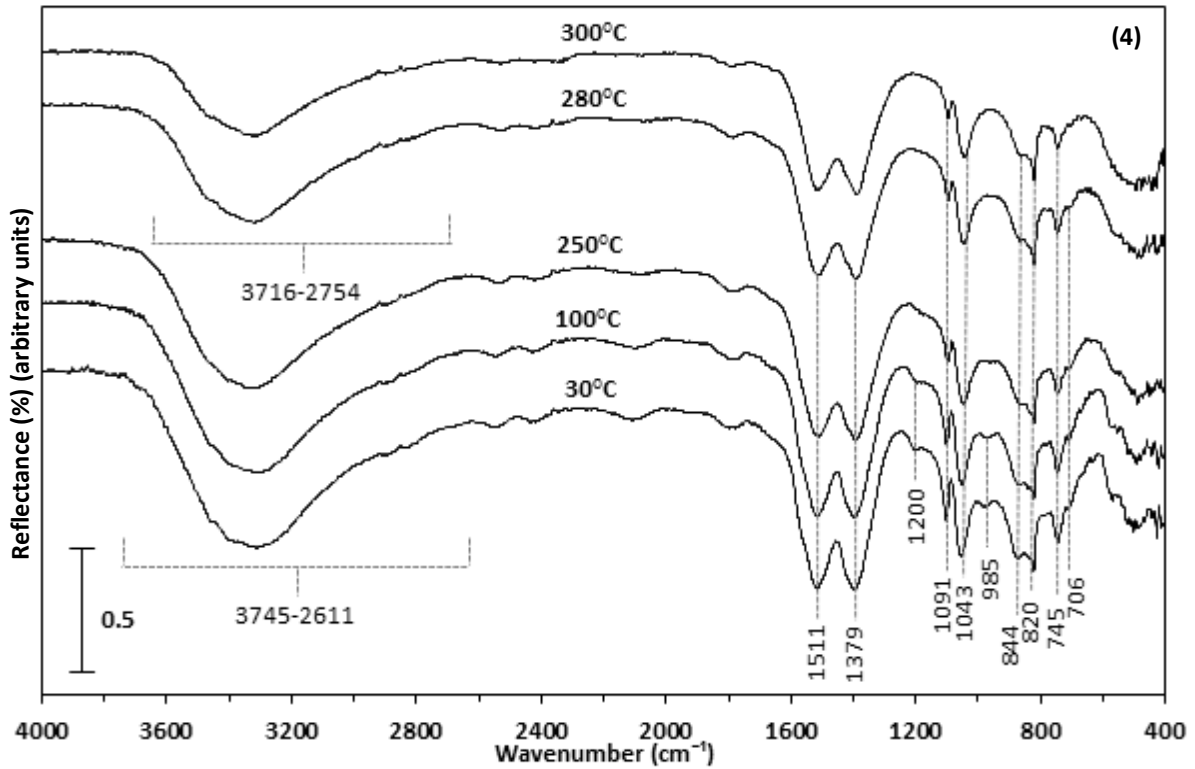
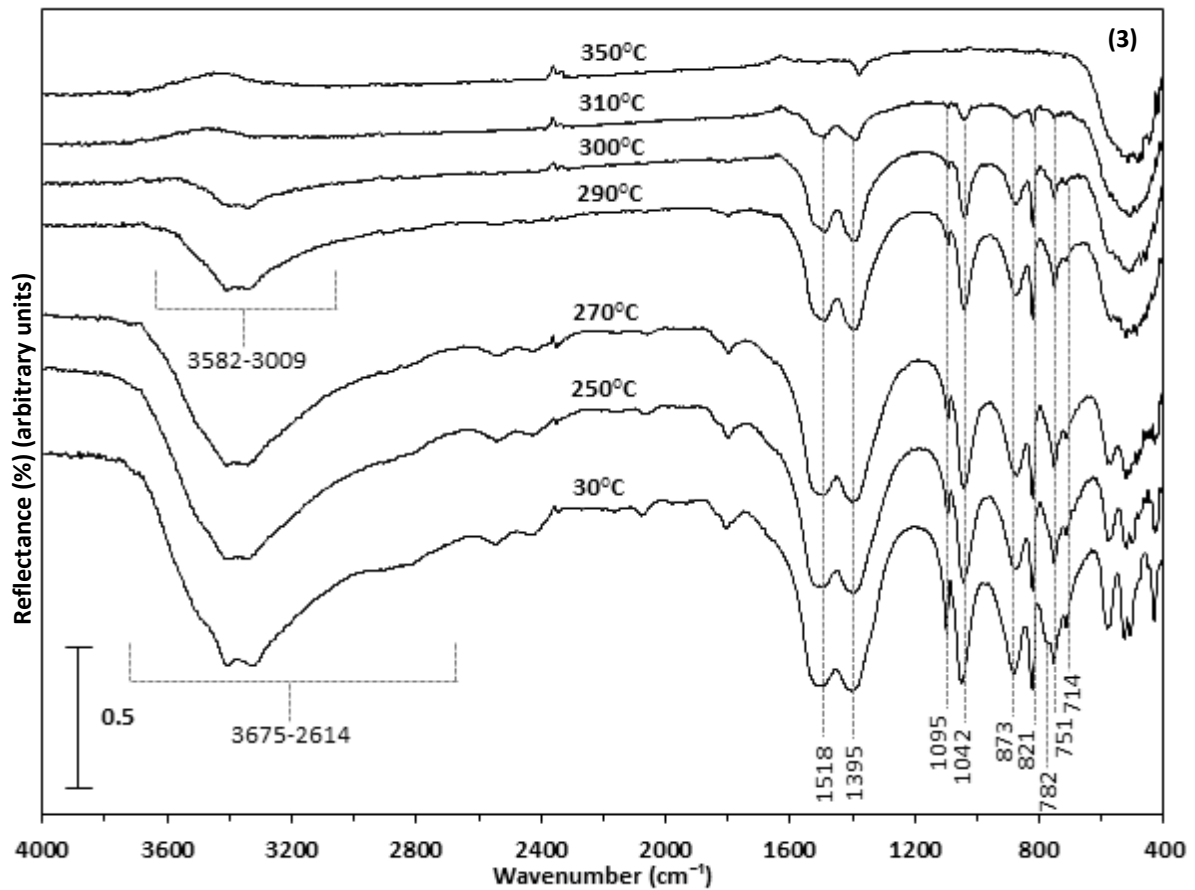


**Figure 4.14.** *In-situ* DRIFTS analysis for the thermal decomposition in air of: (1) Georgeite (2) zincian georgeite (3) malachite (4) zincian malachite. The temperature at which each spectrum was recorded is indicated on each trace. The analysis was carried out using an air flow of 50 ml/min and a ramp rate of 2 °C/min.

fast occurring predominantly between 250-270 °C. This carbonate becomes distorted during its decomposition, with the splitting of the doublet increasing further to 183 cm<sup>-1</sup>. This doublet is last to remain regarding the carbonate bands, with further growth of the Cu-O band observed at these higher temperatures.

The thermal decomposition of the zincian georgeite precursor by comparison is similar with the main change regarding the temperatures accompanying each decomposition step (**Figure 4.14(2)**). The carbonate bands remain unchanged after heating to 100 °C. However, the O-H bending band at 1651 cm<sup>-1</sup> disappears and the broad O-H band in the range 3739-2374 cm<sup>-1</sup> decreases in intensity. This is again attributed to loss of physisorbed and occluded water. The EGA findings indicates that simultaneous decarbonation and dehydroxylation occurs between 150-300 °C, resulting in formation of the optimum carbonate-modified metal oxide precursor. During this temperature range the broad O-H band is lost. The splitting of the  $\nu_3$  carbonate doublet increases from 46 cm<sup>-1</sup> to 109 cm<sup>-1</sup>. The peak position of the  $\nu_2$  mode remains at 833 cm<sup>-1</sup> but increases in intensity. Furthermore the  $\nu_1$  peak shifts from 1033 cm<sup>-1</sup> to 1070 cm<sup>-1</sup> and also increases in intensity. For both georgeite phases, the apparent changes in the carbonate bands with temperature up to formation of the carbonate-modified metal oxide could be attributed to a rearrangement in the co-ordination of the anion, as described by Melian-Cabrera and co-workers<sup>(33)</sup>. This is in agreement with the PDF and EXAFS findings, which indicate that after this heat treatment the local structure is similar to the precursor but subtle differences are still apparent (**Figure S21**. and **S23**). This activation of the HT-CO<sub>3</sub> rearrangement is facilitated by removal of residual low temperature species. This suggests that it is kinetically trapped in the precursor in a thermodynamically unfavourable arrangement. Experiments were also conducted, whereby zincian georgeite was heated to 120 °C and left overnight. The purpose was to examine if the ageing transformation to zincian malachite took place. The findings concluded that even after 24 hours at this temperature the resulting spectrum was characteristic of zincian georgeite. This strengthens the theory that ageing can only occur with the presence of water *via* solution and re-crystallisation rather than *via* a solid state transformation<sup>(13,34)</sup>.

The FT-IR spectra for the malachite and zincian malachite precursors is significantly more complex, with a large number of peaks present (**Figure 4.14(3)**. and **4.14(4)**). These precursors as well as the structurally related rosasite hydroxycarbonate have already been extensively studied by vibrational spectroscopy methods by several research groups<sup>(3,8-9,35-36)</sup>. Therefore, peak assignments herein were made according to this literature (**Table S1**). In brief, regarding both materials, multiple O-H bands are present in the range 2600-3600 cm<sup>-1</sup>. The  $\nu_3$  carbonate doublet is in the range 1379-1518 cm<sup>-1</sup>, but close inspection indicates that these peaks are actually split into 4 bands as a result of symmetry

reduction. The band near  $1090\text{ cm}^{-1}$  relates to the  $\nu_1$  symmetric stretch, whilst the peak at  $1042\text{-}1043\text{ cm}^{-1}$  is an  $\nu(\text{O-H})$  out of plane stretch. Bands in range  $820\text{-}873\text{ cm}^{-1}$  are associated with  $\nu_2$  modes whilst bands in the range  $706\text{-}782\text{ cm}^{-1}$  are associated with  $\nu_4$  modes. For malachite, Goldsmith and Ross assign the band at  $873\text{ cm}^{-1}$  to an  $\nu(\text{O-H})$  out of plane stretch<sup>(8)</sup>. Interestingly, for zincian malachite bands are also shown at  $985$  and  $1200\text{ cm}^{-1}$ . This is close to the values  $976$  and  $1208\text{ cm}^{-1}$  reported by Behrens and co-workers as fingerprint bands for the aurichalcite phase<sup>(3)</sup>. Moreover, they identified a fingerprint band for rosasite at  $666\text{ cm}^{-1}$ , which was not present in agreement with the XRD findings. In direct contrast to the georgeite materials, the infrared pattern of the malachite precursors did not significantly alter with temperature. There were no changes in peak positions and only subtle changes in the intensity ratios was apparent until their complete removal. For malachite, EGA indicates the decomposition step occurs in the range  $200\text{-}300\text{ }^\circ\text{C}$ . The only subtle changes that could be identified, other than the apparent formation of the broad Cu-O band at wavenumbers  $< 600\text{ cm}^{-1}$ , was the slight decrease of the  $\nu_3$  band at  $1518\text{ cm}^{-1}$  in relation to that at  $1395\text{ cm}^{-1}$ . The  $\nu_1$  band at  $1095\text{ cm}^{-1}$  also appears to decrease in intensity at a slightly faster rate than the other carbonate bands. Furthermore, the intensity of the band at  $873\text{ cm}^{-1}$  appears to decrease faster in relation to the  $\nu_2$  band at  $821\text{ cm}^{-1}$ . The same observations are also apparent in the zincian malachite spectra. The main difference in relation to the georgeite samples is the presence of the O-H band up until loss of the carbonate bands, which is in agreement with the TGA/EGA findings and verifies that decomposition of these precursors does result in formation of a carbonate-modified metal oxide. Moreover, the subtle changes in the infrared spectra with temperature correlates to the slight alterations in d-spacing values observed in the XRD findings. Overall, the significant changes observed in the infrared spectra for the georgeite phases in comparison to malachite phases was to be expected. Georgeite is a metastable phase which can be perceived as being kinetically trapped from transforming into the thermodynamically favourable malachite phase. The malachite phase by contrast has no activation barriers to overcome, it is in the most energetically favourable state, and therefore, decomposition does not induce any rearrangement of carbonate groups. *Ex-situ* FT-IR findings determined that loss of all carbonate bands occurred between  $400\text{-}450\text{ }^\circ\text{C}$  for zincian georgeite and between  $350\text{-}375\text{ }^\circ\text{C}$  for zincian malachite, as expected from the TGA/EGA findings (Figure S27.). A related *in-situ* DRIFTS study was also carried on the SAS prepared CuZn acetate phase. Interestingly, the decomposition was similar to the malachite phases, whereby there were no observable changes in peak positions of the acetate bands upon thermal treatment (Figure S28.).

#### 4.3.2. Conclusions from thermal decomposition studies on copper and copper-zinc hydroxycarbonate phases

This extensive study regarding the thermal decomposition of georgeite and malachite precursors has enabled optimisation of their calcination procedure, whilst shedding new light on the differences in thermal behaviour, structural evolution and in particular the role of residual carbonates. It has been illustrated that one of the key roles of zinc is to enhance or promote the thermal stability of these phases. The findings on the binary precursors has also enabled the following conclusions to be drawn:

1.) The optimum calcination temperature is in the range 300-325 °C whilst the influence of time is less significant but should be at least 2 hours. For both precursors this results in non-spherical, highly strained CuO crystallites < 5 nm in size resulting in Cu surface areas  $\geq 29 \text{ m}^2 \text{ g}^{-1}$  from zincian georgeite and  $\geq 22 \text{ m}^2 \text{ g}^{-1}$  from zincian malachite. The highly dispersed nanocrystallites are stabilised by retained residual carbonate. These materials retain the highly porous mesostructure of the precursors and are poorly crystalline. The formation of a carbonate-modified metal oxide from zincian georgeite, whereby HT-CO<sub>3</sub> is retained, gives this precursor an advantage over zincian malachite. The observed role of HT-CO<sub>3</sub> was not only to stabilise the metal oxide crystallites but to suppress the sintering mechanism and hence crystallisation. Its formation proceeds through rearrangement of the carbonate anion which, in addition to the initial formation of metal oxides, results in a subtle change to the local structure of the metal centres. For zincian malachite, the change in local structure after calcination is far more apparent, whereby CuO and ZnO phases (contributing up to 35 wt.%) were clearly observable. This is associated with the formation of larger metal oxide crystallites. Whilst the residual content also appears to suppress sintering, it decomposes at much lower temperature to that observed for HT-CO<sub>3</sub>. There are also subtle distortions in the hydroxycarbonate as it begins to decompose, however, this is not facilitated by a carbonate rearrangement.

2.) At elevated temperatures  $\geq 450 \text{ °C}$ , deactivation is apparent from metal sintering, whereby longer calcination times accelerate this process. All residual carbonate content is removed resulting in the formation of large, segregated CuO and ZnO phases. This means that the chemical memory for both precursors is lost, including the mesostructure with optimum porosity. Therefore, similar Cu surface area values  $\leq 5 \text{ m}^2 \text{ g}^{-1}$  are obtained with metal oxide crystallite sizes  $\geq 10 \text{ nm}$ . For zincian georgeite, as the HT-CO<sub>3</sub> begins to decompose it gets distorted which reduces its capacity to suppress sintering. Evidently, once it fully decomposes the rate of crystallisation accelerates.

Interestingly, though, despite removal of the chemical memory, subtle differences between the two precursors still remain, which indicates that they are still being influenced by their synthetic origin.

#### 4.4. Examining final state catalysts derived from zincian georgeite and zincian malachite from *in-situ* reduction studies

The third and final manufacturing step in the production of Cu/ZnO/Al<sub>2</sub>O<sub>3</sub> catalysts regards reduction of the CuO crystallites to the active metallic Cu species. This process is also often described as the catalyst activation step. The resulting labile Cu crystallites are potentially pyrophoric and will rapidly re-oxidise in the presence of air. For this reason, catalysts are loaded into the reactors in their oxide form with an *in-situ* reduction step carried out prior to testing. This makes analysis of the microstructural properties of the final state catalyst challenging, whereby various *in-situ* analytical techniques are required in order to probe the various physicochemical properties to a high level of legitimacy.

The zincian georgeite and zincian malachite precursors were calcined using the optimum conditions identified in the previous section (300 °C, 2 h, static air). Consequently, an *in-situ* XRD study regarding the reduction process of these calcined materials is presented. In particular, attention focused on the role of residual carbonates retained after the calcination process on the subsequent reduction step. This could then be correlated to structural differences observed between the final state catalysts. Analysis was also carried out on the industrial 51-2 methanol synthesis catalyst for further comparison. The reduction conditions chosen were similar to those used at Johnson Matthey for methanol synthesis: 2% H<sub>2</sub>/N<sub>2</sub> was passed over each calcined material at 60 ml/min, which were heated to 225 °C at 1 °C/min. XRD scans between 35-45 ° (2θ) were run every 5 °C at temperatures ≥ 125 °C. The resulting catalysts were held at 225 °C for 1 hour after reaching this temperature, before a final long scan was run between 30-100 ° (2θ).

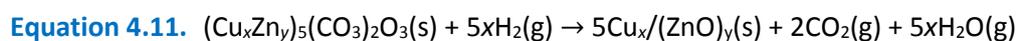
##### 4.4.1. Results and discussion

It is first important to consider the chemical process occurring in this reduction procedure. Several authors have simply expressed this step as reduction of CuO<sup>(37-38)</sup> (**Equation 4.10.**).



It can be seen that this reduction step is twice as exothermic as the LTS reaction at 25 °C (**Equation 1.7.**), which justifies implementing extremely mild conditions for this process. However, this

expression is too simplistic and does not consider the presence of residual carbonate. Therefore, the following expression has been proposed for reduction of the modified-carbonate metal oxide derived from zincian georgeite (**Equation 4.11.**).



$$\Delta m_{\text{theory}} = 28.974\%$$

Whereby in this particular case  $x = 0.67$  and  $y = 0.33$ . The exact expression depends on the amount of residual carbonate present, and so slight variations in total mass loss would be expected.

However, despite this the calculated mass loss is in excellent agreement with that observed for the calcined materials derived from SAS prepared 2/1 zincian georgeite (**Table 3.19.**). Interestingly, Nachtegaal and co-workers have reported from EXAFS studies that the reduction occurs *via* a  $\text{Cu}^+$  intermediate<sup>(39)</sup>. A similar reduction process would be expected for the calcined zincian malachite material also resulting in formation of a Cu/ZnO catalyst.

The evolution of Cu crystallite formation as a function of reduction temperature was investigated by *in-situ* XRD analysis for calcined zincian georgeite (**Figure 4.15.**) and zincian malachite (**Figure 4.16.**). Phase analysis was carried out using phase files obtained from the ICDD database (**Table 4.6.**). For the calcined zincian georgeite material, no change in the XRD pattern was observed up to 205 °C. The material is very poorly crystalline, with only two broad reflections associated with CuO observed in this  $2\theta$  range. The reduction transformation begins between 205-210 °C. Interestingly, the Cu (111) reflection begins to become defined with CuO reflections still present indicating that this process is gradual with at least two Cu oxidation states co-existing. There was also some indication that  $\text{Cu}^+$  was present but this is inconclusive. Unfortunately, the  $\text{Cu}^+$  (111) reflection overlaps with the ZnO (101) reflection. Therefore, the growth of the peak centred at 36.2-36.4 ° could be associated with either phase. However, as the reduction temperature increased further the intensity of this peak dropped which could be associated with the reduction of  $\text{Cu}^+$  to  $\text{Cu}^0$ . Moreover, the initial formation of the  $\text{Cu}^0$  (111) reflection at 210 °C appears to be slightly shifted in relation to its position at higher temperatures which could be attributed to the presence of the (200) reflection for  $\text{Cu}^+$ . Between 215-220 °C, the CuO (111) reflection is lost with growth of the  $\text{Cu}^0$  (111) reflection clearly evident.

In comparison for the calcined zincian malachite material, change is apparent at much lower temperature. The XRD pattern remained unchanged up to 180 °C. Assignment of CuO reflections was not possible as a result of overlap with the various reflections for residual hydroxycarbonate. Between 180-185 °C initial growth of the  $\text{Cu}^0$  (111) reflection is apparent. Interestingly, the

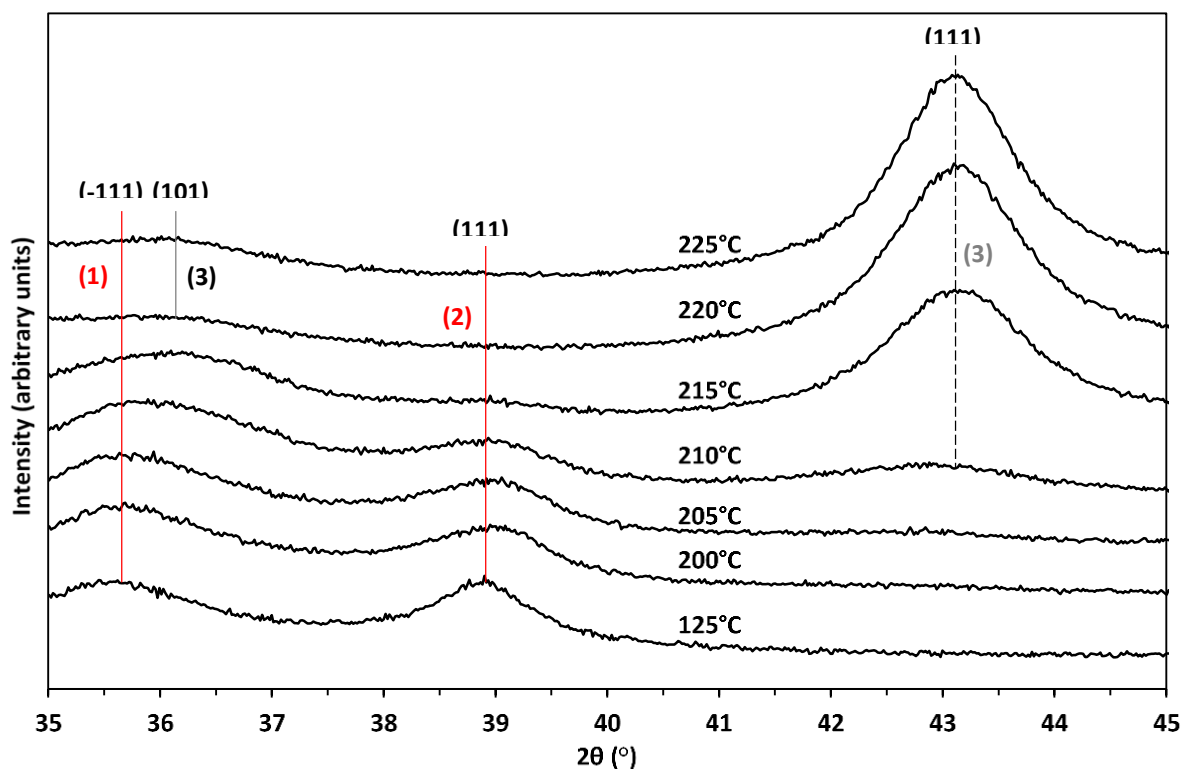


**Figure 4.15.** *In-situ* XRD analysis for the reduction of calcined zincian georgeite in 2%  $H_2/N_2$ . The temperature at which each pattern was recorded is indicated on each trace. The gas flow was 60 ml/min and the ramp rate was 1 °C/min. Scans were taken every 5 °C between 125–225 °C. Reflections assigned as CuO (1. red), Cu (2. hashed black) and ZnO (3. grey) phases.

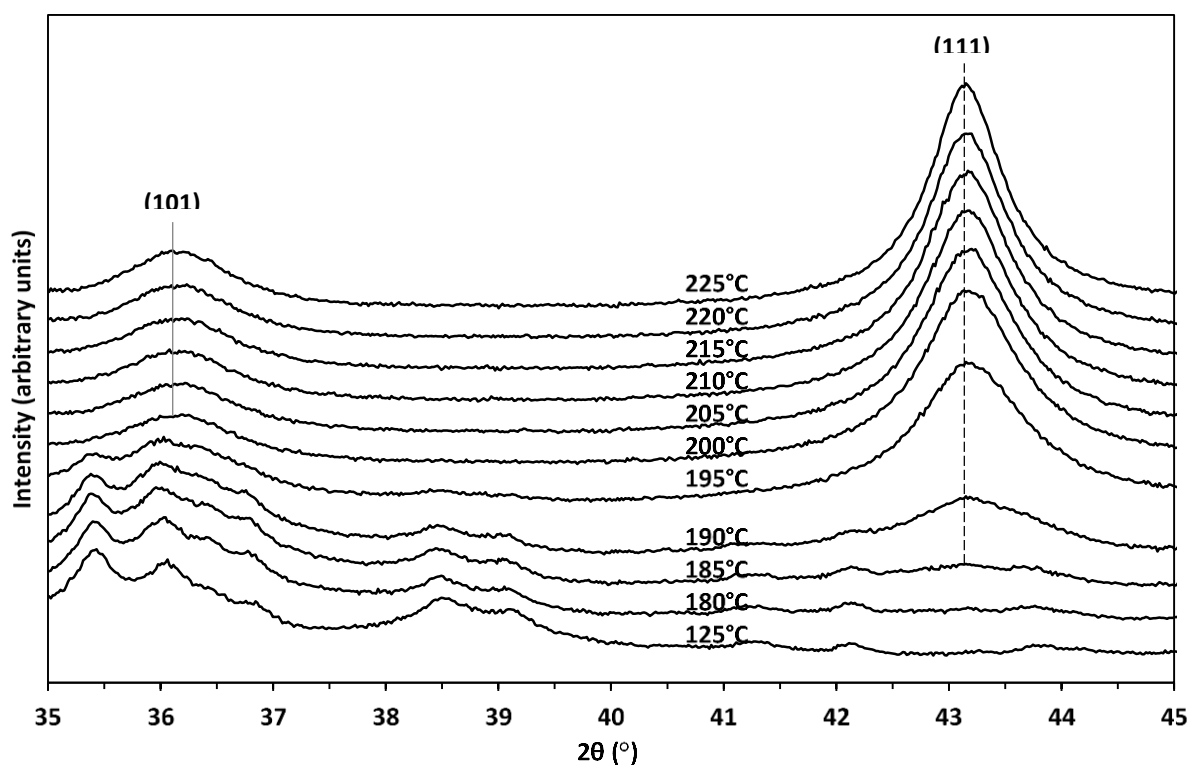


**Figure 4.16.** *In-situ* XRD analysis for the reduction of calcined zincian malachite in 2%  $H_2/N_2$ . The temperature at which each pattern was recorded is indicated on each trace. The gas flow was 60 ml/min and the ramp rate was 1 °C/min. Scans were taken every 5 °C between 125–225 °C. Reflections assigned as Cu (hashed black) and ZnO (grey) phases.

**Table 4.6.** XRD reflections of relevant phases used for assignments regarding *in-situ* reduction work.

Phase	h	k	l	2 $\theta$ (°)	Intensity (%)
CuO	0	0	2	35.4	36
	-1	1	1	35.6	92
	1	1	1	38.7	100
	2	0	0	38.9	61.6
Cu <sub>2</sub> O	1	1	1	36.4	100
	2	0	0	42.3	37
Cu	1	1	1	43.2	100
ZnO	1	0	1	36.2	100
Al <sub>2</sub> O <sub>3</sub>	1	0	4	35.1	100
	1	1	0	37.8	46
	1	1	3	43.3	96

hydroxycarbonate reflections appear present up until at least 195 °C, with metallic Cu clearly present. This could not be distinguished in the findings from the calcined zincian georgeite precursor as the HT-CO<sub>3</sub> appears amorphous. At 200 °C, the residual carbonate appears to have been fully removed with the rate that the Cu<sup>0</sup> (111) reflection increases with temperature also intensifying. There was no indication of an intermediate Cu<sup>+</sup> species during this reduction process. The reduction of the 51-2 methanol synthesis catalyst precursor was also similar to that observed for the calcined zincian malachite material (Figure S29.). The initial formation of Cu<sup>0</sup> appears between 180-185 °C. The most significant difference was that no crystalline hydroxycarbonate reflections were present. Moreover, no Al<sub>2</sub>O<sub>3</sub> reflections were identified which can be attributed to the low content present.

A long scan was run after the reduction process was complete on the resulting Cu/ZnO catalysts derived from zincian georgeite and zincian malachite (Figure 4.17.). Furthermore, the evolution of Cu<sup>0</sup> crystallite size was monitored for both samples during the entire reduction procedure. The XRD patterns show reflections for metallic Cu and ZnO phases as was expected. However, it is clear that the catalyst derived from zincian georgeite has broader reflections of lower intensity, and hence displays a lower degree of crystallinity. Furthermore, there are subtle differences relating to the intensity ratios of various reflections. For instance, the intensity ratio of Cu<sup>0</sup> (111) and (200) reflections ( $I(111) / I(200)$ ) is 1.81 for the zincian georgeite derived catalyst and 2.27 for the zincian malachite derived catalyst. Interestingly, Fujita and co-workers have correlated this particular intensity ratio to the activity of the catalyst for methanol synthesis<sup>(22,24)</sup>. They concluded that the surface structures of Cu crystallites was dictated by the reduction procedure and attributed the higher catalyst activity observed with higher  $I(111) / I(200)$  values to the preferential emergence of

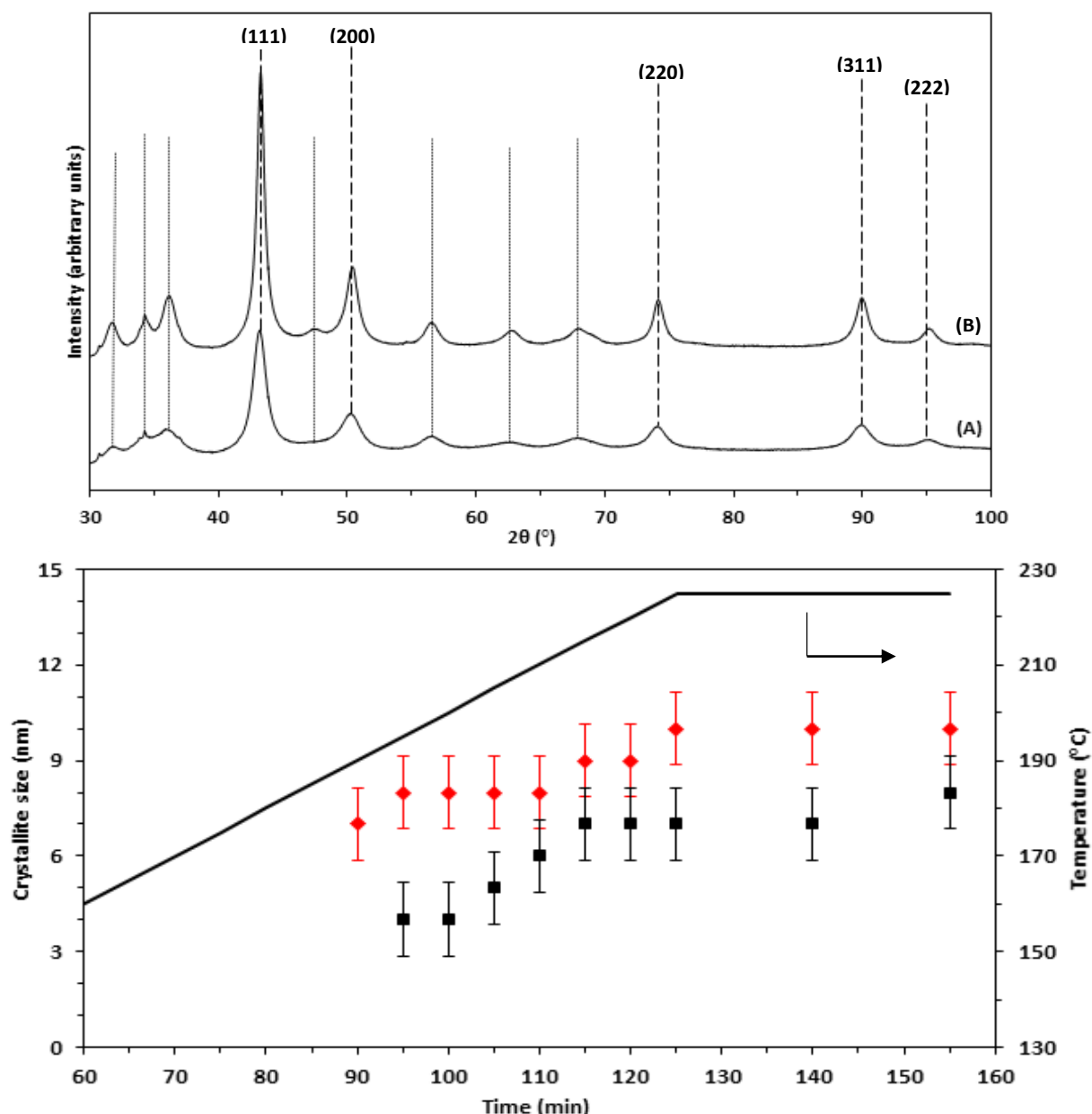


**Figure 4.17.** *In-situ* XRD analysis for the reduction of calcined zincian georgeite and zincian malachite in 2%  $\text{H}_2/\text{N}_2$ . The analysis was carried out using a gas flow of 60 ml/min and a ramp rate of 1  $^\circ\text{C}/\text{min}$ . Top: XRD patterns of Cu/ZnO catalysts derived from (A) zincian georgeite and (B) zincian malachite after being held at 225  $^\circ\text{C}$  for 1 hour. Black hashed and grey solid lines represent Cu and ZnO phases respectively. Bottom: Comparison of Cu crystallite sizes derived from zincian georgeite (black square) and zincian malachite (red diamond) during the reduction procedure. Crystallite sizes were calculated using the Scherrer equation and Cu (111) reflection. An arrow is also provided for clarity.

flat surface Cu sites. However, Behrens and co-workers have identified the active site for this reaction is Cu steps decorated with Zn atoms<sup>(29)</sup>. Moreover, this apparent trend does not correlate with findings on georgeite whereby Kondrat has shown that the zincian georgeite derived catalyst is more active<sup>(23)</sup> whilst presented here to have a lower  $I(111) / I(200)$  ratio.

The average  $\text{Cu}^0$  crystallite size determined once the reduction process was complete for the zincian georgeite and zincian malachite derived catalysts was 7.5 nm and 10.5 nm respectively. For

comparison the literature has reported Cu<sup>0</sup> crystallite sizes varying between 5-15 nm<sup>(29)</sup>. The smaller crystallite sizes determined for the zincian georgeite derived catalyst is in agreement with the broader reflections observed and the improved Cu surface area (**Figure 4.6.**). Crystal growth appears to directly correlate with temperature, and for both materials this seemed to broadly occur at the same rate. The smaller crystallites present in the zincian georgeite derived catalyst would have a higher surface energy and so was expected to show a faster rate of sintering. This could be attributed to the higher degree of mixing between the Cu and Zn phases from the SAS precipitation process. However, the retained HT-CO<sub>3</sub> is also correlated to the apparent stabilisation of smaller crystallites. In related studies, Baltes and co-workers have reported that residual carbonates facilitate the formation of highly active sites during reduction<sup>(26)</sup>. Moreover, the CO<sub>2</sub> released during the reduction was stated to modify the power of the gas phase and thus facilitate a gentler reduction process. Residual carbonate is clearly observed in the XRD pattern for the derived zincian malachite catalyst, whilst Cu<sup>0</sup> is present and continuing to form. The higher thermal stability of HT-CO<sub>3</sub> in the zincian georgeite derived catalyst may result in it being retained for a longer duration. Thus the role of HT-CO<sub>3</sub> is credited with stabilising CuO, Cu and even ZnO crystallites and inhibiting their growth during both the calcination and reduction thermal treatment steps.

#### 4.4.2. Conclusions from *in-situ* reduction studies on final state catalysts derived from zincian georgeite and zincian malachite

Differences in the reduction profiles of georgeite derived and malachite derived catalysts have been identified for the first time from *in-situ* XRD studies. A Cu/ZnO catalyst is produced in both cases, but these systems are not identical. This was clearly illustrated from highlighting subtle differences in the relative intensities of the various reflections. The georgeite derived catalyst also contained smaller Cu<sup>0</sup> crystallites, which justifies the observed higher Cu surface area and correlates to the Cu<sup>0</sup> (111) reflection appearing at higher temperature. It has also previously been shown that both precursors have a related mesostructure consisting of highly porous networks, and therefore, key differences relate to the nanostructure.

The fine atomic arrangement of Cu atoms which are the building blocks for each individual Cu<sup>0</sup> crystallite is governed by the size of these crystals. This attributes to the observed differences in intensities of the various reflections. Smaller crystallites, with a greater degree of mixing between Cu and ZnO, as observed for the zincian georgeite derived catalyst is coupled to higher microstrain<sup>(40)</sup>. The formation of stacking faults is required in order to relieve this strain, resulting in a higher density of labile surface atoms, with co-ordination numbers lower than the bulk value<sup>(29)</sup>. In other words, the structural arrangement at the surface is dictated by crystallite size and the level of mixing. The

crystallite size also determines its geometry, since the individual atoms are arranged in order to adopt the most energetically favourable structure with minimum surface energy. Consequently, as the size decreases the crystals become more distorted and hence less spherical. In comparison, the malachite derived catalysts have larger crystallites which are more spherical, have a lower degree of microstrain and thus a lower fraction of these active sites on the surface. This justifies the initial higher intrinsic activity of georgeite derived catalysts, in comparison to malachite derived catalysts, for methanol synthesis.

The ability of the zincian georgeite derived catalyst to retain smaller crystallites is partly attributed to the SAS precipitation procedure, which enables the processing of materials mixed to a higher capacity free from the contact of sodium reagents. Moreover, the use of an amorphous precursor is a contributing factor as a high order of crystallinity is associated with larger crystallite sizes. In other words, the precursor type plays a pivotal role in influencing the atomic arrangement of the resulting crystallites. However, the key role of residual carbonate in suppressing the sintering phenomenon cannot be underestimated. The findings suggest that the formation, growth and development of the resulting crystals is governed and facilitated by the presence of HT-CO<sub>3</sub>. Whilst both precursors have residual carbonate present after calcination, they are not the same species. It was previously shown that the HT-CO<sub>3</sub> species is thermally more stable and so it is suggested that it is more effective at inhibiting crystallite growth. Therefore, in conclusion, it is proposed that optimum Cu<sup>0</sup> crystallites are manufactured from the high dispersion of poorly structured Cu and Zn phases, from the presence of HT-CO<sub>3</sub> and minimum levels of sodium present, and it is this practicality which makes catalysts derived from georgeite unique to those prepared from conventional malachite precursors.

## 4.5. References

- 1 B. Bems, M. Schur, A. Dassenoy, H. Junkes, D. Herein and R. Schlögl, *Chem. Eur. J.*, 2003, **9**, 2039-2052.
- 2 M. Behrens, *Journal of Catalysis*, 2009, **267**, 24-29.
- 3 M. Behrens, F. Girgsdies, A. Trunschke and R. Schlögl, *Eur. J. Inorg. Chem.*, 2009, **10**, 1347-1357.
- 4 S. Klokishner, M. Behrens, O. Reu, G. Tzolova-Muller, F. Girgsdies, A. Trunschke and R. Schlögl, *J. Phys. Chem. A*, 2011, **115**, 9954-9968.
- 5 M. Behrens and F. Girgsdies, *Z. Anorg. Allg. Chem.*, 2010, **636**, 919-927.

- 6 S. Kaluza, M. Behrens, N. Schiefenhover, B. Kniep, R. Fischer, R. Schlögl and M. Muhler, *ChemCatChem*, 2011, **3**, 189-199.
- 7 G. J. Millar, I. H. Holm, P. J. R. Uwins and J. Drennan, *J. Chem. Soc., Faraday Trans.*, 1998, **94**, 593-600.
- 8 J. A. Goldsmith and S. D. Ross, *Spectrochimica Acta*, 1968, **24**, 2131-2137.
- 9 R. L. Frost, W. N. Martens, L. Rintoul, E. Mahmutagic and J. T. Kloprogge, *J. Raman Spectrosc.*, 2002, **33**, 252-259.
- 10 P. J. Bridge, J. Just and M. H. Hey, *Mineralogical Magazine*, 1979, **43**, 97-98.
- 11 A. M. Pollard, R. G. Thomas and P. A. Williams, *Mineralogical Magazine*, 1991, **55**, 163-166.
- 12 A. F. Rogers, *The Journal of Geology*, 1917, **25**, 515-541.
- 13 A. M. Pollard, M. S. Spencer, R. G. Thomas, P. A. Williams, J. Holt and J. R. Jennings, *Applied Catalysis A: General*, 1992, **85**, 1-11.
- 14 J. Rothe, J. Hormes, H. Bonnemann, W. Brijoux and K. Siepen, *J. Am. Chem. Soc.*, 1998, **120**, 6019-6023.
- 15 B. J. Reddy, R. L. Frost and A. Locke, *Transition Met Chem*, 2008, **33**, 331-339.
- 16 F. M. Michel, S. M. Antao, P. J. Chupas, P. L. Lee, J. B. Parise and M. A. A. Schoonen, *Chem. Mater.*, 2005, **17**, 6246-6255.
- 17 M. M. Harding, B. M. Kariuki, R. Cernik, G. Cressey, *Acta Crystallographica Section B - Structural Science*, 1994, **50**, 673-676.
- 18 E. L. Belokoneva, Y. K. Gubina and J. B. Forsyth, *Phys. Chem. Miner.*, 2001, **28**, 498-507.
- 19 N. Perchiazzi, S. Merlino, *Eur. J. Mineral*, 2006, **18**, 787-792.
- 20 F. Kooli, K. Kosuge and A. Tsunashima, *Journal of Materials Science*, 1995, **30**, 4591-4597.
- 21 A. Tarasov, J. Schumann, F. Girgsdies, N. Thomas and M. Behrens, *Thermochimica Acta*, 2014, **591**, 1-9.
- 22 S. Fujita, S. Moribe, Y. Kanamori, M. Kakudate and N. Takezawa, *Applied Catalysis A: General*, 2001, **207**, 121-128.

- 23 S. A. Kondrat, PhD Thesis, Cardiff University, 2011.
- 24 S. Fujita, S. Moribe, Y. Kanamori, M. Kakudate and N. Takezawa, *React. Kinet. Catal. Lett.*, 2000, **70**, 11-16.
- 25 S. A. Kondrat, T. E. Davies, Z. Zu, P. Boldrin, J. K. Bartley, A. F. Carley, S. H. Taylor, M. J. Rosseinsky and G. J. Hutchings, *Journal of Catalysis*, 2011, **281**, 279-289.
- 26 C. Baltés, S. Vukojevic and F. Schuth, *Journal of Catalysis*, 2008, **258**, 334-344.
- 27 X. Zhang, L. Zhong, Q. Guo, H. Fan, H. Zheng and K. Xie, *Fuel*, 2010, **89**, 1348-1352.
- 28 M. Schur, B. Bems, A. Dassenoy, I. Kassatkine, J. Urban, H. Wilmes, O. Hinrichsen, M. Muhler and R. Schlögl, *Angew. Chem. Int. Ed.*, 2003, **42**, 3815-3817.
- 29 M. Behrens, F. Studt, I. Kasatkin, S. Kuhl, M. Havecker, F. Abild-Pedersen, S. Zander, F. Girgsdies, P. Kurr, B. Kniep, M. Tovar, R. W. Fischer, J. K. Nørskov and R. Schlögl, *Science*, 2012, **336**, 893-897.
- 30 W. Wang, Q. Zhou, X. Fei, Y. He, P. Zhang, G. Zhang, L. Peng and W. Xie, *CrystEngComm*, 2010, **12**, 2232-2237.
- 31 R. Zhang, P. Yin, N. Wang and L. Guo, *Solid State Sciences*, 2009, **11**, 865-869.
- 32 S. Belin, C. L. Bracey, V. Briois, P. R. Ellis, G. J. Hutchings, T. I. Hyde, G. Sankar, *Catal. Sci. Technol.*, 2013, **3**, 2944-2957.
- 33 I. Melian-Cabrera, M. Lopez Granados and J. L. G. Fierro, *Phys. Chem. Chem. Phys.*, 2002, **4**, 3122-3127.
- 34 D. Waller, D. Stirling, F. S. Stone and M. S. Spencer, *Faraday Discuss. Chem. Soc.*, 1989, **87**, 107-120.
- 35 R. L. Frost, D. L. Wain, W. N. Martens, B. J. Reddy, *Spectrochimica Acta Part A*, 2007, **66**, 1068-1074.
- 36 R. L. Frost, *Journal of Raman Spectroscopy*, 2006, **37**, 910-921.
- 37 C. Rhodes, G. J. Hutchings and A. M. Ward, *Catalysis Today*, 1995, **23**, 43-58.
- 38 M. V. Twigg, *Catalyst Handbook*, Second Edition, Manson Publishing, 1989.
- 39 E. Kleymentov, J. Sa, J. Abu-Dahrieh, D. Rooney, J. A. van Bokhoven, E. Troussard, J. Szlachetko, O. V. Safonova and M. Nachtegaal, *Catal. Sci. Technol.*, 2012, **2**, 373-378.

*Georgeite: A rare gem for catalysis*

40 E. N. Muhamad, R. Irmawati, Y. H. Taufiq-Yap, A. H. Abdullah, B. L. Kniep, F. Girgsdies and T. Ressler, *Catalysis Today*, 2008, **131**, 118-124.

## 5.0. Conclusions and future work

### 5.1. Conclusions

The highly established Cu/ZnO/Al<sub>2</sub>O<sub>3</sub> industrial catalyst has been in commercialisation since the early 1960's for methanol synthesis and the LTS reaction<sup>(1-3)</sup>. Throughout this timeframe countless studies have focused on optimising and fine-tuning the entire catalyst manufacturing procedure. Whilst these efforts have resulted in improved catalyst systems, there has not been any radical changes induced to the chemical procedure. Studies have primarily focused on the synthesis of crystalline hydroxycarbonates by co-precipitation, with great emphasis placed on the 'ageing' phenomenon<sup>(4-19)</sup>. A greater understanding of this co-precipitation methodology has now been derived, which has enabled the malachite phase to be identified as the optimum crystalline precursor, at least for methanol synthesis, for these catalysts. However, this field of work has become saturated with these materials now characterised to an unprecedented degree.

The work presented herein attempted to move away from these principles, whereby efforts were made to study the amorphous georgeite hydroxycarbonate and to examine its applicability as an alternative catalyst precursor. The intention was to utilise the knowledge reported in previous literature to assist in the rational design of optimum precipitation routes, which were also in accordance with the principles of green chemistry. This led to investigating the production of georgeite materials using the supercritical anti-solvent (SAS) technique, as well as from a modified co-precipitation route based on the traditional industrial procedure. From simply avoiding nitrate and alkali-metal starting reagents, the environmental burden associated with these synthetic procedures could be minimised whilst simultaneously allowing access to precursors devoid of catalytic poisons. In addition, attention focused on correlating the catalyst performances to the microstructural properties, which is frequently referred to as the 'structure-activity' relationship<sup>(4)</sup>. By directly comparing and examining georgeite and malachite precursors at each fundamental step in the catalyst development, a detailed knowledge could be deciphered regarding the influence of both hydroxycarbonates on the structural evolution of these unique systems. Thus attempts were made to rationalise the remarkable differences illustrated in their catalytic behaviours, which could be implemented in further catalyst development. It is highly anticipated that this work will ultimately change the way georgeite is perceived in relation to applications in heterogeneous catalysis. Moreover, the applicability to prepare large quantities of a high purity and stable form of georgeite, which was previously known to be unstable and rare in mineralogical form, will open up additional

applications from a materials perspective. In conclusion, studies on georgeite have discovered the following:

- The volumetric ratio of water to ethanol in the preparation of metal acetate solutions for SAS precipitation has significant implications on the physicochemical properties of the resulting precipitate. A range of water contents (0-30 vol.%) were investigated in the preparation of binary materials, with a nominal Cu/Zn molar ratio of 2/1. The resulting precipitate always consists of a phase mixture of zincian georgeite and a hydroxyacetate. As the water : ethanol ratio decreases, the georgeite: hydroxyacetate ratio in the resulting precipitate also decreases. Thus with low water contents (0-1%), the acetate is the predominant phase, whilst at high water contents ( $\geq 5\%$ ) the hydroxycarbonate is the predominant phase. Formation of the hydroxyacetate occurs *via* precipitation of the various metal, acetate and hydroxyl components, whilst in the case of georgeite formation an *in-situ* carbonic acid reaction occurs to generate carbonate anions, which subsequently replace the acetate ligands in an 'anionic ligand exchange' reaction. When no water is used, trace amounts will still always be present from the hydrated metal acetate salt reagents, to generate trace amounts of georgeite. Water contents  $\geq 5\%$  result in the formation of an additional acetate species in the starting metal solution, which gets incorporated into the resulting precipitate and therefore trace amounts of acetate will also always be present. All materials after SAS precipitation become amorphous, whilst retained acetate ligands appear to also undergo a change in their co-ordination mode.

Since water is poorly miscible in  $\text{scCO}_2$ , the absence of water favours the SAS precipitation process. This allows optimum nucleation and growth of particulates to coincide within a single homogeneous phase system. Complete miscibility between  $\text{scCO}_2$  and the metal solution means that the surface tension between them disappears at a time scale smaller than jet break-up of the metal solution, resulting in a gas-like mixing and hence gas-to-particle precipitation<sup>(20)</sup>. The metal solution expands to maximum capacity upon contact and mixing with  $\text{scCO}_2$ , resulting in the maximum mole fraction of  $\text{scCO}_2$  is the subsequent phase mixture. This results in maximum supersaturation levels being attained with the anti-solvent property being fully exploited. As a result, precursors with optimum BET surface areas in the range  $152\text{-}162\text{ m}^2\text{ g}^{-1}$  can be obtained with low water contents (0.5-1%). It is expected that even at these low water contents there is a subtle surface tension present upon mixing, whereby water must be completely removed to achieve complete miscibility. However, trace amounts of water are at least essential to achieve 100% yields since aqueous  $\text{Cu}^{2+}$  is highly soluble in the  $\text{scCO}_2/\text{EtOH}$  phase. This results in the desired Cu/Zn molar ratio not being achieved. With increasing water content, the SAS homogeneous system gets disrupted and eventually results in the

formation of scCO<sub>2</sub> rich and water rich phase mixtures. As the water content increases, these co-existing mixtures become less miscible as the surface tension increases. As a result the ability of scCO<sub>2</sub> to diffuse into the water rich solution and mix is suppressed, resulting in reduced expansion and a lower scCO<sub>2</sub> mole fraction in the resulting mixture. Therefore, the anti-solvent property is no longer fully exploited and lower supersaturation levels are attained resulting in non-optimum precipitation. This essentially means that the ability of scCO<sub>2</sub> to act as an anti-solvent is reduced, which results in incomplete metal precipitation when very high water contents (20-30%) are utilised. The aqueous zinc species is more soluble in the water rich phase, which explains why there is a lower yield of zinc in relation to copper as the strength of the anti-solvent is reduced. Consequently, precursors with lower BET surface areas in the range 87-104 m<sup>2</sup> g<sup>-1</sup> are produced using moderate water contents (5-20%), which decreases down to 65 m<sup>2</sup> g<sup>-1</sup> as the water content is further increased to 30%.

Whilst precursors with optimum physicochemical properties are produced by excluding water from the SAS preparation, these hydroxyacetate materials have an undesired exothermic decomposition in the subsequent calcination step. This results in the high BET surface areas being lost after thermal treatment, which reduce down to 19-27 m<sup>2</sup> g<sup>-1</sup>. An 'auto-reduction' phenomenon also coincides with the decomposition resulting in a phase mixture of Cu<sub>2</sub>O/CuO with ZnO. The materials are highly crystalline with Cu<sub>2</sub>O crystallite sizes between 19-27 nm. Evidently, the final state catalysts have poor Cu surface areas ≤ 6 m<sup>2</sup> g<sup>-1</sup>, which concludes that these acetate type phases are poor catalyst precursors. In comparison, decomposition of the zincian georgeite phase is largely thermo-neutral, and therefore, the desired microstructural properties are largely retained after calcination. Therefore, materials made with water contents 5-20% remain amorphous after calcination indicating that the CuO and ZnO crystallite sizes are too small to be measured by XRD. These optimum materials have BET surface areas in the range 67-83 m<sup>2</sup> g<sup>-1</sup> after calcination to generate catalysts with Cu surface areas in the range 26-29 m<sup>2</sup> g<sup>-1</sup>. The reduction in the degree of mixing between Cu and Zn is clearly evident when water contents up to 30% are used. Interestingly, this resulted in a reduction to the decomposition temperature of HT-CO<sub>3</sub>, which subsequently resulted in a moderately crystalline material after calcination with a BET surface area of 48 m<sup>2</sup> g<sup>-1</sup> and a CuO crystallite size of 4.4 nm. Consequently, the Cu surface area of the final state catalyst was only 20 m<sup>2</sup> g<sup>-1</sup>. Overall, this work indicated that optimum water contents lie between 5-15% which reflects a compromise between a high georgeite/hydroxyacetate content and an optimum SAS homogeneous system.

- Varying the binary Cu/Zn molar ratio (4/1, 3/1, 2/1 and 1/1) was investigated in the SAS procedure to develop a better understanding of the system, and in particular, to identify any additional phases. The georgeite phase becomes zincian georgeite when zinc is included in the preparation but no additional phases were identified up to a Cu/Zn molar ratio of 1/1. This suggests that Zn is being completely incorporated into the georgeite phase, with no structural disruptions evident. In comparison, the zincian malachite phase can only incorporate up to 28 at.% Zn before aurichalcite formation begins<sup>(6-7,14)</sup>. This means that the georgeite precursor has a significant advantage, as it is not restricted by meso-structuring effects of resulting by-phases, allowing the nano-structuring effect to be fully exploited. This was investigated further by examining the precipitate prepared when no Cu is included. Since there was no evidence to show that this phase co-existed with the georgeite phase, it suggests that it is more favourable to incorporate all of the Zn into the hydroxycarbonate. This Zn phase could not be identified although it did contain traces of smithsonite, which increased in content, as the pressure of scCO<sub>2</sub> was increased from 110 to 150 bar. It is clear that this unknown phase forms at the expense of hydrozincite, which in addition to aurichalcite cannot be produced by the SAS precipitation route.

The Cu/Zn molar ratio was also varied, in order to further optimise the georgeite precursor. Whilst 100% yields from SAS were always obtained using water contents of 5 or 10%, a small amount of metal is lost from the starting metal acetate solution. This acetate precipitate is facilitated and enhanced with higher Zn contents. Since it has a metal composition of 62% Cu to 38% Zn, a solution prepared with a 1/1 ratio results in a SAS precipitate with a slightly lower Cu/Zn ratio. However, Zn is shown to enhance the thermal stability of georgeite through increased covalent metal-oxygen bonding<sup>(5)</sup>. With increasing Zn content, the decomposition temperature of HT-CO<sub>3</sub> increased illustrating further evidence that it was being fully incorporated into the phase. After calcination, all the materials remained amorphous, with the exception of the 4/1 material. This material had distinct CuO reflections, whereby the crystallite size determined was 5.6 nm. Interestingly, the 1/1 materials after calcination were green, in comparison to all the other materials which were black. This indicated a higher content of residual material retained after calcination, which is attributed to the higher thermal stability. It suggests that formation of the optimum carbonate-modified metal oxide did not follow through to completion. Varying the Cu/Zn molar ratio does not significantly affect the precipitation process, as was apparent with water content and BET surface areas of these precursors ranged between 85-102 m<sup>2</sup> g<sup>-1</sup>. Whilst the 4/1 and 3/1 materials had higher BET surface areas after calcination (60-76 m<sup>2</sup> g<sup>-1</sup>), in comparison to the 1/1 materials (47-53 m<sup>2</sup> g<sup>-1</sup>) this is not an indicator for catalyst screening, since both metal sintering and residual material can influence these values. In fact the catalysts prepared from the 4/1 and 3/1 precursors had significantly lower

normalised Cu surface areas of  $29 \text{ m}^2 \text{ g}_{\text{Cu}}^{-1}$ . This value increased up to  $53 \text{ m}^2 \text{ g}_{\text{Cu}}^{-1}$  from using a Cu/Zn molar ratio of 1/1, as it produced a higher level of Cu dispersion and dilution in the resulting catalyst, allowing it to be utilised to its full potential. However, the promotion in thermal stability of HT-CO<sub>3</sub> with Zn content is also a contributing factor in the preparation of optimum catalysts.

- Several Al reagents (Al boehmite sol, Al acetylacetonate and Al L-lactate) were investigated regarding the incorporation of Al into zincian georgeite by SAS precipitation. The incorporation of Al is essential in promoting the stability and lifetime of the resulting catalysts<sup>(1-3)</sup>. In particular, attempts were made to produce precursors with a nominal metal molar ratio of 6/3/1. For all three reagents the georgeite phase was retained with all the precursors amorphous, with the exception of the Al boehmite phase. This Al boehmite sol does not dissolve in the metal acetate solution, and therefore, does not disrupt the SAS system or undergo precipitation. As a result, 100% yields can be obtained using this reagent with the capacity to fine tune the Cu/Zn/Al molar ratio. The sol gets incorporated into the zincian georgeite precursor during its formation, and therefore, the two phases co-exist. This means that the Al is not incorporated into the georgeite phase. In contrast, the Al(acac)<sub>3</sub> reagent undergoes a complete phase transformation from SAS precipitation. It is suggested that the resulting Al is stabilised from being fully incorporated into the georgeite phase as there was no evidence of additional phases whilst Al<sub>2</sub>(CO<sub>3</sub>)<sub>3</sub> is an unstable compound. However, with the Al L-lactate reagent there was no strong indication that the Al was being fully incorporated into the georgeite phase. Interestingly, the lactate ligands were at least partly retained after SAS precipitation with a subsequent structural rearrangement. This indicated that the precursor consisted of at least two phases. The use of acac and L-lactate salts in the synthesis procedure resulted in a disruption to the SAS system. Unfortunately, the nominal Cu/Zn/Al ratio could not be obtained subsequently resulting in less than 100% yields. The acac salt appeared to inhibit complete precipitation of the Cu component despite efforts to prevent this phenomenon. Interestingly, use of the L-lactate salt appeared to result in a slight Zn deficiency indicating that these salts were disrupting the SAS precipitation by different chemical processes.

The precursors also illustrated differences in their thermal decomposition behaviour. The presence of the Al boehmite sol appeared to disrupt and induce structural changes to the zincian georgeite phase. With increasing content, the amount of HT-CO<sub>3</sub> decreased despite this process being thermo-neutral. This correlated with the presence of defined CuO reflections which had a crystallite size of 4.5 nm for an Al atomic content of 67%. The sol was found to decompose at 470 °C, and therefore, precursors prepared using this reagent are expected to have this phase in the resulting catalyst and not Al<sub>2</sub>O<sub>3</sub>. However, the precursor prepared using Al(acac)<sub>3</sub> remained amorphous after calcination.

This was encouraging as it indicated the formation of optimum CuO crystallites. Furthermore, additional evidence suggesting the incorporation of Al into the georgeite phase was obtained. The decomposition temperature of HT-CO<sub>3</sub> appeared to shift to significantly higher temperature, which illustrates that it is a more powerful promoter than Zn regarding thermal stability. For the boehmite and acac precursors, the addition of Al appeared to increase the surface area in contrast to studies on Zn content. BET surface areas up to 158 m<sup>2</sup> g<sup>-1</sup> were obtained, in comparison to 97 m<sup>2</sup> g<sup>-1</sup> achieved for the 2/1 binary standard. However, this enhancement was not as significant from using the Al boehmite sol, whereby it was also shown that the level of dispersion and mixing of the Al component was not as high as for Cu and Zn. Surprisingly, after calcination the BET surface areas were similar (81-90 m<sup>2</sup> g<sup>-1</sup>) for these materials, which was also similar to the 2/1 binary standard (85 m<sup>2</sup> g<sup>-1</sup>). This broadly correlated with the Cu surface area trend in the resulting catalysts: 23 m<sup>2</sup> g<sup>-1</sup> from using the sol and 27 m<sup>2</sup> g<sup>-1</sup> from the acac, in comparison to 29 m<sup>2</sup> g<sup>-1</sup> for the 2/1 binary standard. It is anticipated that the catalyst prepared from Al(acac)<sub>3</sub> can be optimised further, as the material was green after calcination, suggesting that complete formation of the resulting optimum carbonate-modified metal oxide did not occur. Moreover, this catalyst is of high priority to examine in future testing. The indication of complete incorporation of Al into the georgeite phase with a high degree of intimate, homogeneous mixing between the three metals is likely to result in a significant enhancement of structural and electronic promotional effects<sup>(7)</sup>.

The precursor prepared using Al L-lactate actually had a moderately high BET surface area of 114 m<sup>2</sup> g<sup>-1</sup>, suggesting favourable nucleation and growth occurred during the SAS precipitation process. Unfortunately, the thermal decomposition of this material is highly exothermic and thus unfavourable. This is attributed to the retained lactate ligands, which dominate the decomposition behaviour. As a result, the HT-CO<sub>3</sub> species is lost after calcination, which was correlated to the formation of a crystalline material with a CuO size of 7.3 nm. The Cu surface area of the resulting catalyst was only 10 m<sup>2</sup> g<sup>-1</sup>, which concludes that Al L-lactate is a poor choice of an Al reagent in the construction of optimum catalysts.

- The preparation of zincian georgeite by co-precipitation was investigated using a range of precipitation reagents (Na<sub>2</sub>CO<sub>3</sub>, (NH<sub>4</sub>)<sub>2</sub>CO<sub>3</sub> and (NH<sub>4</sub>)HCO<sub>3</sub>) with emphasis placed on optimising various parameters of this route, and investigating the deactivation phenomenon of residual Na. The precursor can be readily prepared using all three precipitation reagents, illustrating the high versatility of the process. Acetate by-phases in each case were identified, which were still retained after a washing step. All precursors were prepared using a nominal Cu/Zn molar ratio of 2/1.

Optimum precursors are obtained using  $\text{Na}_2\text{CO}_3$  which were determined to have BET surface areas of  $52 \text{ m}^2 \text{ g}^{-1}$ . Furthermore, yields of 100% are achieved allowing the desired Cu/Zn molar ratio to be obtained. After calcination, sodium loadings range between  $5885\text{--}70325 \text{ mg}_{(\text{Na})}\text{kg}_{(\text{CuO/ZnO})}$ , depending on the incorporation of a washing step beforehand. Deactivation from residual Na occurs in the subsequent thermal treatment steps, which significantly alters the physicochemical properties of the material. When a washing step is incorporated the material remains amorphous and BET surface areas up to  $56 \text{ m}^2 \text{ g}^{-1}$ , with a total pore volume of  $0.7 \text{ cm}^3 \text{ g}^{-1}$ , are obtained after calcination. This results in catalysts with Cu surface areas up to  $21 \text{ m}^2 \text{ g}^{-1}$ . In contrast, without a washing step the material after calcination becomes highly crystalline with a CuO crystallite size of 10.1 nm. Consequently, the BET surface area and total pore volume is significantly lower, with values of  $16 \text{ m}^2 \text{ g}^{-1}$  and  $0.15 \text{ cm}^3 \text{ g}^{-1}$  respectively, resulting in catalysts with Cu surface areas of  $3 \text{ m}^2 \text{ g}^{-1}$ . The mechanism for the deactivation process and the Na species present after calcination is still unknown. Interestingly though, the decomposition process is not exothermic with the HT- $\text{CO}_3$  species retained even without washing. Residual sodium is retained through the entire catalyst manufacturing procedure, and therefore, will be present on the final catalyst. It is suggested that it can affect the desorption properties of  $\text{CO}_2$  by enhancing its binding energy to the catalyst surface.

In comparison, the use of ammonium carbonate reagents results in precursors with inferior physicochemical properties, whereby BET surface areas only as high as  $35 \text{ m}^2 \text{ g}^{-1}$  are obtained. Furthermore, 100% yields are not achieved, whereby complete Cu precipitation is inhibited from the simultaneous formation of a copper-ammine complex. It is plausible that this complex is responsible for generating inferior precursors. However, from avoiding alkali-metal reagents sodium loadings in the range  $147\text{--}340 \text{ mg}_{(\text{Na})}\text{kg}_{(\text{CuO/ZnO})}$  are obtained after calcination, depending on the washing treatment beforehand. A washing step is still required to remove the by-phase prior to calcination in order to produce optimum catalysts. It is suggested the by-phase is ammonium acetate, which transforms into acetamide upon heating before completely decomposing. Therefore, after calcination the by-phase is completely removed in contrast to residual Na species. Deactivation associated with the by-phase during the thermal treatment step is again apparent, which is associated with the highly exothermic decomposition. Consequently, low ramp rates as well as washing minimise this unfavourable process. With a washing step included, calcined materials remain amorphous, with BET surface areas and total pore volumes in the range  $30 \text{ m}^2 \text{ g}^{-1}$  and  $0.3 \text{ cm}^3 \text{ g}^{-1}$ , respectively. This is correlated with the retention of HT- $\text{CO}_3$ , which interestingly decomposes at lower temperature, in comparison to precursors prepared using  $\text{Na}_2\text{CO}_3$ . However, Cu surface areas up to  $18 \text{ m}^2 \text{ g}^{-1}$  are still obtained. The lower sodium loading enables these catalysts to compete with those prepared from  $\text{Na}_2\text{CO}_3$ , and since the latter will retain the residual sodium

they are anticipated to illustrate inferior catalytic performances. If washing is excluded, materials are crystalline after calcination, with CuO crystallite sizes ranging between 6.9-8.8 nm. This is associated with loss of HT-CO<sub>3</sub> from the exothermic decomposition. Interestingly, the determined surface areas and porosities values of 28 m<sup>2</sup> g<sup>-1</sup> and 0.3 cm<sup>3</sup> g<sup>-1</sup> are similar to when a washing step is utilised. However, both metal sintering and residual content influence these values, with loss of HT-CO<sub>3</sub> only associated without washing. This results in catalysts with reduced Cu surface areas up to 13 m<sup>2</sup> g<sup>-1</sup>. Therefore, whilst washing is important when using ammonium carbonate reagents it is not as essential as when Na<sub>2</sub>CO<sub>3</sub> is used.

The conventional Cu/ZnO catalyst prepared from the industrial malachite precursor has a Cu surface area of 18 m<sup>2</sup> g<sup>-1</sup> in comparison to these georgeite derived catalysts. Therefore, the significance of this work clearly illustrates that georgeite precursors can be used to prepare catalysts by co-precipitation, with similar microstructural properties and lower Na loadings which can thus rival the malachite hydroxycarbonate as an alternative catalyst precursor.

- Selected georgeite precursors prepared from both SAS and co-precipitation routes were scaled up for testing at Johnson Matthey for methanol synthesis and the LTS reaction. These catalysts were trialled and tested against established industrial standards, which have been in commercialisation since the early 1960's.

For methanol synthesis testing occurred at temperature intervals between 190-250 °C in order to investigate both catalyst activity and stability. It is clear that the severe deactivation rate of the georgeite derived catalysts is the fundamental principle in hindering their capacity to compete against the industrial standard. For the initial 10 hours of testing at 190 °C, all of the SAS prepared catalysts had superior activity (4.3-3 mol<sub>MeOH</sub> h<sup>-1</sup> kg<sup>-1</sup>), in comparison to the 51-2 standard (2.9 mol<sub>MeOH</sub> h<sup>-1</sup> kg<sup>-1</sup>). When the measured Cu surface area values were taken into consideration, these georgeite derived catalysts also have superior intrinsic catalyst activities (8.2-7.8 mol<sub>MeOH</sub> m<sup>2</sup> h<sup>-1</sup> kg<sub>Cu</sub><sup>-1</sup> x 10<sup>5</sup>) in comparison to the standard (7 mol<sub>MeOH</sub> m<sup>2</sup> h<sup>-1</sup> kg<sub>Cu</sub><sup>-1</sup> x 10<sup>5</sup>). This illustrates that the intrinsic activity normalised to Cu surface area provided by the 51-2 standard is inferior, either in terms of catalyst activity from having a lower density of active sites, and/or from having active sites with lower activity. However, the SAS prepared binary catalyst prepared with a 1/1 ratio had the lowest intrinsic catalyst activity (5.8 mol<sub>MeOH</sub> m<sup>2</sup> h<sup>-1</sup> kg<sub>Cu</sub><sup>-1</sup> x 10<sup>5</sup>) of all the catalysts investigated, which could correlate with the binding energies of intermediate species<sup>(21)</sup>. The georgeite derived catalyst prepared from co-precipitation by comparison, had a lower activity than the standard for the 10 hours (2.4 mol<sub>MeOH</sub> h<sup>-1</sup> kg<sup>-1</sup>) but did illustrate a higher intrinsic catalyst activity for the same time frame (7.8 mol<sub>MeOH</sub> m<sup>2</sup> h<sup>-1</sup> kg<sub>Cu</sub><sup>-1</sup> x 10<sup>5</sup>). Overall, this suggests that georgeite derived catalysts provide

superior initial intrinsic activities, in comparison to malachite derived catalysts. This could be attributed to the reduced order of crystallinity, enabling access to a higher density of surface sites of reduced co-ordination. Deactivation was apparent between 10-18 hours of testing. Interestingly, the deactivation rate was not the same for all the catalysts. Whilst higher Al and Zn contents appear to suppress this process, the georgeite derived catalyst prepared by co-precipitation displayed the lowest degree of deactivation. Therefore, it is proposed that catalysts with higher activity deactivate faster because they produce a higher density of Cu transport species, which facilitate agglomeration and sintering<sup>(22)</sup>. At temperatures  $\geq 205$  °C, after initial deactivation, a clear trend is apparent in terms of activity: 51-2 > SAS (6/3/1) > SAS (2/1) (10%)  $\approx$  SAS (2/1) (5%) > SAS (1/1) > CP (2/1). It is clear that incorporation of Al is essential in order to produce optimum catalysts. This is largely attributed to the promotion in catalyst stability and lifetime. At the end of the testing programme the 51-2 standard had deactivated by 16%, the SAS 6/3/1 catalyst had deactivated by 33%, whilst for all the other catalysts deactivation was  $\geq 37\%$ . Overall, the testing data illustrated that the catalytic performances did not correlate with the Cu surface area values and the reduced sodium loadings did not enhance the catalyst performances.

For the LTS reaction, all the georgeite derived catalysts were superior to the 83-0 standard, in terms of activity and stability. The SAS prepared catalysts had higher initial catalyst activities (95.9-96%) than the catalysts prepared by co-precipitation (93.4-94%), but the 83-0 catalyst illustrated the lowest activity (90.6%). However, the enhanced stability of the georgeite catalysts is the most significant finding. After 135 hours online the deactivation rate was lowest for the SAS prepared catalysts (0.9-2.3%), in comparison to those prepared by co-precipitation (3.6-4.4%), but this was still significantly lower than that observed for the 83-0 standard (11%). This is remarkable considering the 83-0 standard contained  $\sim 33\%$  Al<sub>2</sub>O<sub>3</sub>, whereby in comparison, only one of the georgeite catalysts contained Al. In fact, the incorporation of Al was found to be insignificant. These findings will ultimately alter the way this reaction is perceived in relation to these catalysts. It has been reported that higher Al contents are required in this reaction because of the severe conditions used<sup>(2-3)</sup>. The higher stability of the georgeite catalysts is attributed to the lower sodium levels, which makes the role of Al redundant. Interestingly, the reaction was carried out at 220 °C, which is 30 °C higher than the severe deactivation observed in methanol synthesis. Therefore, it is clear that the mechanism of deactivation is not the same for both reactions, and furthermore, it is not simply attributed to thermal deactivation from sintering. Mass and space velocity experiments also determined that all the georgeite derived catalysts were superior to the 83-0 standard, in terms of both mass and volume. Moreover, whilst the methanol selectivity of these catalysts was higher than the standard it

was still overall insignificant in relation to the CO conversion rate. This overall highlights the optimum all round performance of the georgeite derived catalysts for this reaction.

- The microstructural properties of (zincian) georgeite and malachite hydroxycarbonates were examined using a range of state of the art techniques (ICP CHN, helium pycnometry, XAS and PDF analysis). The molecular formulas determined for georgeite and zincian georgeite were  $\text{Cu}_7(\text{CO}_3)_4(\text{OH})_6 \cdot 4\text{H}_2\text{O}$  and  $(\text{Cu}_x\text{Zn}_y)_5(\text{CO}_3)_3(\text{OH})_4 \cdot 3\text{H}_2\text{O}$  respectively. This confirms the presence of occluded water in these amorphous materials, with  $(\text{CO}_3) : (\text{Cu} + \text{Zn})$  ratios of 0.57 and 0.6, respectively, in comparison to 0.5 determined for the malachite precursors. This higher water and carbonate content is attributed to the georgeite precursors having a lower density ( $3\text{-}3.1 \text{ g cm}^{-3}$ ), in comparison to the malachite precursors ( $3.9 \text{ g cm}^{-3}$ ). The malachite precursors are crystalline, with aurichalcite a by-phase present ( $\sim 15\text{-}25 \text{ wt.}\%$ ) in the zincian malachite precursor.

XAS, PDF and DRUVS were all used to investigate the local structures of these materials. Whilst the metal centres present in both phases are coordinated to 6 oxygen atoms with a distorted octahedral geometry, subtle differences are still apparent even down to this scale of ordering. The Jahn-Teller effect is responsible for the distorted octahedral environments of the  $\text{Cu}^{2+}$  centres, which gives rise to elongation of the two axial Cu-O bonds. Average Cu-O bond lengths of 1.94(1) and 1.98 Å were independently determined from the XAS and PDF techniques, respectively, for the georgeite phase. Unfortunately, as a result of scattering path phase phenomena, structural analysis at distances  $> 2 \text{ Å}$  from XAS was problematic for the georgeite phases. However, scattering effects for Cu-Cu neighbours at 3.12 and 3.31 Å was determined in the malachite phase. This was also in good agreement with the PDF findings, whereby a Cu-Cu bond length of 3.3 Å was determined. PDF analysis proved to be the most useful technique since the absence of phase phenomena enabled distances up to 20 Å to be investigated. Consequently, this allowed a Cu-Cu bond length of 3.14 Å to be identified in georgeite, which is shorter than the equivalent bond in malachite. Moreover, the malachite phase had a Cu-Cu peak at 15.27 Å, and therefore, with the complete absence of an equivalent peak in georgeite it was concluded that the local ordering operates well below the length scales associated with the malachite unit cell ( $362.7 \text{ Å}^3$ ). Attempts were also made to compare the georgeite PDF's to a wide range of related hydroxycarbonates, including calculated PDF simulations of malachite and aurichalcite nanoparticles 22 Å in size. The findings concluded that georgeite is a unique phase and is not a nano-scale form of malachite. However, with the level of structural ordering in georgeite so limited, as well as the potential additional complications regarding multiple  $\text{Cu}^{2+}$  species with independent Jahn-Teller effects, a structure for this phase could not be derived.

- The thermal decomposition of the (zincian) georgeite and malachite hydroxycarbonates was extensively studied, with the optimum calcination temperature determined in the range 300-325 °C for the binary precursors. This results in the formation of a poorly crystalline material, with retention of residual hydroxycarbonate species. More specifically for zincian georgeite, the retention of HT-CO<sub>3</sub> results in the formation of a carbonate-modified metal oxide. This is a kinetically stable intermediate species, whereby the remaining carbonate undergoes a rearrangement into a more energetically favourable state, after evolution of lower temperature material. The role of residual carbonate is to stabilise the CuO crystallites and to suppress and minimise their sintering. Since the HT-CO<sub>3</sub> decomposes at higher temperature (~420 °C), in comparison to residual carbonate retained in zincian malachite (~325 °C), it is plausible that it is more effective for this role. This would give the zincian georgeite precursor an advantage when carrying out the thermal treatment steps. For both materials calcination to 300 °C generates highly strained CuO crystallite sizes < 5 nm in highly porous mesostructures retained from the precursors. Consequently, Cu surface areas up to 29 and 22 m<sup>2</sup> g<sup>-1</sup> are obtained from zincian georgeite and zincian malachite, respectively. At elevated temperatures (≥ 450 °C) loss of all residual material results in the formation of large segregated CuO and ZnO phases with the complete destruction of the optimum porous mesostructures. Therefore, identifying structural differences between these two materials becomes difficult, with both having similar CuO crystallite sizes (≥ 10 nm) and hence Cu surface areas (≤ 5 m<sup>2</sup> g<sup>-1</sup>). However, the fact that structural differences remain indicates that they are still influenced by their synthetic origin.

- *In-situ* XRD was used to examine the reduction of zincian georgeite and zincian malachite after they had been calcined to 300 °C. For both materials, this resulted in the formation of the Cu/ZnO catalyst with Cu crystallite sizes of 7.5 and 10.5 nm respectively. Evidence for the presence of Cu<sup>+</sup> species was inconclusive. The loss of residual carbonate is a slow process, whereby evolution is facilitated gradually by the simultaneous growth of Cu crystallites. Complete removal is not evident until the reduction process has gone to completion. Therefore, the residual carbonate suppresses sintering in both the calcination and reduction step with the higher stability of HT-CO<sub>3</sub> enabling the zincian georgeite derived catalyst to retain smaller Cu crystallites. Subtle differences in the relative intensities of the reflections is correlated to variations in the structural make-up of these catalysts, and in particular, the structural arrangements at the surfaces. The zincian georgeite derived catalyst has broader reflections of lower intensity, indicating smaller crystallites and a reduced level of structural order. It can be concluded that the high dispersion of poorly structured Cu and Zn phases, the retention of HT-CO<sub>3</sub> with minimum levels of sodium present are key attributes of an optimum Cu/ZnO catalyst. This provides a fundamental distinction between catalysts prepared from both precursors.

## 5.2. Future work

The work presented herein regarding studies on Cu/ZnO/Al<sub>2</sub>O<sub>3</sub> catalysts has significantly opened up and facilitated the expansion of this saturated field of research. These remarkable findings will permanently alter the way the amorphous georgeite phase is perceived in the context of hydroxycarbonate synthesis, as well as how these catalysts operate during methanol synthesis and the LTS reaction. However, it is clear that future work is warranted in order to consolidate these findings and to improve these catalyst manufacturing processes further in terms of optimization and sustainability. Consequently, the following areas have been proposed and highlighted as future work in order to achieve these long-term aims:

**- Studies regarding catalyst innovation, design and implementation in order to develop a further understanding of the 'structure-activity' relationship for binary and ternary systems:** The work carried out to date has focused on identifying similarities and differences between zincian georgeite and zincian malachite, in terms of their microstructural properties during their evolution into final state catalysts. However, this only considered SAS prepared zincian georgeite and zincian malachite prepared by the conventional co-precipitation route. In order to derive a further understanding of the 'structure-activity' relationship for these hydroxycarbonates it is essential to carry out similar studies (PDF, XAS, ICP CHN, helium pynometry) on zincian georgeite prepared by co-precipitation and zincian malachite prepared by SAS precipitation. This would enable a fairer comparison of these precursors if they are prepared by the same synthesis routes. Moreover, it would enable a greater understanding of how these distinct methodologies manipulate the physicochemical properties of these precursors. Neutron scattering is also highlighted as an alternative state of the art technique which could shed further additional light on the microstructural properties of these materials, and could prove invaluable for investigating the amorphous georgeite phase.

Studies regarding the synthesis of zincian georgeite by co-precipitation should focus on incorporating Al into the structure in order to make this process viable. The resulting catalysts should be tested against the industrial standards. Studies regarding the binary system should investigate if any additional phases are formed from simply varying the Cu/Zn molar ratio as was carried out in the SAS set-up. This would enable a direct comparison against the SAS precursor, whereby no evidence was obtained to suggest that the content of Zn used was not fully incorporated into the georgeite phase. Studies should also focus on preparing precursors using nitrate salts as well

as acetate salts. This would allow the role of the nitrate anion to be examined, and in particular, how it influences the HT-CO<sub>3</sub> content.

Studies regarding the SAS preparation of zincian malachite would enable this precursor to be prepared with low sodium contents, and thus would be a high priority candidate for future testing. Furthermore, the synthesis of zincian malachite by co-precipitation using (NH<sub>4</sub>)<sub>2</sub>CO<sub>3</sub> would be useful as a direct comparison. This would allow the role of sodium to be fully investigated in both georgeite and malachite precursors. Initial studies on the SAS preparation of zincian malachite have already been carried out by Kondrat who reported that smithsonite is the by-phase, which forms at the expense of aurichalcite<sup>(23)</sup>. Therefore, optimization of the Cu/Zn molar ratio for this precursor as carried out for zincian georgeite would enable the role of the smithsonite by-phase to be examined from subsequent testing. The role of HT-CO<sub>3</sub> in the malachite precursor from both SAS and co-precipitation routes is a further area of study. If the precursor can be manufactured with and without HT-CO<sub>3</sub> it would be highly valuable to examine the structures and to correlate this with the catalyst performances. Moreover, it would be extremely valuable to incorporate Al into the zincian malachite precursor using the SAS technique. This can be achieved using the Al acetylacetonate and Al boehmite reagents. It would be interesting to identify the maximum amount of Al that can be incorporated into this precursor, since literature reports only 3.3 at.% can be incorporated from co-precipitation<sup>(7)</sup>.

It would also be extremely insightful to carry out additional *in-situ* reduction studies (DRIFTS, EXAFS, Raman and XPS) to examine final state catalysts in order to yield additional information on their properties. This would complement the *in-situ* XRD findings presented in this work. STEM imaging is currently being implemented in order to probe the fine atomic arrangement, size and morphology of the resulting Cu and ZnO crystallites in georgeite and malachite derived catalysts. *In-situ* EXAFS analysis, to investigate the 'ageing' phenomenon regarding the transformation of georgeite into malachite, is also a future study of interest.

- **Additional testing studies:** The testing carried out in this work has enabled improved catalyst systems to be identified, which will also require testing in order to verify these assumptions. In particular for methanol synthesis, the incorporation of Al was seen as being essential for optimizing the catalyst stability and lifetime, and therefore, future testing should only consider examining ternary catalysts. Testing the catalyst prepared from georgeite using the SAS route with the Al(acac)<sub>3</sub> reagent is high priority for the reasons previously mentioned (**Section 5.1.**). Furthermore, studies by Behrens have optimised the Al content in co-precipitated malachite precursors<sup>(7)</sup>. Therefore, similar studies must also be carried out regarding the georgeite precursor whereby at present it is not

known how much Al can be incorporated into the amorphous phase. This would require a whole series of precursors with various compositions to be tested. Ternary georgeite precursors prepared by co-precipitation must also be prepared and tested for direct comparison. Moreover, the Al reagent type can be further investigated, since Johnson Matthey supply a range of various Al sols, each with unique physicochemical properties.

In direct contrast for the LTS reaction, the incorporation of Al can be excluded, with the primary focus attributed to the role of residual alkali metal loadings on the catalyst activity and stability. Whilst a correlation has been made between the activity and the sodium loading a trend has not yet been determined. This would require a series of doping experiments from either SAS or co-precipitation routes, whereby precursors are prepared with various sodium loadings and tested. It would also be extremely useful to do a similar study regarding potassium loadings in order to understand the different roles of these alkali metals. This can be further examined from catalysts prepared from co-precipitation using  $\text{Rb}_2(\text{CO}_3)$ . It is also seen as high priority to test catalysts with lower sodium loadings than those tested in this work, which is possible since starting material reagents of higher purity grades can be obtained. Finally, it would be useful to investigate alternative reactions including methanol steam reforming and methanol decomposition for all of these catalysts outlined.

**- *In-situ* studies regarding methanol synthesis and the LTS reaction / post experimental analysis of pacified binary and ternary catalysts:** In order to shed new light on the understanding of these chemical processes and the role of the various catalytic components, *in-situ* studies carried out to investigate catalysts under these testing conditions is the pinnacle in achieving these ambitions. However, obtaining the reaction conditions for the LTS reaction will be highly challenging as the entire reaction/analytical chamber will need to be at temperatures  $> 100\text{ }^\circ\text{C}$  in order to prevent condensation of the steam. Achieving high pressures (20 bar) for these analytical studies will also be challenging, but is essential in order to derive the exact same conditions used for testing. Emphasis would be placed on identifying surface species, oxidation states and alloying effects using various *in-situ* techniques (XRD, DRIFTS, Raman, XPS and EXAFS). It would also be possible to monitor the catalyst activity simultaneously in selected studies from using gas chromatography.

An easier alternative to *in-situ* studies is simply to analyse pacified catalysts after testing. Whilst this will not yield the same valuable information it would still produce important findings. In particular, BET and DTF Monte-Carlo analysis could be used to examine physical alterations of the mesostructures induced from testing. TGA would be suitable to investigate potential carbon deposits, which would shed new light on the catalyst deactivation mechanism, and in particular for

methanol synthesis. DRIFTS and STEM analysis could alternatively be used to investigate these surface structures in more detail. Furthermore, identifying any alteration to the Cu oxidation state from XRD and XPS studies would also shed new light on the reaction mechanisms.

**- Studies regarding additional optimisation of the SAS precipitation route:** A significant amount of work has now been carried out regarding the optimisation of the SAS synthesis route for georgeite precursors, with a better overall understanding of the system obtained. However, this methodology must be fully optimised in order to enable the best possible judgement to be made regarding the validity and practicality of this process, as an alternative to the fully optimised co-precipitation route. It must also be noted that if this route is used for the processing of malachite precursors the optimum SAS conditions might not necessarily be the same as those determined for georgeite precursors.

Synthesis parameters of this route which still require optimisation include the  $\text{scCO}_2$ /solvent (metal solution) molar ratio and the nozzle design, in terms of inner and outer nozzle diameter sizes and geometry. Throughout this entire study a ratio of 22/1 was used using a 1 mm diameter inner nozzle size. Therefore, improved catalysts could be produced from investigating changes induced to these variables. Finally, it would be very interesting to fully exploit the SAS process by investigating alternative novel catalyst systems based on  $\text{Cu/ZnO/Al}_2\text{O}_3$ . A series of elements such as Zr, Mg, Ca and possibly Ga can be utilised in the SAS preparation route. Consequently, it is possible to incorporate them into these catalysts as additional refractory metal oxides, resulting in the construction of multicomponent catalysts, which have the potential to exceed performances displayed by the ternary system.

### 5.3. References

- 1 M. V. Twigg and M. S. Spencer, *Topics in Catalysis*, 2003, **22**, 191-203.
- 2 C. Rhodes, G. J. Hutchings and A. M. Ward, *Catalysis Today*, 1995, **23**, 43-58.
- 3 M. V. Twigg, *Catalyst Handbook*, Second Edition, Manson Publishing, 1989.
- 4 B. Bems, M. Schur, A. Dassenoy, H. Junkes, D. Herein and R. Schlögl, *Chem. Eur. J.*, 2003, **9**, 2039-2052.
- 5 A. M. Pollard, M. S. Spencer, R. G. Thomas, P. A. Williams, J. Holt and J. R. Jennings, *Applied Catalysis A: General*, 1992, **85**, 1-11.

- 6 M. Behrens, *Journal of Catalysis*, 2009, **267**, 24-29.
- 7 M. Behrens, S. Zander, P. Kurr, N. Jacobsen, J. Senker, G. Koch, T. Ressler, R. W. Fischer and R. Schlögl, *Journal of the American Chemical Society*, 2013, **135**, 6061-6068.
- 8 C. Baltes, S. Vukojevic and F. Schuth, *Journal of Catalysis*, 2008, **258**, 334-344.
- 9 M. S. Spencer, *Topics in Catalysis*, 1999, **8**, 259-266.
- 10 B. L. Kniep, T. Ressler, A. Rabis, F. Girgsdies, M. Baenitz, F. Steglich and R. Schlögl, *Angew. Chem. Int. Ed.*, 2004, **43**, 112-115.
- 11 D. Waller, D. Stirling, F. S. Stone and M. S. Spencer, *Faraday Discuss. Chem. Soc.*, 1989, **87**, 107-120.
- 12 E. N. Muhamad, R. Irmawati, Y. H. Taufiq-Yap, A. H. Abdullah, B. L. Kniep, F. Girgsdies and T. Ressler, *Catalysis Today*, 2008, **131**, 118-124.
- 13 S. Zander, B. Seidlhofer and M. Behrens, *Dalton Trans.*, 2012, **41**, 13413-13422.
- 14 M. Behrens and R. Schlögl, *Z. Anorg. Allg. Chem.*, 2013, **639**, 2683-2695.
- 15 A. A. Mirzaei, H. R. Shaterian, S. H. Taylor and G. J. Hutchings, *Catalysis Letters*, 2003, **87**, 103-108.
- 16 D. M. Whittle, A. A. Mirzaei, J. S. J. Hargreaves, R. W. Joyner, C. J. Kiely, S. H. Taylor and G. J. Hutchings, *Phys. Chem. Chem. Phys.*, 2002, **4**, 5915-5920.
- 17 B. L. Kniep, F. Girgsdies and T. Ressler, *Journal of Catalysis*, 2005, **236**, 34-44.
- 18 H. Jung, D. Yang, O. Joo and K. Jung, *Bull. Korean Chem. Soc.*, 2010, **31**, 1241-1246.
- 19 G. J. Millar, I. H. Holm, P. J. R. Uwins and J. Drennan, *J. Chem. Soc., Faraday Trans.*, 1998, **94**, 593-600.
- 20 E. Reverchon, I. D. Marco and E. Torino, *J. of Supercritical Fluids*, 2007, **43**, 126-138.
- 21 M. Behrens, F. Studt, I. Kasatkin, S. Kuhl, M. Havecker, F. Abild-Pedersen, S. Zander, F. Girgsdies, P. Kurr, B. Kniep, M. Tovar, R. W. Fischer, J. K. Nørskov and R. Schlögl, *Science*, 2012, **336**, 893-897.
- 22 D. B. Rasmussen, T. V. W. Janssens, B. Temel, T. Bligaard, B. Hinnemann, S. Helveg and J. Sehested, *Journal of Catalysis*, 2012, **293**, 205-2014.
- 23 S. A. Kondrat, PhD Thesis, Cardiff University, 2011.

## 6.0. Supplementary

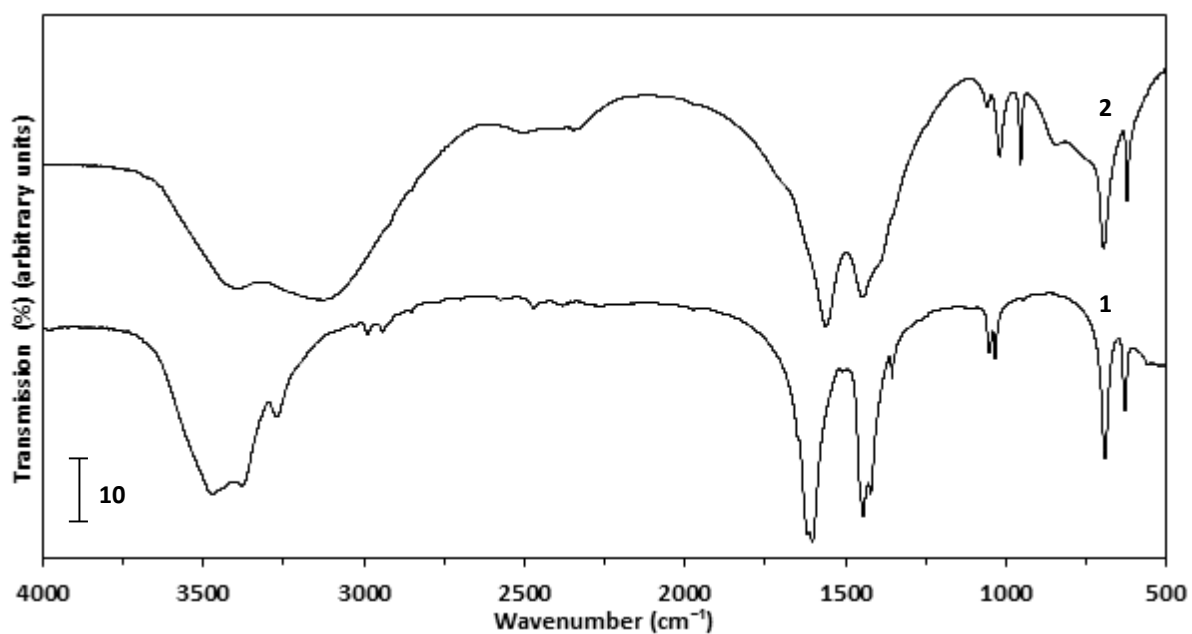


**Figure S1.** FT-IR spectra of starting materials: (1) copper (II) acetate monohydrate (2) zinc (II) acetate dihydrate.

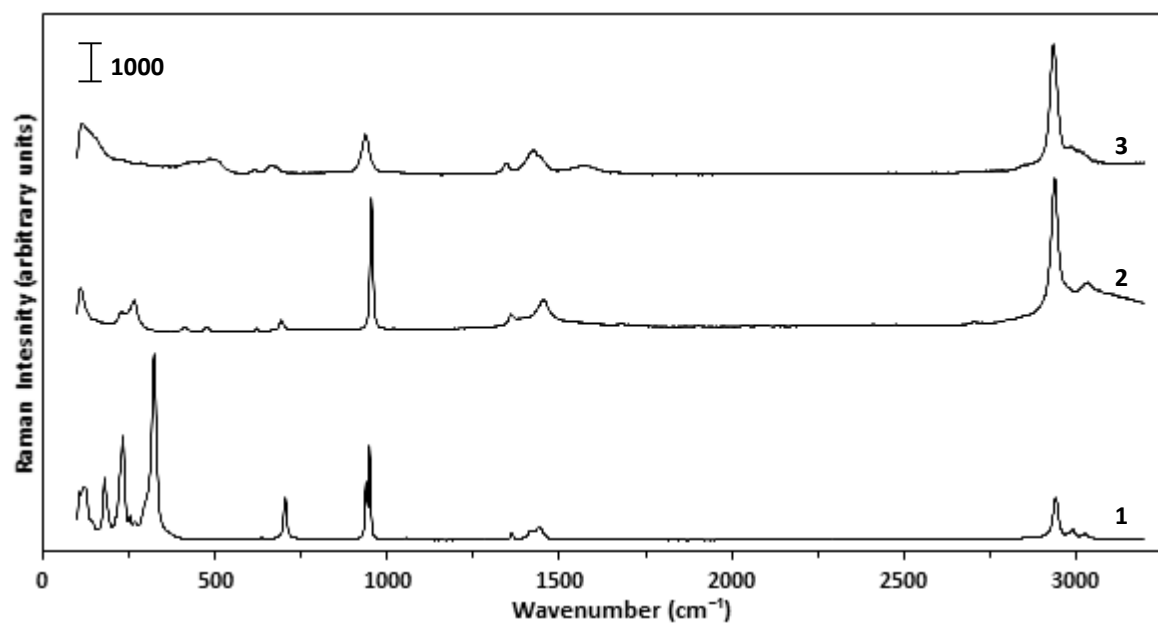


**Figure S2.** Raman spectra of acetate materials: (1) as received copper (II) acetate monohydrate (2) as received zinc (II) acetate dihydrate (3) precipitated CuZn acetate obtained from starting metal acetate solution.

**Table S1.** FT-IR observed wavenumbers (cm<sup>-1</sup>) and assignments of relevant copper and/or zinc phases.

Copper (II) acetate monohydrate <sup>a</sup>	Zinc (II) acetate dihydrate <sup>a</sup>	SAS Cu acetate	SAS CuZn acetate	SAS georgeite	SAS zincian georgeite	Co-precipitated malachite	Co-precipitated zincian malachite	Co-precipitated aurichalcite	Synthetic smithsonite <sup>1</sup>	Band assignment
3489, 3367, 3304	3378, 3141	3369	3275	3302	3289	3393, 3343	3408, 3325	3392, 3251	3356*	v(O-H)
2989, 2940										v(C-H)
1603, 1597	1560	1574	1560							v <sub>a</sub> (COO) <sup>-</sup>
1444, 1418	1445	1412	1420							v <sub>s</sub> (COO) <sup>-</sup>
				1475, 1403	1475, 1404	1518, 1387	1526, 1488, 1425 1387	1569, 1522, 1393, 1387	1392	v <sub>3</sub> (CO <sub>3</sub> ) <sup>2-</sup>
1354	1382	1397	1344							δ(CH <sub>3</sub> )
						1044, 881	1047, 1023			v(O-H) out of plane
1056, 1036	1051, 1024	1055, 1020	1053, 1043							δ(CH <sub>3</sub> )
				1048	1048	1095	1098	1071, 1060		v <sub>1</sub> (CO <sub>3</sub> ) <sup>2-</sup>
	951									v(C-C)
		832	832	831	835	824, 803	870, 819	829, 816	864, 834	v <sub>2</sub> (CO <sub>3</sub> ) <sup>2-</sup>
						750, 712	776, 742, 706	750, 706	743, 715	v <sub>4</sub> (CO <sub>3</sub> ) <sup>2-</sup>
696	701	679	681							α(COO) <sup>-</sup>
632	619	618	619							π(COO) <sup>-</sup>

<sup>a</sup> Material purchased from Sigma Aldrich.

\* Peak resulting from adsorbed water.

<sup>1</sup> M. C. Hales and R. L. Frost, *Polyhedron*, 2007, **26**, 4955-4962.

Supplementary

**Table S2.** Raman observed wavenumbers (cm<sup>-1</sup>) and assignments of relevant copper and/or zinc phases.

Copper (II) acetate monohydrate <sup>a</sup>	Zinc (II) acetate dihydrate <sup>a</sup>	SAS Cu acetate	SAS CuZn acetate	SAS georgeite	SAS zincian georgeite	Co-precipitated malachite	Co-precipitated zincian malachite	Co-precipitated aurichalcite	Synthetic smithsonite <sup>1</sup>	Band assignment
3022	3059	3496	3496	3380	3381	3379, 3324	3381, 3319	3353	3472, 3265*	$\nu_s(\text{O-H})$
3004	3031									$\nu_a(\text{C-H})$
2942	2938	2931	2934	2934	2934					$\nu(\text{C-H})$
		1564	1566							$\nu_a(\text{COO})^-$
1418	1455	1410	1428							$\nu_s(\text{COO})^-$
						1495, 1375	1503, 1472, 1380	1496	1408	$\nu_3(\text{CO}_3)^{2-}$
1441, 1362	1361		1347							$\delta_s(\text{C-H})$
			1092	1086	1091	1101	1087	1075	1092	$\nu_1(\text{CO}_3)^{2-}$
						1054	1079			$\delta(\text{O-H})$
949	954	938	938	938	938					$\nu(\text{C-C})$
						817	819			$\nu_2(\text{CO}_3)^{2-}$
				753, 708	771, 724	761, 722	748, 722	751, 716	730	$\nu_4(\text{CO}_3)^{2-}$
703	693		677							$\alpha(\text{COO})^-$
	644		612							$\pi(\text{COO})^-$
	478		503							$\gamma(\text{COO})^-$

<sup>a</sup> Material purchased from Sigma Aldrich.

\* Peaks resulting from adsorbed water.

<sup>1</sup> M. C. Hales and R. L. Frost, *Polyhedron*, 2007, **26**, 4955-4962.

**Note:** The SAS CuZn acetate displays a carbonate band at 1092 cm<sup>-1</sup> indicating residual amounts of zincian georgeite present. No carbonate bands were found though regarding SAS Cu acetate. However it does have an FT-IR band at 832 cm<sup>-1</sup> which confirms that the georgeite phase is present in this material.

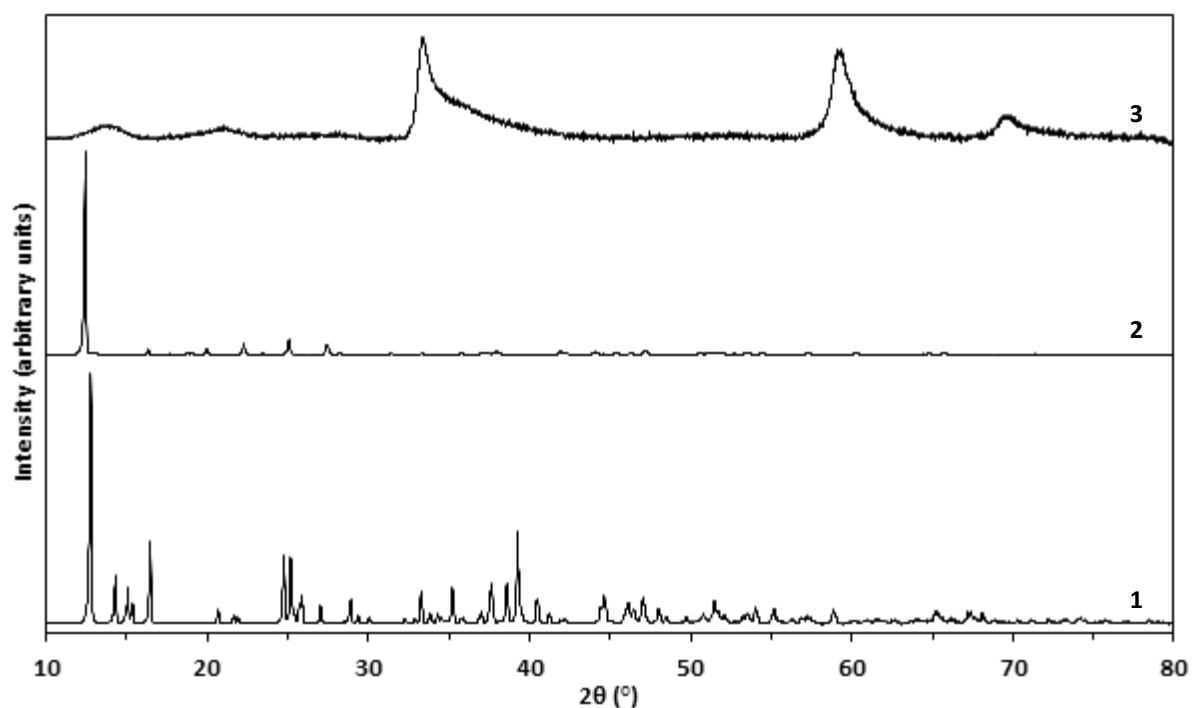


**Figure S3.** XRD patterns of acetate phases: (1) as received copper (II) acetate monohydrate (2) as received zinc (II) acetate dihydrate (3) CuZn acetate precipitate obtained from starting metal acetate solution. Peaks at 33.4 and 59.1 ° shown in (3) can be seen in georgeite samples prepared using water contents  $\geq 5$  vol.%.

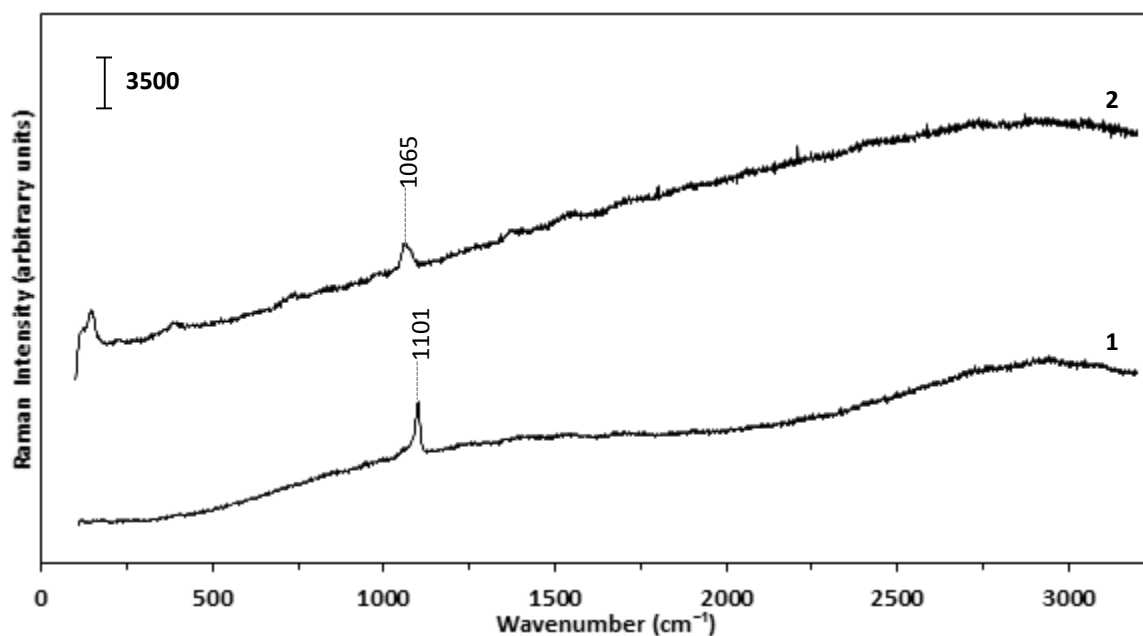


**Figure S4.** Raman spectra of zinc carbonate phases: (1) SAS prepared using standard conditions of 110 bar and 40 °C (2) as received zinc carbonate, basic.

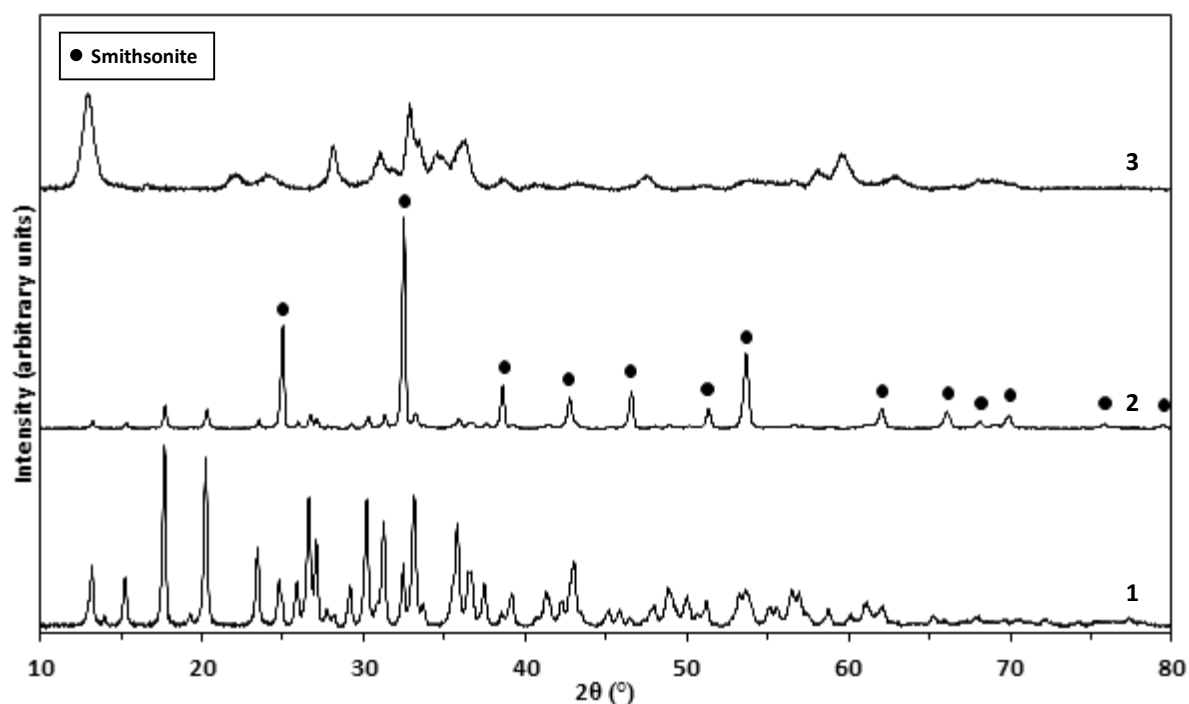


**Figure S5.** XRD patterns of zinc carbonate phases: (1) SAS prepared using standard conditions of 110 bar and 40 °C (2) SAS prepared at 150 bar, 60 °C (3) as received zinc carbonate, basic. Phase analysis determined that all reflections present in (3) match the hydrozincite phase.

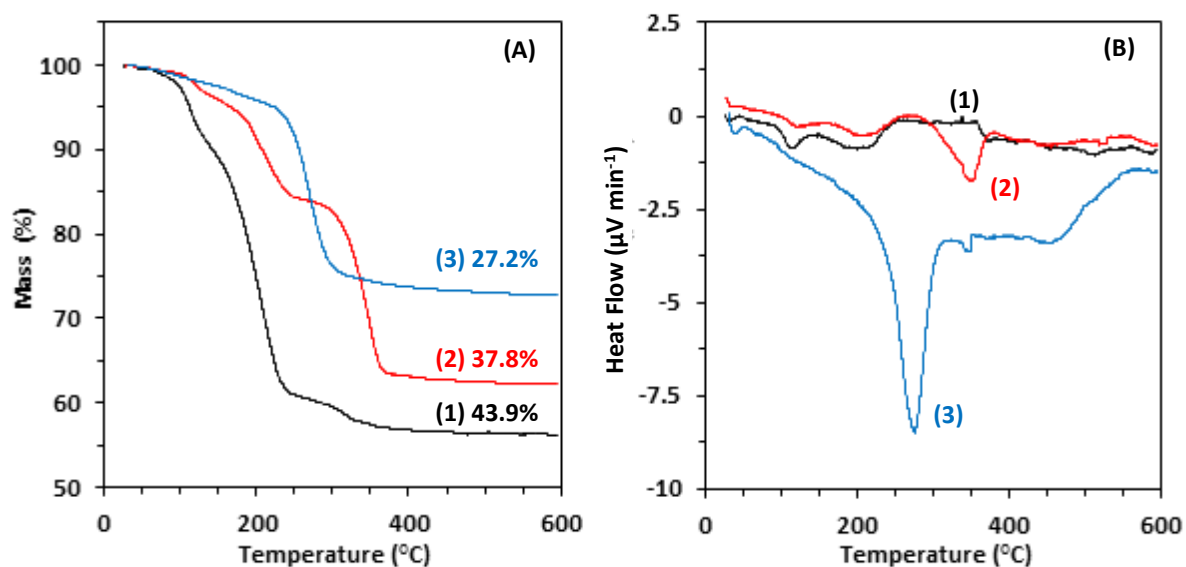


**Figure S6.** (A) TGA and (B) DTA of zinc carbonate phases: (1. black) SAS prepared using standard conditions of 110 bar and 40 °C (2. red) SAS prepared at 150 bar, 60 °C (3. blue) as received zinc carbonate, basic. For clarity, the total mass loss is indicated for each material.

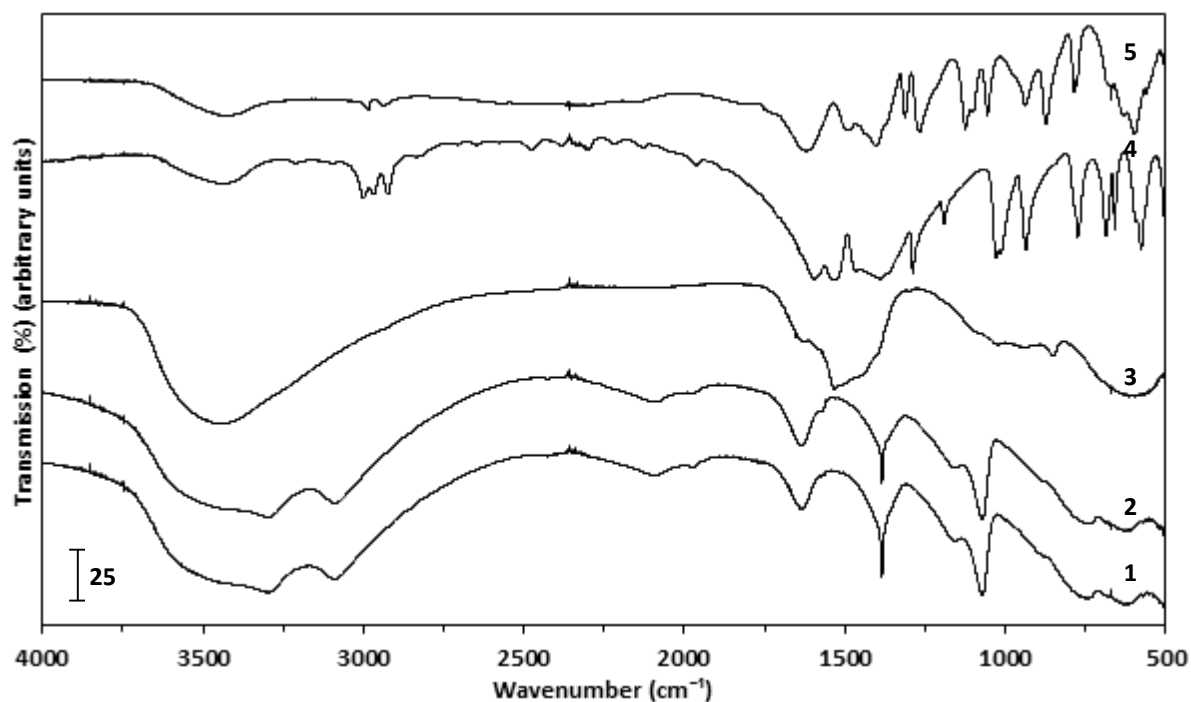


**Figure S7.** FT-IR spectra of as received aluminium reagents and after SAS precipitation: (1) SAS prepared aluminium boehmite (2) as received aluminium boehmite (3) SAS prepared aluminium acetylacetonate (4) as received aluminium acetylacetonate (5) as received aluminium L-lactate.

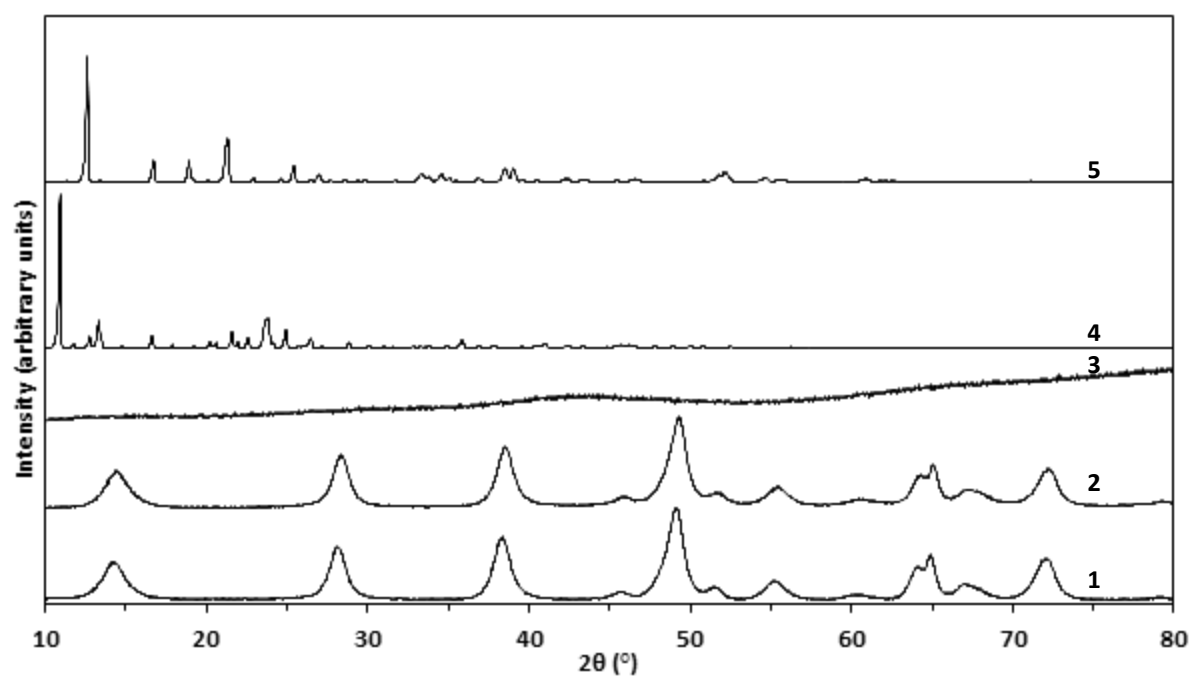


**Figure S8.** XRD patterns of as received aluminium reagents and after SAS precipitation: (1) SAS prepared aluminium boehmite (2) as received aluminium boehmite (3) SAS prepared aluminium acetylacetonate (4) as received aluminium acetylacetonate (5) as received aluminium L-lactate.

**Table S3.** EDX analysis of SAS prepared georgeite precursors formed using aluminium acetylacetonate with various solvent mixtures and pressures. The nominal Cu/Zn/Al molar ratio was 6/3/1.

Water content (%)	Pressure (bar)	Atomic (%) <sup>a</sup>			Determined Cu/Zn/Al molar ratio
		Cu	Zn	Al	
5	110	52.5	29	18.5	5.3/2.9/1.8
10	110	54	29	17	5.4/2.9/1.7
10	150	52	28	20	5.2/2.8/2
20	110	55.5	29	15.5	5.6/2.9/1.5

<sup>a</sup> Standard deviation  $\pm 3\%$ .

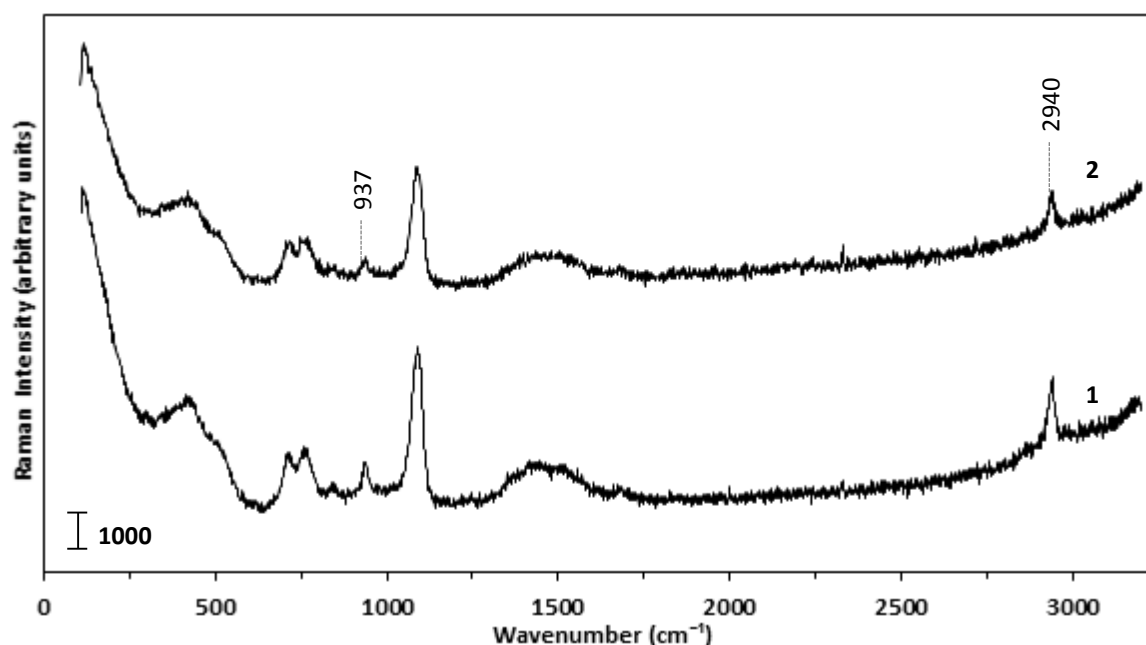


**Figure S9.** Raman spectra of zincian georgeite prepared by co-precipitation using ammonium carbonate with: (1) no washing step included (2) washing step included. Peaks shown at 937 and 2940  $\text{cm}^{-1}$  indicate the acetate phase is also present and remains after the washing step. The nominal Cu/Zn molar ratio was 2/1.

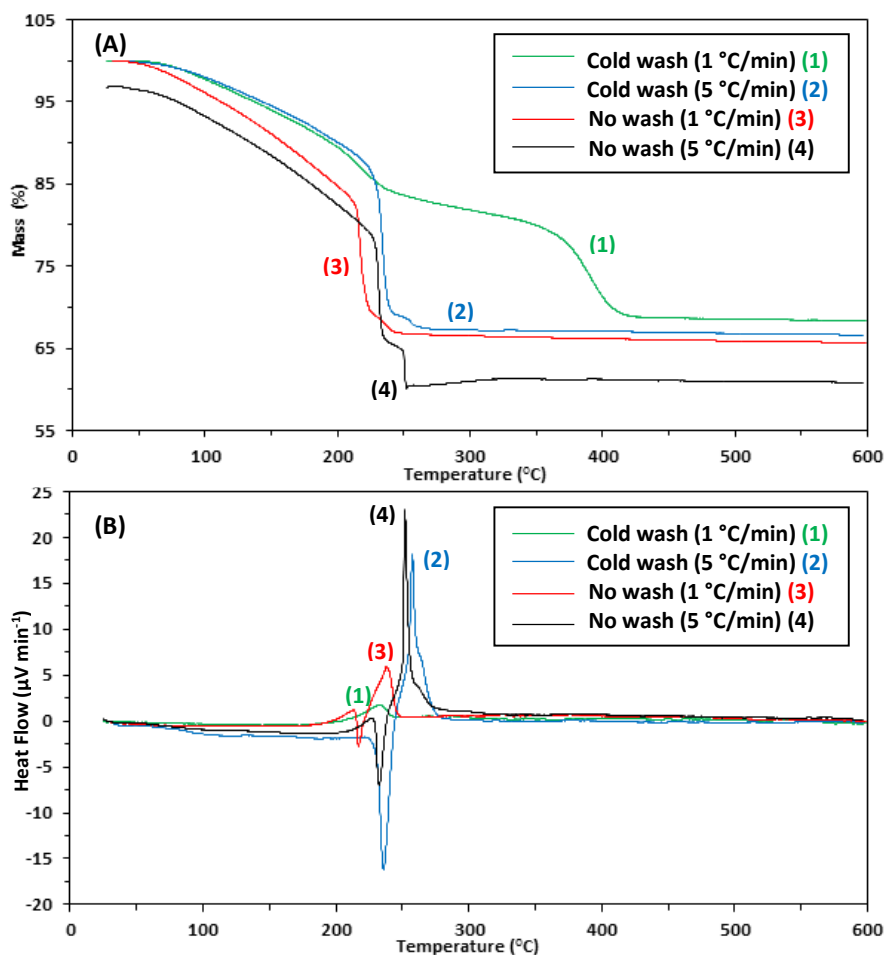


**Figure S10.** (A) TGA and (B) DTA of zincian georgeite prepared by co-precipitation using ammonium bicarbonate to investigate the effect of washing treatment and ramp rate on the thermal decomposition process. The nominal Cu/Zn molar ratio was 2/1. A numbered key is also provided for clarity.

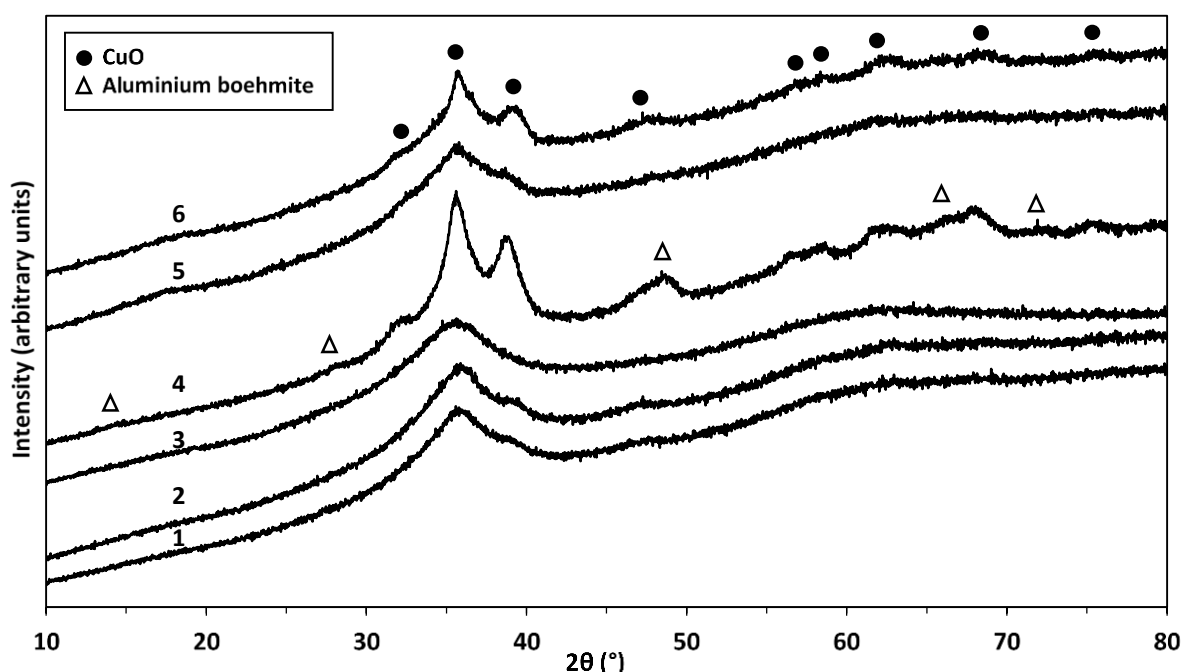


**Figure S11.** XRD patterns of calcined georgeite materials tested at JM in Billingham for methanol synthesis and the LTS reaction. Preparation details of each sample: (1) SAS using 10 vol.% H<sub>2</sub>O, Cu/Zn = 2/1 (2) SAS using 5 vol.% H<sub>2</sub>O, Cu/Zn = 2/1 (3) SAS using 5 vol.% H<sub>2</sub>O, Cu/Zn = 1/1 (4) SAS using 5 vol.% H<sub>2</sub>O, Cu/Zn/Al = 6/3/1 (5) CP using 15 mg/ml copper acetate, Cu/Zn = 2/1 (6) CP using 70 mg/ml copper acetate, Cu/Zn = 2/1.

**Table S4.** Summary of catalyst testing for methanol synthesis. Reaction temperature was increased 15 °C every 18 hours between 190-235 °C before being decreased back to 190 °C. The MeOH productivity recorded at the end of each step is presented for each catalyst.

Temperature (°C)	MeOH space time yield (mol <sub>MeOH</sub> h <sup>-1</sup> kg <sup>-1</sup> )					
	A	B	C	D	E	F
190	2.8501	2.7391	2.2243	3.0248	2.1795	2.861
205	3.947	3.967	3.2533	4.4585	2.9597	4.6536
220	5.7717	5.8009	4.8499	6.6811	4.1232	7.2174
235	7.5636	7.5076	6.5091	8.3775	5.4797	8.7007
250	6.9751	6.9768	6.4363	7.186	5.8184	7.2656
190	1.6025	1.6217	1.4017	2.0402	1.2348	2.4108
<b>Final stability (%)</b>	<b>56</b>	<b>59</b>	<b>63</b>	<b>67</b>	<b>57</b>	<b>84</b>

Catalysts: (A) SAS 10% H<sub>2</sub>O (2/1) (B) SAS 5% H<sub>2</sub>O (2/1) (C) SAS 5% H<sub>2</sub>O (1/1) (D) SAS 5% H<sub>2</sub>O (6/3/1) (E) CP (2/1) (F) JM 51-2 methanol synthesis industrial catalyst.

**Table S5.** Comparison of methanol formation rates of catalysts tested for the LTS reaction.

Catalyst details	Time on line (h)	MeOH (ppm)	MeOH formation rate (mmol h <sup>-1</sup> )	Relative MeOH ratio	CO conversion rate (mmol h <sup>-1</sup> )	MeOH formation relative to CO conversion (x10 <sup>6</sup> )
SAS 10% 2/1	67.5	806	0.0003	3.17	41.551	7.22
	91.5	887	0.0003	3.59	41.34	7.26
SAS 5% 2/1	67.5	769	0.0003	3.03	41.651	7.2
	91.5	777	0.0003	3.17	41.638	7.2
SAS 5% 1/1	67.5	594	0.0002	2.2	43.097	4.64
	91.5	587	0.0002	2.34	42.985	4.65
SAS 5% 6/3/1	67.5	805	0.0003	3.16	41.663	7.2
	91.5	764	0.0003	3.1	41.663	7.2
CP (15mg/ml)	67.5	438	0.0002	1.62	41.301	4.84
	91.5	452	0.0002	1.82	41.386	4.83
CP (70mg/ml)	67.5	461	0.0002	1.82	40.291	4.96
	91.5	480	0.0002	1.96	39.971	5
JM 83-0 Std	67.5	252	0.0001	1	36.86	2.71
	91.5	244	0.0001	1	36.301	2.75

Mass velocity = 75000 L h<sup>-1</sup> kg<sup>-1</sup>, Gas flow rate = 25 L/h and exit water flow rate = 0.0087 L/h. All other reaction conditions are the same as previously specified.

**Table S6.** XAFS fitting parameters for georgeite.

Georgeite Cu K edge					
Abs Sc.	N	R (Å)	2σ <sup>2</sup> (Å) <sup>2</sup>	E <sub>f</sub> (ev)	R <sub>factor</sub>
Cu-O	4 (fixed)	1.94 (1)	0.004 (1)	2 (1)	0.007
Cu-O	2 (fixed)	2.45 (fixed)	0.03 (fixed)		

Fitting parameters: S<sub>0</sub><sup>2</sup> = 0.72 as deduced by CuO standard; Fit range 3 < k < 12, 1 < R < 3.5; # of independent points = 14.

**Table S7.** XAFS fitting parameters for malachite.

Malachite Cu K edge					
Abs Sc.	N	R (Å)	2σ <sup>2</sup> (Å) <sup>2</sup>	E <sub>f</sub> (ev)	R <sub>factor</sub>
Cu-O	4 (fixed)	1.92 (2)	0.007 (2)	-1 (1)	0.014
Cu-O	2 (fixed)	2.45 (7)	0.02 (1)		
Cu-C	3 (fixed)	3.01 (4)	0.002 (6)		
Cu-Cu	2 (fixed)	3.12 (4)	0.006 (5)	-1 (1)	0.014
Cu-Cu	3 (fixed)	3.31 (3)	0.007 (3)		

Fitting parameters: S<sub>0</sub><sup>2</sup> = 0.72 as deduced by CuO standard; Fit range 3 < k < 12, 1 < R < 3.5; # of independent points = 14.

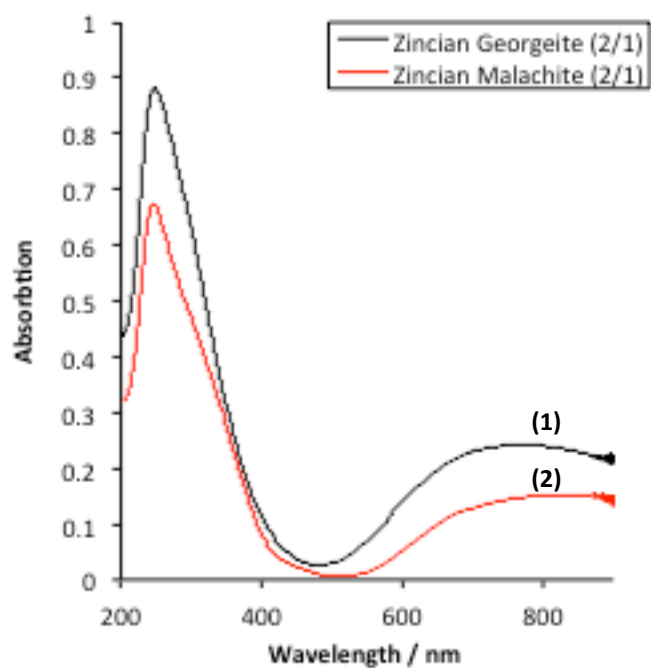


**Figure S12.** DRUVS spectra of (1) zincian georgeite and (2) zincian malachite.

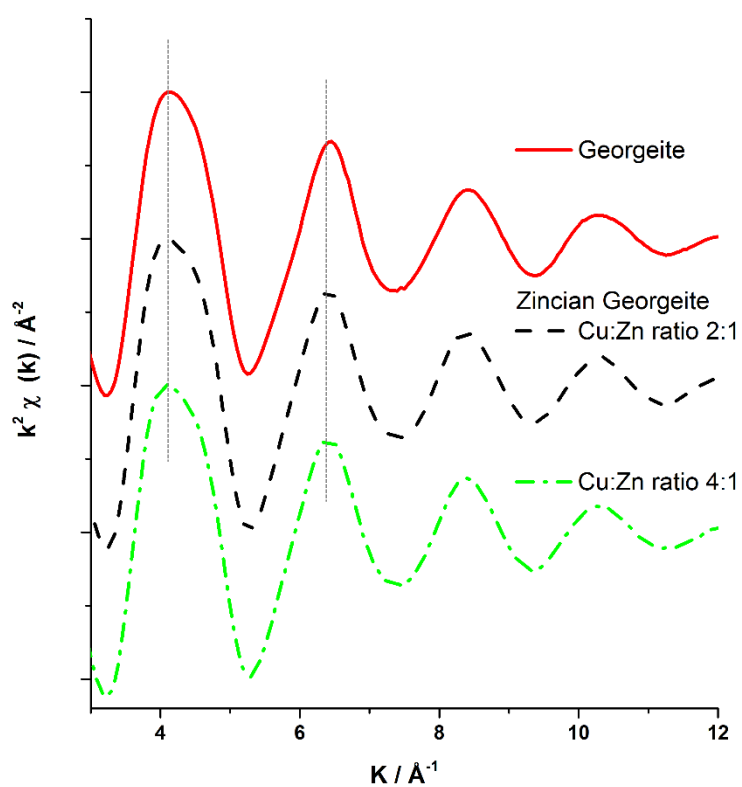


**Figure S13.** Cu K edge EXAFS ( $\chi$ ) analysis of georgeite and zincian georgeite (2/1 and 4/1 metal molar ratios) used to identify any short order structural changes from varying the degree of zinc incorporation into the georgeite phase. Grey hashed lines are provided to assist with comparisons.

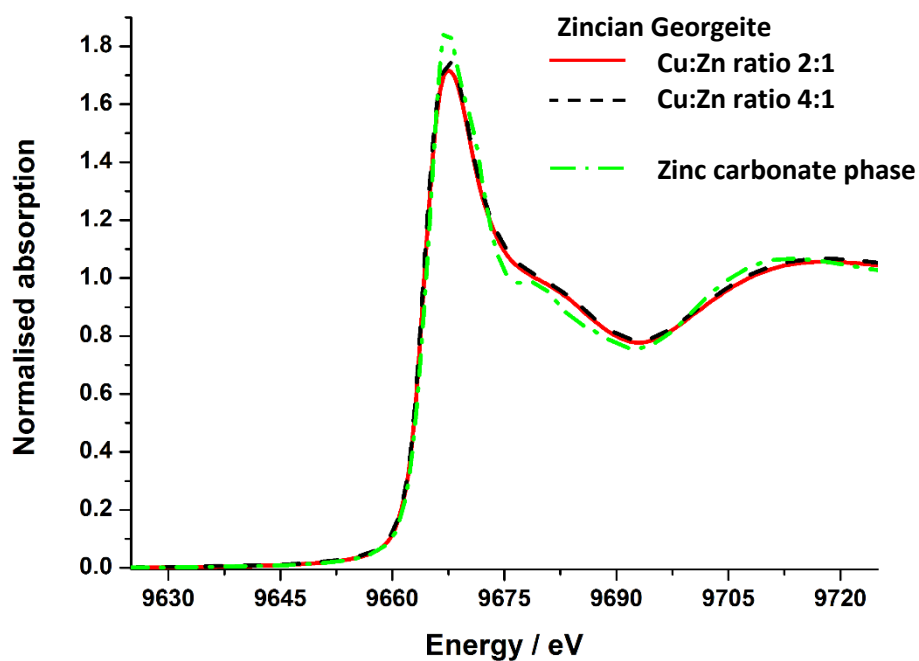


**Figure S14.** Zn K edge XANES spectra of zincian georgeite (2/1 and 4/1 metal molar ratios) and the SAS prepared zinc carbonate phase.

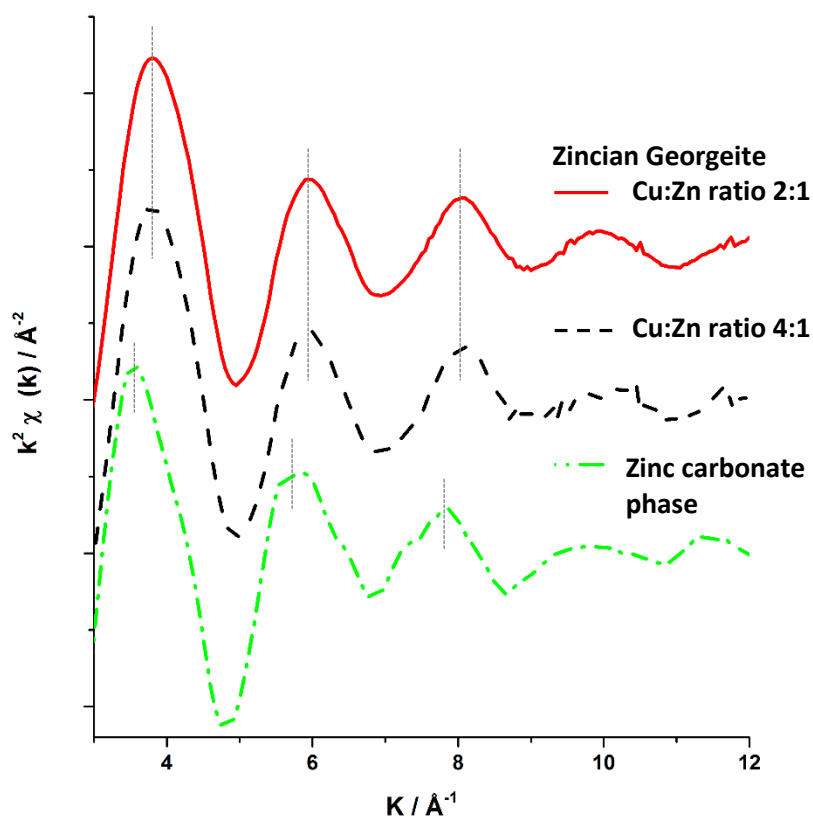


**Figure S15.** Zn K edge EXAFS ( $\chi$ ) analysis of zincian georgeite (2/1 and 4/1 metal molar ratios) and the SAS prepared zinc carbonate phase. Grey hashed lines are provided to assist with comparisons.

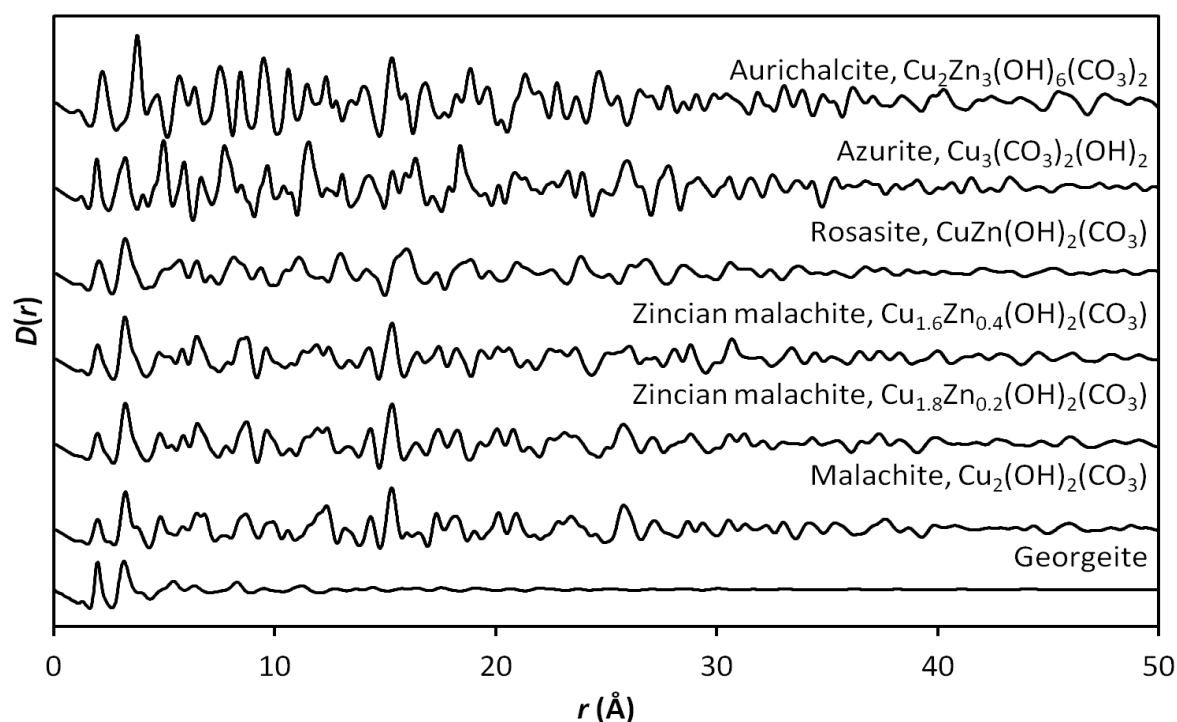


**Figure S16.** PDF analysis to compare observed data for georgeite against simulated data of crystalline hydroxycarbonates with similar compositions.

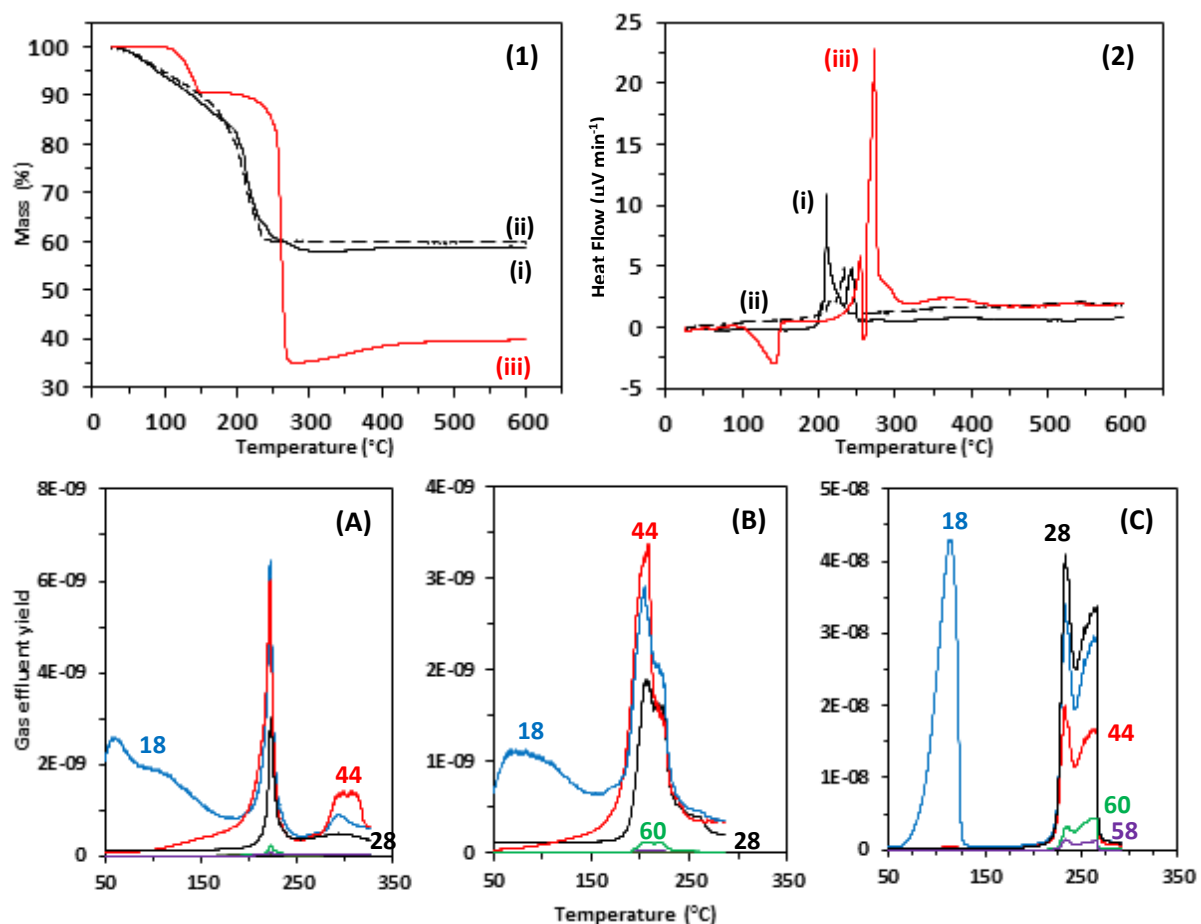


**Figure S17.** (1) TGA and (2) DTA of: SAS prepared CuZn acetate (i. black) and Cu acetate (ii. dashed black) with as received Cu acetate (iii. red). Notations are also provided for clarity. EGA analysis of: (A) SAS prepared CuZn acetate and (B) Cu acetate with (C) as received Cu acetate. Mass spectrometry traces presented for  $m/z$  values of: 60 (green) 58 (purple) 44 (red) 28 (black) 18 (blue) and 16 (brown). Main traces are illustrated for clarity.

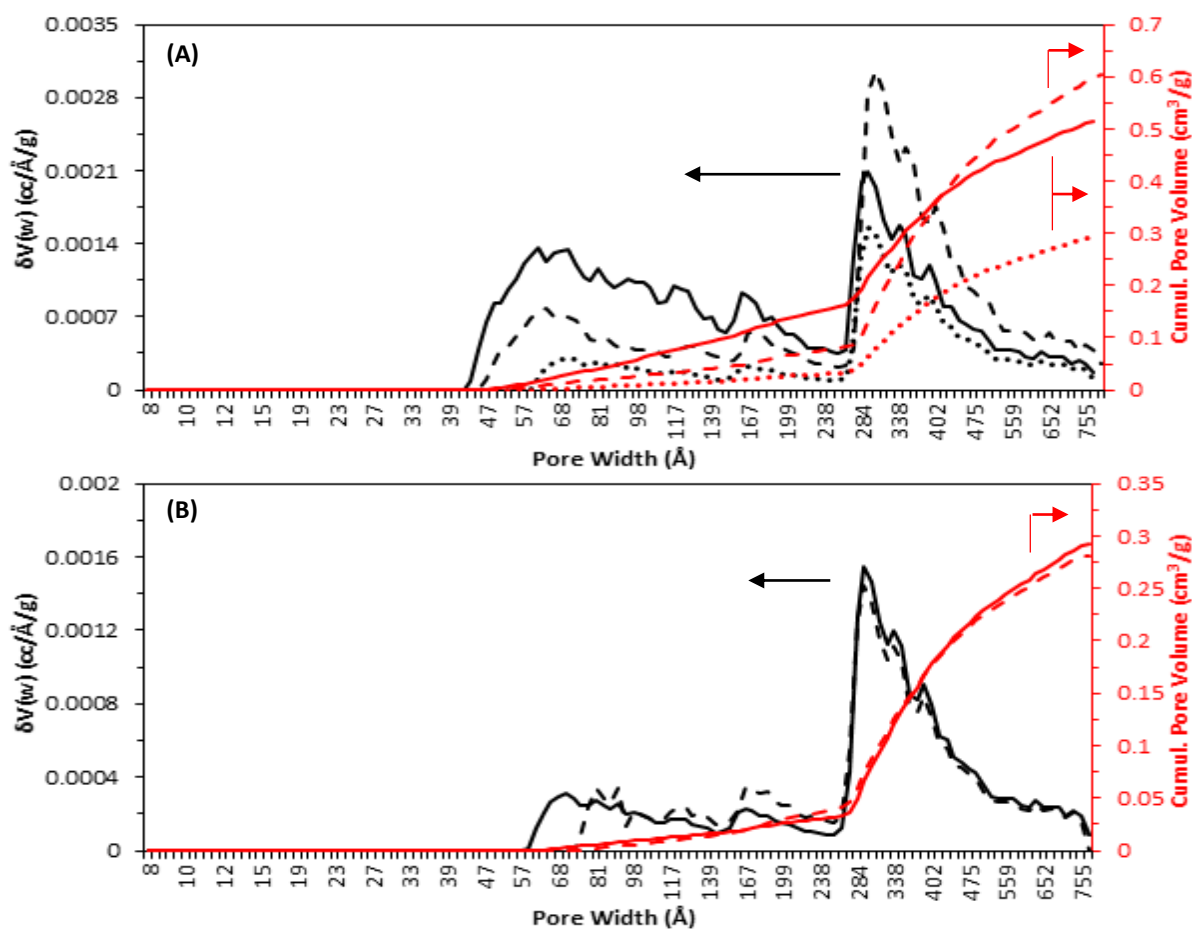


**Figure S18.** DFT Monte-Carlo pore size distribution and cumulative pore volume of materials before and after calcination: (A) Zincian georgeite prepared by SAS using 5% (solid) and 10% (hashed) vol. H<sub>2</sub>O and by co-precipitation (dotted). (B) Zincian georgeite (solid) and zincian malachite (hashed) prepared by co-precipitation. Solid lines represent the precursors with hashed lines representing materials after calcination using optimum conditions (300 °C, 2 h). Arrows are also presented for clarity.

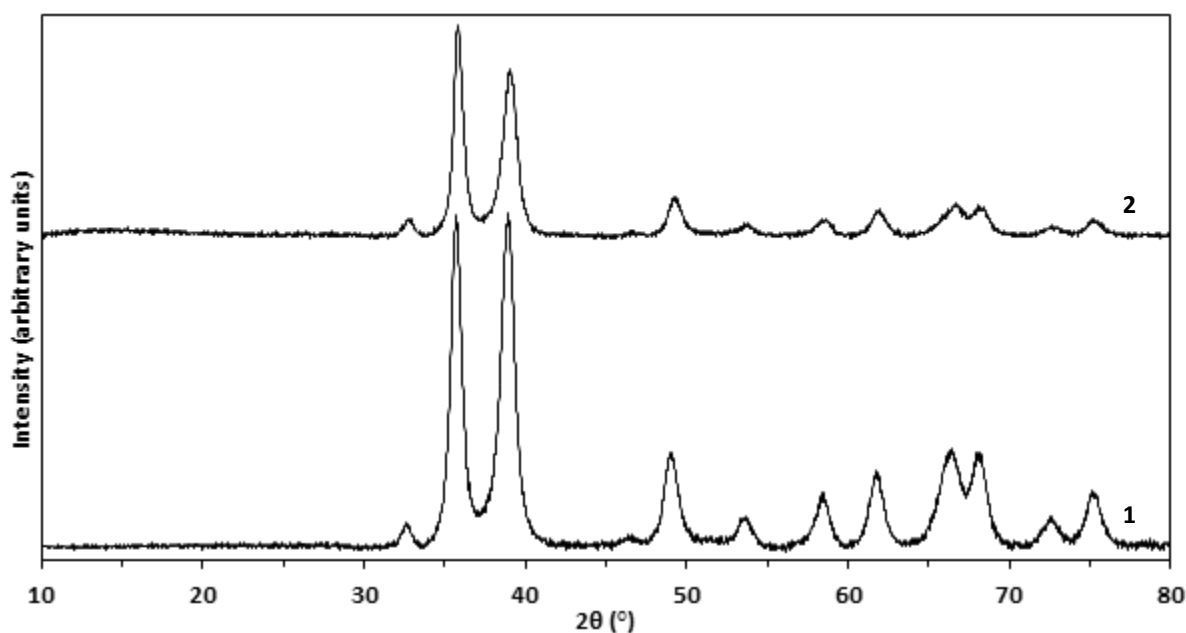


**Figure S19.** XRD patterns of: (1) Georgeite and (2) malachite after being calcined using standard conditions (300 °C, 2 h). Phase analysis indicated that all reflections are associated with the CuO phase. Clear differences are apparent in the relative intensities of (-111) and (111) reflections at 35.5 and 38.7 ° respectively.

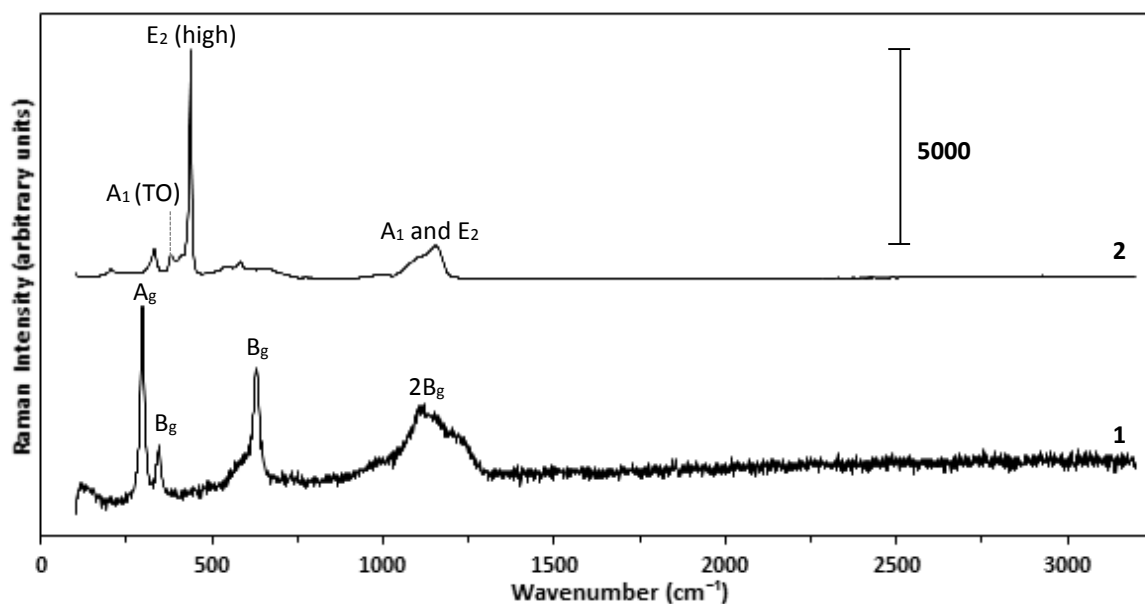


**Figure S20.** Raman spectra of as received: (1) CuO and (2) ZnO. Peaks have been assigned according to the literature (see main text).

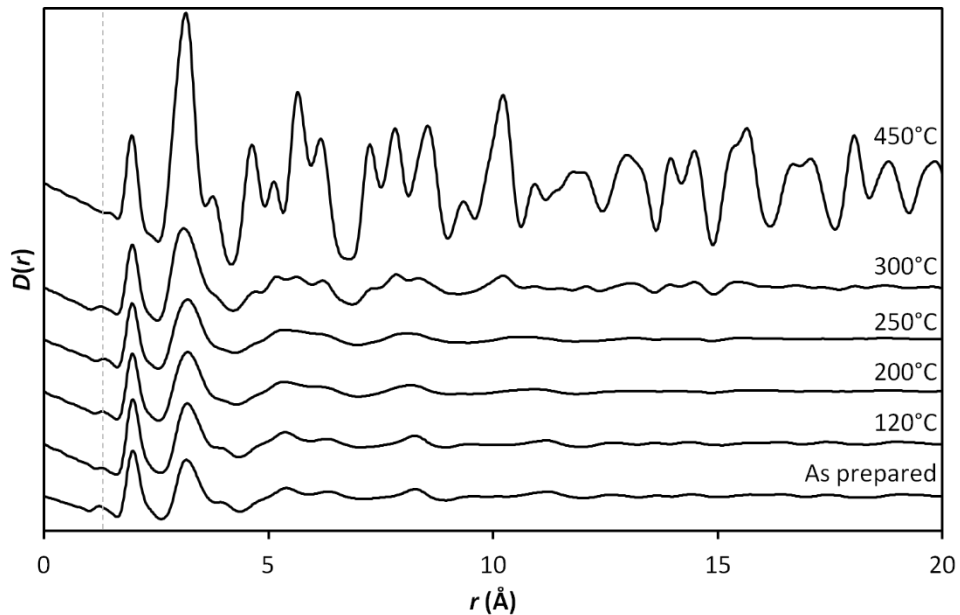


**Figure S21.** PDF analysis of zincian georgeite (2/1) before and after calcination using the temperatures indicated. The grey hashed line represents the position of the C-O peak which is retained until 300 °C and little change is observed up until this temperature.

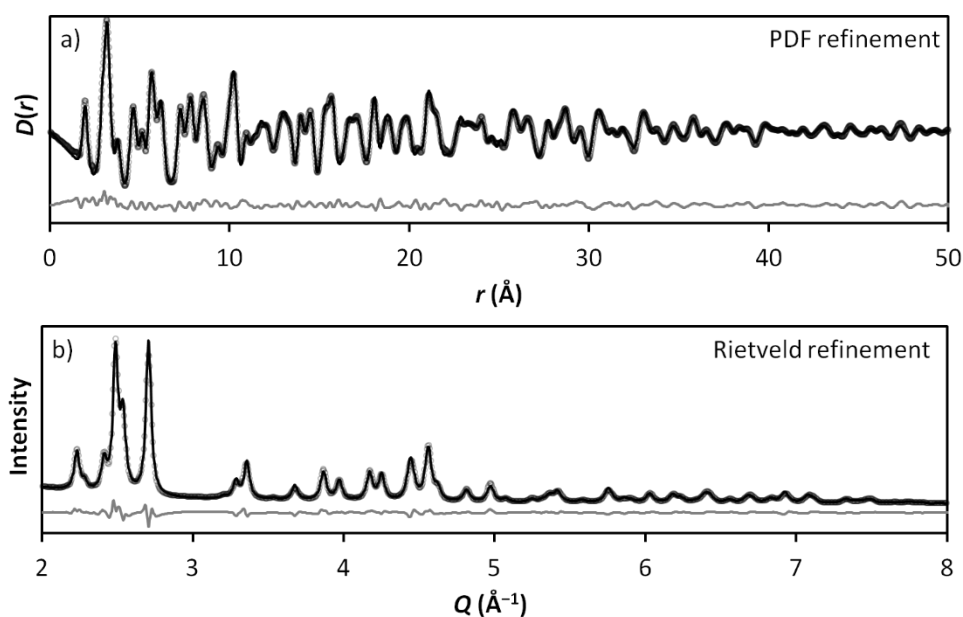


**Figure S22.** (a) PDF and (b) Rietveld fits of zincian georgeite (2/1) after calcination at 450 °C for 2 hours. The observed data is shown as open circles, the fit is a solid black line and the difference is the grey line. Both techniques determine the product to be a mixture of CuO and ZnO (weight ratio of 68:32 by PDF and 67.7(4):32.3(4) by Rietveld).

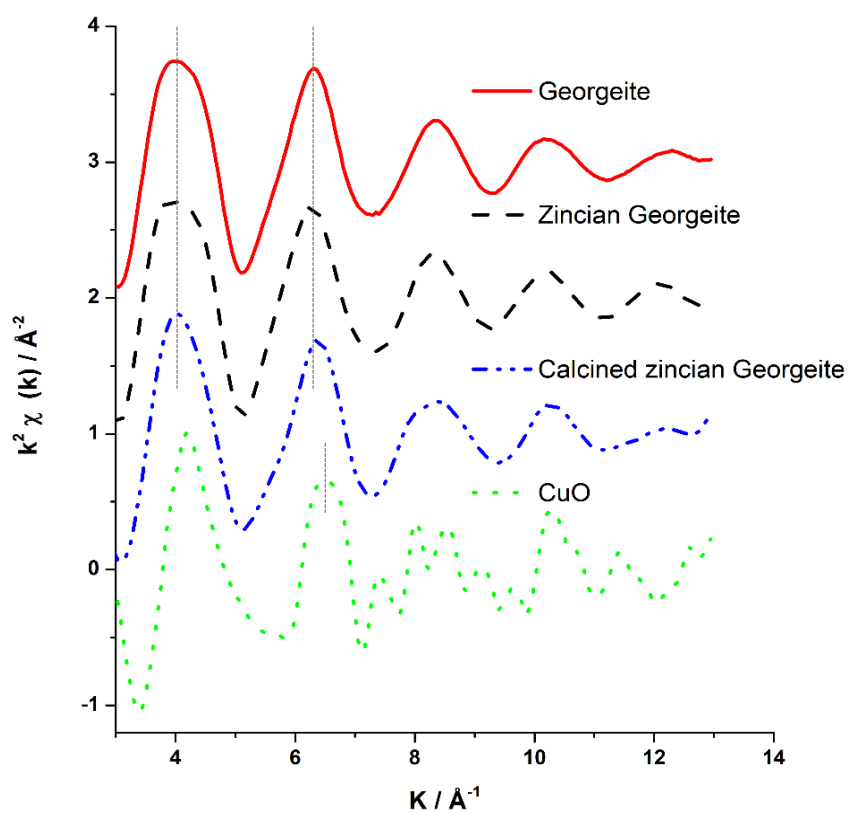


**Figure S23.** Cu K edge EXAFS ( $\chi$ ) analysis of zincian georgeite (2/1) before and after calcination using standard conditions. Georgeite and CuO also provided with grey hashed lines to assist comparisons.

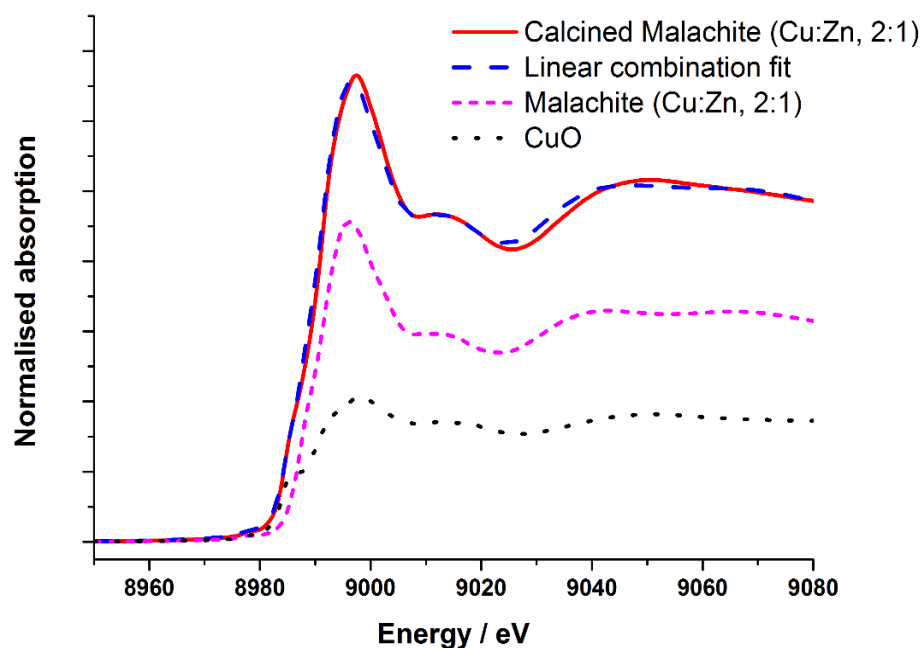


**Figure S24.** Cu K edge XANES spectra providing a linear combination fit of zincian malachite (2/1) calcined at 300 °C with CuO.

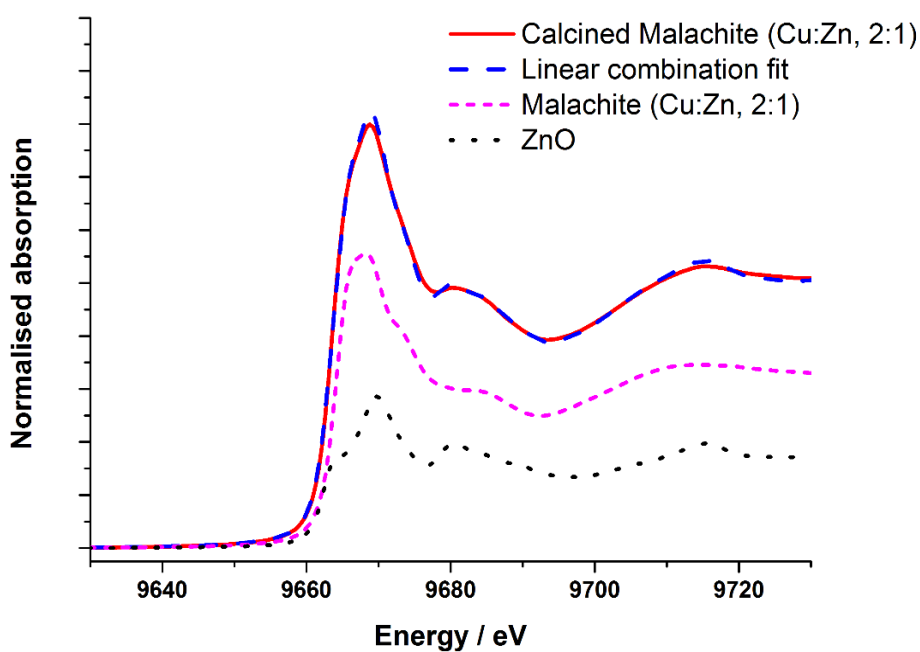


**Figure S25.** Zn K edge XANES spectra providing a linear combination fit of zincian malachite (2/1) calcined at 300 °C with ZnO.

**Table S8.** Linear combination fit of XANES spectra of zincian malachite (2/1) calcined at 300 °C.

Cu K edge	35% CuO	$R_{\text{factor}} = 0.003$
	65% Starting material	
Zn K edge	35% ZnO	$R_{\text{factor}} = 0.0006$
	65% Starting material	

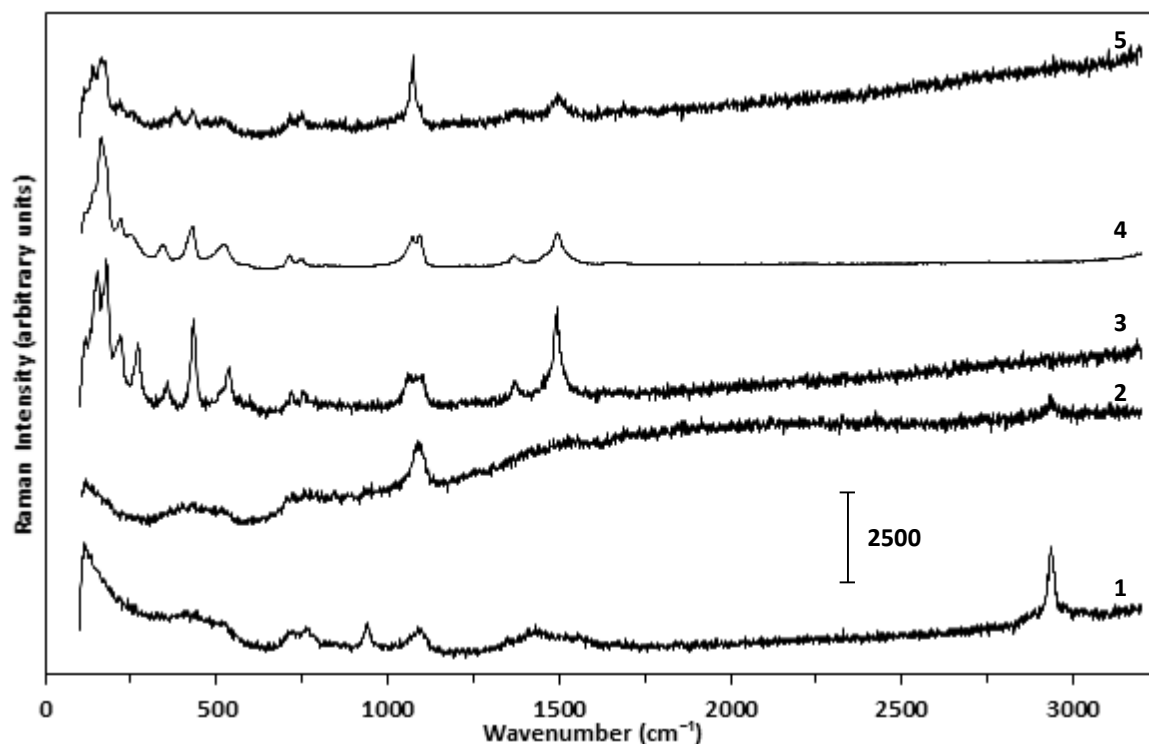


**Figure S26.** Raman spectra of copper and copper-zinc hydroxycarbonate minerals: (1) Georgeite (2) zincian georgeite (2/1) (3) malachite (2/1) (4) zincian malachite (2/1) (5) aurichalcite (1/1). Cu/Zn metal molar ratios provided in brackets.

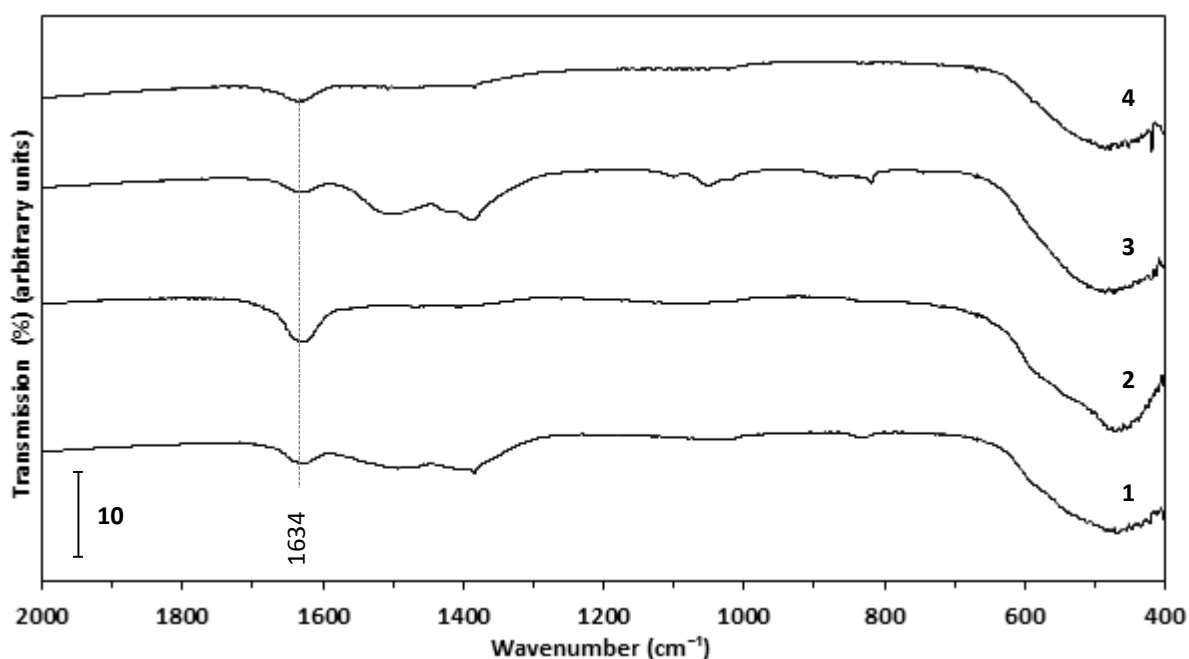


**Figure S27.** FT-IR spectra of zincian georgeite (2/1) calcined at: (1) 400 °C and (2) 450 °C. For comparison zincian malachite (2/1) calcined at: (3) 350 °C and (4) 375 °C is also presented illustrating thermal limit of carbonates. Samples were calcined for 2 hours. Peak shown at 1634  $\text{cm}^{-1}$  is assigned as physisorbed water.

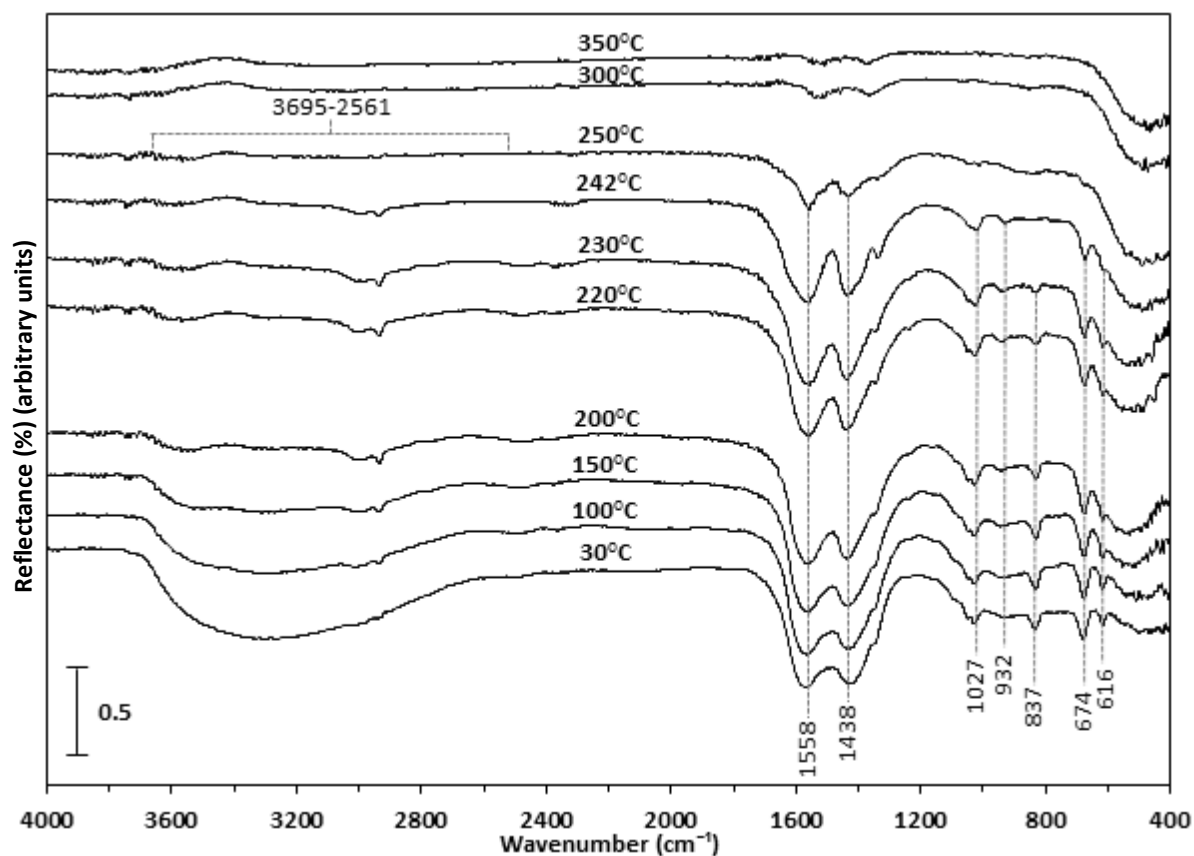


**Figure S28.** *In-situ* DRIFTS analysis for the thermal decomposition in air of SAS prepared CuZn acetate. The temperature at which each spectrum was recorded is indicated on each trace. The analysis was carried out using an air flow of 50 ml/min and a ramp rate of 2 °C/min.

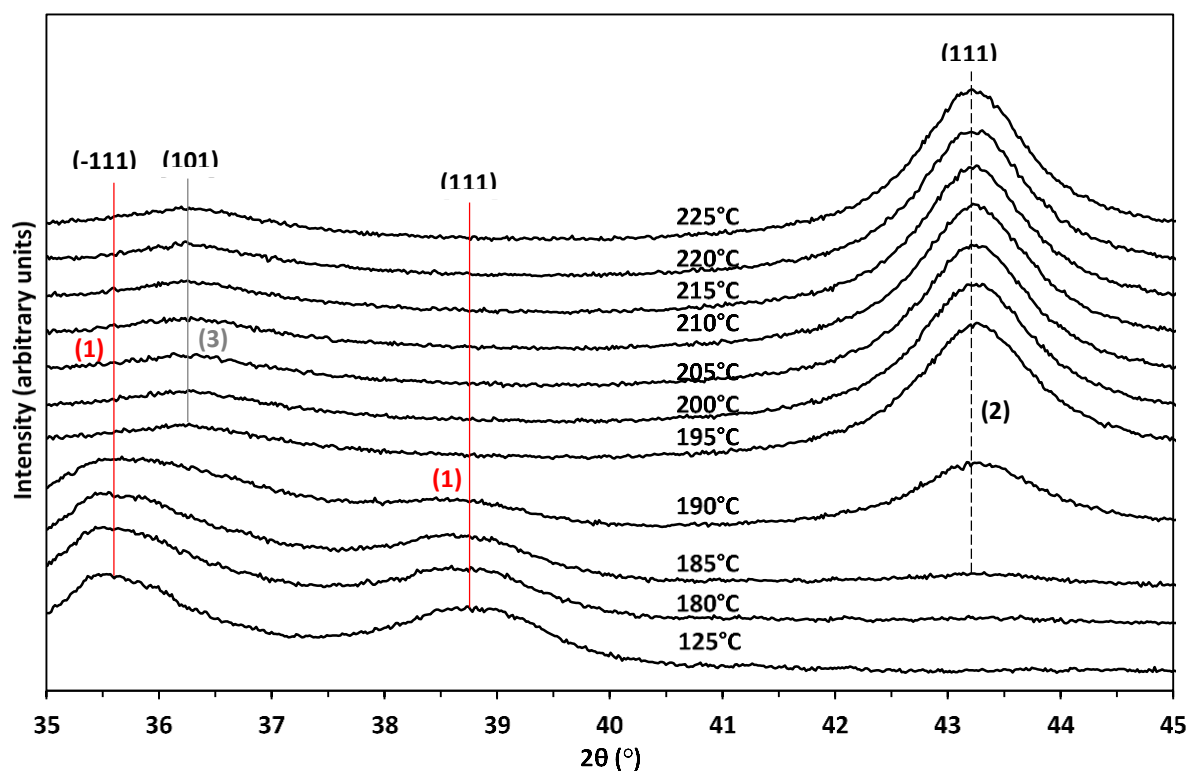


**Figure S29.** *In-situ* XRD analysis for the reduction of the calcined MeOH synthesis 51-2 industrial standard (6/3/1). See main text for reduction conditions. Reflections assigned as CuO (1. red), Cu (2. hashed black) and ZnO (3. grey) phases.